

**UNIVERSITÀ  
DEGLI STUDI  
DI PADOVA**

**UNIVERSITÀ DEGLI STUDI DI PADOVA**

**DEPARTMENT OF CHEMICAL SCIENCES**

---

**PH.D. COURSE IN:** Molecular Sciences

**CURRICULUM:** Chemistry

**CYCLE:** XXIV

**THEORETICAL INVESTIGATION OF TEMPERATURE-DEPENDENT  
EMISSION PARAMETERS IN LANTHANIDE-BASED LUMINESCENT  
MOLECULAR THERMOMETERS**

**COORDINATOR:** Ch.mo Prof. Leonard J. Prins

**SUPERVISOR:** Ch.mo Prof. Maurizio Casarin

**CO-SUPERVISOR:** Dr.ssa Silvia Carlotto

**PH.D. STUDENT:** Luca Babetto



*“A ship in harbor is safe, but that is not what ships are built for.”*  
John A. Shedd, *Salt from My Attic* (**1928**)



## **ABSTRACT**

In this Ph.D. thesis, centred around the study of lanthanide-based luminescent molecular systems with applications in thermometry, several high-level quantistic calculation techniques have been explored; these have been applied to determine parameters and molecular characteristics, which are useful for the comprehension of the underlying mechanisms defining the temperature dependence of the optical properties. After a brief introduction in which the general nature of the systems is discussed, theoretical bases of numerical simulations are illustrated; scientific articles published on international journals with peer review and describing the theoretical modeling results are also included. Theoretical tools obtained from these studies allow not only to rationalise the optical characteristics of the investigated systems, but also to predict the behaviour of systems which have not yet been characterised.

In questa tesi di dottorato, dedicata allo studio di sistemi molecolari luminescenti a base di ioni lantanoidei con applicazioni in termometria, sono state esplorate ed applicate tecniche di calcolo quantistico non routinarie al fine di determinare parametri e caratteristiche molecolari indispensabili per la comprensione dei meccanismi alla base della dipendenza dalla temperatura delle proprietà ottiche di luminescenza. Dopo una breve introduzione dedicata alla descrizione di questi sistemi, sono state descritte le basi teoriche necessarie per la comprensione delle simulazioni numeriche; successivamente, sono stati allegati alla tesi gli articoli scientifici pubblicati su riviste internazionali in cui sono stati riportati e discussi i risultati degli esperimenti numerici. Il tipo di modellizzazione adottato ha reso possibile non solo la razionalizzazione delle caratteristiche ottiche dei composti presi in considerazione, ma ha permesso la previsione del comportamento di sistemi molecolari non ancora caratterizzati.



# TABLE OF CONTENTS

<b>1.</b>	<b>INTRODUCTION .....</b>	<b>1</b>
1.1	A brief history of lanthanides .....	1
1.2	Common commercial applications .....	3
1.3	Modern high-end applications of $\text{Eu}^{3+}$ .....	6
1.4	Characterisation of systems containing $\text{Eu}^{3+}$ .....	8
1.5	Eu-based molecular thermometers .....	9
	References.....	11
<b>2.</b>	<b>THEORETICAL FRAMEWORK .....</b>	<b>15</b>
2.1	The Schrödinger Equation .....	16
2.2	Polyelectronic molecular systems .....	17
2.3	Pauli exclusion principle .....	18
2.4	Variational principle .....	19
2.5	Hartree-Fock method .....	20
2.6	Electron correlation .....	21
2.7	Post-HF Methods .....	23
2.8	Density Functional Theory .....	29
2.9	Hohenberg-Kohn Theorems .....	30
2.10	Kohn-Sham Self-Consistent Field Equations .....	32
2.11	Exchange-correlation functionals .....	34
2.12	Relativistic Effects in Chemistry .....	38
2.13	Dirac Hamiltonian .....	39
2.14	Douglas-Kroll-Hess Hamiltonian .....	40
2.15	Zeroth-order Regular Approximation .....	43
2.16	Time-Dependent QM .....	46
2.17	Electronic Excitations in TD-DFT .....	49
	References.....	51
<b>3.</b>	<b>ENERGY LEVEL STRUCTURE OF THE <math>[\text{Xe}]4f^6</math> CONFIGURATION .....</b>	<b>55</b>
3.1	Antenna effect .....	58
3.2	Non-radiative decay processes in $\text{Eu}^{3+}$ complexes .....	60
	References .....	62

<b>4. LUMINESCENT THERMOMETERS: FROM A LIBRARY OF EUROPIUM(III) B-DIKETONATES TO A GENERAL MODEL FOR PREDICTING THE THERMOMETRIC BEHAVIOUR OF EUROPIUM-BASED COORDINATION SYSTEMS .....</b>	<b>63</b>
<b>5. ANTENNA TRIPLET DFT CALCULATIONS TO DRIVE THE DESIGN OF LUMINESCENT LN<sup>3+</sup> COMPLEXES .....</b>	<b>103</b>
<b>6. MULTIREFERENCE AB INITIO INVESTIGATION ON GROUND AND LOW-LYING EXCITED STATES: SYSTEMATIC EVALUATION OF J–J MIXING IN A EU<sup>3+</sup> LUMINESCENT COMPLEX .....</b>	<b>123</b>
<b>7. NATURE OF THE LIGAND-CENTERED TRIPLET STATE IN GD<sup>3+</sup> B-DIKETONATE COMPLEXES AS REVEALED BY TIME RESOLVED-EPR SPECTROSCOPY AND DFT CALCULATIONS .....</b>	<b>137</b>
<b>8. THERMOCHEMISTRY OF SUPRAMOLECULAR ASSEMBLY IN HETERODINUCLEAR LN-AL COMPLEXES .....</b>	<b>163</b>
8.1 Formation thermodynamics .....	165
8.2 Effects of different lanthanides on the coordination topology .....	171
8.3 Fukui function and bridging atom selectivity .....	173
8.4 Materials and instrumentation (experimental characterisation) .....	178
8.5 Computational details .....	179
References .....	180



## ACRONYMS

**ALDA:** Adiabatic Local Density Approximation

**B3LYP:** Stephens-Devlin-Chablowky-Frisch Hybrid XC functional

**BLYP:** Exchange: Becke; correlation; Lee, Yang, and Parr GGA functional

**BP86:** Exchange: Becke; correlation; Perdew GGA functional

**CASPT2:** Complete Active Space 2<sup>nd</sup>-order Perturbation Theory

**CI:** Configuration Interaction

**DFT:** Density Functional Theory

**DKH:** Douglas-Kroll-Hess two-component relativistic Hamiltonian

**ET:** Energy Transfer

**GGA:** Generalised Gradient Approximation (functional)

**HF:** Hartree-Fock

**HK:** Hohenberg and Kohn

**HSAB:** Hard/Soft Acid/Base

**ISC:** Intersystem Crossing

**KS:** Kohn and Sham

**LDA:** Local Density Approximation (functional)

**LMCT:** Ligand-to-Metal Charge Transfer

**MOFs:** Metal-Organic Frameworks

**Mo6-L:** Yan-Truhlar meta-GGA functional

**MCSCF:** Multiconfiguration Self-Consistent Field

**MP2:** 2<sup>nd</sup>-order Møller-Plesset perturbation theory

**O3LYP:** Cohen-Handy Hybrid XC functional

**OLYP:** Exchange: Handy; correlation: Lee, Yang, and Parr GGA functional

**PBE:** Perdew, Burke, and Ernzerhof GGA functional

**PBEo:** Adamo-Barone hybrid form of the Ernzerhof-Scuseria XC functional

**PW92:** Perdew and Wang LDA functional

**QM:** Quantum Mechanics

**SCF:** Self-Consistent Field

**TD-DFT:** Time-Dependent Density Functional Theory

**TPSS:** Tao-Perdew-Staroverov-Scuseria meta-GGA functional

**VWN:** Vosko, Wilk, and Nusair LDA functional

**XC:** Exchange and Correlation (functional)

**ZORA:** Zeroth-order Regular Approximation relativistic Hamiltonian



# 1. INTRODUCTION

Observation, pattern recognition, and deduction are the founding pillars of human intelligence. The expansion of this paradigm by the formulation of hypotheses and the design of experiments to test such hypotheses has brought forth what is arguably the most powerful tool ever obtained in our existence as a species: the *scientific method*.<sup>1</sup> More than simply forming a causal link between an event and its effects, it allows us to truly understand the first principles by which nature works and to gain a more profound knowledge of the universe around us.<sup>2</sup>

It is with this spirit that we, as scientists, approach scientific research: it is not enough to identify cause and consequence, we need to comprehend the underlying mechanisms by which things happen, so that we are able to predict the behaviour of systems just from prior knowledge, and eventually devise new technology based on the understood science.

The aim of this doctoral thesis is to attempt and apply this approach – utilising the tools offered by computational quantum chemistry – to gain a better understanding of the optical properties of lanthanide-based luminescent molecular systems, with a particular emphasis on luminescent thermometers. Not only are these systems interesting for the possible technical applications, but they also pose a unique challenge from the theoretical standpoint, as the lanthanide centre – which from the computational point of view is already very difficult to treat on its own – only very weakly interacts with the surrounding ligand environment, and it is this weak interaction that ultimately defines the characteristics and performance of the whole system.

We will try to describe – as accurately as our resources allow – every aspect of the molecular system, from its geometrical structure to the individual electronic and magnetic properties of the moieties which build the complex, to a simple yet comprehensive model, which pieces together the interactions between the fragments and is able to predict the optical behaviour of the system.

The computational techniques which will be employed range from well-established routine calculation to complex, very powerful high-level methods. It should be born in mind that, in the same way a skilled carpenter knows which tool is the best for the job, a computational chemist ought to know which methods are best suited for the particular property they are investigating and should exert caution not to overstep the boundaries identified by the “intended” use of the method, each of which has points of strength, but also limitations.

## 1.1 A brief history of lanthanides

Lanthanides – or preferably, *lanthanoids*<sup>3</sup> – identify the 6<sup>th</sup> period elements in the periodic table going from Ce to Lu. As the name lanthanoid means “like lanthanum” the nomenclature does not technically include La, but it has become common usage to consider it a lanthanide, nevertheless.

The first encounter with this group of elements has been in 1789, when Swedish lieutenant and amateur chemist/geologist Karl Axel Arrhenius – not to be confused with the probably more familiar Svante August Arrhenius, eponym of the famous reaction rate equation – stumbled upon an unusually heavy, dark mineral while visiting the feldspar mine near the village of Ytterby.<sup>4</sup> The first chemical analysis of this new mineral – named *ytterbite* after the nearby town – was carried out by Finnish chemist Johann Gadolin and he determined the mineral was composed of a number of known oxides such as beryllium, iron, and silicon, as well as a new unknown *earth* which was given the name of *ytterbia*.<sup>5</sup> It was then discovered that ytterbia was actually a mixture of at least three metal oxides, named yttria, erbia, and terbia.<sup>6</sup> Lanthanides all feature very similar chemical properties, and for this reason ores often contain a mixture of many metal oxides which are difficult to separate and purify. Cerium was the first lanthanide to be isolated in 1803, independently by Jöns Jakob Berzelius and Wilhelm Hisinger in Sweden, and Martin Heinrich Klaproth in Germany, and it was named after the dwarf planet Ceres discovered two years earlier.<sup>7</sup> Yttrium was next, isolated in pure form in 1828 by Friedrich Wöhler.<sup>8</sup> In 1839 Carl Gustav Mosander – one of Berzelius' students – identified lanthanum as well as a new metal closely resembling it, which for this reason he called *didymium*, meaning *twin*.<sup>9</sup> Much later, in 1885, Carl Auer von Welsbach demonstrated that this new metal was actually a mixture of two lanthanides, praseodymium (*green twin*) and neodymium (*new twin*).<sup>10</sup> The same Mosander also identified terbium and erbium as impurities in yttrium oxide  $Y_2O_3$ , although at first the names of the two elements were switched.<sup>11</sup> The identification of the remaining lanthanides – not free of a number of false positives – was greatly aided by the advancement in spectroscopic techniques in the late 1800s. Europium, gadolinium, ytterbium, holmium, thulium, lutetium, and samarium were all identified between 1878 and 1908.<sup>11</sup> Only one space, at atomic number 61, remained to be filled in this row of the periodic table. It was ultimately produced in laboratory by Pool and Quill in 1937 by bombarding neodymium with deuterons, and was isolated and characterized 10 years later by Marinsky *et al.*<sup>12</sup> This element was named promethium, after the Greek god who stole fire from heaven to bestow it upon man. Quoting the discoverers, “*the name not only symbolizes the dramatic way in which the new element was obtained in appreciable quantities, thanks to the harnessing of nuclear energy, but also warns men of the threatening danger of punishment by the vulture of war*”.<sup>11</sup>

The term *earth* was at the time used to include “all substances which possessed the properties of alkalis, did not float and did not change on heating, were almost insoluble in water and evolved gas bubbles during reaction with alkalis”.<sup>13</sup> The term *rare earths* which is commonly used to identify lanthanides is therefore a double misnomer, as they are neither *earths* – the term more appropriately describes the metal *oxide*, not the metal itself – nor are they particularly *rare*: lanthanum, cerium, and neodymium are all more abundant than lithium and lead in the Earth's crust; europium has a similar occurrence as germanium and arsenic, and is much more common than selenium; thulium is the rarest of the rare earths but is orders of magnitude more common than silver, gold, or mercury.<sup>14</sup>

One of the first technical applications of lanthanides was introduced by von Welsbach in 1891 when he invented an incandescent mantle composed of 99% thorium oxide  $ThO_2$  and 1% cerium oxide  $CeO_2$ . The Auer mantle actually stood comparison with electric light for over 40 years.<sup>15</sup> Later on, it was discovered that doping yttrium-based glasses with lanthanide ions produced some interesting optically active materials.<sup>16</sup> For example,  $Y_2O_3:Eu^{3+}$  has

been widely employed as the red phosphor in the now old-fashioned tube monitors and TV screens, while in 1964 Bell Laboratories developed the commonly used neodymium-doped yttrium-aluminium garnet laser YAG:Nd<sup>3+</sup>.<sup>17</sup>

## 1.2 Common commercial applications

Modern widespread applications of lanthanides range widely, here are a few of the most important for each element:

- **Cerium** is mainly used, in its oxide form “ceria” CeO<sub>2</sub>, as a polishing compound in chemical-mechanical planarization processes of high-quality optical devices,<sup>18</sup> where the surface is carefully smoothed by a combination of chemical and mechanical forces. Ceria is also used in the manufacture of gas tungsten arc welding electrodes,<sup>19</sup> where it helps improving the arc stability and decreasing burn-off. “Mischmetal”, a pyrophoric (it sparks when struck) alloy composed of 50% Ce, 25% La, and the remaining 25% a mixture of all other lanthanides, can be used as a catalyst in petroleum cracking.<sup>20</sup> It is this property that notoriously allowed writer Primo Levi to escape the Auschwitz concentration camp with his life, after he bartered a supply of this alloy he had found for food.<sup>21</sup> Ce<sub>2</sub>O<sub>3</sub> is used in the automotive industry for the catalytic oxidation of CO and NO<sub>x</sub> from engine exhaust gases,<sup>22,23</sup> and in the walls of self-cleaning ovens where it acts as a catalyst for the oxidation of hydrocarbons, thus preventing the build-up of cooking residue. Metallic cerium can also be used to enhance the photostability of certain pigments and polymers,<sup>24</sup> as well as to create castable eutectic alloys with improved mechanical and chemical performance.<sup>25</sup> Cerium nitrate Ce(NO<sub>3</sub>)<sub>3</sub> is a broad-spectrum antibacterial agent that creates a leather-like, impermeable eschar when applied and is therefore used in the treatment of 3<sup>rd</sup> degree burns.<sup>26</sup>
- **Praseodymium** was introduced a long time ago as a stain for ceramics and this application still endures to this day; “Praseodymium Yellow” in particular is a dispersed form of Pr<sup>3+</sup> in a crystalline zircon matrix to form a solid solution.<sup>27,28</sup> Like many other lanthanides, Pr<sup>3+</sup> finds use as dopant in optics and photonics applications. More specifically, it is particularly effective in enhancing single-mode optical fibre amplifiers<sup>29</sup> and lasers,<sup>30</sup> upconverting nanoparticles,<sup>31,32</sup> and various phosphors.<sup>27</sup> Besides these standalone applications, praseodymium is often used in combination with other metals to either tune or enhance their properties: with neodymium it creates the powerful magnets with whom we are all very familiar, as well as providing the base component for didymium glass in welding goggles;<sup>28</sup> with nickel it provides a very strong magnetocaloric effect – a phenomenon in which a temperature change is induced by exposing the material to a varying magnetic field – and this has allowed to reach temperatures down to 1/1000<sup>th</sup> of a degree K;<sup>33</sup> with magnesium it creates high-strength material viable for aeronautic applications;<sup>34,35</sup> with the fluorides of other lanthanides it forms the core of carbon arc lights, which are used in the film industry for lighting purposes;<sup>33</sup>

- **Neodymium** magnets are the strongest permanent magnets currently known.<sup>36</sup> This allows the construction of very lightweight, yet powerful magnetic systems with obvious applications in the audiophile industry. High quality microphones, speakers, headphones, and guitar pickups are all based on neodymium magnets for the sound recording or generation. It is also used in lasers, for example in the already mentioned YAG:Nd<sup>3+</sup> laser, and in stained glasses to give a distinct lavender colour when illuminated by daylight, and blue when exposed to fluorescent light, due to the narrow absorption bands of the ion.
- **Promethium** is primarily used in luminous paint for signal lights, as promethium-147 is a beta particle (high-speed electrons/positrons) emitter and the radiation can be caught by a phosphor which in turn emits light.<sup>28,33</sup> The same beta decay can also be exploited in the creation of atomic batteries, this time converting the beta particles into electric current, for an average lifetime of about five years.<sup>28,33</sup>
- **Samarium** is another lanthanide which found wide application in magnet technology: Sm-Co magnets are second only to Nd-based magnets but are more stable at higher temperatures and are more resistant to demagnetisation.<sup>33</sup> It is also used as a catalyst for the decomposition of plastics and dehydrogenation of ethanol,<sup>28</sup> as well as a reducing and coupling agent in a number of syntheses.<sup>37</sup> Samarium-153 is another beta emitter and it is used in oncologic treatments for various types of cancer, such as lung, prostate, and breast cancers, as well as osteosarcoma.<sup>33</sup> Samarium-149 has a very high neutron capture cross-section and is used in control rods for nuclear reactors. Moreover, its decay products are other Sm isotopes which also have good neutron absorption capabilities.<sup>28</sup>
- **Europium**, the main focus of this thesis, is used primarily for its luminescent properties, in white-light LEDs,<sup>38,39</sup> persistent phosphors,<sup>40</sup> and as a label for immunoassay studies.<sup>41</sup> Moreover, it is also commonly used, in the form of europium-doped strontium aluminate, in fluorescent lamps to improve the efficiency and after-glow intensity of the glass.<sup>42</sup> The luminescence properties of europium are also, quite fittingly, used as an anti-counterfeiting method for Euro banknotes.

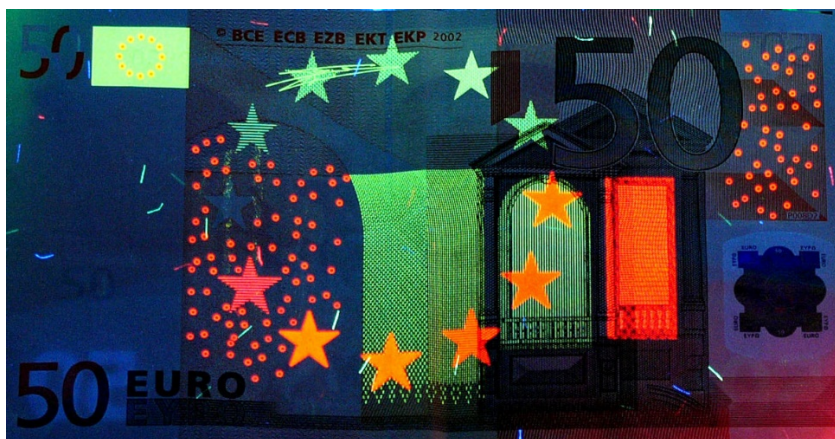


**Figure 1.** 50€ banknote illuminated at 366 nm. The red is given by Eu<sup>3+</sup> while the green and blue are given by Eu<sup>2+</sup>.

- **Gadolinium** has a plethora of different uses. Even in very small percentages (down to 1%) it improves the mechanical properties and malleability of iron and chromium alloys.<sup>28</sup> Gadolinium also has the highest neutron capture characteristics of any known material and therefore finds application in medical neutron therapy as well as a control rod in reactors.<sup>28</sup> Due to its strongly ferromagnetic character and high Curie temperature (the temperature above which ferromagnetism vanishes), it is also frequently used as a contrast agent in magnetic resonance imaging,<sup>43</sup> as well as in audio devices such as compact disks.
- **Terbium** is used as a dopant in solid-state devices and in combination with  $ZrO_2$  can be used to stabilise fuel cells at high temperatures.<sup>28</sup> An interesting Tb-based alloy, named Terfenol-D ( $Tb_xDy_{1-x}Fe_2$ ,  $x \approx 0.3$ ), possesses magnetostrictive properties, *i.e.* it is able to contract or expand in the presence of a magnetic field.<sup>44</sup>
- **Dysprosium**, like many other lanthanides, possesses a high neutron absorption cross-section and for this reason finds use in control rods for nuclear reactors.<sup>45</sup> In combination with vanadium and other lanthanides it also finds application in laser technology,<sup>28</sup> as well as in the already mentioned Terfenol-D alloy. Dysprosium is also used in dosimeters for the measurement of ionising radiation:  $CaSO_4$  or  $CaF_2$  crystals are doped with  $Dy^{3+}$  and when exposed to radiation, the  $Dy^{3+}$  ions provide luminescence.<sup>33</sup>
- **Holmium** possesses the highest magnetic strength of any element. When coupled with strong magnets as poles, it can generate incredibly intense artificial magnetic fields via what is known as *flux concentration*, for fields up to about a dozen Tesla units.<sup>46</sup> Besides this, it is also commonly used in laser devices for use in medical applications,<sup>47</sup> as well as for calibration of optical spectrophotometers due to the very sharp absorption peaks of solution containing holmium.<sup>48</sup>
- **Erbium** is primarily used, once again, in laser technology due to its optical properties, and control rod thanks to its neutron absorption cross-section, similarly to other lanthanides.<sup>28</sup> Given its particular pinkish colour it is also frequently used as a photographic filter<sup>49</sup> and in jewelry.<sup>33</sup> It improves workability of vanadium-based alloys and when combined with nickel it provides an alloy with an unusually high specific heat capacity at liquid helium temperatures, which makes it effective in cryocooling devices.<sup>28</sup>
- **Thulium** is a relatively expensive material compared to the other lanthanides. For this reason, it has not found many commercial applications, besides the odd laser/radioactive applications similarly to other lanthanides.<sup>28</sup>
- **Ytterbium** can be used to create portable X-ray machines for situations in which electricity might not be readily available.<sup>28</sup> It is also used as a dopant to improve various mechanical properties of stainless steel,<sup>28</sup> as well as to tune solid state lasers and optical fibre communications.<sup>50</sup> An interesting application exploits the fact that the electrical resistivity of ytterbium increases when subjected to high stress to monitor ground deformation during earthquakes.<sup>51</sup>
- **Lutetium** is another expensive lanthanide with not many commercial applications. It mainly finds use as a catalyst in a number of reactions such as petroleum

cracking, alkylation, hydrogenation, and polymerization.<sup>28</sup> Lutetium is also employed in positron emission tomography scan detectors.<sup>16,52</sup>

This thesis will be primarily focused on systems featuring the  $\text{Eu}^{3+}$  ion, but the principles and protocols employed have general validity and can easily be expanded to other lanthanides. The reason behind this choice was two-fold: *i*) we were lucky enough to be able to work closely with the experimental research group led by Prof. Lidia Armelao, and at the time they were focusing on Eu-based molecular systems; *ii*) it is generally simpler and more efficient to focus time and energy into refining procedures on a single “test subject” until a satisfactory accuracy is reached, and then translate it to similar systems via minor adjustments.

### 1.3 Modern high-end applications of $\text{Eu}^{3+}$

As already mentioned, the most common use of  $\text{Eu}^{3+}$  is as a red phosphor in fluorescent materials; this is due to its incredible versatility, as its characteristic red emission can be achieved not only via direct excitation with UV-Vis light, but also by many other means such as: *cathodoluminescence* (irradiation with electron beams),<sup>53,54</sup> *radioluminescence* (excitation with X-rays,  $\gamma$ -rays,  $\alpha$ - and  $\beta$ -particles),<sup>55-58</sup> *electroluminescence* (excitation with strong electric fields),<sup>59,60</sup> *triboluminescence* (excitation by mechanical agitation),<sup>61-63</sup> and *chemiluminescence* (excitation by chemical reaction).<sup>64</sup> Its particular optical characteristics are due to its electronic structure, which will be described in more detail in a later chapter. Here we will run through some of the more cutting-edge applications of the  $\text{Eu}^{3+}$  ion in modern technologies.

**Solar cells.** One of the first natural applications exploiting characteristics of  $\text{Eu}^{3+}$  is in solar cell technologies. Photovoltaic panels absorb sunlight (*photo-*) to create an electric potential (*-voltaic*) which is then used to generate electric current. There two ways of achieving this: *i*) semiconductor-based solar panels, which possess high conversion efficiencies<sup>65</sup> – the amount of light energy which is converted into electrical energy – but are expensive to build, are high-maintenance, and only relatively small wafers can be obtained; *ii*) dye-sensitised solar panels, built on organic chromophores, which are much cheaper and easier to make, and can be scaled up almost arbitrarily.<sup>66</sup> The drawback is that at the present time it has not been possible to attain efficiencies larger than 12%.<sup>67</sup> The primary reason behind this is the mismatch between the solar emission spectrum – the energy “faucet”, which has the highest power output in the visible region – and the dye absorption spectrum – the energy “sink”, which generally peaks in the UV region for the most effective dyes. In fact, dyes whose absorption spectra do peak in the visible region are much more sensitive to photodegradation due to the inherently more delicate structure of organic systems compared to inorganic ones.<sup>68</sup> Lanthanides are the ideal candidates to be used as wavelength converting layers given their optical characteristics: they can absorb radiation in spectral regions where the photosensitive dye does not absorb particularly well and then emit in the range where the photosensitive material operates at higher efficiency.<sup>69-71</sup>  $\text{Eu}^{3+}$ -doping of polymeric dyes can improve the surface morphology of the polymer as well as its electric conductivity, while also



down-shifting high-energy UV light into usable radiation, significantly enhancing the characteristics of some dyes without risking direct exposure of the dye and its subsequent photodegradation;<sup>72</sup> when combining different dyes it is possible to play with multiple excitation and conversion pathways to provide synergic co-sensitised dyes and devices<sup>73</sup>.  $\text{Eu}^{3+}$  can also be used to improve the efficiency of inorganic solar cells, in particular for perovskite-based technologies. Doping of  $\text{CsPbI}_2\text{Br}$  with  $\text{Eu}^{3+}$  has proven to stabilise the active  $\alpha$  phase as well as improving the open-circuit voltage of the cell,<sup>74</sup> while addition of Eu-doped  $\text{TiO}_2$  helps protecting the perovskite from damaging UV radiation, thanks to the conversion abilities of the  $\text{Eu}^{3+}$  ion.<sup>75</sup> Doping with  $\text{Eu}^{3+}$  can also further enhance the efficiency of traditional silicon-based cells, once again thanks to the light converting properties of the ion.<sup>76</sup>

**Molecular imaging.** Organic chromophores can be used as biomarkers for tracking particular targets/pathways *in vivo*.<sup>77,78</sup> Unlike traditional imaging techniques, the probe itself is part of the chemical environment it is tracking and this opens up the possibility of tailoring its chemistry so it will interact with the biological system in very specific ways, enabling unprecedented possibilities for biomedical applications, especially for studies on drug delivery and metabolism.<sup>79</sup> Unfortunately organic chromophores are sensitive to photobleaching and possess short-lived excited states. This latter behaviour especially renders difficult – if not straight impossible in some cases – the separation of the probe signal from the autofluorescence background. In this regard, lanthanide complexes provide a major improvement: they possess easily recognisable spectral line shapes, are almost immune to photobleaching, feature excited states with a sufficiently long lifetime to be used in time-resolved spectroscopy and the ligands can be easily modified to bind with drugs and markers.<sup>80–82</sup> Responsive contrast agents based on lanthanide complexes have successfully been employed in magnetic resonance imaging, where the complex was tailored to modify its luminescence based on the proton exchange rate between bulk and coordination water;<sup>83</sup> similar strategies have been employed to study atherosclerosis<sup>84</sup> and to study extracellular pH *in vivo*;<sup>85</sup> lanthanide chelates have also been used to detect lesions due to oral cancer in hamsters,<sup>86</sup> and to track delivery of radiopharmaceuticals.<sup>87</sup> Recently, research is being devoted towards finding lower energy excitation pathways which do not rely on potentially harmful (even if narrowly localized) UV light, but rather on harmless visible radiation.<sup>88</sup>

**Ion sensors.** A fair number of ions are of great importance in environmental and ecological systems. Some first-row transition metal cations such as  $\text{Cu}^{2+}$ ,  $\text{Fe}^{2+}/3+$ , and  $\text{Zn}^{2+}$  are involved in many essential steps within biological metabolisms and an excess or deficiency of these elements can lead to diseases such as Alzheimer's, while heavier elements such as  $\text{Hg}^{2+}$ ,  $\text{Pb}^{2+}$ , and  $\text{Cd}^{2+}$  are known for their toxicity even in very low concentrations. Anions are just as important:  $\text{I}^-$  regulates thyroidal function,  $\text{PO}_4^{3-}$  deficiency can cause bone pain and fractures, and exposure to  $\text{CN}^-$  may lead to deadly poisoning. Many Lanthanide Metal-Organic Frameworks (Ln-MOFs) have been developed with the ability of selectively detect specific ions and their characteristic optical fingerprint renders measurements of luminescence intensity simple.<sup>80,89–91</sup>

**Molecular thermometers.** Temperature is one of the fundamentally important physical variables. It influences dynamics and kinetics of basically any system, natural and

artificial alike. Temperature readings are usually carried out by thermal conduction, where an external probe is put in direct contact with the system and heat is exchanged. The exchanged heat is then correlated with the temperature of the system and the temperature reading is obtained. This way of gauging temperature is not applicable to very small systems – such as in microelectronics, micro-optics, photonics, nanomedicine, etc. – as the measurement procedure itself would alter the temperature of the system.<sup>92</sup> If, instead of direct contact and heat exchange with a probe, a molecular-sized thermometric probe could be embedded directly in the system, the temperature reading could be carried out in a non-invasive way, circumventing this issue. That is where *molecular thermometers* find employment. Lanthanide-based molecular thermometers are especially suited for this task given the high photostability and extreme flexibility in terms of spectroscopic properties these systems possess.<sup>15,93</sup> In the recent years it has been possible to achieve submicrometric spatial resolutions and temperature resolutions in the order of milli-Kelvins.<sup>94–97</sup> These represent one of the most interesting classes of compounds due to the interplay between many competing phenomena involving the excited electronic states of the molecule; as we will see later in the thesis even differences as small as a few hundred  $\text{cm}^{-1}$  – which is in the instrumental uncertainty range for some spectrophotometers – can lead to very significant differences in the thermal response of the system. It is for this reason that an accurate theoretical description of each single element of the complex represents a holy grail not only for the theoreticians, but for the experimentalists as well, whose work would be aided enormously by the availability of tools able to guide the design of newer systems with specific applications in mind.

#### 1.4 Characterisation of systems containing $\text{Eu}^{3+}$

Lanthanides can be introduced in a number of systems, from crystalline structures to molecular complexes, and their photophysical properties have been characterised in an extensive way in the scientific literature. The luminescence spectra of various  $\text{Ln}^{3+}$  ions are governed by their characteristic narrow emission bands and particular attention is given to all the possible processes which can inhibit emission, such as vibronic coupling with high-energy oscillators from either ligand or solvent molecules.<sup>98</sup> As with many other classes of compounds, the synergic combination of organic and inorganic components to create a hybrid material usually results in very advantageous properties. These Metal-Organic Frameworks (MOFs) can be obtained through relatively simple syntheses including solvothermal techniques<sup>99–101</sup> which can often be carried out in a single step minimising wastes of reactants. Due to their peculiar electronic structures (more information will be discussed in detail in the following chapters) the optical behaviour of a lanthanide complex in solution is mostly solvent-independent and this allows the embedding of these systems in basically any kind of rigid matrices such as resins<sup>102</sup>, gels,<sup>103</sup> or glasses<sup>104,105</sup> without altering the characteristics studied in solution.

From the point of view of experimental characterisation, structural and optical properties are usually investigated. X-ray crystallography is the technique of choice to determine the geometry of the complex/MOF in case,<sup>106–108</sup> but in many instances, it is not possible to

obtain crystals of sufficient quality for X-ray analysis. Should this be the case, IR and  $^1\text{H}$ -NMR spectra become the only indirect experimental sources of information for determining the geometrical structure of the system. Optical characterisations mostly involve the determination of UV-Vis absorption spectra and luminescence properties, such as photoluminescence spectra and excited state lifetime determination.<sup>106–109</sup> If the complex in question is to be used as a molecular thermometer, the latter are usually recorded at various temperatures in order to assess the performance of the system.<sup>110</sup>

Where experimental techniques fail, or are simply not applicable, theoretical modelling tools can help fill in the gaps and help the experimentalists in the rationalisation of other measured data or in the design of new systems. For example, geometry optimisations can provide reliable structures if crystals for X-ray analysis are not available. Given the fact that the optical properties of the lanthanide and of the ligands are mostly independent from each other,<sup>111–113</sup> these are often treated separately from a computational point of view, in order to simplify the calculations. A detailed rundown of all the state-of-the-art techniques used in these theoretical studies can be found in the next chapters.

## 1.5 Eu-based molecular thermometers

One of the technical applications of Eu-based luminescent systems, as mentioned briefly in Section 1.3, is in the field of thermometry. The advantage of a molecular thermometer, which gauges the temperature based on intrinsic properties of the material itself, is that it allows for a non-invasive measurement of the temperature, crucial in systems where a traditional contact-based procedure would alter the temperature of the system.

There are different properties which may be monitored to gauge the temperature, and the ones exploited in luminescent molecular thermometers are obviously related to the spectroscopic characteristics of the system. In particular, emission intensities or excited state lifetimes can be taken as the thermometric parameter. We will show<sup>114</sup> that the latter are regulated solely by metal-centred decay processes and therefore are less susceptible to eventual non-radiative decay processes which are completely ligand-centred. This can be an advantage in terms of stability of the measurements, but it limits the possibilities for new designs and the overall sensitivity of the system. Furthermore, the experimental setup required to measure excited state lifetimes is significantly more complicated than the one needed to measure emission spectra, severely limiting the commercial/technical material exploitability.<sup>115</sup> We will therefore focus on measurements based on emission intensities.

If the emission intensity  $I(T)$  of a luminescent system is temperature-dependent, it can be used as the thermometric parameter to determine the temperature of the system. The problem is, however, that the absolute value of  $I(T)$  is not univocally relatable to the temperature, as many other factors, such as the concentration of the luminescent molecule in the material, instrumental sensitivity, power fluctuations of the excitation source, and interference of the material itself can influence its value.<sup>116</sup> In order to accurately determine the temperature response of the system, a calibration curve of the temperature response needs to be built and used for subsequent measurements. This results in a low overall sensitivity because the temperature dependence is not extrapolated from comparison with a temperature-independent

quantity (such as when comparing the measurement against a temperature-independent blank), but it is easy to implement as it does not need an external reference. For instance, in Eu-based luminescent systems, the spectroscopic quantity often taken as the thermometric parameter is the integrated intensity of the  ${}^5D_0 \rightarrow {}^7F_2$  transition (Figure 2).

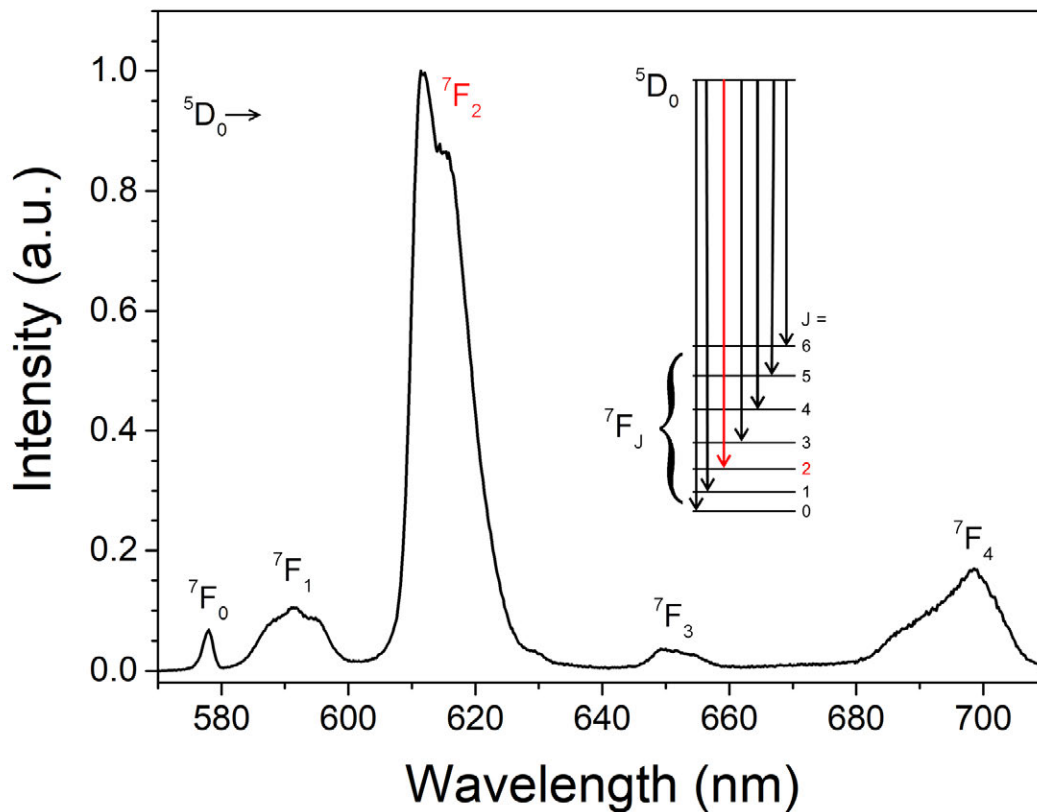


**Figure 2.** Emission spectrum of a Eu<sup>3+</sup> complex.<sup>114</sup> The  ${}^5D_0 \rightarrow {}^7F_2$  emission transition can be correlated with the temperature of the system via a calibration curve.

The theoretical modelling of the thermometric response, as well as an in-depth description of the various non-radiative deactivation channels which contribute to the temperature dependence of the Eu-based emission will be tackled in the following chapters.

## References

- (1) Kant, I. *Kritik Der Reinen Vernunft*; 1787.
- (2) Galilei, G. *Lettere Al Velseri*; 1611.
- (3) Fluck, E. *Pure Appl. Chem.* **1988**, 60 (3), 431–436.
- (4) Dinér, P. *Nat. Chem.* **2016**, 8 (2), 192–192.
- (5) Gadolin, J. *Kgl. Sven. Vetenskapsakad. Handl.* **1794**, 15, 137.
- (6) Mosander, C. G. *Ann. Phys. Chem.* **1843**, 60, 297–315.
- (7) Klopogge, J. T.; Ponce, C. P.; Loomis, T. A. *The Periodic Table: Nature's Building Blocks*; Elsevier, 2021.
- (8) Wöhler, F. *Ann. Phys. Chem.* **1828**, 13, 577–582.
- (9) Mosander, C. G. *Report of the Thirteens meeting of the British Association for the Advancement of Science.* 1843.
- (10) von Welsbach, C. A. *Monatshefte für Chemie und verwandte Teile anderer Wissenschaften* **1885**, 6, 477–491.
- (11) Evans, C. H. *Biochemistry of the Lanthanides*; Springer US: Boston, MA, 1990.
- (12) Marinsky, J. A.; Glendenin, L. E.; Coryell, C. D. *J. Am. Chem. Soc.* **1947**, 69 (11), 2781–2785.
- (13) Trifonov, D. N. *The Rare-Earth Elements*; Pergamon Press, New York, 1963.
- (14) Taylor, S. R. *Geochim. Cosmochim. Acta* **1964**, 28 (8), 1273–1285.
- (15) Bünzli, J. C. G.; Eliseeva, S. V. *Chem. Sci.* **2013**, 4 (5), 1939–1949.
- (16) Haxel, G. B.; Hedrick, J. B.; Orris, G. J. *United States Geol. Surv. Fact Sheet* **2002**, 087, 4.
- (17) Geusic, J. E.; Marcos, H. M.; Van Uitert, L. G. *Appl. Phys. Lett.* **1964**, 4 (10), 182–184.
- (18) Reinhardt, K.; Winkler, H. *Ullmann's Encycl. Ind. Chem.* **2000**, No. Mm.
- (19) *Guide for Root Pass Welding of Pipe Without Backing*; American Welding Society, Inc. (AWS), 2007.
- (20) Greenwood, N. N.; Earnshaw, A. *Chemistry of the Elements*; Elsevier, 1997.
- (21) Levi, P. *Il Sistema Periodico*; Einaudi, 1975.
- (22) Marshall, C.; Neylon, M. US7220692, 2007.
- (23) Bleiwas, D. I. *U.S. Geol. Surv.* **2013**, 1–10.
- (24) Gleń, M.; Grzmil, B. *Pure Appl. Chem.* **2012**, 84 (12), 2531–2547.
- (25) Sims, Z. C.; Weiss, D.; McCall, S. K.; McGuire, M. A.; Ott, R. T.; Geer, T.; Rios, O.; Turchi, P. A. E. *JOM* **2016**, 68 (7), 1940–1947.
- (26) In *Meyley's Side Effects of Drugs*; Elsevier, 2016; pp 470–472.
- (27) McGill, I. In *Ullmann's Encyclopedia of Industrial Chemistry*; Wiley-VCH Verlag GmbH & Co. KGaA: Weinheim, Germany, 2000; pp 183–227.
- (28) *CRC Handbook of Chemistry and Physics*; CRC press, 2015.
- (29) Jha, A.; Naftaly, M.; Jordery, S.; Samson, B. N.; Taylor, E. R.; Hewak, D.; Payne, D. N.; Poulain, M.; Zhang, G. *Pure Appl. Opt. J. Eur. Opt. Soc. Part A* **1995**, 4 (4), 417–424.
- (30) Smart, R. G.; Hanna, D. C.; Tropper, A. C.; Davey, S. T.; Carter, S. F.; Szebista, D. *Electron. Lett.* **1991**, 27 (14), 1307.
- (31) Prinse, T. J.; Karami, A.; Moffatt, J. E.; Payten, T. B.; Tsiminis, G.; Teixeira, L. D. S.; Bi, J.; Kee, T. W.; Klantsataya, E.; Sumby, C. J.; et al. *Adv. Opt. Mater.* **2021**, 2001903.
- (32) Kolesov, R.; Reuter, R.; Xia, K.; Stöhr, R.; Zappe, A.; Wrachtrup, J. *Phys. Rev. B* **2011**, 84 (15), 153413.
- (33) Emsley, J. *Nature's Building Blocks: An A-Z Guide to the Elements.*; Oxford University Press, 2011.

- (34) Rokhlin, L. L. *Magnesium Alloys Containing Rare Earth Metals: Structure and Properties*; CRC Press, 2003.
- (35) Suseelan Nair, K.; Mittal, M. C. *Mater. Sci. Forum* **1991**, *30*, 89–104.
- (36) Fraden, J. *Handbook of Modern Sensors: Physics, Designs, and Applications*; Springer, 2010.
- (37) Cotton, F. A.; Wilkinson, G.; Murillo, C. A.; Bochmann, M. *Advanced Inorganic Chemistry*; Wiley, 2007.
- (38) Smet, P. F.; Parmentier, A. B.; Poelman, D. *J. Electrochem. Soc.* **2011**, *158* (6), R37.
- (39) Lin, Y.-C.; Karlsson, M.; Bettinelli, M. *Top. Curr. Chem.* **2016**, *374* (2), 21.
- (40) Van den Eeckhout, K.; Smet, P. F.; Poelman, D. *Materials (Basel)*. **2010**, *3* (4), 2536–2566.
- (41) Hemmilä, I.; Dakubu, S.; Mukkala, V. M.; Siitari, H.; Lövgren, T. *Anal. Biochem.* **1984**, *137* (2), 335–343.
- (42) Stwertka, A. *A Guide to the Elements*; Oxford University Press, 1996.
- (43) Raymond, K. N.; Pierre, V. C. *Bioconjug. Chem.* **2005**, *16* (1), 3–8.
- (44) Rodríguez, C.; Rodríguez, M.; Orue, I.; Vilas, J. L.; Barandiarán, J. M.; Gubieda, M. L. F.; Leon, L. M. *Sensors Actuators A Phys.* **2009**, *149* (2), 251–254.
- (45) Sinha, A.; Sharma, B. P. *J. Am. Ceram. Soc.* **2005**, *88* (4), 1064–1066.
- (46) Hoard, R.; Mance, S.; Leber, R.; Dalder, E.; Chaplin, M.; Blair, K.; Nelson, D.; Van Dyke, D. *IEEE Trans. Magn.* **1985**, *21* (2), 448–450.
- (47) WOLLIN, T. A.; DENSTEDT, J. D. *J. Clin. Laser Med. Surg.* **1998**, *16* (1), 13–20.
- (48) Macdonald, R. P. *Clin. Chem.* **1964**, *10*, 1117–1120.
- (49) Awwad, N. S.; Gad, H. M. H.; Ahmad, M. I.; Aly, H. F. *Colloids Surfaces B Biointerfaces* **2010**, *81* (2), 593–599.
- (50) Gruk, D. A.; Bogatyrev, V. A.; Sysolyatin, A. A.; Paramonov, V. M.; Kurkov, A. S.; Dianov, E. M. *Quantum Electron.* **2004**, *34* (3), 247–248.
- (51) Gupta, C. K.; Krishnamurthy, N. *Extractive Metallurgy of Rare Earths*; CRC Press, 2004.
- (52) Daghighian, F.; Shenderov, P.; Pentlow, K. S.; Graham, M. C.; Eshaghian, B.; Melcher, C. L.; Schweitzer, J. S. *IEEE Trans. Nucl. Sci.* **1993**, *40* (4), 1045–1047.
- (53) Abdel-Kader, A.; Elkholy, M. M. *J. Mater. Sci.* **1992**, *27* (11), 2887–2895.
- (54) Ozawa, L.; Itoh, M. *Chem. Rev.* **2003**, *103* (10), 3835–3856.
- (55) Seregina, E. A.; Seregin, A. A.; Tikhonov, G. V. **2002**, *36* (4), 257–262.
- (56) Zych, E.; Trojan-Piegza, J. *J. Lumin.* **2007**, *122–123* (1–2), 335–338.
- (57) Zych, E.; Wójtowicz, M.; Dobrowolska, A.; Kepiński, L. *Opt. Mater. (Amst)*. **2009**, *31* (12), 1764–1767.
- (58) Barbanel, Y. A.; Kolin, V. V.; Kotlin, V. P. *Sov. Radiochem.* **1991**, *33*, 130–133.
- (59) Chen, F.; Bian, Z.; Huang, C. *J. Rare Earths* **2009**, *27* (3), 345–355.
- (60) Kuz'mina, N. P.; Eliseeva, S. V. *Russ. J. Inorg. Chem.* **2006**, *51* (1), 73–88.
- (61) Hendra, P. J. *Nature* **1966**, *212* (5058), 179.
- (62) Chen, X. F.; Duan, C. Y.; Zhu, X. H.; You, X. Z.; Shanmuga Sundara Raj, S.; Fun, H. K.; Wu, J. *Mater. Chem. Phys.* **2001**, *72* (1), 11–15.
- (63) Sage, I.; Bourhill, G. *J. Mater. Chem.* **2001**, *11* (2), 231–245.
- (64) Elbanowski, M.; Małowska, B.; Staninski, K.; Kaczmarek, M. *J. Photochem. Photobiol. A Chem.* **2000**, *130* (2–3), 75–81.
- (65) Tibbits, T. N.; Beutel, P.; Grave, M.; Karcher, C.; Oliva, E.; Siefer, G.; Wekkeli, A.; Schachtner, M.; Dimroth, F.; Bett, A. W.; et al. *Proceedings of the 29th European Photovoltaic Solar Energy Conference and Exhibition*. 2014, pp 1–4.
- (66) Grätzel, M. *J. Photochem. Photobiol. C Photochem. Rev.* **2003**, *4* (2), 145–153.
- (67) Yella, A.; Lee, H.-W.; Tsao, H. N.; Yi, C.; Chandiran, A. K.; Nazeeruddin, M. K.; Diau, E. W.-G.; Yeh, C.-Y.; Zakeeruddin, S. M.; Gratzel, M. *Science (80- )*. **2011**, *334* (6056), 629–634.

- (68) Griffini, G.; Brambilla, L.; Levi, M.; Del Zoppo, M.; Turri, S. *Sol. Energy Mater. Sol. Cells* **2013**, *111*, 41–48.
- (69) Xie, G.; Wei, Y.; Fan, L.; Wu, J. *J. Phys. Conf. Ser.* **2012**, *339* (1), 012010.
- (70) Chen, S.; Zhou, G.; Su, F.; Zhang, H.; Wang, L.; Wu, M.; Chen, M.; Pan, L.; Wang, S. *Mater. Lett.* **2012**, *77*, 17–20.
- (71) Jin, T.; Inoue, S.; Machida, K.; Adachi, G. *J. Electrochem. Soc.* **1997**, *144* (11), 4054–4058.
- (72) Mohammad, T.; Bharti, V.; Kumar, V.; Mudgal, S.; Dutta, V. *Org. Electron.* **2019**, *66* (December 2018), 242–248.
- (73) Zhang, L.; Wang, X.; Sun, X. *New J. Chem.* **2019**, *43* (33), 13249–13255.
- (74) Xiang, W.; Wang, Z.; Kubicki, D. J.; Tress, W.; Luo, J.; Prochowicz, D.; Akin, S.; Emsley, L.; Zhou, J.; Dietler, G.; et al. *Joule* **2019**, *3* (1), 205–214.
- (75) Chen, P.; Wang, Z.; Wang, S.; Lyu, M.; Hao, M.; Ghasemi, M.; Xiao, M.; Yun, J. H.; Bai, Y.; Wang, L. *Nano Energy* **2020**, *69*, 104392.
- (76) Katsagounos, G.; Stathatos, E.; Arabatzis, N. B.; Keramidis, A. D.; Lianos, P. *J. Lumin.* **2011**, *131* (8), 1776–1781.
- (77) Ressler, S.; Bartkova, J.; Niederegger, H.; Bartek, J.; Scharffetter-Kochanek, K.; Jansen-Dürr, P.; Wlaschek, M. *Aging Cell* **2006**, *5* (5), 379–389.
- (78) Wieckowska, A.; Zein, N. N.; Yerian, L. M.; Lopez, A. R.; McCullough, A. J.; Feldstein, A. E. *Hepatology* **2006**, *44* (1), 27–33.
- (79) Kobayashi, H.; Longmire, M. R.; Ogawa, M.; Choyke, P. L. *Chem. Soc. Rev.* **2011**, *40* (9), 4626–4648.
- (80) Tian, L.; Dai, Z.; Zhang, L.; Zhang, R.; Ye, Z.; Wu, J.; Jin, D.; Yuan, J. *Nanoscale* **2012**, *4* (11), 3551–3557.
- (81) Cheng, Z.; Ma, P.; Hou, Z.; Wang, W.; Dai, Y.; Zhai, X.; Lin, J. *Dalt. Trans.* **2012**, *41* (5), 1481–1489.
- (82) Zhai, X.; Yu, M.; Cheng, Z.; Hou, Z.; Ma, P.; Yang, D.; Kang, X.; Dai, Y.; Wang, D.; Lin, J. *Dalt. Trans.* **2011**, *40* (48), 12818–12825.
- (83) Coman, D.; Kiefer, G. E.; Rothman, D. L.; Sherry, A. D.; Hyder, F. *NMR Biomed.* **2011**, *24* (10), 1216–1225.
- (84) Amirbekian, V.; Aguinaldo, J. G. S.; Amirbekian, S.; Hyafil, F.; Vucic, E.; Sirol, M.; Weinreb, D. B.; Le Greneur, S.; Lancelot, E.; Corot, C.; et al. *Radiology* **2009**, *251* (2), 429–438.
- (85) Liu, G.; Li, Y.; Sheth, V. R.; Pagel, M. D. *Mol. Imaging* **2012**, *11* (1), 7290.2011.00026.
- (86) Bornhop, D. J.; Griffin, J. M. M.; Goebel, T. S.; Sudduth, M. R.; Bell, B.; Motamedi, M. *Appl. Spectrosc* **2003**, *57*, 1216–1222.
- (87) Hu, Z.; Qu, Y.; Wang, K.; Zhang, X.; Zha, J.; Song, T.; Bao, C.; Liu, H.; Wang, Z.; Wang, J.; et al. *Nat. Commun.* **2015**, *6* (150).
- (88) Ma, Y.; Wang, Y. *Coord. Chem. Rev.* **2010**, *254* (9–10), 972–990.
- (89) Xu, H.; Xiao, Y.; Rao, X.; Dou, Z.; Li, W.; Cui, Y.; Wang, Z.; Qian, G. *J. Alloys Compd.* **2011**, *509* (5), 2552–2554.
- (90) Shi, P. F.; Hu, H. C.; Zhang, Z. Y.; Xiong, G.; Zhao, B. *Chem. Commun.* **2015**, *51* (19), 3985–3988.
- (91) Chen, B.; Wang, L.; Xiao, Y.; Fronczek, F. R.; Xue, M.; Cui, Y.; Qian, G. *Angew. Chemie* **2009**, *121* (3), 508–511.
- (92) Brites, C. D. S.; Lima, P. P.; Silva, N. J. O.; Millán, A.; Amaral, V. S.; Palacio, F.; Carlos, L. D. *Adv. Mater.* **2010**, *22* (40), 4499–4504.
- (93) Binnemans, K. *Coord. Chem. Rev.* **2015**, *295*, 1–45.
- (94) Arai, S.; Suzuki, M.; Park, S. J.; Yoo, J. S.; Wang, L.; Kang, N. Y.; Ha, H. H.; Chang, Y. T. *Chem. Commun.* **2015**, *51* (38), 8044–8047.
- (95) Aigouy, L.; Tessier, G.; Mortier, M.; Charlot, B. *Appl. Phys. Lett.* **2005**, *87* (18), 1–3.
- (96) Mecklenburg, M.; Hubbard, W. A.; White, E. R.; Dhall, R.; Cronin, S. B.; Aloni, S.;

- Regan, B. C. *Science* (80-. ). **2015**, 347 (6222), 629–632.
- (97) Okabe, K.; Inada, N.; Gota, C.; Harada, Y.; Funatsu, T.; Uchiyama, S. *Nat. Commun.* **2012**, 3.
- (98) Lis, S. *J. Alloys Compd.* **2002**, 341 (1–2), 45–50.
- (99) Murray, L. J.; Dincă, M.; Long, J. R. *Chem. Soc. Rev.* **2009**, 38 (5), 1294.
- (100) Li, J.-R.; Kuppler, R. J.; Zhou, H.-C. *Chem. Soc. Rev.* **2009**, 38 (5), 1477.
- (101) Ma, L.; Abney, C.; Lin, W. *Chem. Soc. Rev.* **2009**, 38 (5), 1248.
- (102) Lenaerts, P.; Driesen, K.; Van Deun, R.; Binnemans, K. *Chem. Mater.* **2005**, 17 (8), 2148–2154.
- (103) Matthews, L.; Knobbe, E. T. *Chem. Mater.* **1993**, 5 (12), 1697–1700.
- (104) Streck, W.; Sokolnicki, J.; Legendziewicz, J.; Maruszewski, K.; Reisfeld, R.; Pavich, T. *Opt. Mater. (Amst)*. **1999**, 13 (1), 41–48.
- (105) Binnemans, K.; Lenaerts, P.; Driesen, K.; Görrler-Walrand, C. *J. Mater. Chem.* **2004**, 14 (2), 191–195.
- (106) Peng, C.; Zhang, H.; Yu, J.; Meng, Q.; Fu, L.; Li, H.; Sun, L.; Guo, X. *J. Phys. Chem. B* **2005**, 109 (32), 15278–15287.
- (107) Li, Y.; Yan, B.; Yang, H. *J. Phys. Chem. C* **2008**, 112 (10), 3959–3968.
- (108) Feng, N.; Xie, J.; Zhang, D. *Spectrochim. Acta Part A Mol. Biomol. Spectrosc.* **2010**, 77 (1), 292–296.
- (109) Gulino, A.; Lupo, F.; Condorelli, G. G.; Motta, A.; Fragalà, I. L. *J. Mater. Chem.* **2009**, 19 (21), 3507.
- (110) Balabhadra, S.; Debasu, M. L.; Brites, C. D. S.; Nunes, L. A. O.; Malta, O. L.; Rocha, J.; Bettinelli, M.; Carlos, L. D. *Nanoscale* **2015**, 7 (41), 17261–17267.
- (111) Faustino, W. M.; Malta, O. L.; Teotonio, E. E. S.; Brito, H. F.; Simas, A. M.; De Sa, G. F. *J. Phys. Chem. A* **2006**, 110 (7), 2510–2516.
- (112) Crosby, G. A.; Whan, R. E.; Freeman, J. J. *J. Phys. Chem.* **1962**, 66 (12), 2493–2499.
- (113) Tobita, S.; Arakawa, M.; Tanaka, I. *J. Phys. Chem.* **1985**, 89 (26), 5649–5654.
- (114) Carlotto, A.; Babetto, L.; Carlotto, S.; Miozzi, M.; Seraglia, R.; Casarin, M.; Bottaro, G.; Rancan, M.; Armelao, L. *ChemPhotoChem* **2020**, 4 (9), cptc.202000116.
- (115) Dramićanin, M. *Luminescence Thermometry: Methods, Materials, and Applications.*; Woodhead Publishing, 2018.
- (116) Brites, C. D. S.; Lima, P. P.; Silva, N. J. O.; Millán, A.; Amaral, V. S.; Palacio, F.; Carlos, L. D. *Nanoscale* **2012**, 4 (16), 4799.



## 2. THEORETICAL FRAMEWORK

Quantum mechanics (QM) describes the behaviour (mechanics) of systems at the atomic (quantum) level. Many weird things start to happen at this scale; particles start behaving like waves, waves start behaving like particles, and neither can be completely thought of as one *or* the other. This chapter is not strictly fundamental for the comprehension of the “practical” work carried out, but it will highlight strengths and shortcomings of the various computational methods employed, for a better understanding of the reason behind the choice of a particular method. This chapter also should not be taken as a comprehensive formal description of the various techniques within but rather as a general dusting and refreshing of the most important key concepts useful for getting a rough idea of how the various methods perform.

It is only assumed the reader is familiar with basic concepts of calculus such as integrals, derivatives, and elementary linear algebra. We will use a particular kind of notation throughout the text, which is known as Dirac notation,<sup>1</sup> or *bra-ket* notation. This will allow us to manipulate the quantum mechanical wave-functions as vectors in the Hilbert space, leveraging as such the formal structure of linear algebra, which renders equations written in this notation simpler to read and understand.

First of all, cursive letters denote scalar variables, such as coordinates or indices (*e.g.*  $x, i$ ); bold cursive letters indicate tensors, *i.e.* mathematical entities with more than one component such as vectors and matrices (*e.g.*  $\mathbf{v}, \mathbf{S}$ ); a hat above a letter indicates that we are dealing with an operator, *i.e.* an object which acts upon a function (*e.g.*  $\hat{H}, \hat{p}$ ). The adjoint of an operator is identified by a dagger symbol (*e.g.*  $\hat{U}^\dagger$ ) and is defined by the relation  $\langle f | \hat{U} | g \rangle = \langle \hat{U}^\dagger f | g \rangle$ . Similarly, for a complex function its conjugate is expressed with an asterisk (*e.g.*  $\phi^*$ ). The writing  $\hat{A}f(x, y, z)$ , for example, means that the operator  $\hat{A}$  acts on the function  $f$  with coordinates  $x, y, z$ .

The *bra* notation for a state vector  $\mathbf{v}$  is given as  $\langle \mathbf{v} |$ , while the *ket* notation for the same state vector is given as  $|\mathbf{v}\rangle$ . If  $\mathbf{v}$  is complex, the *bra*  $\langle \mathbf{v} |$  refers to its complex conjugate transposed (adjoint)  $(\mathbf{v}^*)^T = \mathbf{v}^\dagger$ . The scalar product between two state vectors is then defined as:

$$\langle \mathbf{v} | \mathbf{u} \rangle \equiv \mathbf{v}^\dagger \cdot \mathbf{u} = \sum (\mathbf{v}^* \cdot \mathbf{e}_i)^T (\mathbf{e}_j \cdot \mathbf{u}) = \sum v_i^* u_j \delta_{ij} \quad (1)$$

where  $\delta_{ij}$  is the Kronecker delta,<sup>2</sup> a function that is 1 if  $i = j$  and 0 otherwise;  $\mathbf{e}_i$  and  $\mathbf{e}_j$  are the unit vectors defining the vector space in which the  $\mathbf{v}$  and  $\mathbf{u}$  vectors belong;  $v_i$  and  $u_i$  are the projection of vectors  $\mathbf{v}$  and  $\mathbf{u}$  on the directions  $i$  and  $j$ , respectively. This notation is especially useful because the wave-functions we will use can be represented by vectors in a particular vector space (the complex Hilbert space) and therefore operations of multiplication and integration over the three-dimensional space can be reduced to simple vector operations on the components. For example, given two functions  $f(x, y, z)$  and  $g(x, y, z)$  the projection of  $f$  onto  $g$  can be written in cartesian coordinates very compactly as:

$$\iiint_{-\infty}^{+\infty} dx dy dz f(x, y, z) \cdot g(x, y, z) = \langle f|g \rangle \quad (2)$$

If this integral is zero, it means that the function  $f$  has no projection onto  $g$ , which is the equivalent of saying that in the vector space  $f$  and  $g$  are orthogonal.

## 2.1 The Schrödinger Equation

At the QM level the physical state of a particle is fully described by a mathematical – in general complex – function of its space coordinates  $\mathbf{r} = (x, y, z)$  and of the time coordinate  $t$ . This takes the name of *wavefunction* of the system and is represented by the Greek letter  $\Psi$ .

According to the Copenhagen interpretation of quantum mechanics,<sup>3</sup> the wavefunction of a particle in itself has no precise physical meaning, but its square modulus is associated with the probability  $p$  of finding the particle described by the wavefunction at a given point and time:

$$|\Psi(\mathbf{r}, t)|^2 d\mathbf{r} = \langle \Psi(\mathbf{r}, t) | \Psi(\mathbf{r}, t) \rangle = p(\mathbf{r}, t) \quad (3)$$

The time evolution of this function is governed by its Hamiltonian  $\hat{H}$ , *i.e.* the operator corresponding to the total energy of the system, and is described by the fundamental equation of QM, the time-dependent Schrödinger equation:<sup>4</sup>

$$i\hbar \frac{\partial \Psi(\mathbf{r}, t)}{\partial t} = \hat{H} \Psi(\mathbf{r}, t) \quad (4)$$

The form of the Hamiltonian defines energy spectrum of the quantum system and therefore the wavefunction can be written as a linear combination of solutions of the following eigenvalue problem:

$$\hat{H} \Psi_i(\mathbf{r}, t) = \varepsilon_i \Psi_i(\mathbf{r}, t) \quad (5)$$

where the eigenvalue  $\varepsilon_i$  is the energy associated with the  $i$ -th eigenstate  $\Psi_i$  of the quantum system. This is also known as the time-independent Schrödinger equation. The definition of the Hamiltonian operator is therefore a problem of primary importance.

Operators are directly associated with the physical observables they represent. The link between the quantum and “macroscopic” realms is made in terms of *expectation values* of these operators. An expectation value represents the average value for a given physical observable on a given system.<sup>5</sup> For a generic operator  $\hat{A}$  it is defined as:

$$\langle \hat{A} \rangle \equiv \frac{\int d\tau \Psi^* \hat{A} \Psi}{\int d\tau \Psi^* \Psi} = \frac{\langle \Psi | \hat{A} | \Psi \rangle}{\langle \Psi | \Psi \rangle} \quad (6)$$

In general, it is useful to represent the wavefunction of a system in terms of a linear combination of states, which are chosen as the complete set (*eigenbasis*) of orthonormal *eigenfunctions*  $|n\rangle$  of the Hamiltonian  $\hat{H}$  for the specific problem of interest:

$$|\Psi(t)\rangle = \sum_n c_n |n\rangle \left( e^{-\frac{iE_n t}{\hbar}} \right) \quad (7)$$

where the expansion coefficients  $c_n$  are the projections of each state  $|n\rangle$  on the wavefunction  $|\Psi\rangle$ :

$$c_n = \langle n | \Psi(0) \rangle \quad (8)$$

and the time-dependent part in parentheses represents how these coefficients evolve (oscillate) over time.

## 2.2 Polyelectronic molecular systems

If the wavefunction describes a molecular system with  $N$  electrons, the probability density of finding *any* single electron in a point of space and time – the *electron density* – is:

$$\begin{aligned} \rho(\mathbf{r}_1, t) &= N \int_{-\infty}^{+\infty} d\mathbf{r}_2 d\mathbf{r}_3 \dots d\mathbf{r}_N |\Psi(\mathbf{r}_1, \mathbf{r}_2, \mathbf{r}_3, \dots, \mathbf{r}_N, t)|^2 \\ &= \int_{-\infty}^{+\infty} d\mathbf{r}_2 d\mathbf{r}_3 \dots d\mathbf{r}_N \Psi^*(\mathbf{r}_1, \mathbf{r}_2, \mathbf{r}_3, \dots, \mathbf{r}_N, t) \cdot \Psi(\mathbf{r}_1, \mathbf{r}_2, \mathbf{r}_3, \dots, \mathbf{r}_N, t) \end{aligned} \quad (9)$$

where  $\Psi^*$  is the complex conjugate of  $\Psi$ . If integrated again, it yields the total number of electrons  $N$ :

$$\int_{-\infty}^{+\infty} d\mathbf{r}_1 \rho(\mathbf{r}_1, t) = N \quad (10)$$

We can also calculate the probability of finding one electron in  $\mathbf{r}_1$  and another electron in  $\mathbf{r}_2$  *simultaneously*. This is known as the *electron pair density*:

$$\Pi(\mathbf{r}_1, \mathbf{r}_2, t) = \frac{N(N-1)}{2} \int_{-\infty}^{+\infty} d\mathbf{r}_3 \dots d\mathbf{r}_N |\Psi(\mathbf{r}_1, \mathbf{r}_2, \mathbf{r}_3, \dots, \mathbf{r}_N, t)|^2 \quad (11)$$

In a non-relativistic approach, the Hamiltonian operator for a chemical system with  $N$  electrons ( $i, j, \dots$ ) and  $M$  nuclei ( $p, q, \dots$ ) with charges  $Z_p, Z_q, \dots$  can be written – in atomic units, where the fundamental electron charge, its mass, and the Planck constant  $\hbar$  are set equal to 1 – as:

$$\hat{H} = -\frac{1}{2} \sum_{p=1}^M \frac{1}{m_p} \hat{v}_p^2 - \frac{1}{2} \sum_{i=1}^N \hat{v}_i^2 - \sum_{i=1}^N \sum_{p=1}^M \frac{Z_p}{\hat{r}_{ip}} + \sum_{p=1}^M \sum_{q>p}^M \frac{Z_p Z_q}{\hat{R}_{pq}} + \sum_{i=1}^N \sum_{j>i}^N \frac{1}{\hat{r}_{ij}} \quad (12)$$

where the first and second terms are the kinetic energies of the nuclei and electrons, respectively; the third term is the Coulomb electron-nucleus attractive interaction; the fourth and fifth terms are the Coulomb nucleus-nucleus and electron-electron repulsions, respectively. The operator  $\hat{r}_{ab} = |\hat{\mathbf{r}}_b - \hat{\mathbf{r}}_a|$  identifies the distance between particles  $a$  and  $b$  as the difference between the position operators  $\hat{\mathbf{r}}_a$  and  $\hat{\mathbf{r}}_b$ , which return the coordinates for each particle.

Since the difference in the masses of electron and nuclei is very large – even in the hydrogen atom the nucleus, a single proton, is 1837 times more massive than the electron – their respective motions can be treated separately and the total Hamiltonian becomes a sum of nuclear and electronic contributions. This is known as the Born-Oppenheimer approximation.<sup>6</sup> The Hamiltonian of the quantum system can therefore be rewritten in terms of the electronic one:

$$\hat{H}_{el} = -\frac{1}{2} \sum_{i=1}^N \hat{v}_i^2 - \sum_{i=1}^N \sum_{p=1}^M \frac{Z_p}{\hat{r}_{ip}} + \sum_{i=1}^N \sum_{j>i}^N \frac{1}{\hat{r}_{ij}} \quad (13)$$

where the nuclear coordinates ( $p, q, \dots$ ) are treated parametrically and the nuclear repulsion – the fourth term in the right-hand side (r.h.s.) of Eq. 12 – can be considered as a constant value for each nuclear configuration  $R_{pq}$ . Incidentally, Eq. 13 shows that the system of interest defines the Hamiltonian through the position ( $p, q, \dots$ ) and nature ( $Z_p, Z_q, \dots$ ) of the nuclei, the total number of electrons  $N$ , and nothing more.

### 2.3 Pauli exclusion principle

There is one requirement the wavefunction of electrons – and in general of *fermions*, *i.e.* particles with half-integer spin – must satisfy. This was first formulated by Pauli before the whole contemporary QM framework was even introduced:

*In an atom there cannot be two or more equivalent electrons for which the values of all quantum numbers coincide. If an electron exists in an atom for which all of these numbers have definite values, then this state is “occupied”.*<sup>1</sup>

Without going too much into detail, this is equivalent to requiring that wavefunctions of fermions be *antisymmetric* with respect to the exchange of any two particles:

$$|\Psi(\mathbf{r}_1, \mathbf{r}_2, \dots, \mathbf{r}_N)\rangle = -|\Psi(\mathbf{r}_2, \mathbf{r}_1, \dots, \mathbf{r}_N)\rangle \quad (14)$$

This is strictly a postulate with a phenomenological nature, even though it can be rationalized to some extent by the use of relativistic arguments, which are beyond the scope of this discussion.<sup>7</sup> A general way of ensuring this happens is to write the wavefunction of an  $N$ -electronic system as a Slater determinant:

$$|\Psi(\mathbf{1}, \mathbf{2}, \dots, \mathbf{N})\rangle = \frac{1}{\sqrt{N!}} \begin{vmatrix} \phi_1(\mathbf{1}) & \phi_2(\mathbf{1}) & \dots & \phi_N(\mathbf{1}) \\ \phi_1(\mathbf{2}) & \phi_2(\mathbf{2}) & \dots & \phi_N(\mathbf{2}) \\ \vdots & \vdots & \ddots & \vdots \\ \phi_1(\mathbf{N}) & \phi_2(\mathbf{N}) & \dots & \phi_N(\mathbf{N}) \end{vmatrix} \equiv |\phi_1(\mathbf{1}), \phi_2(\mathbf{2}), \dots, \phi_N(\mathbf{N})\rangle \quad (15)$$

where  $\mathbf{1}, \mathbf{2}, \dots, \mathbf{N}$  represent the coordinates – both spatial and spin – of electrons  $1, 2, \dots, N$  and  $\phi_i$  are the spin-orbitals forming the eigenbasis on which the wavefunction can be constructed (see Eq. 7). The r.h.s. of Eq. 15 is a commonly used shorthand notation for writing down a Slater determinant. The prefactor  $\frac{1}{\sqrt{N!}}$  simply ensures the normalisation of the wavefunction and is not strictly required.

## 2.4 Variational principle

The exact solution for the Schrödinger equation can only be found for a system with only one electron, such as hydrogen, singly ionized helium, doubly ionized lithium, etc.<sup>8</sup> There is no closed-form solution to the differential Schrödinger equations describing polyelectronic atoms or molecules.<sup>9</sup> One way to obtain an approximate solution to this equation is to use the variational theorem.

Consider a system with Hamiltonian  $\hat{H}$ . The various eigenstates  $\phi_n$  each with energy  $\varepsilon_n$  form a complete eigenbasis and a generic wavefunction  $\Psi$  can be expanded in terms of these eigenstates according to Eq. 7. The expectation value of the Hamiltonian for the wavefunction  $\Psi$  is:

$$\frac{\langle \Psi | \hat{H} | \Psi \rangle}{\langle \Psi | \Psi \rangle} = \frac{\sum_n c_n^* c_n \langle \phi_n | \hat{H} | \phi_n \rangle}{\sum_n c_n^* c_n = 1} = \sum_n |c_n|^2 \varepsilon_n \geq \varepsilon_0 \quad (16)$$

where the expectation value is equal to the ground state energy  $\varepsilon_0$  if and only if all coefficients besides  $c_0$  are zero and  $c_0 = 1$ , *i.e.*  $\Psi = \phi_0$ . This allows us to search for the best approximation of the true ground state wavefunction even if we do not know the functional form of the eigenstates  $\phi_n$ . As long as it is complete and the functions are orthonormal – *i.e.*  $\langle \phi_i | \phi_j \rangle = \delta_{ij}$  – any generic *basis set* can be used to expand the wavefunction. The generic functions  $\phi_n$  just need to be thought themselves as an expansion on the true eigenstates  $\phi_n$  with unknown coefficients  $c_n$ .

## 2.5 Hartree-Fock method

We can apply the variational principle to obtain the optimal coefficients for a generic wavefunction  $\Psi$  written in the form of a Slater determinant (Eq. 15). This idea was first introduced by D. R. Hartree in 1927,<sup>10</sup> but the wavefunction was simply defined as a direct product of mono-electronic functions therefore violating the Pauli principle. V. A. Fock as well as Slater himself independently pointed out this issue<sup>11,12</sup> and eventually the algorithm was reformulated to use Slater determinants as wavefunctions.<sup>13</sup>

The method is based on a Self-Consistent Field (SCF) approach, in which one-electron Schrödinger equations are solved iteratively, starting from a trial wavefunction, until convergence is reached and the best coefficients  $c_n$  are obtained. The one-electron equations are also known as Fock equations:

$$\hat{f}_i \phi_i = \varepsilon_i \phi_i \quad (17)$$

where  $f_i$  is the Fock operator:

$$\hat{f}_i \equiv -\frac{1}{2} \hat{\nabla}_i^2 - \sum_{p=1}^M \frac{Z_p}{\hat{r}_{ip}} + \frac{1}{2} \sum_{j=1}^N [2\hat{J}_j(\mathbf{i}) - \hat{K}_j(\mathbf{i})] \quad (18)$$

The first two terms in Eq. 18 are the exact kinetic energy and the electron-nuclear attraction Coulomb term already found in Eq. 13. The last sum includes an approximate version of the last electron-electron repulsion term in Eq. 13, in the form of single electron Coulomb ( $\hat{J}_j$ ) and exchange ( $\hat{K}_j$ ) operators:

$$\begin{aligned} \hat{J}_j(\mathbf{i}) \phi_i(\mathbf{i}) &= \left\langle \phi_j(\mathbf{j}) \left| \frac{1}{\hat{r}_{ij}} \right| \phi_j(\mathbf{i}) \right\rangle \phi_i(\mathbf{i}) = \int d\mathbf{r}_j \phi_j^*(\mathbf{j}) \frac{1}{\hat{r}_{ij}} \phi_j(\mathbf{j}) \cdot \phi_i(\mathbf{i}) \\ \hat{K}_j(\mathbf{i}) \phi_i(\mathbf{i}) &= \left\langle \phi_j(\mathbf{j}) \left| \frac{1}{\hat{r}_{ij}} \right| \phi_i(\mathbf{i}) \right\rangle \phi_j(\mathbf{i}) = \int d\mathbf{r}_j \phi_j^*(\mathbf{j}) \frac{1}{\hat{r}_{ij}} \phi_i(\mathbf{j}) \cdot \phi_j(\mathbf{i}) \end{aligned} \quad (19)$$

Note that for the operators  $\hat{J}_j(\mathbf{i})$  and  $\hat{K}_j(\mathbf{i})$  the integration coordinate  $\mathbf{r}_j$  when acting on orbital  $\phi_i$  is the one associated with electron  $j$ .

The total electronic energy  $E_{el}$  is obtained by summing the single-electron contribution for all  $N$  electrons given by the Slater determinant built on orbitals that satisfy Eq. 17:

$$E_{el} = \sum_{i=1}^N \varepsilon_i + \frac{1}{2} \sum_{i=1}^N \sum_{j=1}^N (2J_{ij} - K_{ij}) \quad (20)$$

where  $J_{ij}$  and  $K_{ij}$  are the Coulomb and exchange integrals, respectively:

$$\begin{aligned}
 J_{ij} &= \left\langle \phi_i(\mathbf{i})\phi_j(\mathbf{j}) \left| \frac{1}{\hat{r}_{ij}} \right| \phi_i(\mathbf{i})\phi_j(\mathbf{j}) \right\rangle \equiv \langle ij|ij \rangle \\
 K_{ij} &= \left\langle \phi_i(\mathbf{i})\phi_j(\mathbf{j}) \left| \frac{1}{\hat{r}_{ij}} \right| \phi_i(\mathbf{j})\phi_j(\mathbf{i}) \right\rangle \equiv \langle ij|ji \rangle
 \end{aligned}
 \tag{21}$$

The physical meaning of  $J_{ik}$  is straightforward and represents the repulsive interaction between electron  $i$  in orbital  $\phi_i$  and electron  $j$  in the orbital  $\phi_j$ . The second term  $K_{ij}$  has a slightly more intricate interpretation and can be thought of as a correction term taking into account the fact that electrons do not interact with themselves.<sup>14</sup> Also note that in this formalism the electron-electron interaction – represented by the Coulomb and exchange terms – is treated in a *mean field* approach, with each electron interacting with the average static field created by all other electrons.

**Performance of HF calculations.** The single-determinant nature of the method renders it unable to describe bond formation and dissociation, as the separate fragments after the bond cleavage are each appropriately described by at least one Slater determinant each. This can be somewhat mitigated by applying an *unrestricted* calculation, in which spin up and spin down orbitals can have different occupation numbers, but this is still a rough approximation and the calculated dissociation energies are very inaccurate.<sup>15</sup> For closed-shell molecular systems that can be appropriately described by a single determinant, some properties are actually computed accurately by HF theory if such properties are not strongly related to electron correlation effects (*vide infra*). Protonation/deprotonation energies are reproduced well due to the fact that the lost proton does not carry any electrons.<sup>16</sup> Ionisation potentials are also very well reproduced due to a cancellation of errors and this is probably one of the very few applications for which HF is still used today.<sup>17</sup> Ground state geometries are reproduced qualitatively if a sufficiently large basis set is used, but the tendency of overemphasise occupation of bonding orbitals leads to a general underestimation of bond lengths. Ironically, this means that in some cases using a basis set that is *too large* leads to worse results than using a smaller size one.<sup>15</sup> HF completely fails to correctly determine excited state geometries and transition states due to the lack of electron correlation, even if in some lucky cases error compensation can accidentally lead to acceptable results.<sup>18</sup>

## 2.6 Electron correlation

The Hartree-Fock method is a fundamental milestone in the development of modern computational quantum chemistry. However, the approximations within render it not accurate enough for the quantitative study of complex chemical problems. This method accounts for about 99% of the exact energy for the ground state wavefunction, but that remaining 1% of neglected energy is precisely in the range typically characteristic of chemical reactions. This discrepancy was named *electron correlation*<sup>19,20</sup> and is defined as the difference between the true ground state energy and the calculated HF energy in the limit of an infinitely large basis set:

$$E_{corr} = E_{exact} - E_{HF} \quad (22)$$

In fact, this small discrepancy is so important that the vast majority of research in the field of computational quantum chemistry has been devoted to developing methods for recovering this correlation energy.

What is the origin of the correlation energy? Consider the Hamiltonian in Eq. 13, that is the true Hamiltonian for the real wavefunction. The rightmost contribution contains the term  $1/r_{ij}$ , which gives infinity for  $r_{ij} = 0$ . This is not compatible with the system having a finite energy, therefore the wavefunction and the pair electron density  $\Pi(\mathbf{r}_1, \mathbf{r}_2)$  must both annihilate at  $r_{ij} = 0$ . For electrons with the same spin this is already covered by the Pauli exclusion principle. Incidentally, this is also called a *Fermi* or *exchange hole*,<sup>14</sup> as it arises from the requirement that the wavefunction be antisymmetric with respect to the exchange of two electrons. This does however not apply to electrons with paired spins, therefore this physical condition that  $\Psi_{r_{ij} \rightarrow 0} = 0$  for *any* pair of electrons is an additional requirement the wavefunction must satisfy and this takes the name of a *Coulomb hole*, as it can be associated with electrons repelling each other at close distance. This obviously results in an overall energy gain compared to the uncorrelated wavefunction, as the electrons of the correlated wavefunction stay further away from each other than in the uncorrelated wavefunction therefore reducing the repulsive interaction.

It can be easily shown that the HF wavefunction does not intrinsically possess this last property and is therefore considered an *uncorrelated* method. Consider a simple system of two electrons **1** and **2** in orbitals  $\phi_1$  and  $\phi_2$  with spin  $\sigma_1$  and  $\sigma_2$ . The HF Slater determinant for this wavefunction is:

$$\Psi_{HF}(\mathbf{r}_1, \mathbf{r}_2) = \frac{1}{\sqrt{2}} [\phi_1(\mathbf{r}_1)\sigma_1(\mathbf{1})\phi_2(\mathbf{r}_2)\sigma_2(\mathbf{2}) - \phi_1(\mathbf{r}_2)\sigma_1(\mathbf{2})\phi_2(\mathbf{r}_1)\sigma_2(\mathbf{1})] \quad (23)$$

If the electrons have the same spin ( $\sigma_1 = \sigma_2$ ) the wavefunction and consequently the electron pair density both annihilate for  $\mathbf{r}_1 = \mathbf{r}_2$ . Unpaired electrons therefore interact and repel each other, even in different spatial orbitals. The Hartree-Fock method is therefore not *completely* uncorrelated but does include the exchange correlation arising from the Pauli principle.

If, however, the electrons have anti-parallel spin ( $\sigma_1 \neq \sigma_2$ ) the wavefunction does not annihilate for  $\mathbf{r}_1 = \mathbf{r}_2$  even if the electrons reside in the same orbital  $\phi = \phi_1 = \phi_2$ , and the electron pair density takes the following form:

$$\begin{aligned} \Pi_{HF}^{\sigma_1 \neq \sigma_2}(\mathbf{r}_1, \mathbf{r}'_1) &= \frac{1}{2} \int d\mathbf{r}_1 d\mathbf{r}'_1 |\Psi_{HF}^{\sigma_1 \neq \sigma_2}(\mathbf{r}_1, \mathbf{r}'_1)|^2 \\ &= \frac{1}{2} [|\phi^{\sigma_1}(\mathbf{r}_1)|^2 |\phi^{\sigma_2}(\mathbf{r}'_1)|^2 + |\phi^{\sigma_1}(\mathbf{r}'_1)|^2 |\phi^{\sigma_2}(\mathbf{r}_1)|^2] \\ &= \frac{1}{2} [\rho^{\sigma_1}(\mathbf{r}_1)\rho^{\sigma_2}(\mathbf{r}'_1) + \rho^{\sigma_1}(\mathbf{r}'_1)\rho^{\sigma_2}(\mathbf{r}_1)] = \rho^{\sigma_1}(\mathbf{r}_1)\rho^{\sigma_2}(\mathbf{r}'_1) \end{aligned} \quad (24)$$



in which the coordinate  $\mathbf{r}'_1 = \mathbf{r}_2$  is numerically equal to  $\mathbf{r}_1$  but is the one associated with electron 2. Given that the electrons must be indistinguishable,  $\rho(\mathbf{r}_1) = \rho(\mathbf{r}_2)$ . The electron pair density is therefore simply the product of the individual electron densities, which means the motion of the two electrons with unpaired spins is completely uncorrelated.

It is a common practice to separate electron correlation in two types, the so-called *static* and *dynamic* correlations. It must be stressed that there is no marked physical difference in the definition of the two and it is mostly a conceptual distinction originating from the different way in which computational techniques attempt to recover this missing electron correlation. *Dynamic* correlation is mostly associated with the description we have just made and is assigned to the correlated motion of the electrons. It is mainly recovered by higher order perturbative approaches, which try and account for more than the mean field interaction between electrons representing the 1<sup>st</sup> order perturbation in this framework. *Static* correlation arises from the intrinsic single-determinant nature of the HF method and the fact that many systems – open-shell ions, highly correlated delocalized wavefunctions, etc. – are not appropriately described by a single Slater determinant but require a linear combination of several.

The reason why this distinction might be misleading is that both “methods” of recovering correlation eventually converge to the exact wavefunction, either by considering infinitely many orders of perturbation or by including an infinitely large number of determinants.

## 2.7 Post-HF Methods

As the HF method is still able to recover most of the exact energy of the system, the HF wavefunction is surely a good starting point on which to build. Methods for recovering electron correlation by processing the HF wavefunction are called post-HF methods.

**Configuration Interaction.** One of the main limitations of HF theory is that the wavefunction is described by a *single* Slater determinant, so the first logical step is to write the wavefunction as a linear combination of several (in the exact limit, infinitely many) determinants. This is known as Configuration Interaction (CI):

$$\Psi_{CI} \equiv \sum_{n=0}^{\infty} c_n \Psi_n = c_0 \Psi_0^{HF} + c_1 \Psi_1 + \dots \quad (25)$$

$\Psi_0^{HF}$  is the HF ground state wavefunction and since it is not a terrible approximation for the ground state, in general  $c_0$  will be the largest expansion coefficient of the series.  $\Psi_{n>0}$  are  $n$ -tuply excited Slater determinants obtained by changing  $n$  spin-orbitals in the reference wavefunction from a previously occupied orbital to a virtual one. It is convenient to group together wavefunctions by the total number of excitations:

$$\Psi_{CI} = c_0 \Psi_0^{HF} + \sum_{ar} c_a^r \Psi_a^r + \sum_{\substack{a<b \\ r<s}} c_{ab}^{rs} \Psi_{ab}^{rs} + \dots \quad (26)$$

where  $\Psi_a^r$  means that the occupied spin-orbital  $\phi_a$  in the reference  $\Psi_0^{HF}$  wavefunction was replaced by the previously unoccupied spin-orbital  $\phi_r$ , and so on. The restrictions  $a < b, r < s$ , etc. ensure each excited determinant is included in the total wavefunction only once. If the basis set is complete, this procedure will give the exact ground state wavefunction; this would however require an infinite number of spin-orbitals in the basis set and subsequently an infinite number of possible excitations. A truncation must necessarily occur at some point and the  $N$ -electron basis set must be limited to  $K$  functions, and therefore  $\binom{K}{N}$  possible excitations. Despite this constraint, CI still gives the best possible wavefunction for a given basis set, therefore representing an upper limit to the exact ground state energy. The main issue is that even for very small molecules the number of determinants can become intractably large even for moderately sized basis sets, therefore rendering this method inapplicable for actual QM calculations. Some simplifications could be made, for instance Brillouin’s theorem<sup>21</sup> states that single excitations do not directly mix with the ground state, *i.e.*  $\langle \Psi_0^{HF} | \hat{H} | \Psi_a^r \rangle = 0$ . Similarly, matrix elements of the Hamiltonian between Slater determinants differing by 3 or more spin-orbitals are zero, which for example means that single excitations do not mix with quadruples. However, this does not mean that their effect on the ground state is zero, because they can interact with other higher-order excitations, which in turn do mix with the ground state, therefore contributing indirectly to its wavefunction.

**Multiconfiguration Self-Consistent Field.** It is now clear that CI is not an applicable method for relevant chemical problems due to the extremely large number of determinants involved. We have also noticed that many of these excited determinants actually contribute very little to the overall wavefunction via indirect effects. We should therefore try and include only the most relevant number of configurations and reduce our “active calculation” only to those. This approach takes the name of Multiconfiguration Self-Consistent Field (MCSCF) and can be considered as a truncated version of the CI method:

$$\Psi_{MCSCF} \equiv \sum_{n=active} c_n \Psi_n \quad (27)$$

The main difference compared to the traditional CI method is that *both* the coefficients  $c_n$  and the wavefunctions  $\Psi_n$  are optimised during the procedure. The equations involved are considerably more complicated than Roothaan’s equations<sup>22</sup> for HF theory and the discussion is very much beyond the scope of this text. The principal takeaway is that the calculation is separated into an *active space* calculation – *i.e.* a selection of orbitals to include in a CI calculation – and *inactive* orbitals, either occupied or unoccupied, which are either considered always fully occupied or always completely empty (Figure 3).

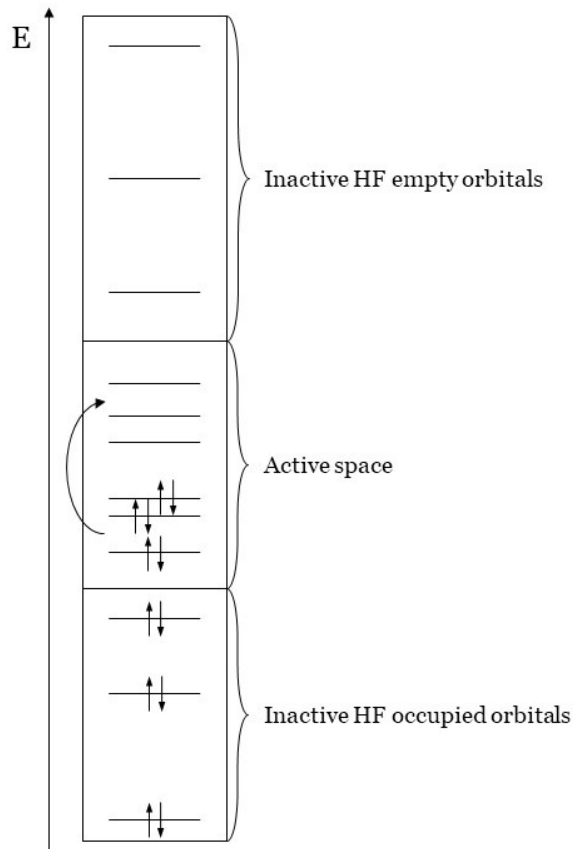


**Figure 3.** Schematic representation of a MCSCF calculation. The inactive space is composed of HF orbitals, which remain either occupied or empty throughout the calculation. In the active space, a CI calculation is carried out, which considers all the possible excitations of all electrons within the orbitals of the active space.

The active space needs to be chosen by the user and should include all the orbitals giving rise to the multideterminant character of the wavefunction. For example, in calculations on a transition metal ion the active space is represented by the 5 *d* orbitals while all the inner orbitals can remain fully occupied and the higher energy *s*, *p*, etc. orbitals can remain unoccupied. It is obvious here that this method presents a further source of difficulty as the users need to already possess a deep enough knowledge of the electronic structure of their chemical system to know which orbitals should be included in the active space.

If the CI in the active space is a full-CI calculation, meaning that *all* possible excitations within the active space are taken into account, the calculation is called Complete Active Space Self-Consistent Field (CASSCF) and is generally described by the number of electrons and orbitals in the active space. For example, a CASSCF calculation with 3 electrons in 5 orbitals is referred to as CAS(3,5). If an appropriate active space is chosen a CASSCF calculation can give results very close to a full-CI calculation, while requiring only a fraction of the computational power.

**Many-Body Perturbation Theory.** The fact that the HF wavefunction already is a fairly decent approximation of the exact ground state suggests that it is possible to get closer to the true wavefunction with a perturbative approach, but this time focusing on the

Hamiltonian instead of adding corrections to the wavefunction itself. The Hamiltonian in this framework takes the following form:

$$\begin{aligned}\hat{H} &= \hat{H}_0 + \lambda\hat{H}' \\ \hat{H}|\Psi\rangle &= W|\Psi\rangle \\ \hat{H}_0|\psi_i\rangle &= E_i|\psi_i\rangle\end{aligned}\tag{28}$$

where  $\hat{H}_0$  is the unperturbed Hamiltonian,  $\hat{H}'$  is the perturbation – small compared to  $\hat{H}_0$  – and  $\lambda$  is a variable parameter identifying the strength of the perturbation.  $|\psi_i\rangle$  are the eigenfunctions of the unperturbed Hamiltonian  $\hat{H}_0$ . For simplicity we will only consider time-independent perturbations at the moment. If  $\lambda = 0$ , then  $\hat{H} = \hat{H}_0$  and the ground state wavefunction is  $|\Psi_0\rangle = |\psi_0\rangle$  with energy  $W_0 = E_0$ . If  $\lambda$  is increased continuously from 0 to a finite value, the corresponding energy  $W$  and the wavefunction  $|\Psi\rangle$  must also change continuously, and can be written as a Taylor expansion of  $\lambda$ :

$$\begin{aligned}|\Psi\rangle &= \lambda^0|\Psi_0\rangle + \lambda^1|\Psi_1\rangle + \lambda^2|\Psi_2\rangle + \dots \\ W &= \lambda^0W_0 + \lambda^1W_1 + \lambda^2W_2 + \dots\end{aligned}\tag{29}$$

where  $|\Psi_1\rangle, |\Psi_2\rangle, \dots$  are the first-order, second-order corrections and so on. The corresponding Schrödinger equation when using the wavefunction from Eq. 29 in the Hamiltonian of Eq. 28 is:

$$\begin{aligned}[\hat{H}_0 + \lambda\hat{H}'](\lambda^0|\Psi_0\rangle + \lambda^1|\Psi_1\rangle + \lambda^2|\Psi_2\rangle + \dots) \\ = (\lambda^0W_0 + \lambda^1W_1 + \lambda^2W_2 + \dots)(\lambda^0|\Psi_0\rangle + \lambda^1|\Psi_1\rangle + \lambda^2|\Psi_2\rangle + \dots)\end{aligned}\tag{30}$$

We can collect the terms with the same power of  $\lambda$  to obtain:

$$\begin{aligned}\lambda^0: \hat{H}_0|\Psi_0\rangle &= W_0|\Psi_0\rangle \\ \lambda^1: \hat{H}_0|\Psi_1\rangle + \hat{H}'|\Psi_0\rangle &= W_0|\Psi_1\rangle + W_1|\Psi_0\rangle \\ \lambda^2: \hat{H}_0|\Psi_2\rangle + \hat{H}'|\Psi_1\rangle &= W_0|\Psi_2\rangle + W_1|\Psi_1\rangle + W_2|\Psi_0\rangle \\ \lambda^n: \hat{H}_0|\Psi_n\rangle + \hat{H}'|\Psi_{n-1}\rangle &= \sum_{i=0}^n W_i|\Psi_{n-i}\rangle\end{aligned}\tag{31}$$

where each power  $n$  represents the  $n$ -th order perturbation to the equation. The zero-order perturbation is the Schrödinger equation for the unperturbed problem, and the solutions  $\Phi_i$  generate a complete basis set. We can therefore expand the first order functions onto this basis set:

$$\begin{aligned}|\Psi_1\rangle &= \sum_i c_i|\Phi_i\rangle \\ (\hat{H}_0 - W_0)\sum_i c_i|\Phi_i\rangle + (\hat{H}' - W_1)|\Phi_0\rangle &= 0\end{aligned}\tag{32}$$

Left-multiplying by  $\langle \Phi_0 |$  and integrating yields:

$$\begin{aligned}
\sum_i c_i \langle \Phi_0 | \hat{H}_0 | \Phi_i \rangle - W_0 \sum_i c_i \langle \Phi_0 | \Phi_i \rangle + \langle \Phi_0 | \hat{H}' | \Phi_0 \rangle - W_1 \langle \Phi_0 | \Phi_0 \rangle &= 0 \\
\sum_i c_i E_i \langle \Phi_0 | \Phi_i \rangle - c_0 E_0 + \langle \Phi_0 | \hat{H}' | \Phi_0 \rangle - W_1 &= 0 \\
c_0 E_0 - c_0 E_0 + \langle \Phi_0 | \hat{H}' | \Phi_0 \rangle - W_1 &= 0 \\
W_1 &= \langle \Phi_0 | \hat{H}' | \Phi_0 \rangle
\end{aligned} \tag{33}$$

The last equation shows that the 1<sup>st</sup>-order correction to the energy is an average of the perturbation operator over the unperturbed wavefunction. The 1<sup>st</sup>-order correction to the wavefunction are represented by the 1<sup>st</sup>-order coefficients  $c_j$  and can be obtained by left-multiplying by a different function  $\langle \Phi_{j \neq 0} |$  and integrating:

$$\begin{aligned}
\sum_i c_i \langle \Phi_j | \hat{H}_0 | \Phi_i \rangle - W_0 \sum_i c_i \langle \Phi_j | \Phi_i \rangle + \langle \Phi_j | \hat{H}' | \Phi_0 \rangle - W_1 \langle \Phi_j | \Phi_0 \rangle &= 0 \\
\sum_i c_i E_i \langle \Phi_j | \Phi_i \rangle - c_j E_0 + \langle \Phi_j | \hat{H}' | \Phi_0 \rangle &= 0 \\
c_j E_j - c_j E_0 + \langle \Phi_j | \hat{H}' | \Phi_0 \rangle &= 0 \\
c_j &= \frac{\langle \Phi_j | \hat{H}' | \Phi_0 \rangle}{E_0 - E_j}
\end{aligned} \tag{34}$$

Analogous formulae can be obtained for the 2<sup>nd</sup>-order perturbations on the energy and the 2<sup>nd</sup>-order wavefunction coefficients  $d_j$ :

$$\begin{aligned}
W_2 &= \sum_i c_i \langle \Phi_0 | \hat{H}' | \Phi_i \rangle = \sum_{i \neq 0} \frac{\langle \Phi_0 | \hat{H}' | \Phi_i \rangle \langle \Phi_i | \hat{H}' | \Phi_0 \rangle}{E_0 - E_i} \\
d_j &= \sum_{i \neq 0} \frac{\langle \Phi_j | \hat{H}' | \Phi_i \rangle \langle \Phi_i | \hat{H}' | \Phi_0 \rangle}{(E_0 - E_j)(E_0 - E_i)} - \frac{\langle \Phi_j | \hat{H}' | \Phi_0 \rangle \langle \Phi_0 | \hat{H}' | \Phi_0 \rangle}{(E_0 - E_j)^2}
\end{aligned} \tag{35}$$

So far, this theory has been described in a completely general way, without specifying the form of either the unperturbed Hamiltonian or the perturbation. The most common choice is represented by the so-called Møller-Plesset perturbation theory,<sup>23</sup> which takes the unperturbed Hamiltonian as a sum over the Fock operators for the first  $n$  occupied orbitals:

$$\begin{aligned}
\hat{H}_0 &= \sum_i^n \hat{f}_i \\
\hat{H}_0 | \Psi_0^{HF} \rangle &= \sum_i^n \varepsilon_i | \Psi_0^{HF} \rangle
\end{aligned} \tag{36}$$

and the reference wavefunction is the HF one. Note that this is *not* how the electronic energy is usually calculated in HF theory, but rather it is the expectation value for the *correct* Hamiltonian and the HF wavefunction that defines that energy. The error is represented by the fact that each orbital energy  $\varepsilon_i$  includes the repulsion of the occupying  $i$ -th electron with every other electrons, thus counting the electron-electron repulsion *twice*. This allows us to take the perturbation term as the difference between the correct Hamiltonian  $\hat{H}$  and  $\hat{H}_0$ :

$$\hat{H}' = \sum_i^n \sum_{j>i}^n \frac{1}{\hat{r}_{ij}} - \frac{1}{2} \sum_i^n \sum_j^n (2\hat{J}_{ij} - \hat{K}_{ij}) \quad (37)$$

**Complete Active Space Perturbation Theory.** CASSCF recovers electron correlation by describing the wavefunction as a combination of Slater determinants, which accounts for the *static* correlation we have mentioned. Perturbation theory recovers the *dynamic* correlation originating from the correlated motion of the electrons, which feel each other’s presence in their motion. It is possible to combine these approaches to simultaneously recover both static and dynamic correlation, in particular by applying perturbation theory (usually at 2<sup>nd</sup> order) on a CASSCF wavefunction rather than the standard HF one. This is called Complete Active Space 2<sup>nd</sup>-order Perturbation Theory (CASPT2) and currently represents one of the most accurate methods for computing the energy of both ground and excited states, especially for inherently multireference systems such as those containing transition metals or lanthanides.

**Performance of post-HF methods.** Full Configuration Interaction gives the best possible wavefunction for a given basis set, therefore it is the most accurate QM method currently available. However, due to the prohibitive computational cost it is only applicable to very small systems and is primarily used as a benchmark for other types of calculations in the absence of experimental data.<sup>24</sup> 2<sup>nd</sup>-order Møller-Plesset perturbation theory (MP2) calculations give excellent ground state geometries for a relatively modest increase in computational cost compared to the base HF calculation and currently represents one of the most advantageous methods for price/performance as well as numerical robustness.<sup>25</sup> CASSCF is a necessary tool for the *ab initio* treatment of any system with a multideterminant nature. This includes transition metal ions<sup>26</sup> and lanthanides,<sup>27</sup> as well as delocalised aromatic organic systems and radicals,<sup>28</sup> reaction path studies<sup>29,30</sup> and multiplets.<sup>31</sup> The perturbed CASPT2 variation is especially effective in calculations of excited state energies and excitation energies,<sup>32,33</sup> while the unperturbed CASSCF is mostly relegated to ground state calculations.

## 2.8 Density Functional Theory

One of the main problems with using the wavefunction  $\Psi$  as the fundamental object in QM calculations is that it is essentially uninterpretable *per se*, especially for systems with multiple electrons. Only its square modulus  $|\Psi|^2$  is associated with a physical observable, *i.e.* the electronic probability density. Density Functional Theory (DFT) builds upon this conundrum and takes a different approach.

It can be noticed that the Hamiltonian in Eq. 13 depends only on the position and atomic number of the nuclei, and on the *total* number of electrons. It is then reasonable to attempt and use the electron density  $\rho(\mathbf{r}_1, t)$  from Eq. 9 as the fundamental item in the calculation, since: *i*) integrated over all of the space it gives the total number of electrons  $N$ ; *ii*) the positions of the nuclei, which are effectively point charges, naturally correspond to cusps in the electron density; and *iii*) the height of these cusps define the corresponding nuclear charges, and therefore the type of nuclei. Another point to bear in mind is that, since the wavefunction is defined by the Hamiltonian (Eq. 5), and the wavefunction defines every physically observable property of the quantum system (Eq. 6), defining the Hamiltonian via the electron density is equivalent to finding the wavefunction for the system and solving the quantum problem.

DFT has its roots in the *free electron gas* model developed by Thomas and Fermi,<sup>34–38</sup> according to which the quantum state of a uniform gas composed of free electrons can be fully described by its electronic density  $\rho_0$  instead of its wavefunction. The electron density can be expressed as a function of the Fermi momentum  $p_f$ , which is defined for the highest energy one-electron occupied level as:

$$\begin{aligned} p_f &= \hbar k_f \\ k_f &= \left( \frac{3\pi^2 N}{V_f} \right)^{\frac{1}{3}} \end{aligned} \quad (38)$$

where  $N$  is the number of electrons,  $V_f$  is the volume of the *Fermi sphere*, defined in the reciprocal momentum space as the boundary between occupied and unoccupied electron states at 0 K, and  $k_f$  is the *Fermi wavevector*, which identifies the radius of the Fermi sphere. The corresponding energy

$$\varepsilon_f = \frac{\hbar^2 k_f^2}{2m} \quad (39)$$

is called the *Fermi energy*.<sup>39</sup> The electron density  $\rho_0$  for a uniform electron gas therefore is:

$$\rho_0 = \frac{p_f^3}{3\pi^2 \hbar^3} \quad (40)$$

This formulation – which is *exact* for a uniform electron gas – has then been extended to inhomogeneous electron densities such as those characterising atoms, molecules, and solids in the presence of an external potential  $v(\mathbf{r})$ . If the inhomogeneous electron density at the point  $\mathbf{r}$  is denoted by  $\rho(\mathbf{r})$ , when the equation defining  $\rho_0$  is applied locally at  $\mathbf{r}$ , the expression for the total electronic energy becomes:

$$E_{TF}[\rho(\mathbf{r})] = \frac{3}{10} (3\pi^2)^{\frac{2}{3}} \int d\mathbf{r} \rho^{\frac{5}{3}}(\mathbf{r}) + \int d\mathbf{r} v(\mathbf{r})\rho(\mathbf{r}) + \frac{1}{2} \int d\mathbf{r}_1 d\mathbf{r}_2 \frac{\rho(\mathbf{r}_1)\rho(\mathbf{r}_2)}{|\mathbf{r}_2 - \mathbf{r}_1|} \quad (41)$$

$$= T[\rho(\mathbf{r})] + V_{ne}[\rho(\mathbf{r})] + V_{ee}[\rho(\mathbf{r})]$$

The first term of the r.h.s. of Eq. 41  $T[\rho]$  represents the kinetic energy of the electrons, the second  $V_{ne}[\rho]$  the attraction between electrons and nuclei, and the third term  $V_{ee}[\rho]$  accounts for inter-electronic repulsion. Note the conceptual resemblance with the standard electronic Hamiltonian in Eq. 13. The important result reached is that the electronic energy for a system with  $N$  electrons – and therefore the Hamiltonian  $\hat{H}$  – could be expressed as a *functional* of the charge density  $\rho(\mathbf{r})$ . Mathematically a functional is a linear mapping from a vector space into a scalar field, or in simpler terms it is something that takes a function as input (the density) and returns a number as output (the energy). The innovative aspect of this approach is that, for the first time, the ground-state energy of a quantum system was calculated on the basis of a physical observable such as the electron density.

The Thomas-Fermi theory gives a reasonable description of the charge density for heavy atoms. In fact, it can be demonstrated<sup>39</sup> that this theory is exactly valid in the limit of an atomic number  $Z \rightarrow \infty$ . Nevertheless, it fails if applied to molecular systems, because it is unable to predict the existence of any chemical bond: in the scope of this theory, the minimum energy for an aggregate of atoms is always given by nuclei at infinite distance.<sup>40</sup>

## 2.9 Hohenberg-Kohn Theorems

Hohenberg and Kohn (HK)<sup>41</sup> revolutionised the world of theoretical chemistry by demonstrating that the Thomas-Fermi model had to be considered as an approximate form of an exact theory, which is now known as DFT. This is the direct consequence of the first two HK theorems.

*First HK theorem.* Electrons interact with one another, and with the external potential generated by the presence of the nuclei. As stated before, the integration of the electron density gives the total number of electrons, therefore this external potential is all that is left to define to find the functional form of the Hamiltonian. We then need to prove that the electron density *determines entirely and univocally* this external potential. Let us assume that instead there are *two different* external potentials  $v_a$  and  $v_b$ , which can both be consistent with the same ground-state electron density  $\rho_0$ . These two potentials naturally define two different Hamiltonians  $\hat{H}_a$  and  $\hat{H}_b$ . With each different Hamiltonian, a particular ground state wavefunction  $\Psi_0^{a,b}$  and an associate ground state energy  $E_0^{a,b}$  are identified. By



definition of the variational theorem (Eq. 16), the Hamiltonian  $\hat{H}_a$  applied to the wavefunction  $\Psi_0^b$  must return a higher energy than when applied to its ground-state wavefunction  $\Psi_0^a$ :

$$\frac{\langle \Psi_0^b | \hat{H}_a | \Psi_0^b \rangle}{\langle \Psi_0^b | \Psi_0^b \rangle} > E_0^a \quad (42)$$

If the wavefunctions are normalised, we can consider  $\langle \Psi_0^b | \Psi_0^b \rangle = 1$ . We can rewrite this expression as:

$$\begin{aligned} E_0^a &< \langle \Psi_0^b | \hat{H}_a - \hat{H}_b + \hat{H}_b | \Psi_0^b \rangle \\ &< \langle \Psi_0^b | \hat{H}_a - \hat{H}_b | \Psi_0^b \rangle + \langle \Psi_0^b | \hat{H}_b | \Psi_0^b \rangle \\ &< \langle \Psi_0^b | v_a - v_b | \Psi_0^b \rangle + E_0^b \end{aligned} \quad (43)$$

Since the potentials  $v_a$  and  $v_b$  are one-electron operators, the last line in Eq. 43 can be rewritten in terms of the ground-state density:

$$E_0^a < \int d\mathbf{r} [v_a(\mathbf{r}) - v_b(\mathbf{r})] \rho_0(\mathbf{r}) + E_0^b \quad (44)$$

A similar procedure can be carried out swapping  $a$  and  $b$  to obtain the equivalent for  $E_0^b$ :

$$E_0^b < \int d\mathbf{r} [v_b(\mathbf{r}) - v_a(\mathbf{r})] \rho_0(\mathbf{r}) + E_0^a \quad (45)$$

Now, we sum the inequalities in Eq. 44 and 45 together:

$$\begin{aligned} E_0^a + E_0^b &< \int d\mathbf{r} [v_a(\mathbf{r}) - v_b(\mathbf{r})] \rho_0(\mathbf{r}) + \int d\mathbf{r} [v_b(\mathbf{r}) - v_a(\mathbf{r})] \rho_0(\mathbf{r}) + E_0^b + E_0^a \\ &< \int d\mathbf{r} [v_a(\mathbf{r}) - v_b(\mathbf{r}) + v_b(\mathbf{r}) - v_a(\mathbf{r})] \rho_0(\mathbf{r}) + E_0^b + E_0^a \\ &< E_0^b + E_0^a \end{aligned} \quad (46)$$

The assumption that the same ground-state density  $\rho_0$  could be associated with two different potentials  $v_a$  and  $v_b$  led to an impossible result, therefore this assumption must be incorrect per *reductio ad absurdum*. In other words, the ground-state electron density  $\rho_0(\mathbf{r})$  *univocally* defines the external potential  $v(\mathbf{r})$  and subsequently the Hamiltonian  $\hat{H}$ , and thus the wavefunction  $\Psi$ . Note that even though the Hamiltonian is defined by the ground-state density, it in turn defines not just the ground-state wavefunction but also all the excited state ones.

Unfortunately, this first theorem is merely an *existence* theorem, in the sense that it states that there is an electron density able to define the quantum system as a whole, but it says nothing on how to actually find it. Hohenberg and Kohn however demonstrated in their second theorem that the density, just as the wavefunction, obeys a variational principle.

*Second HK theorem.* Consider a “trial” electron density that integrates to the appropriate number of electrons  $N$  and is mathematically well-behaved. The first theorem indicates that there is a unique potential associated with this density, which defines the Hamiltonian and thus the wavefunction. It is possible to evaluate the expectation value for the energy in the usual way, and according to the variational principle its energy must be equal or greater than the true ground state energy:

$$\langle \Psi_{trial} | \hat{H}_{trial} | \Psi_{trial} \rangle = E_{trial} \geq E_0 \quad (47)$$

It would be possible, in principle, to keep trying different electron densities  $\rho_{trial}$  and the lower the calculated energy expectation value, the better the wavefunction. This is obviously a rather wasteful approach as there is still no guidance on what to change in the trial density to approach the best result. Moreover, we are still relying on solving the Schrödinger equation to calculate the energy, which defies the whole point of the DFT approach.

## 2.10 Kohn-Sham Self-Consistent Field Equations

In 1956 Kohn and Sham (KS)<sup>42</sup> proposed what is currently the most successful approach for applying the HK variational principle to obtain the best ground state electron density. They started by considering that the Hamiltonian of a fictitious system of *non-interacting* electrons would be extremely simple to solve, as all the terms would be easily computable one-electron operator terms. They also were aware that once the electron density is defined, the Hamiltonian and therefore the wavefunction could be computed. The crucial turning point was realising that it would be possible to take a fictitious system of non-interacting electrons that just *happens* to possess the same overall electron density as the real system of interacting electrons under consideration. Since the two systems have the same electron density, all other properties necessarily must also be identical.

In order to simplify the forthcoming discussion, let us briefly redefine the energy functional from Eq. 41 as:

$$E[\rho(\mathbf{r})] = T_{ni}[\rho(\mathbf{r})] + V_{ne}[\rho(\mathbf{r})] + V_{ee}[\rho(\mathbf{r})] + \Delta T[\rho(\mathbf{r})] + \Delta V_{ee}[\rho(\mathbf{r})] \quad (48)$$

where  $T_{ni}[\rho(\mathbf{r})]$  is the kinetic energy term for the non-interacting electrons;  $V_{ne}[\rho(\mathbf{r})]$  and  $V_{ee}[\rho(\mathbf{r})]$  are the *classical* nuclear-electron and electron-electron interactions, respectively;  $\Delta T[\rho(\mathbf{r})]$  is the correction term applied to  $T_{ni}[\rho(\mathbf{r})]$ , which derives from the previously neglected interacting nature of the electrons; and  $\Delta V_{ee}[\rho(\mathbf{r})]$  is the correction term applied to the electron-electron interaction accounting for *all* non-classical factors, including the interacting nature of the electrons. Rewriting the energy functional in terms of a more traditional orbital expression yields:

$$E[\rho(\mathbf{r})] = \sum_i^N \left( -\frac{1}{2} \langle \phi_i | \hat{\nabla}_i^2 | \phi_i \rangle - \sum_{p=1}^M \left\langle \phi_i \left| \frac{Z_p}{\hat{r}_{ip}} \right| \phi_i \right\rangle + \frac{1}{2} \left\langle \phi_i \left| \int d\mathbf{r}' \frac{\rho(\mathbf{r}')}{|\mathbf{r}_i - \mathbf{r}'|} \right| \phi_i \right\rangle \right) + E_{xc}[\rho(\mathbf{r})] \quad (49)$$

where  $N$  and  $M$  are the total number of electrons and nuclei, respectively;  $E_{xc}[\rho(\mathbf{r})] = \Delta T[\rho(\mathbf{r})] + \Delta V_{ee}[\rho(\mathbf{r})]$  is a single *exchange and correlation* term that includes all the necessary corrections with respect to the system of non-interacting electrons; and we have used for  $\rho(\mathbf{r})$  the electron density for a Slater determinant – which incidentally is the exact eigenstate for the system of non-interacting electrons:

$$\rho(\mathbf{r}) = \sum_i^N \langle \phi_i | \phi_i \rangle \quad (50)$$

We can now take the same approach as with the HF-SCF method and find the orbitals  $\phi_i$  that minimise the energy and satisfy the one-electron eigenvalue equations:

$$\hat{h}_i^{KS} \phi_i = \varepsilon_i \phi_i \quad (51)$$

where  $h_i^{KS}$  is the Kohn-Sham one-electron operator:

$$\hat{h}_i^{KS} \equiv -\frac{1}{2} \hat{\nabla}_i^2 - \sum_{p=1}^M \frac{Z_p}{\hat{r}_{ip}} + \int d\mathbf{r}' \frac{\rho(\mathbf{r}')}{|\mathbf{r}_i - \mathbf{r}'|} + V_{xc}[\rho(\mathbf{r})] \quad (52)$$

Note the conceptual resemblance with the Fock operator from Eq. 18, in particular between the Coulomb term  $\hat{J}_j(\mathbf{i})$  and the Coulomb interaction in the third term of the r.h.s. of Eq. 52 and between the exchange term  $\hat{K}_j(\mathbf{i})$  and the exchange-correlation potential  $V_{xc}$ , which is defined as:

$$V_{xc}[\rho(\mathbf{r})] = \frac{\delta E_{xc}[\rho(\mathbf{r})]}{\delta \rho(\mathbf{r})} \quad (53)$$

and represents the functional derivative of the exchange-correlation energy  $E_{xc}$  with respect to the electron density  $\rho(\mathbf{r})$ . Note that since we are minimising the *exact* energy  $E[\rho(\mathbf{r})]$  the obtained electron density  $\rho(\mathbf{r})$  must also be the exact one and the minimum of the energy must be the real ground state energy. The issue is that we do not have any analytical form for the  $E_{xc}$  term and therefore some approximations will necessarily be required. DFT can therefore be considered an exact theory with an approximate solution, in contrast with HF which is an approximate method that can be solved exactly.

## 2.11 Exchange-correlation functionals

Since there is no direct expression for the exchange-correlation (XC) functional, some approximate functional form must be used. The vast majority of the theoretical research regarding the development of DFT has been directed towards the definition of increasingly accurate and elaborate functionals. The choice of the functional is what ultimately differentiates between DFT calculations so one needs to know the strengths and weaknesses of the various implementations not only from an applicative standpoint as a user, but also as a reader who wants to better understand the computational work carried out by computational chemists.

Even though we do not have any analytical form for the true XC functional, there are a number of properties that we know it must possess:<sup>43,44</sup>

1. The XC functional needs to be *self-interaction-free*: for a one-electron system, such as a neutral hydrogen atom, the exchange energy should exactly cancel out the Coulomb energy and the resulting correlation should be zero.
2. If the density becomes constant in a certain spatial region, the XC functional must yield the same result as for a Thomas-Fermi uniform electron gas.
3. The coordinate scaling of the exchange energy should be linear, *i.e.* multiplying the coordinates of the electrons by a constant factor should result in an analogous linear scaling for the exchange energy.
4. Unlike the exchange energy, there is no rigid scaling law for the correlation energy. However, multiplying the electron coordinates by a factor larger than 1 should at least increase the magnitude of the correlation energy, and *vice versa*. In the limit of low density, the scaling should become linear as for the exchange energy.
5. As the scaling parameter approaches infinity, the correlation energy for a finite system must asymptotically reach a negative constant value.
6. There is an upper bound to the XC energy relative to Local Density Approximation (*vide infra*) functionals, as dictated by the Lieb-Oxford condition:<sup>45</sup>

$$E_x[\rho(\mathbf{r})] \geq E_{xc}[\rho(\mathbf{r})] \geq 2.273E_x^{LDA}[\rho(\mathbf{r})] \quad (54)$$

7. The exchange potential should show an asymptotic  $-1/r$  behaviour for  $r \rightarrow \infty$ .<sup>46</sup> The XC potential should also be discontinuous as a function of the number of electrons  $N$ , by an amount corresponding to the difference between the ionization potential and the electron affinity.<sup>46</sup>
8. The correlation potential should show an asymptotic  $-\alpha/2r^4$  behaviour for  $r \rightarrow \infty$ , with  $\alpha$  being the polarizability of the singly ionized system.

As there is a plethora of possible choices – only to name one piece of software, the Amsterdam Density Functional<sup>47</sup> code currently counts 111 XC functionals, which is also possible to combine in various ways – we will not look into every single one, but rather explore the features of the most important “families” of functionals.

**Local Density Approximation (LDA) functionals.** This term refers to XC functionals for which the value of the exchange and correlation energy at a point  $\mathbf{r}$  can be computed exclusively from the value of the electron density  $\rho(\mathbf{r})$  in that point, *i.e.* the *local* density:

$$E_{xc}^{LDA}[\rho(\mathbf{r})] = \int d\mathbf{r} \rho(\mathbf{r}) \varepsilon_{xc}^{TF}[\rho(\mathbf{r})] \quad (55)$$

where  $\varepsilon_{xc}^{TF}$  is the exchange-correlation energy density given by the Thomas-Fermi theory. These are incredibly simple and crude functionals and their only effective use is in calculations where the electron density resembles that of a homogeneous electron gas, like in calculations for solid metals. Note that, in the case of a molecular system, these functionals do not assume that the density is constant and homogeneous throughout all of space, but rather that the XC energy at every position in space is only dependent on the local electron density and is equal to that of a uniform electron gas with the same density as found for the molecule in that position. Only two parametrisations are worth mentioning for this family, as they are basically the only two still used for any type of modelling:

- **VWN:** Vosko, Wilk and Nusair<sup>48</sup> LDA functional
- **PW92:** Perdew and Wang<sup>49</sup> LDA functional

Note that the name of a XC functional often is composed by the initial letters of the developers who parametrized it.

**Generalised Gradient Approximation (GGA) functionals.** As the electron density for a molecular system is usually far from uniform, the first reasonable improvement over LDA is to take into account how the density changes over space, *i.e.* including the *gradient* of the electron density in the expression for the XC energy. If LDA can be considered the “zeroth order” of the Taylor expansion for the exact XC energy, GGAs would then include the first order term. Functionals of this family take the general form

$$E_{xc}^{GGA}[\rho(\mathbf{r})] = E_{xc}^{LDA}[\rho(\mathbf{r})] - \int d\mathbf{r} g(\chi) \rho(\mathbf{r})^{\frac{4}{3}} \quad (56)$$

where the specific form of  $g(\chi)$  depends on the particular functional used but is in general a function of the parameter  $\chi$ , which incorporates the density gradient as a dimensionless reduced quantity:

$$\chi = \frac{|\nabla\rho(\mathbf{r})|}{\rho(\mathbf{r})^{\frac{4}{3}}} \quad (57)$$

Here we also start to see some differentiation in the development of XC functionals, with a separate treatment for the exchange and correlation parts. Most commonly used GGA functionals therefore include separate functional forms for each:

- **BP86:** Exchange: Becke;<sup>43</sup> correlation: Perdew<sup>50</sup>

- **PBE**: Perdew, Burke, and Ernzerhof<sup>51,52</sup> XC functional
- **BLYP**: Exchange: Becke;<sup>43</sup> correlation: Lee, Yang, and Parr<sup>53,54</sup>
- **OLYP**: Exchange: Handy’s OPTX modification to Becke’s functional;<sup>53,54</sup> correlation: Lee, Yang, and Parr<sup>53,54</sup>

These functionals are generally rather accurate for calculations on molecular systems considering their relative simplicity and low computational power cost. For larger systems they are sometimes the only viable option since more accurate functionals would require more resources – either in terms of memory or storage – than may be available in the computing centre. Since they only include parameters directly related to the electron density they are also sometimes referred to as “pure” functionals.

**Meta-GGA functionals.** The next logical step for reaching an increasingly more accurate XC functional is obviously to include the next 2<sup>nd</sup> order term in the expansion. This would be represented by the second derivative of the electron density, *i.e.* the Laplacian. These functionals are known as meta-GGA as they go beyond the simple gradient correction of traditional GGA. The increased accuracy for these functionals is not actually set back by a significant increase in computational power requirements, as the calculation of the Laplacian is not extremely tasking. However, in some situations these functionals do suffer from numerical stability issues due to the characteristic of the Laplacian and therefore require a high integration accuracy.<sup>16</sup> The two most commonly used examples of meta-GGA functionals are:

- **TPSS**: Tao-Perdew-Staroverov-Scuseria<sup>55,56</sup> XC functional
- **Mo6-L**: Yan-Truhlar<sup>57,58</sup> XC functional

**Hybrid functionals.** It can be demonstrated<sup>59</sup> that an exact connection can be made between the XC energy and the corresponding hole potential connecting the non-interacting fictitious reference system and the real system. The resulting equation takes the name of *Adiabatic Connection Formula* and includes a parameter  $\lambda$ , which acts like a “switch” that turns on or off the electron-electron interaction:

$$E_{xc} = \int_0^1 d\lambda \langle \Psi_\lambda | \mathbf{v}_{xc}^{hole}(\lambda) | \Psi_\lambda \rangle \quad (58)$$

For  $\lambda \rightarrow 0$  the electrons are not interacting and there is no correlation energy, only the exchange term survives. Moreover, as the *exact* wavefunction for a system of non-interacting electrons is a single Slater determinant the exact exchange energy is given by Hartree-Fock theory. This allows the HF exchange to be included as a component of the overall XC functional definition, hence the denomination *hybrid* functional. These currently include some of the functionals with the highest accuracy and most widespread adoption:

- **B3LYP**: Stephens-Devlin-Chablowsky-Frisch<sup>60</sup> XC functional, with 20% HF exchange
- **O3LYP**: Cohen-Handy<sup>61</sup> XC functional, with 12% HF exchange

- **PBE0:** Adamo-Barone<sup>62</sup> hybrid form (25% HF exchange) of the Ernzerhof-Scuseria<sup>63</sup> XC functional

**Other functionals.** As previously stated, the definition of new and improved forms for XC functionals is a bustling branch of active research. Some of the newest approaches involve for example the definition of *meta-hybrid* functionals, which include higher-order expansions of the density dependence as well as exact the exchange contribution from HF theory; *range-separated hybrids*, which split the percentage of HF exchange in the Coulomb operator between short and long range interactions; and *double hybrids*, which not only include the HF exchange contribution but also 2<sup>nd</sup> order perturbative effects at the MP2 level.

**Performance of DFT calculations.** DFT has substantially established itself as the *de facto* standard base method for a large variety of QM calculations due to its striking balance between accuracy, computational efficiency, and ease of use. Calculation of atomisation energies on a large set of molecules including substituted hydrocarbons, radicals, inorganic hydrides, unsaturated ring hydrocarbons, and polyhalogenated organic and inorganic molecules (Table 1) show that the performance of DFT is substantially superior to HF for energetics.

**Table 1.** Comparison of the performance of various DFT methods. Root Mean Square (RMS) and Mean Absolute Deviation (MAD) errors for atomization energies over the G3/99 test set<sup>64</sup> are reported.

Functional	RMS (kJ/mol)	MAD (kJ/mol)
HF	649	885
LDA	439	510
PW91	80	99
PBE	87	93
PBE0	50	28
BLYP	41	40
B3LYP	40	21
OLYP	40	25
VSXC	39	14
TPSS	n/a	24

Not all functionals behave equally, however. LDA functionals are clearly inadequate for accurate calculations despite still providing an improvement over HF theory. Hybrid methods tend to perform better than their pure counterpart (PBE/PBE0, BLYP/B3LYP) but more modern GGA functionals such as OLYP and VSXC have comparable performance with hybrids. This represents a significant advantage since hybrid functionals are much more expensive than GGA due to the need to calculate the HF exchange integrals required in these calculations.

For geometries and vibrational frequencies, DFT generally performs as well as MP2 but with a cost comparable with that of HF.<sup>65</sup> In systems with a marked multireference character, DFT methods with a high quality functional often provide results comparable with those

of actual multireference calculations<sup>66</sup> and therefore represent a tantalising alternative to the more complicated *ab initio* alternatives at least for structural properties.

Another significant advantage of DFT methods is that they are much less prone to “spin contamination” for open-shell systems compared to traditional wavefunction methods. That is,  $\langle S^2 \rangle \sim S_z(S_z + 1)$ . This is due to the fact that the electron correlation is somewhat included even in the single-reference function in DFT by means of the  $E_{XC}$  functional, and renders DFT a very effective method to study multiplet systems as long as the number of unpaired electrons is not exceedingly large.

DFT is not immune to failures, though. Weak interactions due to dispersion forces are included explicitly in correlated wavefunction methods and this is something that is still treated poorly by DFT.<sup>67,68</sup> In particular, gas atoms correctly display a slight attraction, but in most cases a purely repulsive energy curve is displayed and the few functionals that do predict an attraction severely underestimate the intensity of the interaction. Anions are another class of systems which are extremely difficult for DFT methods, especially with functionals that do not include self-interaction corrections or possess a correct long-range behaviour. Since loosely bound electrons have by definition a large part of their associated density far away from the nuclei, the self-interaction error might actually be larger than the binding energy, therefore leading to an erroneously calculated unbound electron. Special care must therefore be exerted in the treatment of anionic systems and loosely-bound electrons in general. Despite these difficulties, reasonably accurate results can still be achieved in the right conditions.<sup>69</sup>

## 2.12 Relativistic Effects in Chemistry

One of the fundamental remarks of special relativity<sup>70</sup> is that it is impossible to accelerate particles to speeds higher than that of light. This is caused by the fact that the mass of the particle increases (to infinity) as it approaches the speed of light  $c$ , therefore requiring an increasingly large force to produce further acceleration:

$$m_{rel} = m_0 \gamma = \frac{m_0}{\sqrt{1 - \left(\frac{v}{c}\right)^2}} \quad (59)$$

where  $m_0$  is the particle rest mass at null velocity,  $v$  is its speed and  $\gamma$  is the so-called *Lorentz factor*, which is the term that expresses how much the measurement of the physical property in question – in this case the rest mass, but an equivalent form is also valid for time, length, etc. – changes due to effects of special relativity. In chemistry, relativistic effects entail three primary effects:<sup>71</sup>

1. The concomitant spatial contraction and energetic stabilisation of the  $s$  and  $p$  orbitals. The expression for the Bohr radius  $a_0$ , representing the most probable distance at which an electron is found relative to the nucleus, contains the electron mass  $m_{el}$  at the denominator:



$$a_0 = \frac{4\pi\epsilon_0\hbar^2}{Zm_e e^2} \quad (60)$$

Where  $Z$  is the atomic number for the element and  $\epsilon_0$  is the vacuum dielectric constant. The contraction of the relativistic average radius – up to 20% for the heavier elements – is a consequence of the reduction of the effective Bohr radius for the inner electrons, which have higher speed near the nucleus.

2. Spin-orbit splitting. In a relativistic approach neither  $l$ , the quantum number associated with the *orbital angular momentum*  $\mathbf{l}$ , nor  $s$ , the one associated with the *spin angular momentum*  $\mathbf{s}$ , are “good” quantum numbers. Within the *jj* coupling scheme the *total quantum number*  $\mathbf{j} = \mathbf{l} + \mathbf{s}$  and its projection on the  $z$  axis  $m_j$  are considered good quantum numbers.<sup>71</sup> Thus, for a  $p$  electron ( $l = 1, s = \pm 1/2$ ), we have a splitting in two spin-orbit states with  $j = 1/2$  and  $j = 3/2$ . The energy splitting between these states is more pronounced with increasing  $Z$ , therefore this is another effect that is more noticeable for heavier atoms – such as lanthanides.
3. The radial expansion and consequent energetic destabilisation of the  $d$  and  $f$  orbitals. The effective potential experienced by  $d$  and  $f$  electrons is weaker than the theoretical one due to an indirect effect: the  $s$  and  $p$  orbitals, which are more contracted due to the 1<sup>st</sup> effect we have described, screen the nuclear attraction potential more efficiently. This leads to a radial expansion for the  $d$  and  $f$  orbitals and their resultant energetic destabilisation.

These relativistic phenomena affect many aspects of the chemistry and optical properties for systems containing heavy elements. Bond lengths are different from the ones calculated in a non-relativistic method due to orbital contraction/expansion, absorption and emission spectra are sometimes entirely dictated by transition within spin-orbit states which would not be normally observed, and some entirely otherwise inexplicable phenomena such as intersystem crossing between different spin states take place. It is therefore necessary to account for relativistic effects in accurate calculations. Two primary approaches exist, one more suited for DFT calculations and one developed more towards wavefunction methods. They both feature a two-component approximate form of the four-component Dirac equation, the former utilizes an elimination technique while the latter uses a transformation approach. For a comprehensive description of the two methods, the interested reader may refer to the original papers in Refs. 72–75. In this text we will only provide a brief summary for the primary concepts.

### 2.13 Dirac Hamiltonian

The starting point for any relativistic QM calculation is the Dirac Hamiltonian, which represents the relativistic analogue of the Schrödinger equation:

$$\hat{H}_D = c\boldsymbol{\alpha} \cdot \hat{\mathbf{p}} + (\boldsymbol{\beta} - 1)c^2 + V_{nuc} \quad (61)$$

where  $\boldsymbol{\alpha} = (\boldsymbol{\alpha}_x \boldsymbol{\alpha}_y \boldsymbol{\alpha}_z)$  is a 3-vector, in which each component is a traceless  $4 \times 4$  diagonal matrix:

$$\boldsymbol{\alpha}_\xi = \begin{pmatrix} \mathbf{0} & \boldsymbol{\sigma}_\xi \\ \boldsymbol{\sigma}_\xi & \mathbf{0} \end{pmatrix}; \quad \xi = x, y, z \quad (62)$$

and  $\boldsymbol{\sigma}_\xi$  are the Pauli spin matrices:

$$\boldsymbol{\sigma}_x = \begin{pmatrix} 0 & 1 \\ 1 & 0 \end{pmatrix}; \quad \boldsymbol{\sigma}_y = \begin{pmatrix} 0 & -i \\ i & 0 \end{pmatrix}; \quad \boldsymbol{\sigma}_z = \begin{pmatrix} 1 & 0 \\ 0 & -1 \end{pmatrix}; \quad (63)$$

$\hat{\mathbf{p}}$  is the usual momentum operator

$$\hat{\mathbf{p}} = -i\hbar\nabla \quad (64)$$

$\boldsymbol{\beta}$  is a diagonal  $4 \times 4$  matrix with entries  $(1, 1, -1, -1)$ ,  $c$  is the speed of light and  $V_{nuc}$  is the external potential exerted by the nuclei. The corresponding eigenvectors  $\psi$  are therefore necessarily 4-component vectors. These 4 components can be divided into two different two-component functions  $\phi$  and  $\chi$ , which are called the *large* and *small* component, respectively:

$$\psi(\mathbf{r}, t) = \begin{pmatrix} \phi_1(\mathbf{r}, t) \\ \phi_2(\mathbf{r}, t) \\ \chi_1(\mathbf{r}, t) \\ \chi_2(\mathbf{r}, t) \end{pmatrix} = \begin{pmatrix} \phi(\mathbf{r}, t) \\ \chi(\mathbf{r}, t) \end{pmatrix} \quad (65)$$

$\phi_1, \chi_1$  and  $\phi_2, \chi_2$  represent the spin-up and spin-down of the free electron, respectively. The small component is usually negligible compared to the large one for atoms with  $Z < 100$ , which is the vast majority of the periodic table, therefore enabling the attempt to reduce the calculation to a two-component Hamiltonian.

As for the Schrödinger equation, an exact solution for the Dirac equation can only be obtained for a hydrogen-like system.<sup>76</sup>

## 2.14 Douglas-Kroll-Hess Hamiltonian

The Douglas-Kroll-Hess formalism is based on a transformation technique. This unitary transformation aims at block-diagonalising the Dirac Hamiltonian in two blocks:

$$\hat{H}_{BD} = \mathbf{U}\hat{H}_D\mathbf{U}^\dagger = \begin{pmatrix} \hat{H}_+ & 0 \\ 0 & \hat{H}_- \end{pmatrix} \quad (66)$$

Of these two block Hamiltonians, the upper  $\hat{H}_+$  is the one responsible for the positive energy states (electrons) while the lower  $\hat{H}_-$  is responsible for negative energy positron states and can therefore be neglected. The resulting four-component wavefunction takes the form

$$\psi' = \mathbf{U}\psi = \mathbf{U} \begin{pmatrix} \phi \\ \chi \end{pmatrix} = \begin{pmatrix} \phi' \\ \chi' = 0 \end{pmatrix} = \phi' \quad (67)$$

where  $\chi' = 0$  for electron states. This reduces the effective Hamiltonian problem to a two-component equation significantly simplifying the calculation. The unitary transformation matrix  $\mathbf{U}$  can be given in closed form<sup>77</sup> but the describing equation is rather complicated and needs to be solved iteratively. The Douglas-Kroll-Hess (DKH) Hamiltonian is constructed by decoupling the various elements of  $\mathbf{U}$  in a sequence of unitary transformations, which block-diagonalize the Dirac Hamiltonian stepwise:

$$\begin{aligned} \mathbf{U} &= \cdots \mathbf{U}_2 \mathbf{U}_1 \mathbf{U}_0 \\ \hat{H}_{BD} &= \cdots \mathbf{U}_2 \mathbf{U}_1 \mathbf{U}_0 \hat{H}_D \mathbf{U}_0^\dagger \mathbf{U}_1^\dagger \mathbf{U}_2^\dagger \cdots \end{aligned} \quad (68)$$

with each step  $\mathbf{U}_i$  chosen such as to diminish the off-diagonal terms order by order. This assumes the existence of an expansion of the block-diagonal Hamiltonian  $\hat{H}_{BD}$  in terms of an expansion parameter, which identifies block-diagonal operators  $\hat{\mathcal{E}}_k$  of order  $k$ :

$$\hat{H}_{BD} = \sum_{k=0}^{\infty} \hat{\mathcal{E}}_k \quad (69)$$

In the DKH decoupling procedure this expansion parameter is the external potential  $V_{nuc}$ . If one wants to obtain a partially transformed Hamiltonian  $\hat{H}_{PT}$  it is simply possible to stop after the  $n$ -th unitary transformation:

$$\hat{H}_{PT} = \sum_{k=0}^{2n+1} \hat{\mathcal{E}}_k + \sum_{k=2n+2}^{\infty} \hat{\mathcal{E}}_k^{(n+1)} + \sum_{k=n+1}^{\infty} \hat{\mathcal{O}}_k^{(n+1)} \quad (70)$$

Note that the  $(2n + 1)$  boundary in the first term is due to the fact each unitary transformation gives two orders  $k$  of the expansion parameter  $V_{nuc}$  still containing off-diagonal operators  $\mathcal{O}_k$  of the third term, which need to be removed by the subsequent unitary transformations. The second term indicates that the operators with  $k \geq 2n + 2$  are not reached at iteration  $n$ . Another stipulation must be made, ensuring that successive unitary transformations do not touch lower order terms that have already been transformed. Both requirements can be fulfilled by expanding each unitary matrix  $\mathbf{U}_n$  into a power series:

$$\begin{aligned}
\mathbf{U}_n &= \sum_{j=0}^{\infty} a_{n,j} \mathbf{W}_n^j = \mathbf{1} + \sum_{j=1}^{\infty} a_{n,j} \mathbf{W}_n^j \\
\mathbf{U}_n^\dagger &= \sum_{j=0}^{\infty} (-1)^j a_{n,j} \mathbf{W}_n^j = \mathbf{1} + \sum_{j=1}^{\infty} (-1)^j a_{n,j} \mathbf{W}_n^j
\end{aligned} \tag{71}$$

where it was chosen that  $a_{n,0} = 1$  and that each term of the series is defined solely by the order  $k = m \times j$  with respect to the expansion parameter  $V_{nuc}$ .

The first step in the DKH transformation needs to be carried out explicitly and is referred to a free-particle Foldy-Wouthuysen transformation:<sup>74,78</sup>

$$\mathbf{U}_0 = \begin{pmatrix} A & AR \\ -AR & R \end{pmatrix} \tag{72}$$

where  $A$  and  $R$  are kinematical operators defined as

$$A = \sqrt{\frac{E_0 + c^2}{2E_0}}; \quad R = \frac{c\boldsymbol{\sigma} \cdot \hat{\mathbf{p}}}{E_0 + c^2} \tag{73}$$

with  $E_0$  the total energy of the electron (in atomic units) in the absence of the external potential:

$$E_0 = \sqrt{c^4 + p^2 c^2} \tag{74}$$

The application of  $\mathbf{U}_0$  to the Dirac Hamiltonian  $\hat{H}_D$  gives the 1<sup>st</sup>-order block-diagonalized Hamiltonian  $\hat{H}_1$ :

$$\hat{H}_1 = \mathbf{U}_0 \hat{H}_D \mathbf{U}_0^\dagger = \hat{\mathcal{E}}_0 + \hat{\mathcal{E}}_1 + \hat{\mathcal{O}}_1 \tag{75}$$

where

$$\hat{\mathcal{E}}_0 = \begin{pmatrix} E_0 & 0 \\ 0 & -E_0 \end{pmatrix}; \quad \hat{\mathcal{E}}_1 = \begin{pmatrix} E_1 & 0 \\ 0 & E_1 \end{pmatrix}; \quad \hat{\mathcal{O}}_1 = \begin{pmatrix} 0 & O_1 \\ -O_1 & 0 \end{pmatrix}; \tag{76}$$

with

$$E_1 = AV_{nuc}A + ARV_{nuc}RA; \quad O_1 = ARV_{nuc}A - AV_{nuc}RA \tag{77}$$

It can be easily seen that this is still a four-component Hamiltonian, but now in block form. The two-component Hamiltonian is simply obtained by only keeping the upper diagonal block for all operators. The resulting two-component 1<sup>st</sup>-order DKH Hamiltonian is therefore

$$\hat{H}_{DKH1} = E_0 - c^2 + E_1 \quad (78)$$

The successive transformation, *i.e.* the one yielding the 2<sup>nd</sup>-order DKH Hamiltonian, is the one currently used in most computational chemistry software and its effective two-component form is given as

$$\hat{H}_{DKH2} = \hat{H}_{DKH1} - \frac{1}{2}[W_1, [W_1, E_0]_+]_+ \quad (79)$$

where  $[...]_+$  is the anticommutator and  $W_1$  is determined by the relation

$$W_1 E_0 + E_0 W_1 = O_1 \quad (80)$$

## 2.15 Zeroth-order Regular Approximation

In contrast with the DKH Hamiltonian, the Zeroth-Order Regular Approximation is based on an elimination procedure starting from an expansion on the Dirac equation. Let us start from considering the total relativistic energy of the electron  $E_0$  as found in Eq. 74, in the presence of an external potential  $V$  (could be  $V_{nuc}$  but does not need to be):

$$E_0 = \sqrt{c^4 + p^2 c^2} + V \quad (81)$$

If we redefine this energy as  $E = E_0 - c^2$  the previous equation can be rewritten as:

$$E = c^2 \left( \sqrt{1 + \frac{p^2}{c^2}} - 1 \right) + V \quad (82)$$

We can now develop this equation in  $p/c$  as the Taylor expansion of  $\sqrt{1 + x^2}$ :

$$E = V + \frac{p^2}{2} - \frac{p^4}{8c^2} + \dots \quad (83)$$

The use of this expression is obviously not justified if  $p/c > 1$ . Unfortunately, this is always the case for a Coulomb-like potential ( $V \sim -1/r$ ), for which there is always a region of space where the potential is so negative that the momentum  $p$  of the particle is larger than  $c$ . Another expression can however be found, for which the only restriction is that the total energy is not too large:

$$|E| < (2c^2 - V) \quad (84)$$

which is always the case for chemical systems. To find this alternative formulation, we must rewrite Eq. 82 as:

$$\begin{aligned}
E &= \sqrt{c^4 + p^2 c^2} - c^2 + V \\
&= \frac{p^2 c^2}{c^2 + \sqrt{c^4 + p^2 c^2}} + V \\
&= \frac{p^2 c^2}{2c^2 + E - V} + V \\
&= \frac{p^2}{2 \left[ 1 + \frac{E - V}{2c^2} \right]} + V \\
&= \frac{p^2 c^2}{(2c^2 - V) \left[ 1 + \frac{E}{2c^2 - V} \right]} + V
\end{aligned} \tag{85}$$

with the last term written down to more clearly exhibit the kind of expansions that can be made. Expanding in  $(E - V)/2c^2$  will give the same expression as found in Eq. 83. Note that now the equation is quadratic in energy, therefore it also possesses a solution with negative total energy. This spurious solution can be thrown away by expanding in  $1/(2c^2 - V)$ . At zeroth and first order the expressions for the energy are:

$$\begin{aligned}
E_0 &= V + \frac{p^2 c^2}{2c^2 - V} \\
E_1 &= E_0 - \frac{E_0 p^2 c^2}{(2c^2 - V)^2}
\end{aligned} \tag{86}$$

We can now use this information for the energy derived by applying the Dirac Hamiltonian in Eq. 61 to a four-component wavefunction  $\psi = (\phi, \chi)$ :

$$V\phi + c\boldsymbol{\alpha} \cdot \hat{p}\chi = E\phi; \quad (V - 2c)\chi + c\boldsymbol{\alpha} \cdot \hat{p}\phi = E\chi; \tag{87}$$

The elimination technique previously mentioned consists in the elimination of the small component, which can be achieved by rewriting the second equation in Eq. 87:

$$\chi = \frac{1}{2c^2 + E - V} c\boldsymbol{\alpha} \cdot \hat{p}\phi = \frac{1}{2c} \left( 1 + \frac{E - V}{2c^2} \right)^{-1} \boldsymbol{\alpha} \cdot \hat{p}\phi \equiv \bar{X}\phi \tag{88}$$

and substituting in the first one:

$$\hat{H}_{ESC}\phi \equiv V\phi + c\boldsymbol{\alpha} \cdot \hat{p}\bar{X}\phi = V\phi + \frac{1}{2}\boldsymbol{\alpha} \cdot \hat{p} \left( 1 + \frac{E - V}{2c^2} \right)^{-1} \boldsymbol{\alpha} \cdot \hat{p}\phi = E\phi \tag{89}$$

The Hamiltonian  $\hat{H}_{ESC}$  now acts only on the large component  $\phi$ , which unlike the total wavefunction  $\psi$  is not normalised. A normalised two-component wavefunction  $\Phi = \hat{O}\phi$  therefore needs to be generated by a normalisation operator  $\hat{O}$ :

$$\int d\mathbf{r} \Phi^* \Phi = \int d\mathbf{r} \phi^* \hat{O}^\dagger \hat{O} \phi = \int d\mathbf{r} \psi^* \psi = \int d\mathbf{r} (\phi^* \phi + \chi^* \chi) = 1 \quad (90)$$

Eliminating the small component gives:

$$\int d\mathbf{r} (\phi^* \phi + \chi^* \chi) = \int d\mathbf{r} \phi^* (1 + \bar{\mathbf{X}}^\dagger \bar{\mathbf{X}}) \phi \quad (91)$$

Therefore, a possible choice for the operator  $\hat{O}$  is simply:

$$\hat{O} = \sqrt{1 + \bar{\mathbf{X}}^\dagger \bar{\mathbf{X}}} \quad (92)$$

and the Hamiltonian for  $\Phi$  becomes:

$$\hat{H}_{ESC} = \sqrt{1 + \bar{\mathbf{X}}^\dagger \bar{\mathbf{X}}} (V + c\boldsymbol{\alpha} \cdot \hat{\mathbf{p}} \bar{\mathbf{X}}) \frac{1}{\sqrt{1 + \bar{\mathbf{X}}^\dagger \bar{\mathbf{X}}}} \quad (93)$$

The standard procedure (cfr. Berestetskii, Lifshitz, and Pitaevskii,<sup>79</sup> McWeeny,<sup>80</sup> and Sakurai<sup>81</sup>) consists in expanding the factor  $[1 + (E - V)/2c^2]$  both in  $\bar{\mathbf{X}}$  and  $\hat{H}_{ESC}$  in  $(E - V)/2c^2$ , but as previously mentioned this is not justified for a Coulomb-like potential such as in the case of a molecular system. We are instead going to expand it once again in  $1/(2c^2 - V)$ . The procedure is not too complicated, and the interested reader may refer to the paper from Schwartz *et al.*<sup>82</sup> for a thorough demonstration. The resulting Hamiltonian has the following form:

$$\hat{H}_{ESC} \approx V + \boldsymbol{\alpha} \cdot \hat{\mathbf{p}} \frac{c^2}{2c^2 - V} \boldsymbol{\alpha} \cdot \hat{\mathbf{p}} - \boldsymbol{\alpha} \cdot \hat{\mathbf{p}} \left( \frac{E}{2c^2 - V} \right) \frac{c^2}{2c^2 - V} \boldsymbol{\alpha} \cdot \hat{\mathbf{p}} + \dots \quad (94)$$

and by taking the first two terms (cfr. Eq. 86) we obtain the zeroth-order Hamiltonian:

$$\hat{H}_{ZORA} = V + \boldsymbol{\alpha} \cdot \hat{\mathbf{p}} \frac{c^2}{2c^2 - V} \boldsymbol{\alpha} \cdot \hat{\mathbf{p}} \quad (95)$$

which can be further expanded into:

$$\hat{H}_{ZORA} = V + \hat{\mathbf{p}} \frac{c^2}{2c^2 - V} \hat{\mathbf{p}} + \frac{c^2}{(2c^2 - V)^2} \boldsymbol{\alpha} \cdot (\nabla V \times \hat{\mathbf{p}}) = \hat{H}_{ZORA}^{SR} + \hat{H}_{ZORA}^{SO} \quad (96)$$

This shows that the zeroth-order Hamiltonian naturally includes both scalar and spin-orbit effects.

## 2.16 Time-Dependent QM

Until this point, we have focused on the time-independent solutions of the Hamiltonian eigenvalue problem. However, most of the chemical characteristics of interest – from reactivity, to optical properties, to energy transfer processes – are closely related to how these solutions evolve over time and therefore require the solution of the time-dependent Schrödinger equation. As is the case in the classical world, even in the quantum realm a system remains at equilibrium until some external perturbation affects its equilibrium condition. If such a perturbation is relatively weak, the response of the system can be considered linear with respect to it. This allows us to solve the problem with a perturbative approach.

Maintaining the same formalism used in Chapter 2.1, we consider a time-dependent Schrödinger equation in which the Hamiltonian can be divided into a time-independent part  $\hat{H}_0(\mathbf{r})$  and a time-dependent interaction potential  $\hat{V}(\mathbf{r}, t)$  that determines the evolution of a wavefunction  $|\Psi(\mathbf{r}, t)\rangle$ , which can be expanded onto the basis set  $|\phi_n(\mathbf{r})\rangle$  of the eigenfunctions of the time-independent Hamiltonian  $\hat{H}_0(\mathbf{r})$ :

$$\begin{aligned} i\hbar \frac{\partial \Psi(\mathbf{r}, t)}{\partial t} &= \hat{H}(\mathbf{r}, t) |\Psi(\mathbf{r}, t)\rangle = [\hat{H}_0(\mathbf{r}) + \hat{V}(\mathbf{r}, t)] |\Psi(\mathbf{r}, t)\rangle \\ |\Psi(\mathbf{r}, t)\rangle &= \sum_n c_n(t) |\phi_n(\mathbf{r})\rangle e^{-\frac{iE_n t}{\hbar}} \\ \hat{H}_0(\mathbf{r}) |\phi_n(\mathbf{r})\rangle &= E_n |\phi_n(\mathbf{r})\rangle \end{aligned} \quad (97)$$

To determine the time-dependent coefficients  $c_n(t)$  at  $t > 0$  we substitute the second line of Eq. 97 into the first line. For the left-hand side we get:

$$\begin{aligned} i\hbar \frac{\partial |\Psi(\mathbf{r}, t)\rangle}{\partial t} &= i\hbar \frac{\partial}{\partial t} \left( \sum_n c_n(t) |\phi_n(\mathbf{r})\rangle e^{-\frac{iE_n t}{\hbar}} \right) \\ &= i\hbar \sum_n \left[ \dot{c}_n(t) - \frac{i}{\hbar} E_n c_n(t) \right] |\phi_n(\mathbf{r})\rangle e^{-\frac{iE_n t}{\hbar}} \end{aligned} \quad (98)$$

where  $\dot{c}_n(t) \equiv dc_n(t)/dt$ ; for the r.h.s. we get:

$$\begin{aligned} [\hat{H}_0(\mathbf{r}) + \hat{V}(\mathbf{r}, t)] |\Psi(\mathbf{r}, t)\rangle &= \sum_n c_n(t) [\hat{H}_0(\mathbf{r}) + \hat{V}(\mathbf{r}, t)] |\phi_n(\mathbf{r})\rangle e^{-\frac{iE_n t}{\hbar}} \\ &= \sum_n c_n(t) [E_n + \hat{V}(\mathbf{r}, t)] |\phi_n(\mathbf{r})\rangle e^{-\frac{iE_n t}{\hbar}} \end{aligned} \quad (99)$$

The terms containing  $E_n$  cancel out and the resulting overall equation is:

$$i\hbar \sum_n \dot{c}_n(t) |\phi_n(\mathbf{r})\rangle e^{-\frac{iE_n t}{\hbar}} = \sum_n c_n(t) \hat{V}(\mathbf{r}, t) |\phi_n(\mathbf{r})\rangle e^{-\frac{iE_n t}{\hbar}} \quad (100)$$



Multiplying by  $\langle \phi_k(\mathbf{r}) |$  and integrating gives:

$$i\hbar \sum_n \dot{c}_n(t) \langle \phi_k(\mathbf{r}) | \phi_n(\mathbf{r}) \rangle e^{-\frac{iE_n t}{\hbar}} = \sum_n c_n(t) \langle \phi_k(\mathbf{r}) | \hat{V}(\mathbf{r}, t) | \phi_n(\mathbf{r}) \rangle e^{-\frac{iE_n t}{\hbar}} \quad (101)$$

$$\dot{c}_k(t) = -\frac{i}{\hbar} \sum_n c_n(t) V_{kn}(t) e^{i\omega_{kn} t}$$

where we have defined  $V_{kn}(t) \equiv \langle \phi_k(\mathbf{r}) | \hat{V}(\mathbf{r}, t) | \phi_n(\mathbf{r}) \rangle$  and  $\omega_{kn} \equiv (E_k - E_n)/\hbar$ . If we assume that the system was initially in one precise eigenstate  $\phi_m(\mathbf{r})$ , *i.e.*  $c_k(0) = \delta_{km}$ , we have all the boundary conditions to solve the differential equations in Eq. 101.

If the interaction  $V_{kn}(t)$  is small enough that the change in  $c_n(t)$  is small, we can in first approximation assume that the  $c_n(t)$  in the r.h.s. of the second line in Eq. 101 are unchanged from their initial value  $\delta_{nm}$ . The solution of  $\dot{c}_k(t)$  is then given by:

$$\dot{c}_k^{(1)}(t) = -\frac{i}{\hbar} V_{km}(t) e^{i\omega_{km} t} \quad (102)$$

which upon integration yields:

$$c_k^{(1)}(t) = \delta_{km} - \frac{i}{\hbar} \int_0^t dt' V_{km}(t') e^{i\omega_{km} t'} \quad (103)$$

From Eq. 97 we also observe that the projection of  $|\Psi(\mathbf{r}, t)\rangle$  onto  $|\phi_k(\mathbf{r})\rangle$  is:

$$\langle \phi_k(\mathbf{r}) | \Psi(\mathbf{r}, t) \rangle = c_k e^{-\frac{iE_k t}{\hbar}} \quad (104)$$

and the absolute square of this value gives the probability  $P_k(t)$  (at first order) of finding the system in state  $k$  at time  $t$ :

$$P_k(t) = \left| c_k^{(1)}(t) \right|^2 = \frac{1}{\hbar^2} \left| \int_0^t dt' V_{km}(t') e^{i\omega_{km} t'} \right|^2 \quad (105)$$

A similar procedure can be expanded to Time-Dependent Density Functional Theory (TD-DFT). In 1984 Runge and Gross demonstrated the analogous of the HK theorems for time-dependent systems.<sup>83</sup> By solving Eq. 97 with different potentials  $\hat{V}(\mathbf{r}, t)$  and a fixed initial state  $|\Psi_0(\mathbf{r}, t)\rangle$  a one-to-one mapping between the time-dependent potential and the time-dependent state can be obtained. It is then possible to calculate the densities from all the time-dependent wavefunctions resulting from this mapping, therefore obtaining a direct one-to-one mapping between the potential and the density. Runge and Gross provided proof of this correspondence for two particular cases:

- The potential  $\hat{V}(\mathbf{r}, t)$  is a function with a periodic dependence on time.

- The potential  $\hat{V}(\mathbf{r}, t) = \hat{V}_0(\mathbf{r}) + \hat{V}'(\mathbf{r}, t)$  consists of a static part  $\hat{V}_0(\mathbf{r})$  and a small time-dependent perturbation  $\hat{V}'(\mathbf{r}, t)$ .

The latter is the case of interest for this discussion. Analogously to ground-state DFT, where the density of the system is provided by the KS equations, Runge and Gross started from non-interaction electrons moving in a local potential  $\hat{V}(\mathbf{r}, t)$  to find the time-dependent density of the chemical system. A set of time-dependent KS (TD-KS) equations are introduced to define the density of a time-dependent system and are then solved iteratively in a SCF scheme:<sup>84</sup>

$$\rho(\mathbf{r}, t) = \sum_{i=1}^{occ} n_i |\phi_i(\mathbf{r}, t)|^2 \quad (106)$$

$$i\hbar \frac{\partial |\phi_i(\mathbf{r}, t)\rangle}{\partial t} = \left[ -\frac{1}{2} \nabla^2 + \hat{V}_{KS}(\mathbf{r}, t) \right] |\phi_i(\mathbf{r}, t)\rangle$$

In the same fashion as the static case, the time-dependent KS potential  $\hat{V}_{KS}(\mathbf{r}, t)$  is defined as:

$$\hat{V}_{KS}(\mathbf{r}, t) = \hat{V}_{ext}(\mathbf{r}, t) + \hat{V}_H(\mathbf{r}, t) + \hat{V}_{XC}(\mathbf{r}, t) \quad (107)$$

where the Hartree potential  $\hat{V}_H(\mathbf{r}, t)$  is calculated from the density  $\rho(\mathbf{r}, t)$  as:

$$\hat{V}_H(\mathbf{r}, t) = \int d\mathbf{r}' \frac{\rho(\mathbf{r}', t)}{|\mathbf{r} - \mathbf{r}'|} \quad (108)$$

and the time-dependent exchange-correlation potential  $\hat{V}_{XC}(\mathbf{r}, t)$  is again an unknown functional of the time-dependent density.

If the external potential  $\hat{V}'(\mathbf{r}, t)$  is switched on adiabatically at time  $t = t_0$  it can be expressed by the following structure:

$$\hat{V}'(\mathbf{r}, t) = \begin{cases} \hat{V}_0(\mathbf{r}) & \text{if } t < t_0 \\ \hat{V}_0(\mathbf{r}) + \hat{V}'(\mathbf{r}, t) & \text{if } t \geq t_0 \end{cases} \quad (109)$$

The linear density response function  $\rho_1(\mathbf{r}, t)$  in this case can be evaluated in terms of the full response function  $\chi(\mathbf{r}, t; \mathbf{r}', t')$  of the interacting system:

$$\rho_1(\mathbf{r}, t) = \int d\mathbf{r}' \int_0^\infty dt' \chi(\mathbf{r}, t; \mathbf{r}', t') V'(\mathbf{r}', t') \quad (110)$$

Or alternatively, since the TD-KS equations provide an exact way to compute the time-dependent electron density in a similar way to the standard KS equation (Eq. 106), the linear density response of the interacting system can be calculated as the density response of the non-interacting KS system described by its response function  $\chi_{KS}(\mathbf{r}, t; \mathbf{r}', t')$ :

$$\rho_1(\mathbf{r}, t) = \int d\mathbf{r}' \int_0^\infty dt' \chi_{KS}(\mathbf{r}, t; \mathbf{r}', t') V'_{KS}(\mathbf{r}', t') \quad (111)$$

$V'_{KS}(\mathbf{r}', t')$  is the KS potential calculated to the first-order of the perturbing potential  $V'(\mathbf{r}, t)$ :

$$V'_{KS}(\mathbf{r}', t') = V'(\mathbf{r}', t') + \int d\mathbf{r}'' \frac{\rho(\mathbf{r}'', t')}{|\mathbf{r}'' - \mathbf{r}'|} + \int d\mathbf{r}'' \int dt'' f_{XC}(\mathbf{r}, t; \mathbf{r}'', t'') \rho_1(\mathbf{r}'', t'') \quad (112)$$

where  $f_{XC}(\mathbf{r}, t; \mathbf{r}', t')$  is the exchange-correlation response kernel, defined as the functional derivative of the time-dependent exchange-correlation potential  $V_{XC}(\mathbf{r}, t)$  with respect to the electron density  $\rho(\mathbf{r}', t')$  evaluated at the initial ground-state density  $\rho_0(\mathbf{r})$ :

$$f_{XC}(\mathbf{r}, t; \mathbf{r}', t') = \left. \frac{dV_{XC}[\rho](\mathbf{r}, t)}{d\rho(\mathbf{r}', t')} \right|_{\rho=\rho_0} \quad (113)$$

The  $f_{XC}$  kernel represents the first-order variation of the time-dependent exchange-correlation potential  $V_{XC}$  due to the applied perturbation. Adopting some appropriate approximations for it, the TD-KS equations provide a SCF scheme to evaluate the linear density response  $\rho_1(\mathbf{r}, t)$  as a consequence of the activation of the external perturbation. The so-called Adiabatic Local Density Approximation (ALDA)<sup>85</sup> is the simplest TD-DFT approximation for the treatment of the  $f_{XC}$  kernel, which is reduced to a real function local in space, frequency-independent, and evaluated on the LDA XC potential in correspondence of the local SCF electron density  $\rho_0(\mathbf{r})$ :

$$f_{XC}^{ALDA}(\mathbf{r}, \mathbf{r}') = \delta(\mathbf{r} - \mathbf{r}') \left. \frac{dV_{XC}^{LDA}(\mathbf{r}, t)}{d\rho(\mathbf{r}', t')} \right|_{\rho=\rho_0} \quad (114)$$

## 2.17 Electronic Excitations in TD-DFT

In this brief section we will quickly illustrate how the excitation energies for the simulation of absorption spectroscopy experiments in TD-DFT are evaluated. A more comprehensive description is reported in Refs. 84,86. The corresponding eigenvalue equation for such a problem is:

$$\Omega \mathbf{F}_I = \omega_I^2 \mathbf{F}_I \quad (115)$$

The components of the matrix  $\Omega$  are:

$$\begin{aligned}
\Omega_{ia\sigma,jb\tau} &= \delta_{ij}\delta_{ab}\delta_{\sigma\tau}(\varepsilon_{a\sigma} - \varepsilon_{i\sigma})^2 + 2\sqrt{\varepsilon_{a\sigma} - \varepsilon_{i\sigma}}K_{ia\sigma,jb\tau}\sqrt{\varepsilon_{b\tau} - \varepsilon_{j\tau}} \\
K_{ia\sigma,jb\tau} &= K_{ia\sigma,jb\tau}^{Coul} + K_{ia\sigma,jb\tau}^{XC} \\
K_{ia\sigma,jb\tau}^{Coul} &= \int d\mathbf{r} \int d\mathbf{r}' \phi_{a\sigma}^*(\mathbf{r})\phi_{b\tau}^*(\mathbf{r}) \frac{1}{|\mathbf{r} - \mathbf{r}'|} \phi_{i\sigma}(\mathbf{r})\phi_{j\tau}(\mathbf{r}) \\
K_{ia\sigma,jb\tau}^{XC} &= \int d\mathbf{r} \int d\mathbf{r}' \phi_{a\sigma}^*(\mathbf{r})\phi_{b\tau}^*(\mathbf{r}) f_{XC}^{\sigma\tau} \times \delta(\mathbf{r} - \mathbf{r}')\phi_{i\sigma}(\mathbf{r})\phi_{j\tau}(\mathbf{r})
\end{aligned} \tag{116}$$

where  $a, b$  are the indices for the virtual orbitals,  $i, j$  are those for the occupied orbitals,  $\sigma, \tau$  are the indices for spin,  $\varepsilon$  is the orbital energy,  $\phi$  are the KS orbitals and  $f_{XC}^{\sigma\tau}$  is the XC kernel within the adiabatic approximation.  $\omega_l$  are the excitation energies while the corresponding intensities are given by the oscillator strengths obtained from the  $\mathbf{F}_l$  eigenvectors. The direct solution of this eigenvalue problem is possible in principle, but it is generally infeasible due to computational and storage requirements. For this reason, it is preferable to solve the eigenvalue problem iteratively by employing the Davidson algorithm,<sup>87</sup> which requires low computational costs even for large matrices. In this algorithm it is possible to restrict the calculation to a few selected eigenvalues, generally the lowest-energy excitations. In the initial hypothesis for the first iteration of  $\mathbf{F}_l$  it is generally considered that the excitation energies are simply the difference between the energies of occupied and virtual KS orbitals.

## References

- (1) Dirac, P. A. M. *Math. Proc. Cambridge Philos. Soc.* **1939**, *35* (3), 416–418.
- (2) Riley, K. F.; Hobson, M. P.; Bence, S. J. *Mathematical Methods for Physics and Engineering*; Cambridge University Press, 2006.
- (3) Kober, M. *Copenhagen Interpretation of Quantum Theory and the Measurement Problem*; 2009.
- (4) Schrödinger, E. *Phys. Rev.* **1926**, *28* (6), 1049–1070.
- (5) Margenau, H.; Murphy, G. M. *The Mathematics of Physics and Chemistry*; D. Van Nostrand Company, 1956.
- (6) Born, M.; Oppenheimer, R. *Ann. Phys.* **1927**, *389* (20), 457–484.
- (7) Massimi, M. *Pauli's Exclusion Principle: The Origin and Validation of a Scientific Principle*; Cambridge University Press, New York, 2005.
- (8) Griffith, J. S. *The Theory of Transition Metal Ions*; Cambridge University Press, New York, 1971.
- (9) Poincaré, H. *Acta Math.* **1890**, *13* (1).
- (10) Hartree, D. R. *Math. Proc. Cambridge Philos. Soc.* **1928**, *24* (1), 89–110.
- (11) Fock, V. *Zeitschrift für Phys.* **1930**, *61* (1–2), 126–148.
- (12) Slater, J. C. *Phys. Rev.* **1930**, *35* (2), 210–211.
- (13) Hartree, D. R.; Hartree, W. *Proc. R. Soc. London. Ser. A - Math. Phys. Sci.* **1935**, *150* (869), 9–33.
- (14) Slater, J. C. *Phys. Rev.* **1951**, *81* (3), 385–390.
- (15) Feller, D.; Peterson, K. A. *J. Chem. Phys.* **1998**, *108* (1), 154–176.
- (16) Cramer, C. J. *Essentials of Computational Chemistry*; Wiley, 2004.
- (17) Maksić, Z. B.; Vianello, R. *J. Phys. Chem. A* **2002**, *106* (27), 6515–6520.
- (18) Wiest, O.; Montiel, D. C.; Houk, K. N. *J. Phys. Chem. A* **1997**, *101* (45), 8378–8388.
- (19) Löwdin, P. O. *Phys. Rev.* **1955**, *97* (6), 1509–1520.
- (20) Löwdin, P.-O. *Phys. Rev.* **1955**, *97* (6), 1474–1489.
- (21) Szabo, A.; Ostlund, N. S. *Modern Quantum Chemistry*; Dover, 1996.
- (22) Roothaan, C. C. J. *Rev. Mod. Phys.* **1951**, *23* (2), 69–89.
- (23) Møller, C.; Plesset, M. S. *Physical Review*. 1934, pp 618–622.
- (24) Bauschlicher, C. W.; Taylor, P. R. *Theor. Chim. Acta* **1987**, *71* (4), 263–276.
- (25) Scheiner, A. C.; Baker, J.; Andzelm, J. W. *J. Comput. Chem.* **1997**, *18* (6), 775–795.
- (26) Daniel, C.; Matsubara, T.; Stor, G. *Coord. Chem. Rev.* **1994**, *132* (C), 63–74.
- (27) Halbach, R. L.; Nocton, G.; Amaro-Estrada, J. I.; Maron, L.; Booth, C. H.; Andersen, R. A. *Inorg. Chem.* **2019**, *58* (18), 12083–12098.
- (28) Bearpark, M. J.; Robb, M. A.; Yamamoto, N. *Spectrochim. Acta - Part A Mol. Biomol. Spectrosc.* **1999**, *55* (3), 639–646.
- (29) Li, Y.; Houk, K. N. *J. Am. Chem. Soc.* **1993**, *115* (16), 7478–7485.
- (30) Fang, W. H. *J. Am. Chem. Soc.* **1999**, *121* (36), 8376–8384.
- (31) Sinnecker, S.; Neese, F. *J. Phys. Chem. A* **2006**, *110* (44), 12267–12275.
- (32) Schreiber, M.; Silva-Junior, M. R.; Sauer, S. P. A.; Thiel, W. *J. Chem. Phys.* **2008**, *128* (13).
- (33) Heydová, R.; Gindensperger, E.; Romano, R.; Sýkora, J.; Vlček, A.; Zálíš, S.; Daniel, C. *J. Phys. Chem. A* **2012**, *116* (46), 11319–11329.
- (34) von Weizsäcker, C. *Zeitschrift für Phys.* **1935**, *96*, 431.
- (35) Fermi, E. *Zeitschrift für Phys.* **1928**, *48* (1–2), 73–79.
- (36) Fermi, E. *Rend. Accad. Naz. Lincei* **1927**, *6*, 32.
- (37) Thomas, L. H. *Math. Proc. Cambridge Philos. Soc.* **1927**, *23* (5), 542–548.
- (38) Wigner, E. *Phys. Rev.* **1934**, *46* (11), 1002–1011.
- (39) Kittel, C. *Introduction to Solid State Physics*; Wiley, 2005.

- (40) Teller, E. *Rev. Mod. Phys.* **1962**, *34* (4), 627–631.
- (41) Hohenberg, P.; Kohn, W. *Phys. Rev.* **1964**, *136* (3B), B864–B871.
- (42) Kohn, W.; Sham, L. J. *Phys. Rev.* **1965**, *140* (4A), A1133–A1138.
- (43) Becke, A. D. *Phys. Rev. A* **1988**, *38* (6), 3098–3100.
- (44) Levy, M.; Perdew, J. P. *Phys. Rev. A* **1985**, *32* (4), 2010–2021.
- (45) Lieb, E. H.; Oxford, S. *Int. J. Quantum Chem.* **1981**, *19* (3), 427–439.
- (46) Perdew, J. P.; Parr, R. G.; Levy, M.; Balduz, J. L. *Phys. Rev. Lett.* **1982**, *49* (23), 1691–1694.
- (47) ADF2013.01 Program, SCM, Theoretical Chemistry, Vrije Universiteit, Amsterdam, The Netherlands. <http://www.scm.com>.
- (48) Vosko, S. H.; Wilk, L.; Nusair, M. *Can. J. Phys.* **1980**, *58* (8), 1200–1211.
- (49) Perdew, J. P.; Wang, Y. *Phys. Rev. B* **1992**, *45* (23), 13244–13249.
- (50) Perdew, J. P. *Phys. Rev. B* **1986**, *33* (12), 8822–8824.
- (51) Perdew, J. P.; Burke, K.; Ernzerhof, M. *Phys. Rev. Lett.* **1997**, *78* (7), 1396–1396.
- (52) Perdew, J. P.; Burke, K.; Ernzerhof, M. *Phys. Rev. Lett.* **1996**, *77* (18), 3865–3868.
- (53) Lee, C.; Yang, W.; Parr, R. G. *Phys. Rev. B* **1988**, *37* (2), 785–789.
- (54) Miehlich, B.; Savin, A.; Stoll, H.; Preuss, H. *Chem. Phys. Lett.* **1989**, *157* (3), 200–206.
- (55) Staroverov, V. N.; Scuseria, G. E.; Tao, J.; Perdew, J. P. *J. Chem. Phys.* **2003**, *119* (23), 12129–12137.
- (56) Tao, J.; Perdew, J. P.; Staroverov, V. N.; Scuseria, G. E. *Phys. Rev. Lett.* **2003**, *91* (14), 3–6.
- (57) Zhao, Y.; Truhlar, D. G. *J. Chem. Phys.* **2006**, *125* (19).
- (58) Zhao, Y.; Truhlar, D. G. *Theor. Chem. Acc.* **2008**, *120* (1–3), 215–241.
- (59) MacDonald, J. K. L. *Phys. Rev.* **1933**, *43* (10), 830–833.
- (60) Stephens, P. J.; Devlin, F. J.; Chabalowski, C. F.; Frisch, M. J. *J. Phys. Chem.* **1994**, *98* (45), 11623–11627.
- (61) Cohen, A. J.; Handy, N. C. *Mol. Phys.* **2001**, *99* (7), 607–615.
- (62) Adamo, C.; Barone, V. *J. Chem. Phys.* **2002**, *116* (14), 5933–5940.
- (63) Ernzerhof, M.; Scuseria, G. E. *J. Chem. Phys.* **1999**, *110* (11), 5029–5036.
- (64) Curtiss, L. A.; Raghavachari, K.; Redfern, P. C.; Pople, J. A. *J. Chem. Phys.* **2000**, *112* (17), 7374–7383.
- (65) Jensen, F. *Introduction to Computational Chemistry*; Wiley, 2007.
- (66) Oliphant, N.; Bartlett, R. J. *J. Chem. Phys.* **1994**, *100* (9), 6550–6561.
- (67) Meijer, E. J.; Sprik, M. *J. Chem. Phys.* **1996**, *105* (19), 8684–8689.
- (68) Cybulski, S. M.; Seversen, C. E. *J. Chem. Phys.* **2005**, *122* (1).
- (69) Rienstra-Kiracofe, J. C.; Tschumper, G. S.; Schaefer, H. F.; Nandi, S.; Ellison, G. B. *Chem. Rev.* **2002**, *102* (1), 231–282.
- (70) Einstein, A. *Ann. Phys.* **1905**, *18*, 639–641.
- (71) Pyykkö, P. *Chem. Rev.* **1988**, *88* (3), 563–594.
- (72) Hess, B. A. *Phys. Rev. A* **1986**, *33* (6), 3742–3748.
- (73) Hess, B. A. *Phys. Rev. A* **1985**, *32* (2), 756–763.
- (74) Douglas, M.; Kroll, N. M. *Ann. Phys. (N. Y.)* **1974**, *82* (1), 89–155.
- (75) Lenthe, E. van; Baerends, E. J.; Snijders, J. G. *J. Chem. Phys.* **1993**, *99* (6), 4597–4610.
- (76) Darwin, C. G. *Proc. R. Soc. London. Ser. A, Contain. Pap. a Math. Phys. Character* **1928**, *118* (780), 654–680.
- (77) Heully, J. L.; Lindgren, I.; Lindroth, E.; Lundqvist, S.; Martensson-Pendrill, A. M. *J. Phys. B At. Mol. Phys.* **1986**, *19* (18), 2799–2815.
- (78) Foldy, L. L. *Phys. Rev.* **1990**, *78* (1), 29–36.
- (79) Berestetskii, V. B.; Lifshitz, E. M.; Pitaevskii, L. P. *Relativistic Quantum Theory*; Pergamon, Oxford, 1971.

- (80) McWeeny, R.; Sutcliffe, B. T. *Methods of Molecular Quantum Mechanics*; Academic, London, 1976.
- (81) Sakurai, J. J. *Advanced Quantum Mechanics*; Addison-Wesley, 1967.
- (82) Schwarz, W. H. E.; Van Wezenbeek, E. M.; Baerends, E. J.; Snijders, J. G. *J. Phys. B At. Mol. Opt. Phys.* **1989**, *22* (10), 1515–1529.
- (83) Runge, E.; Gross, E. K. U. *Phys. Rev. Lett.* **1984**, *52* (12), 997–1000.
- (84) Van Gisbergen, S. J. A.; Snijders, J. G.; Baerends, E. J. *Comput. Phys. Commun.* **1999**, *118* (2), 119–138.
- (85) Gross, E. K. U.; Kohn, W. *Phys. Rev. Lett.* **1985**, *55* (26), 2850–2852.
- (86) Wang, F.; Ziegler, T. *Mol. Phys.* **2004**, *102* (23–24), 2585–2595.
- (87) Davidson, E. R. *J. Comput. Phys.* **1975**, *17* (1), 87–94.





### 3. ENERGY LEVEL STRUCTURE OF THE $[\text{Xe}]4f^6$ CONFIGURATION

In this chapter we will collect all the relevant information useful to understand the various phenomena involved in lanthanide-based luminescence. While the previous chapter was devoted to illustrating the methods used to calculate such properties, this section will be used to describe the actual physics at play and how the various pieces in a molecular complex can interact.

Europium, element number 63 of the periodic table, is typically used in its trivalent ion form  $\text{Eu}^{3+}$ . Trivially, this ion has 60 electrons, of which 54 belong to the internal closed shell of the Xe electron configuration, where all the shells up to  $5p$  are completely filled. The remaining 6 valence electrons are located in the  $4f$  shell. Despite being at a lower energy, the filled  $5s$  and  $5p$  shells are actually found at a greater average distance from the nucleus (Figure 4) and this shields the valence  $4f$  electrons from the perturbing effects of the external environment. This is the reason why all lanthanides possess similar chemistries and why the optical properties of lanthanide-based compounds featuring the same ion are comparable even for wildly different systems.

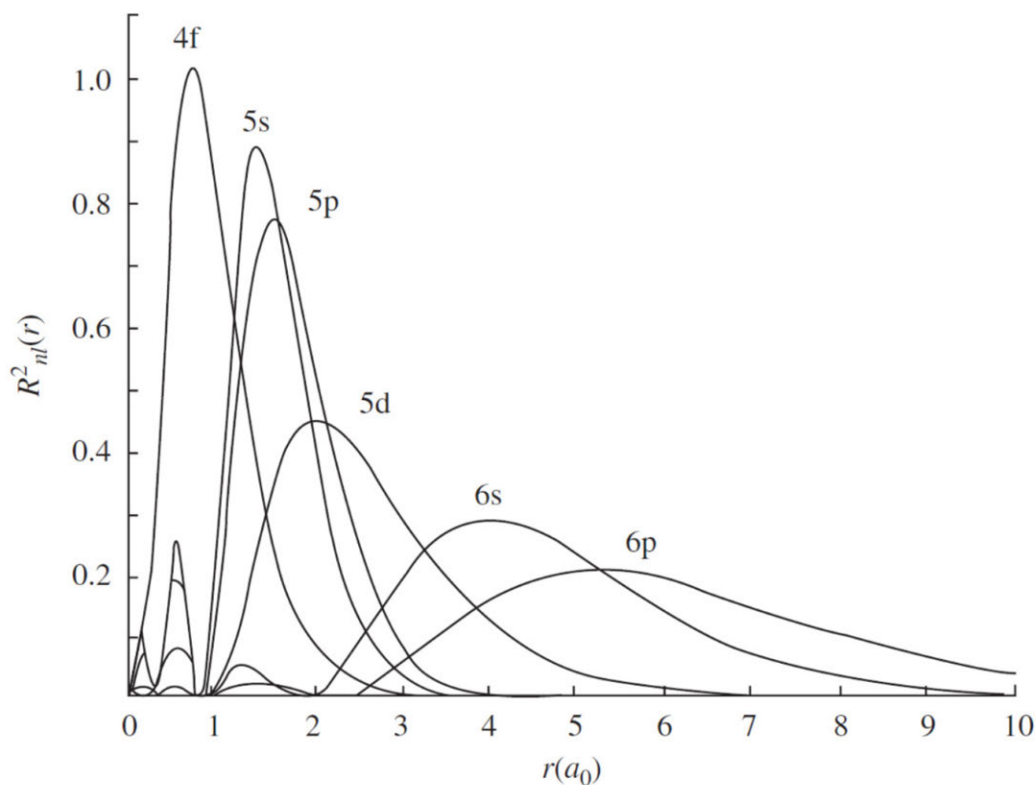


**Figure 4.** Radial probability distribution for the  $4f$ ,  $5s$ ,  $5p$ ,  $5d$ ,  $6s$ , and  $6p$  orbitals. The innermost  $4f$  orbitals are shielded by the outer filled  $5s$  and  $5p$  shells. (Z.B. Goldschmidt, "Atomic properties (free atom)," in K.A. Gschneidner and L. Eyring (eds.), *Handbook on the Physics and Chemistry of Rare Earths*, volume I, 2nd edition, North Holland Publishing Company, Amsterdam. © 1978)

The 6 valence electrons can be arranged in various ways within the 14 spin-orbitals of the 4*f* shell. Each of these is called a *microstate*. The total number of possible arrangements is given by the binomial coefficient:<sup>1</sup>

$$\binom{14}{6} = \frac{14!}{6!(14-6)!} = 3003 \quad (117)$$

All of these configurations, disregarding any kind of perturbation acting on the electrons, should possess the same energy. The 4*f*<sup>6</sup> configuration, therefore, is 3003 times degenerate in the absence of any interaction. As should be obvious by now, each electron is not in a vacuum by itself and there are numerous perturbations affecting it. In decreasing order of intensity, these interactions are: electron-electron repulsion, spin-orbit coupling, and crystal-field effects.

Electrostatic repulsion between the different electrons in the same shell represents the term with the largest impact. After its inclusion, the 4*f*<sup>6</sup> configuration is characterised by 119 <sup>2*S*+1</sup>*L*(*τ*) terms, where each term is (2*S* + 1)(2*L* + 1) times degenerate. *S* is the *total spin quantum number*, *L* is the *total orbital angular momentum quantum number* and *τ* is an additional quantum number used to differentiate between terms with the same values for *S* and *L*. According to the first Hund rule,<sup>2,3</sup> the ground state for a given electron configuration is given by the term with the highest spin multiplicity. For the 4*f*<sup>6</sup> configuration we can arrange each of the 6 electrons in its own orbital, all with parallel spins, as to give a *septet* term. The second Hund rule states that, amongst the terms with the same spin multiplicity, the lowest energy one is the one with the highest orbital angular momentum. In our case, there is actually only one septet term and it is an *F* term (*L* = 3). The ground state for the 4*f*<sup>6</sup> configuration after including electron repulsion is therefore the <sup>7</sup>*F* term. The separation in energy between the lowest terms is of the order of 10<sup>4</sup> cm<sup>-1</sup>.

In heavy atoms such as Eu, even the outermost electrons possess such high velocities that relativistic effects cannot be neglected. Two major aspects require consideration when it comes to relativistic corrections, as we described in section 2.12: the scalar correction to the kinetic energy – which is relevant when the electron travels at a speed close to that of light – and spin-orbit coupling. The motion of a charged particle through space, such as an electron moving in an orbital with non-nil angular momentum, generates a magnetic field.<sup>4</sup> The intrinsic magnetic spin moment of the particle then interacts with this magnetic field, and the total energy needs to be corrected taking this into account. Incidentally, this also implies that *L* and *S* are not good quantum numbers anymore, and the *total angular quantum number* *J* = *L* + *S* needs to be considered. The inclusion of spin-orbit coupling generates 295 <sup>2*S*+1</sup>*L*(*τ*)<sub>*J*</sub> states. For each <sup>2*S*+1</sup>*L* term, the possible values of *J* are given by the Clebsch-Gordan series<sup>5</sup> *L* + *S*, *L* + *S* – 1, ..., |*L* – *S*|. Each free-ion level is described by a <sup>2*S*+1</sup>*L*(*τ*)<sub>*J*</sub> label and is 2*J* + 1 times degenerate. According to the third Hund rule, for a shell which is less than half-filled as is the case of the 4*f*<sup>6</sup> configuration, the lowest energy state will be the one with the smallest *J*. The spin-orbit ground state for the Eu<sup>3+</sup> ion will therefore be <sup>7</sup>*F*<sub>0</sub>.

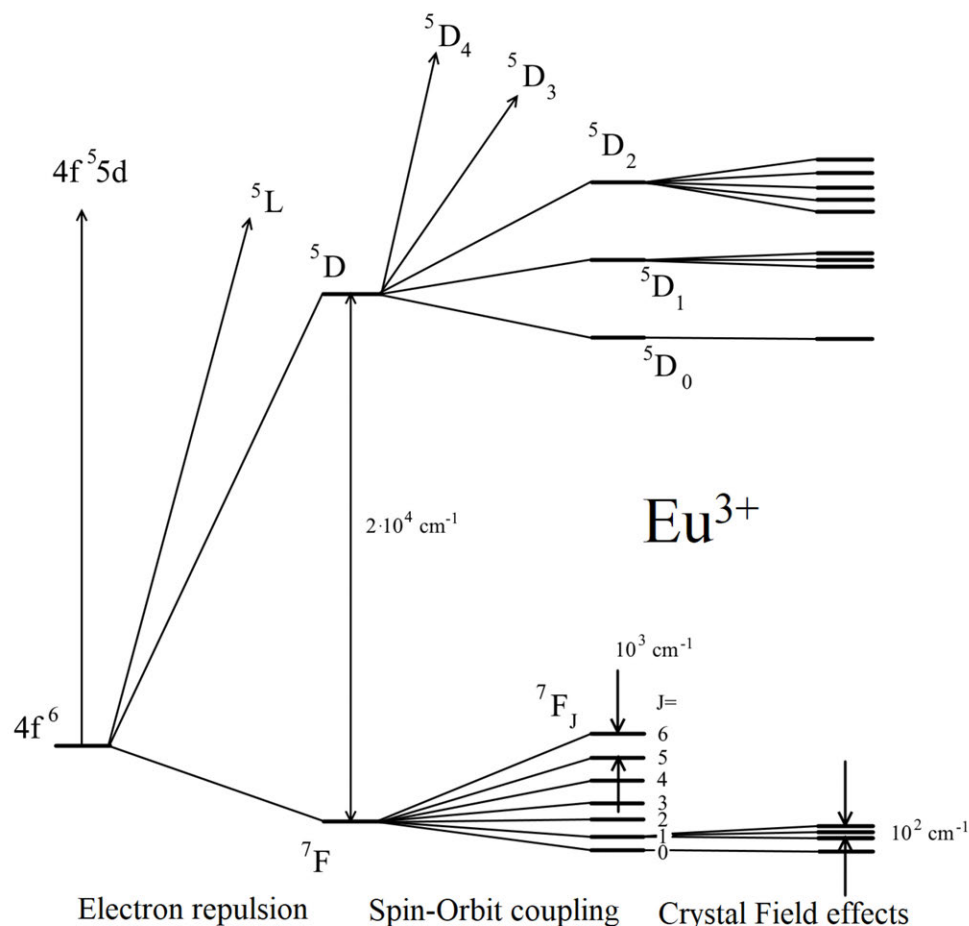


**Figure 5.** Energy levels of the  $4f^6$  configuration. The degeneracy is lifted when taking into account, in order, electron repulsion, spin-orbit coupling, and crystal-field effects.

The splitting of spin-orbit states is of the order of  $10^3 \text{ cm}^{-1}$ , about an order of magnitude smaller than the splitting induced by electron repulsion (Figure 5).

Traditionally, spin-orbit states are described in the terms of the Russel-Saunders coupling scheme.<sup>6</sup> This assumes that spin-orbit coupling is a weak perturbation compared to the electronic repulsion interaction, which is verified for the vast majority of elements, but not for lanthanides. This scheme cannot therefore be rigorously applied. The so-called *jj coupling scheme* needs to be invoked.<sup>7</sup> In this framework, the wavefunction is rewritten as a linear combination of Russel-Saunders states. The most relevant consequence is that states with the same  $J$  can mix, regardless of their  $S$  and  $L$  originating values, and this results in a relaxation of the selection rules on electronic transitions.

The degeneracy of the free ion spin-orbit states is then further lifted by the presence of crystal field effects, as exerted by the ligands. The energy levels are now described by the irreducible representation of the  $\text{Eu}^{3+}$  site point group.<sup>8</sup> Unlike in complexes of transition metal ions, crystal field effects in lanthanide ion complexes are severely mitigated by the shielding effects of the outer  $5s$  and  $5p$  shells on the  $4f$  electrons, and the resulting splitting is of the order of a few hundred  $\text{cm}^{-1}$  at most.

### 3.1 Antenna effect

In systems which exploit the luminescence properties of the lanthanide ion, it is obviously necessary to populate the emitter excited state ( ${}^5D_0$  for  $\text{Eu}^{3+}$ ) in the first place. This can be achieved via direct excitation of the lanthanide centre through light absorption, but it is an extremely inefficient process for a number of reasons.

The intensity of an electric dipole transition between two electronic states is directly related to the transition dipole moment  $\mu_{if}$  between the two states of interest:

$$\mu_{if} = \langle \Psi_i | \hat{\mu} | \Psi_f \rangle = -e \int d\mathbf{r} \Psi_i^* \hat{\mathbf{r}} \Psi_f \quad (118)$$

where  $\Psi_i$  and  $\Psi_f$  are the initial (ground) and final (excited) wavefunctions, respectively;  $e$  is the electron charge and  $\hat{\mathbf{r}}$  is the position operator. Group theory – for a more detailed discussion on group theory, the interested reader may refer to Cotton, F. A. *Chemical Applications of Group Theory*, 3rd ed.; Wiley, 1989 – tells us that in order for the integral in Eq. 118 to be non-vanishing, the product within must contain the totally symmetric representation for the point group of the system. In layman’s terms, this means that this product must have *gerade* ( $g$ ) parity, *i.e.* it must maintain the same sign under inversion. The operator  $\hat{\mathbf{r}}$  (and by consequence  $\hat{\mu}$ ) transforms simply as the coordinates  $x, y, z$  and is therefore antisymmetric (*ungerade*,  $u$ ) with respect to the inversion operation ( $r \rightarrow -r$ ). The parity of an electronic state is directly related to its orbital quantum number  $l$ , more specifically it has parity  $(-1)^l$ , so  $s$  and  $d$  orbitals are *gerade*, while  $p$  and  $f$  orbitals are *ungerade*. Let us be reminded that the product of two terms with *gerade*/*ungerade* symmetries follows these rules:

$$\begin{aligned} g \times g &= g \\ g \times u &= u \times g = u \\ u \times u &= g \end{aligned} \quad (119)$$

It emerges naturally, that in order for the product  $\Psi_i^* \times \hat{\mathbf{r}} \times \Psi_f$  to have *gerade* symmetry,  $\Psi_i^*$  and  $\Psi_f$  cannot have the same parity, as one of them must have  $u$  symmetry to “neutralise” the dipole operator and the other must have  $g$  symmetry to maintain the even parity. This is also known as the Laporte rule,<sup>9</sup> which forbids transitions between electronic states with the same parity. The  $f$ - $f$  transition involved in the direct excitation of  $\text{Ln}^{3+}$  ions are therefore formally forbidden.

As the electric field of the incident radiation does not act on the spin of the electrons, an allowed electric dipole transition must also maintain the same spin state in the initial and final wavefunctions. The  ${}^7F_0 \rightarrow {}^5D_0$  transition is a *septet-quintet* transition and is therefore also spin-forbidden.

Furthermore, the  ${}^7F_0 \rightarrow {}^5D_0$  is also forbidden by the standard Judd-Ofelt theory, in particular it violates the selection rules on  $\Delta J$ .<sup>10</sup>

All of these factors reflect on the very low molar absorption coefficients for these kind of electronic transitions, which are in the order of  $\epsilon \approx 1 - 10 \text{ M}^{-1} \text{ cm}^{-1}$ .

In order to effectively exploit the luminescence properties of  $\text{Eu}^{3+}$  (and of  $\text{Ln}^{3+}$  ions in general), it is necessary to find an alternative, more efficient way to populate the  $^5\text{D}_0$  state. It is possible to greatly enhance the population of the emitter level through the so-called *antenna effect*, in which an organic chromophore –  $\epsilon \approx 10^4 - 10^5 \text{ M}^{-1} \text{ cm}^{-1}$  in the UV region – is used as a ligand in the complex.<sup>11</sup>

The chromophore ligand absorbs light and undergoes excitation from its ground state  $S_0$  to a higher energy excited state. Regardless of the final electronic level, relaxation to the first singlet excited state  $S_1$  (Kasha's rule).<sup>12</sup> From here, intersystem crossing (ISC), which incidentally is induced by spin-orbit coupling and is enhanced by the presence of the heavy metal centre, promotes the population of the lowest-lying triplet state  $T_1$ . From this triplet state, energy transfer (ET) to the emitter level  $^5\text{D}_0$  occurs and the characteristic emission of  $\text{Eu}^{3+}$  takes place. The process is schematically illustrated in Figure 6.

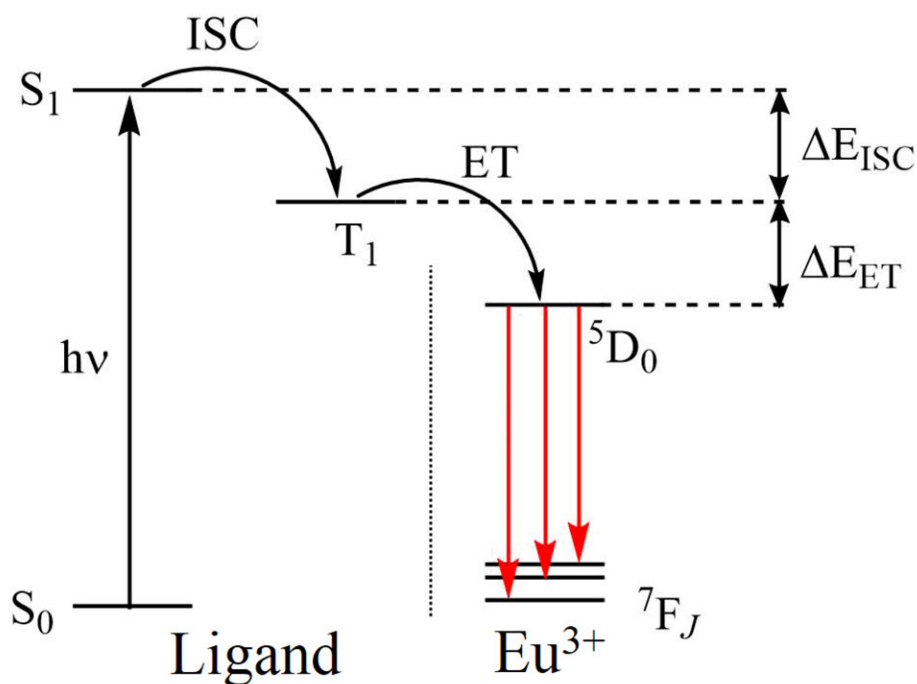


**Figure 6.** Energy levels diagram for the antenna effect. The chromophore (ligand) in the ground state  $S_0$  absorbs the UV radiation and reaches the excited state  $S_1$ . After intersystem crossing (ISC) to the triplet state  $T_1$  energy transfer (ET) to the  $^5\text{D}_0$  state of  $\text{Eu}^{3+}$  can occur. This sensitization process greatly enhances the emission intensity of the lanthanide centre.

There are some optimal values for the energy gaps between  $S_1$  and  $T_1$  in ISC ( $\Delta E_{\text{ISC}}$ ), and between  $T_1$  and  $^5\text{D}_0$  in ET ( $\Delta E_{\text{ET}}$ ). If the energy gap is too wide, the mismatch inhibits an efficient conversion, whereas too small of a gap could result in the electron “jumping back” to the initial state, via back-energy transfer processes. The optimal energy caps for efficient ISC and ET are  $\Delta E_{\text{ISC}} \approx 5000 \text{ cm}^{-1}$  and  $\Delta E_{\text{ET}} \approx 3500 \text{ cm}^{-1}$ , respectively.<sup>13</sup>

For all the reasons we illustrated previously, the  $4f$  electrons of  $\text{Eu}^{3+}$  are barely affected by the surrounding environment, and the  $^5\text{D}_0$  state is always found at around the same energy,

about 17200 cm<sup>-1</sup> above the ground state <sup>7</sup>F<sub>0</sub>.<sup>14</sup> This behaviour is reported extensively in the literature, where it can be seen that even for massively different complexes the difference in energy for the emitter state is at most of a few hundred cm<sup>-1</sup>.<sup>11,14-21</sup> The only way to modify ΔE<sub>ISC</sub> and ΔE<sub>ET</sub> is therefore to act on the S<sub>1</sub> and T<sub>1</sub> states of the ligand, and therefore a deep theoretical knowledge of its electronic states is crucial to the design of new systems with improved performance.

Once the emitter level is populated, radiative decay (*i.e.* emission) is not the only pathway the excitation can follow. Non-radiative decay can occur either in the form of back-energy transfer to the triplet state, if T<sub>1</sub> is sufficiently close in energy to the emitter state, or by luminescence quenching due to the coupling between electronic and vibrational levels. The former is characteristic of systems in which the triplet state is less than 1850 cm<sup>-1</sup> higher in energy than the <sup>5</sup>D<sub>0</sub> state,<sup>22</sup> while the latter is found in concurrence with the presence of high energy oscillator in the ligand molecules (*e.g.* O-H, N-H groups). Incidentally, it is these non-radiative deactivation pathways which can be exploited for the construction of molecular thermometers, as these processes are usually temperature-dependent.

### 3.2 Non-radiative decay processes in Eu<sup>3+</sup> complexes

Eu<sup>3+</sup>-based molecular thermometers use the luminescence of the central lanthanide ion as the thermometric parameter for gauging the temperature. As we just mentioned, the non-radiative decay processes quenching the luminescence are what gives the ability to correlate the luminescence intensity (or the excited state lifetimes) with the temperature, as these are temperature-dependent phenomena. In fact, if these did not exist, luminescence would be constant at every temperature thus making impossible this kind of correlation. Understanding the mechanisms behind these processes is fundamental for the development of new systems with improved performance, and the modelling of the thermometric response of Eu<sup>3+</sup>-based molecular thermometers is the main focus of the next chapter.

Two primary pathways for the non-radiative quenching of the Eu<sup>3+</sup> excited state exist: back-energy transfer to another excited state, and vibronic coupling with a high-energy oscillator. As far as the former is concerned, this back-energy transfer can take place towards either the same triplet which populated the emitter state in the first place, or to eventual ligand-to-metal charge transfer (LMCT) states. In general, an energy transfer rate  $W_{ET}$  is given by some appropriately manipulated form of the Fermi golden rule equation:<sup>23</sup>

$$W_{ET} = \frac{2\pi}{\hbar} \langle \Psi_f | \hat{H} | \Psi_i \rangle^2 \delta(E_f - E_i) \quad (120)$$

where  $\Psi_i$  and  $\Psi_f$  are the initial and final electronic states, respectively, while  $E_i$  and  $E_f$  are the energies of the two electronic states, and  $\delta$  is a Kronecker delta which is 1 when the two energies are the same and 0 otherwise. Obviously, this is a “pure” limit case and in the real world this perfect resonance condition needs not be satisfied so tightly. This equation tells us that the closer the two electronic states (*e.g.* T<sub>1</sub> and <sup>5</sup>D<sub>0</sub>) are in energy, the more efficient the energy transfer, and therefore the population of the emitter state is. However, this is not

a one-way road, and the excitation can also back-transfer to the triplet state. In particular, the back-energy transfer rate  $W_{BT}$  is obtained by multiplying the corresponding direct transfer rate  $W_{ET}$  by the Boltzmann factor:<sup>24</sup>

$$W_{BT} = W_{ET} \cdot e^{-\frac{E_f - E_i}{k_B T}} \quad (121)$$

where  $k_B$  is the Boltzmann constant and  $T$  is the temperature. A perfect resonance would therefore result in an equal population of the triplet and emitter state, as is intuitive. Increasing the energy of the triplet state reduces the effectiveness of back-energy transfer, boosting luminescence intensity, but also reduces the temperature sensitivity, so a delicate balance needs to be achieved for building an efficient molecular thermometer.

The second non-radiative decay path, *i.e.* vibronic coupling with a high-energy oscillator such as a OH or NH group, is not as straightforward to treat. A rigorous theoretical explanation for this phenomenon has not yet been devised, and the current agreement is to treat this as a “back-energy transfer” to a fictitious electronic state placed considering a harmonic of the oscillator frequency.<sup>25–28</sup> For example, with a OH oscillating at 3450 cm<sup>-1</sup>, the “active” state would be the 4<sup>th</sup> harmonic at 13800 cm<sup>-1</sup>. This is not resonant with the <sup>5</sup>D<sub>0</sub> → <sup>7</sup>F<sub>0</sub>, but rather with the <sup>5</sup>D<sub>0</sub> → <sup>7</sup>F<sub>6</sub> transition, which is found at about 12200 cm<sup>-1</sup>.<sup>11</sup> In theory, it would be possible to take any harmonic of even a low-energy oscillator to “fill the gap” necessary to quench the <sup>5</sup>D<sub>0</sub> → <sup>7</sup>F<sub>6</sub> transition, but experimental data suggests that the efficacy of vibronic quenching is reduced exponentially with higher harmonics, therefore limiting this phenomenon only to high energy oscillators.<sup>25</sup>

It must be stressed that this is a highly approximate picture and a lot of work still needs to be done to rigorously explain this occurrence. For example, it is assumed these high-energy oscillators are purely harmonic, therefore the higher overtones are taken simply as a multiple of the fundamental oscillation frequency. This is however far from true, as OH oscillators, especially those who participate in hydrogen bonding such as the case of water, one of the most widely used vibronic quencher, are strongly anharmonic.<sup>29,30</sup>

## References

- (1) Peijzel, P. S.; Meijerink, A.; Wegh, R. T.; Reid, M. F.; Burdick, G. W. *J. Solid State Chem.* **2005**, *178* (2), 448–453.
- (2) Hund, F. *Zeitschrift für Phys.* **1925**, *33* (1), 345–371.
- (3) Hund, F. *Linienspektren Und Periodisches System Der Elemente*; Springer-Verlag, 1927.
- (4) Purcell, E. M.; Morin, D. J. *Electricity and Magnetism*, 3rd ed.; Cambridge University Press, 2012.
- (5) Wigner, E. P. *Group Theory and Its Application to the Quantum Mechanics of Atomic Spectra*; Academic Press, 1959.
- (6) Russell, H. N.; Saunders, F. A. *Astrophys. J.* **1925**, *61*, 38.
- (7) Condon, E. U.; Shortley, G. H. *The Theory of Atomic Spectra*; Cambridge University Press, 1959.
- (8) Griffith, J. S. *The Theory of Transition-Metal Ions*; Cambridge University Press, 1971.
- (9) Laporte, O.; Meggers, W. F. *J. Opt. Soc. Am.* **1925**, *11* (5), 459.
- (10) Wybourne, B. G.; Smentek, L. CRC press 2007.
- (11) Binnemans, K. *Coord. Chem. Rev.* **2015**, *295*, 1–45.
- (12) Kasha, M. *Discuss. Faraday Soc.* **1950**, *9*, 14.
- (13) Steemers, F. J.; Verboom, W.; Reinhoudt, D. N.; van der Tol, E. B.; Verhoeven, J. W. *J. Am. Chem. Soc.* **1995**, *117* (37), 9408–9414.
- (14) Carnall, W. T.; Crosswhite, H.; Crosswhite, H. M. *Energy Level Structure and Transition Probabilities in the Spectra of the Trivalent Lanthanides in LaF<sub>3</sub>*; Argonne, IL (United States), 1978.
- (15) Bünzli, J.-C. G.; Eliseeva, S. V. *Chem. Sci.* **2013**, *4* (5), 1939.
- (16) Armelao, L.; Quici, S.; Barigelletti, F.; Accorsi, G.; Bottaro, G.; Cavazzini, M.; Tondello, E. *Coord. Chem. Rev.* **2010**, *254* (5–6), 487–505.
- (17) Brites, C. D. S.; Lima, P. P.; Silva, N. J. O.; Millán, A.; Amaral, V. S.; Palacio, F.; Carlos, L. D. *Adv. Mater.* **2010**, *22* (40), 4499–4504.
- (18) Aiga, F.; Iwanaga, H.; Amano, A. *J. Phys. Chem. A* **2005**, *109* (49), 11312–11316.
- (19) Aiga, F.; Iwanaga, H.; Amano, A. *J. Phys. Chem. A* **2007**, *111* (48), 12141–12145.
- (20) Batista, H. J.; de Andrade, A. V. M.; Longo, R. L.; Simas, A. M.; de Sá, G. F.; Ito, N. K.; Thompson, L. C. *Inorg. Chem.* **1998**, *37* (14), 3542–3547.
- (21) Beltrán-Leiva, M. J.; Cantero-López, P.; Zúñiga, C.; Bulhões-Figueira, A.; Páez-Hernández, D.; Arratia-Pérez, R. *Inorg. Chem.* **2017**, *56* (15), 9200–9208.
- (22) Latva, M.; Takalo, H.; Mukkala, V.-M.; Matachescu, C.; Rodríguez-Ubis, J. C.; Kankare, J. *J. Lumin.* **1997**, *75* (2), 149–169.
- (23) Dirac, P. A. M. *Proc. R. Soc. London. Ser. A, Contain. Pap. a Math. Phys. Character* **1927**, *114* (767), 243–265.
- (24) Malta, O. L.; Brito, H. F.; Menezes, J. F. S.; Silva, F. R. G. e; Alves, S.; Farias, F. S.; de Andrade, A. V. M. *J. Lumin.* **1997**, *75* (3), 255–268.
- (25) Stein, G.; Würzberg, E. *J. Chem. Phys.* **1975**, *62* (1), 208–213.
- (26) Heller, A. *J. Am. Chem. Soc.* **1966**, *88* (9), 2058–2059.
- (27) Dickins, R. S.; Parker, D.; Sousa, A. S. De; Williams, J. A. G. **1996**, 697–698.
- (28) Beeby, A.; Clarkson, I. M.; Dickins, R. S.; Faulkner, S.; Parker, D.; Royle, L.; de Sousa, A. S.; Williams, J. A. G.; Woods, M. *J. Chem. Soc. Perkin Trans. 2* **1999**, No. 3, 493–504.
- (29) Nibbering, E. T. J.; Elsaesser, T. *Chem. Rev.* **2004**, *104* (4), 1887–1914.
- (30) Akiva, A.; Chuntanov, L. *J. Chem. Phys.* **2020**, *152* (7).

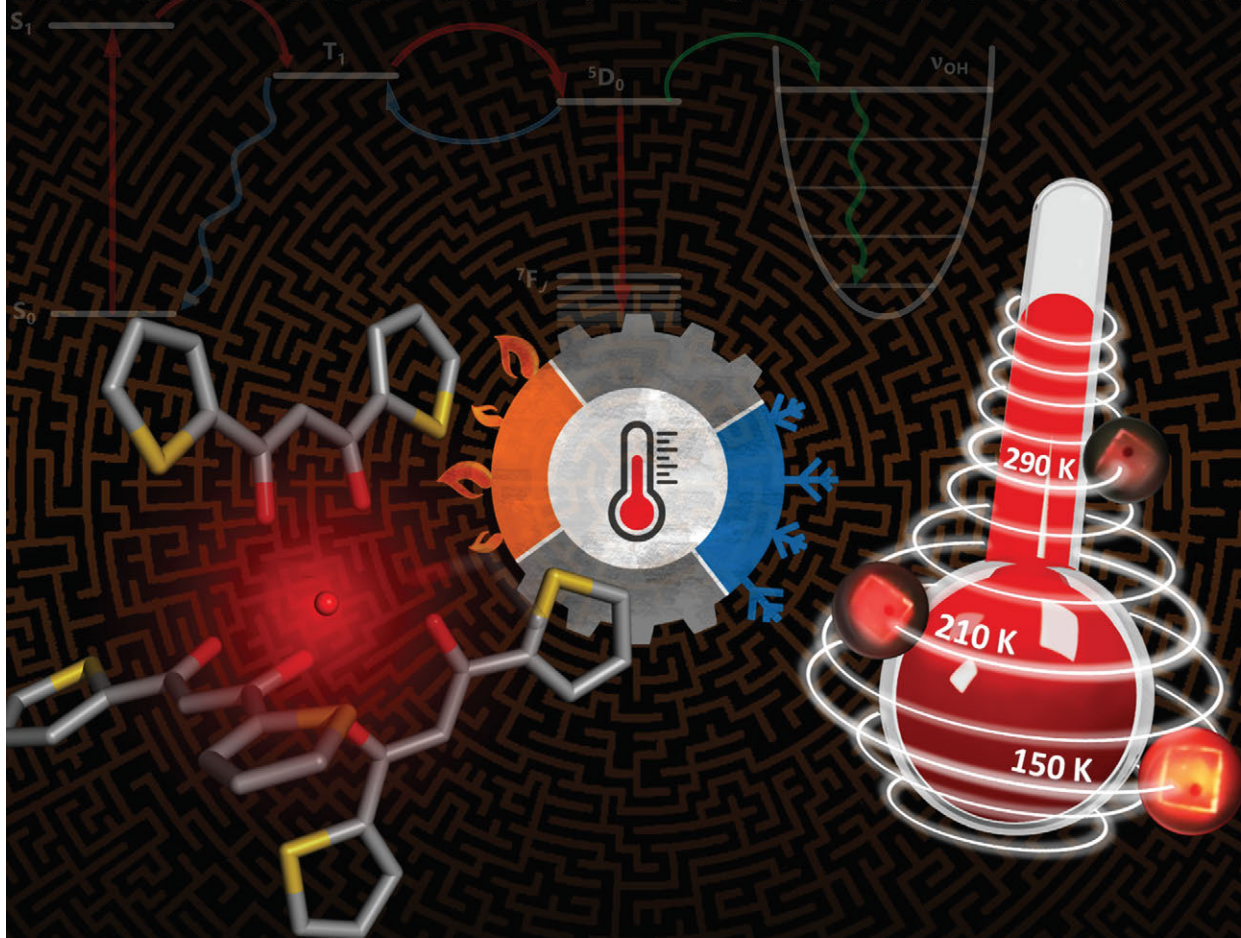




**Front Cover:**

*Gregorio Bottaro, Marzio Rancan and co-workers*

Luminescent Thermometers: From a Library of Europium(III)  $\beta$ -Diketonates to a General Model for Predicting the Thermometric Behaviour of Europium-Based Coordination Systems



# Luminescent Thermometers: From a Library of Europium(III) $\beta$ -Diketonates to a General Model for Predicting the Thermometric Behaviour of Europium-Based Coordination Systems



Alice Carlotto



Luca Babetto



Silvia Carlotto



Massimo Miozzi



Roberta Seraglia



Maurizio Casarin



Gregorio Bottaro



Marzio Rancan



Lidia Armelao



The front cover artwork is provided by the Functional Molecules and Inorganic Nanosystems Lab at ICMATE-CNR and University of Padova (Italy). The image shows a europium luminescent molecular thermometer (LMT) with a maze on the background. It symbolizes the dead-ends behind the design of new Eu-LMTs for which we propose a predictive tool, named ThesEuS, developed from a library of Eu(III)- $\beta$ -diketonates, in order to get out of the maze. Read the full text of the Article at 10.1002/cptc.2020000116.

## What prompted you to investigate this topic?

Luminescent molecular thermometers (LMTs) are fascinating materials. Our interest on this topic arises from a collaboration between ICMATE-CNR and INM-CNR in order to develop new temperature sensitive paints. Soon, we realized that to get application-tailored LMTs, a better understanding of the mechanisms regulating their response and range of applicability is paramount. Thus, we involved other colleagues from University of Padova, and planned a research program on LMTs with a strong interplay between experiments and computational methods.

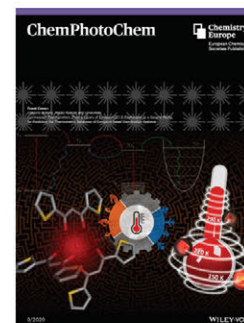
## How would you describe to the layperson the most significant result of this study?

Luminescent materials can act as thermometers at the molecular- and nanoscale. This property is very appealing for many applications ranging from material science and engineering to nanomedicine. In this context, a key question arises: is it possible

to predict the thermometric properties of LMTs, and guide the tailoring of new systems with a desired thermometric response? In this study, we prepared a series of Eu emitting compounds, and studied and rationalized their behaviour to develop a predictive tool for thermometric applications. The proposed model has been also embedded in a freeware program named ThesEuS (Thermometric Europium Simulator). The goal is to apply it to drive the design of new LMTs.

## Acknowledgements

The authors would like to thank CNR (Italian National Research Council) and University of Padova for financial support.



# Luminescent Thermometers: From a Library of Europium (III) $\beta$ -Diketonates to a General Model for Predicting the Thermometric Behaviour of Europium-Based Coordination Systems

Alice Carlotto<sup>+, [a]</sup>, Luca Babetto<sup>+, [a]</sup>, Silvia Carlotto,<sup>[a, d]</sup> Massimo Miozzi,<sup>[b]</sup> Roberta Seraglia,<sup>[c]</sup> Maurizio Casarin,<sup>[a, d]</sup> Gregorio Bottaro,<sup>\*, [d]</sup> Marzio Rancan,<sup>\*, [d]</sup> and Lidia Armelao<sup>[a, c]</sup>

A new model with the aim to predict the temperature dependence of europium emission in coordination systems is presented. The model has been developed from a library of  $\text{Eu}^{3+}$  complexes of general formula  $\text{EuL}_3\text{A}_2$ , where L is a  $\beta$ -diketone, and A is an ancillary ligand. Three possible deactivation channels have been considered: two competitive metal-related terms describing the primary deactivation channels, *i.e.* back energy transfer and multiphonon quenching, and a third ligand-related term to describe non-radiative deactivation of the antenna triplet. As many parameters as possible are taken from measurable chemical-physical properties, such as ligand triplet and multiphonon quenching energies. The other param-

eters have been deduced from selected  $\text{EuL}_3\text{A}_2$  compounds and used as *one-size-fits-all* values. The model proved to be very effective in describing the interplay between back energy transfer and multiphonon deactivation channels. Finally, the model has been implemented in a freeware standalone MATLAB application. Users need to input only the energy of the sensitizer triplet level and choose the coordinated quencher, if present. It simulates the range of applicability of the molecular thermometers and the shape of the thermometric sensitivity curve  $S_r$  employing as thermometric parameter either emission intensity or lifetime.

## 1. Introduction

Lanthanide (Ln)-based luminescent thermometers have been attracting increasing interest in the last ten years.<sup>[1]</sup> These systems exploit the peculiar luminescence properties of the lanthanide centres to sense and map temperature through a semi/non-invasive approach, easily reaching sub-micrometric spatial resolutions and high temperature resolutions, *i.e.* the smallest temperature variation that can be revealed, down to

the order of milli-Kelvins. Such materials are therefore particularly valuable for a wide range of applications ranging from material science and engineering to nanomedicine.<sup>[2–5]</sup>

An important parameter in thermometry is the relative thermal sensitivity ( $S_r$ ) defined<sup>[6]</sup> according to Equation (1):

$$S_r = \frac{1}{\Delta} \left| \frac{\partial \Delta}{\partial T} \right| \quad (1)$$

where  $\Delta$  is the thermometric parameter – *i.e.* the spectroscopic property used to monitor the temperature variation as for instance emission intensity or lifetime – and T is the temperature. This figure of merit has the advantage of being independent of the nature of the thermometer, thus enabling the comparison of systems with different chemical nature and thermometric parameters.

The main features outlining and characterizing a lanthanide-based thermometer have been recently reviewed.<sup>[7–9]</sup> Amongst all the possible Ln compounds, coordination-driven architectures – *i.e.* complexes and Lanthanide-Organic Frameworks (LOFs) – are very appealing since they allow a molecular-based design of the luminescent material and, in the case of discrete systems, ensure high processability. The use of coordination-driven architectures paves the way to a plethora of different compounds for which the characteristics of the luminescent thermometer – such as working range (from cryogenic values to 400 K *ca.*) and  $S_r$  value – can be widely modulated. Even if LOF architectures are the most studied<sup>[9]</sup> discrete coordination complexes are still the basis of important

[a] A. Carlotto,<sup>+</sup> L. Babetto,<sup>+</sup> Dr. S. Carlotto, Prof. M. Casarin, Prof. L. Armelao  
Department of Chemical Sciences  
University of Padova  
via Marzolo 1, 35131 Padova (Italy)

[b] Dr. M. Miozzi  
Institute of Marine Engineering (INM)  
National Research Council (CNR)  
via di Vallerano, 139, 00128 Roma (Italy)

[c] Dr. R. Seraglia, Prof. L. Armelao  
Institute of Condensed Matter Chemistry and Technologies for Energy (ICMATE)  
National Research Council (CNR)  
Corso Stati Uniti 4, 35127 Padova (Italy)

[d] Dr. S. Carlotto, Prof. M. Casarin, Dr. G. Bottaro, Dr. M. Rancan  
Institute of Condensed Matter Chemistry and Technologies for Energy (ICMATE)  
National Research Council (CNR)  
c/o Department of Chemical Sciences, University of Padova  
via Marzolo 1, 35131 Padova (Italy)  
E-mail: gregorio.bottaro@cnr.it  
marzio.rancan@cnr.it

[†] These authors equally contributed to this work.

Supporting information for this article is available on the WWW under <https://doi.org/10.1002/cptc.202000116>

applications even in the form of simple single-centre emitters. An example is the development of temperature sensitive paints (TSP).<sup>[10]</sup> In these materials, the luminescent molecules are embedded in a polymeric matrix and applied on the surface of a suitable substrate to gauge and understand the factors affecting the fluid dynamics<sup>[11]</sup> or heat transfer properties of the substrate itself. It is worth noting that for these applications the use of two emitters, to obtain a ratiometric luminescent thermometer, is not required. Instead, the ratio of an image taken at test conditions to an image taken at a known reference conditions is used.

The variation of the emission intensity with temperature is essentially driven by thermally activated non-radiative decay of the luminophore excited states. Depending on the emitters involved and on the considered temperature range,  $\Delta$  vs.  $T$  curves can have three different shapes: *i*) a straight line, *ii*) an exponential curve or *iii*) a sigmoid.<sup>[7-9]</sup> For wide temperature ranges (100–200 K or wider), the most commonly encountered  $\Delta(T)$  dependence is the third, and is usually fitted on the basis of the Mott-Seitz model (MS),<sup>[12-16]</sup> which accounts for the contribution of radiative and non-radiative transitions of the emitting centre according to Equation (2):

$$\Delta(T) = \frac{\Delta_0}{1 + \sum_i \alpha_i e^{-\frac{\Delta E_i}{k_B T}}} \quad (2)$$

where  $\Delta_0$  is the thermometric parameter at  $T=0$  K,  $\alpha_i$  the ratio between the probabilities of non-radiative and radiative deactivation paths,  $\Delta E_i$  the activation energy of the  $i$ -th thermal quenching process,  $k_B$  the Boltzmann constant, and  $T$  the absolute temperature. Eq. (2) is usually employed to fit the experimental  $\Delta$  vs.  $T$  curves, and the determined  $\Delta E_i$  values are correlated with parameters linked to the molecular system such as the energy of ligand triplet states, ligand-to-metal charge transfer (LMCT) states, and oscillators involved in multiphonon (MP) quenching of excited states.

After acknowledging the presence of these correlations, a question arises: is it possible to use Equation (2) (or some derived forms) to predict the thermometric properties of a luminescent molecule or, even better, to guide the design of a new system with a thermometric response determined *a priori* in a particular temperature range? Only recently, some works<sup>[8,17]</sup> have started to consider the possibility of using MS equation or “thermally coupled levels” models to predict the behaviour – in the form of  $\Delta(T)$  and/or  $S_i(T)$  – of a molecular luminescent thermometer.

In this work, a new model is proposed and embedded in a freeware MATLAB program available for download (see Experimental Section) as standalone application named ThesEuS (Thermometric Europium Simulator). The model is based on a modified form of the MS equation, with the aim of predicting the thermometric response of europium-based luminescent thermometers using specific molecular parameters. To develop and validate the model, a series of  $\text{Eu}^{3+}$  tris( $\beta$ -diketonate) complexes coupled to different ancillary ligands, ethanol (EtOH) or triphenylphosphine oxide (TPPO), were synthesised and characterised. This class of compounds is well-known<sup>[18]</sup> and its

thermometric response can be readily modulated through straightforward synthetic tools: the back energy transfer (BEnT) can be tuned by varying the triplet state energy of the antenna ligand, while the MP quenching channel can effectively be enabled or disabled by changing the ancillary ligand. All the terms in the equation describing the presented model have been deduced from experimental data of selected europium complexes. Once these parameters were determined, the model was successfully applied, through the ThesEuS application, to other examples taken from the literature. To perform a simulation, ThesEuS needs only the energy of the sensitizer triplet level and the type of coordinated MP quencher, if present, as input parameters.

## 2. Results and Discussion

### 2.1. Europium(III) $\beta$ -Diketonates Library

In order to evaluate the interplay between back energy transfer (from  $\text{Eu}^{3+}$  emitting levels to antenna triplet ( $T_1$ ) level) and MP quenching as temperature dependent non-radiative deactivation channels, we developed a small library of  $\text{Eu}^{3+}$  tris( $\beta$ -diketonate) complexes with the following main features: *i*) small energy gap ( $<2000 \text{ cm}^{-1}$ ) between the  $\text{Eu}^{3+}$  emitting level ( ${}^5D_0$ ) and the  $T_1$  level, and *ii*) presence of  $-\text{OH}$  groups (EtOH) directly bonded to  $\text{Eu}^{3+}$  as high energy oscillators, which can be easily substituted with non-quenching molecules (TPPO). The former point is required to ensure an efficient BEnT from  $\text{Eu}^{3+}$  to  $T_1$  since it is well-known that, when this energy gap is lower than  $2500 \text{ cm}^{-1}$ , the process is strongly enhanced.<sup>[19]</sup> The possibility to easily insert or remove  $-\text{OH}$  oscillators in the europium coordination sphere is instead used to evaluate the role of MP processes. The studied compounds have general formula  $\text{EuL}_3\text{A}_2$ , where **L** is a  $\beta$ -diketonate and **A** is the ancillary ligand (EtOH or TPPO). Three different  $\beta$ -diketonate ligands, named **L1**, **L2** and **L3** (Figure 1a–c) were synthesised via Claisen condensation (SI). **L1**-based Eu complexes have shown outstanding thermometric properties in TSP applications.<sup>[20,21]</sup> Since it is well-known that the expansion of  $\pi$ -conjugation in aromatic systems leads to a shift of the absorption band towards the visible range of the electromagnetic spectrum – *i.e.* a decrease in the energy of singlet and triplet excited states<sup>[22]</sup> – we designed two new ligands, **L2** and **L3**, in which one of the thienyl groups is replaced by a polycyclic aromatic hydrocarbon (PAH) moiety: naphthyl and phenanthryl for **L2** and **L3**, respectively (SI, Figure S1–4). Two classes of complexes,  $[\text{EuL}_3(\text{EtOH})_2]$  (Figure 1d–f), and  $[\text{EuL}_3(\text{TPPO})_2]$  (Figure 1g–i), were prepared and characterised (SI, Figure S5, 6 Table S1–2). Throughout the text, they will be labelled as **EunE** and **EunT**, where *n* is the number that identifies the ligand and **E** or **T** refers to EtOH or TPPO, respectively. As evidenced in Figure 1, in all compounds the coordination sphere of the Eu centre has a similar ligands arrangement. For compounds based on ligand **L2** and **L3** it was not possible to obtain suitable single crystals and their structure were optimised by DFT calculations. The comparison of X-ray

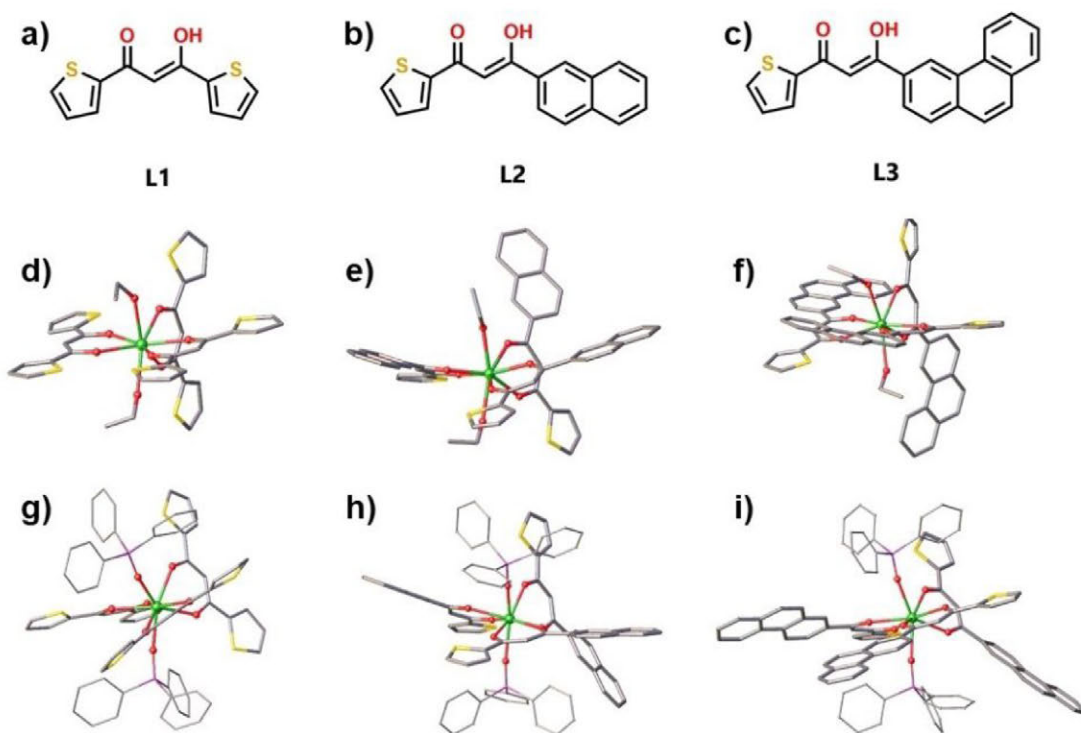


**Figure 1.** Ligands (a–c) and structures of the Eu(III)- $\beta$ -diketonates library. **Eu1E** and **Eu1T** (d,g) XRD structures, **Eu2E**, **Eu2T**, **Eu3E** and **Eu3T** (e, f, h, i, respectively) DFT-optimised structures. Colour code: C = grey, O = red, S = yellow, Eu = green, P = purple. H atoms and disordered parts omitted as well as TPPO molecules bond radius smaller for clarity. For clarity, H atoms and disordered parts were omitted, and the bond radii within TPPO molecule were drawn thinner.

and calculated structures for **Eu1E** and **Eu1T** shows that optimised structures are in very good agreement with the experimental ones (Figure S5).

## 2.2. Thermometric Properties

Room temperature absorption and photoluminescence (PL) spectra (Figure S8–9) of the complexes embedded in polystyrene films have similar profiles. PL spectra are dominated by the hypersensitive  ${}^5D_0 \rightarrow {}^7F_2$  transition whose intensity is *ca.* one order of magnitude larger than the other emission lines ( ${}^5D_0 \rightarrow {}^7F_j$  for,  $J=0, 1, 3$  and  $4$ ). These features have been observed in other Eu- $\beta$ -diketonato compounds and are ascribable to the low local symmetry – typically  $C_1$  – of the europium site.<sup>[18,23]</sup> The most significant luminescence data are reported on Table S3. The emission spectrum of each sample was recorded in the 83–303 K range using an excitation wavelength corresponding to the maximum of the excitation spectrum in the different compounds (Figure S10). The emission intensity of all the complexes decreases at increasing temperatures, without substantial variations of the spectrum shape (Figure 2a), indicating the absence of distortions on the Eu coordination geometry induced by the temperature variation.

The integrated intensity of the  ${}^5D_0 \rightarrow {}^7F_2$  transition was chosen as the thermometric parameter ( $\Delta$ ) and its temperature dependence is showed in Figure 2b for all the complexes. Besides some slight differences in the curve shape, it is interesting to note that for the **Eu1E/Eu1T** and **Eu2E/Eu2T** pairs the change of the ancillary ligands produces a remarkable variation in  $\Delta(T)$ , not detected for **Eu3E/Eu3T**. A similar behaviour is observed for the relative thermal sensitivity ( $S_r$ , Figure 2c). Two different trends can be highlighted. Compounds **Eu1T** and **Eu2T** start to show high thermal sensitivity in the range 240–300 K ( $S_r > 1\% \cdot K^{-1}$  arbitrary chosen as minimum requirement to define the thermometric response as good).<sup>[8]</sup> The other four compounds (**Eu1E**, **Eu2E**, **Eu3E** and **Eu3T**) show  $S_r > 1\% \cdot K^{-1}$  in a wider temperature range (170–300 K), reaching similar maximum values ( $4\% \cdot K^{-1} < S_r < 5\% \cdot K^{-1}$ ) in the interval 240–300 K. Such values are amongst the highest  $S_r$  reported so far at room temperature regime for  $Ln^{3+}$ -based luminescent thermometers.<sup>[8,9]</sup> Four out of six compounds can therefore be effectively used as luminescent molecular thermometers in a wide temperature range starting from 170 K and all the compounds have their best performances around room temperature.

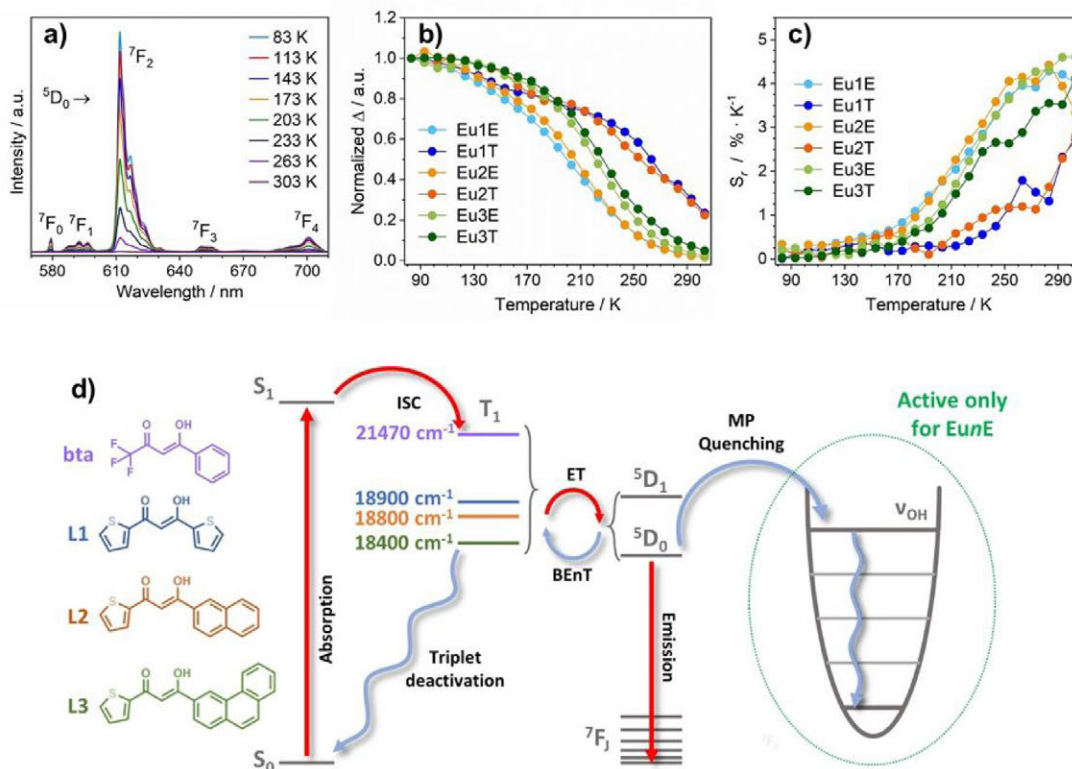


**Figure 2.** a) Emission spectra at different temperatures (83–303 K) of complex **Eu1E** in polystyrene thin films. The other complexes have an analogous behaviour. b) Normalized (83 K)  $\Delta$  vs.  $T$  curves for **EunE** and **EunT** complexes. c) Experimental  $S_T$  values for **EunE** and **EunT** complexes. d) Involved energy levels and energy transfer channels.

## 2.3. Towards a General Predictive Model

### 2.3.1. Definition of the Model

It is a common procedure, in lanthanide-based luminescence thermometry,<sup>[24–29]</sup> to describe the temperature effect on emission intensities ( $I$ ) and/or excited state lifetimes ( $\tau$ ), where  $\Delta(T)$  is  $I(T)$  or  $\tau(T)$ , in the framework of the Mott-Seitz model. The fitting of experimental  $\Delta$  vs.  $T$  can be used to infer the number of non-radiative deactivation pathways that contribute to the modulation of the luminescence properties. In most cases, these are: *i*) BEnT from  $\text{Eu}^{3+}$  to the ligand triplet level, *ii*) MP relaxation promoted by high energy oscillators (mainly  $-\text{OH}$  and  $-\text{NH}$  groups) coordinated to the metal centre, and *iii*) energy transfer to LMCT states. Depending on the activation energies, more than one process can operate. Other deactivation paths can also be encountered but are far less common (ion-ion interaction, donor-acceptor phenomena, etc).

A qualitative preliminary evaluation of the thermometric data of Figures 2b and 2c can be done. Two temperature dependent deactivation channels are considered: back energy transfer to the antenna triplet level and MP relaxation, the latter active only for the **EunE** family. In the complexes featuring **L1** and **L2** ligands, the nature of the coordinated

ancillary ligand determines the channel ruling the thermometric response. In the presence of a high energy oscillator near the metal centre ( $-\text{OH}$  from EtOH, in **Eu1E** and **Eu2E**), the value of  $\Delta(T)$  decreases steeply going from 83 to 303 K, which reflects in a high relative thermal sensitivity. The quencher (EtOH) therefore acts as a booster of the thermometric response both in terms of  $S_T$  and range of applicability. Figures 2b and 2c show an evident thermometric response ( $T > 170$  K) for **Eu1E** and **Eu2E** due to the activation of the MP non-radiative relaxation channel. If EtOH is substituted by TPPO (**Eu1T** and **Eu2T**), the thermometric response starts to be significant only when the triplet back energy transfer channel is thermally activated ( $T > 240$  K). On the other hand, **Eu3E** and **Eu3T** show essentially an identical behaviour. This can be explained by the fact that in **L3** the  $T_1$  level is lower in energy (Figure S9c and Table S3), therefore the triplet deactivation channel becomes active at lower temperatures, which ends up practically coinciding with the MP channel. In this case, the introduction of a quencher as EtOH has no visible effects on the thermometric properties, since the non-radiative deactivation can proceed, at the same temperatures, also through the triplet channel.

The proper comprehension of the mechanisms governing temperature-dependent photophysical properties is essential in

order to develop more efficient thermometers and to accurately tailor their properties. In this perspective, the possibility of having a tool, which can predict the thermometric response of a given system from easily achievable parameters, becomes very intriguing. Starting from the experimental data of the complexes illustrated in the previous section, we developed a predictive model which is able to describe the behaviour of  $\text{Eu}^{3+}$ -based luminescent coordination-driven thermometers by taking into account three deactivation channels: two metal-centred (BEnT and MP) and one ligand-centred. To aid the reader, a sketch of the involved energy levels and energy transfer channels is reported in Figure 2d.

The model [Eq. (3)] is based on a modified Mott-Seitz equation [Eq. (2)],<sup>[12–16]</sup> where the non-radiative deactivation processes are included in a modular way. Equation (3) is composed of two terms. The former,  $M(T)$ , refers to metal-related processes, describing the primary deactivation channels (BEnT and MP); the latter,  $L(T)$ , includes a multiplicative ligand-related term which takes into account non-radiative deactivation of the antenna triplet. The description of the temperature-dependent intensity emission is as follows:

$$\Delta(T) = M(T) \cdot L(T) \quad (3)$$

$$M(T) = \left( \frac{\gamma}{1 + c_B \cdot e^{-\frac{\Delta_B}{kT}}} + \frac{1 - \gamma}{1 + c_Q \cdot e^{-\frac{\Delta_Q}{kT}}} \right) \quad (3.1)$$

$$L(T) = \left( 1 - c_D \cdot e^{-\frac{\Delta_D}{kT}} \right) \quad (3.2)$$

$$\gamma(\Delta_B, \Delta_Q, \alpha) = \frac{1}{1 + e^{[-(\Delta_Q - \Delta_B) \cdot \alpha]}} \quad (4)$$

$$\Delta_B = T_1 - {}^5D_0 \quad (5)$$

$$\Delta_Q = 4 \cdot h\nu_{\text{OH}} - \Delta E_{00-06} \quad (6)$$

The correlation between  $\Delta(T)$  and  $S_r$  is reported in Eq. (1). The function  $\gamma(\Delta_B, \Delta_Q, \alpha)$  [Eq. (4)] weights the contribution of the BEnT versus MP quenching processes. Parameter  $\alpha$  is a shape factor for the function  $\gamma$ .  $\Delta_B$  [Eq. (5)] is the difference between the triplet level and the  ${}^5D_0 \rightarrow {}^7F_0$   $\text{Eu}^{3+}$  level ( $17227 \text{ cm}^{-1}$ , energy of the transition of free-ion,<sup>[23]</sup> and it ranges from  $1700$  to  $1100 \text{ cm}^{-1}$  going from L1- to L3-based systems, Table 1.  $\Delta_Q$  [Eq. (6)] is the energy difference between the fourth harmonic of the OH stretching ( $4 \cdot h\nu_{\text{OH}}$  determined

using the experimental frequency of OH stretching in **Eu**n**E** compounds, Figure S7) and  $\Delta E_{00-06}$ , *i.e.* the energy difference between  ${}^5D_0 \rightarrow {}^7F_0$  and  ${}^5D_0 \rightarrow {}^7F_6$  for the free-ion.<sup>[23]</sup> Hence,  $\Delta_Q$  has the same value ( $1145 \text{ cm}^{-1}$ ) for all the **Eu**n**E** compounds. The  $\Delta_D$  parameter is a ligand-dependent parameter which is correlated with the temperature dependence of the ligand phosphorescence and therefore with the triplet state population. The parameters  $\alpha$  and  $\Delta_D$  will be discussed in detail later.

The  $\gamma$  function ranges from 0 (only MP quenching, high energy triplet) to 1 (absence of MP or low energy triplet) and is determined *a priori*, once  $\Delta_B$  and  $\Delta_Q$  values are known. When  $\gamma$  is close to 0.5, BEnT and MP channels have the same importance. As previously described,  $\Delta_B$  and  $\Delta_Q$  do not come from a fitting procedure as usually done using the Mott-Seitz equation, but they are obtained from observable properties, namely the energies of: *i*) ligand-based excited state, *ii*) vibrational modes and *iii*)  $\text{Eu}^{3+}$  excited states. The pre-exponential factors  $c_B$ ,  $c_Q$ ,  $c_D$  and the  $\Delta_D$  activation energy are the only parameters which have been obtained from the fitting of experimental data. Each parameter was derived by carefully choosing a particular set of Eu complexes, and once obtained it can be used as a universal quantity valid for a wide range of  $\text{Eu}^{3+}$  coordination systems.

### 2.3.2. Determination of $c_B$ , $c_Q$ and $\alpha$

Considering the values of  $\Delta_B$  and  $\Delta_Q$  (Table 1) for the **Eu**n**E** and **Eu**n**T** complexes, we decided to use the **Eu3T/Eu3E** pair to determine the values of  $c_B$  and  $c_Q$ . The reason for this choice is that with these two complexes we are in the situations  $\gamma = 1$  (**Eu3T**) and  $\gamma \approx 0.5$  (**Eu3E**). The pre-exponential factor  $c_B$  was determined by fitting with Equation (3.1) the experimental  $\Delta(T)$  curve for **Eu3T** where there is no contribution from the MP channel. The term  $\Delta_B$  was fixed at its experimental value ( $1173 \text{ cm}^{-1}$ ). The effect of variations in the value of  $c_B$  and the best fitting value ( $c_B = 2000$ ) are reported in Figures S11a and S11b, respectively. By substituting TPPO with EtOH, an efficient and equivalent MP deactivation channel is added: for **Eu3E**  $\Delta_B \cong \Delta_Q$  which means that the thermally activated MP and BEnT channels should have comparable effects on the variations of emission intensity. In fact, experimental  $\Delta(T)$  curves (Figure 2b) for these two compounds almost overlap. Based on these considerations,  $c_Q$  and  $c_B$  were set equal ( $c_Q = c_B = 2000$ ). For both **Eu1E** and **Eu2E**,  $\gamma$  is approximately zero: MP is favoured over BEnT in all the investigated temperature range given the significantly lower activation energy of the MP channel ( $\Delta_Q$ ). This is evidenced in Figure 3a, where the exponential terms of Eq. (3.1) are plotted against temperature for the **Eu**n**E** compounds. The graph in Figure 3a shows that, under our hypothesis, MP is favoured over BEnT also for **Eu3E**, but to a much smaller extent since  $\gamma$  for this compound should be close to 0.5. All this information has been combined to find the appropriate value for the shape factor  $\alpha$  (Eq. (4), Figures S12 and 3b). The shape of  $\gamma$  is very sensitive to variations of  $\alpha$  and for  $\alpha > 0.016$  quickly approaches a step function (Figure S12a–c). Considering our hypothesis, the best agreement was

**Table 1.** Triplet energies ( $T_1$ ),  $\Delta_Q$  and  $\Delta_B$  values used for the different compounds.

	$T_1$ [ $\text{cm}^{-1}$ ]	$\Delta_B$ [ $\text{cm}^{-1}$ ]	$\Delta_Q$ [ $\text{cm}^{-1}$ ]
<sup>[a]</sup> <b>Eu1E (Eu1T)</b>	18900	1673	1145 (0)
<sup>[a]</sup> <b>Eu2E (Eu2T)</b>	18800	1573	1145 (0)
<sup>[a]</sup> <b>Eu3E (Eu3T)</b>	18400	1173	1145 (0)

[a]  $\Delta_Q = 0$  for **Eu**n**T** family.

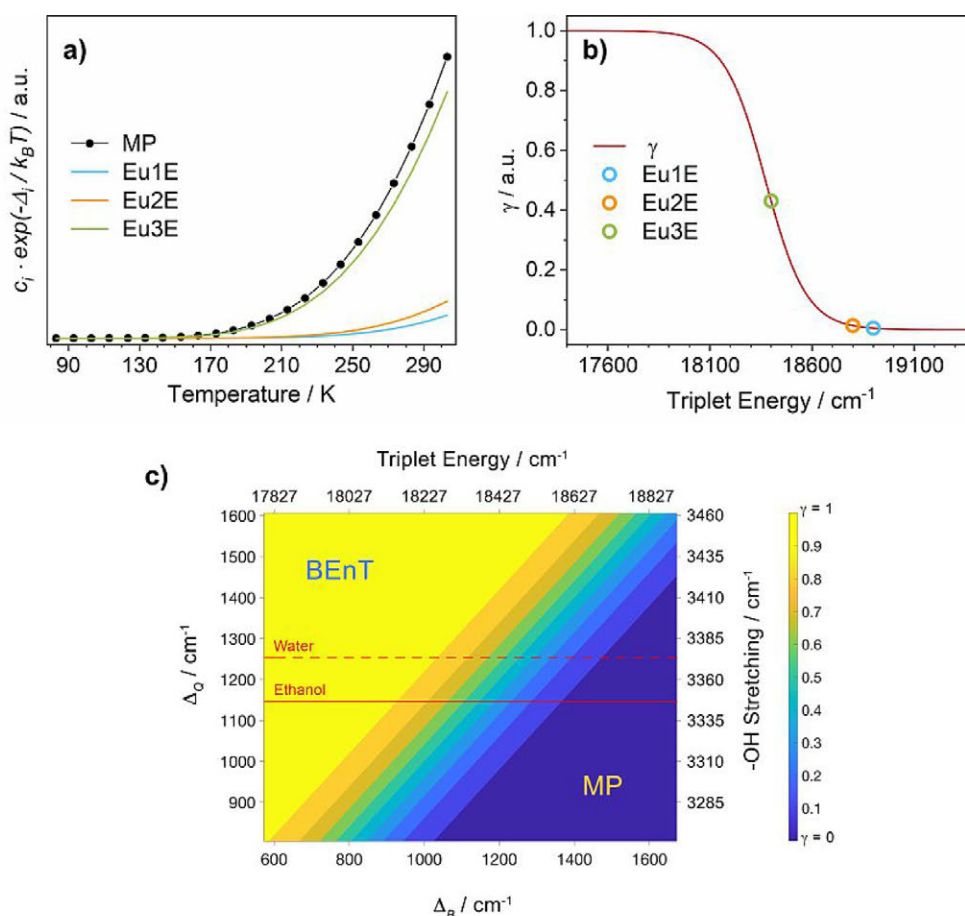


**Figure 3.** a) Temperature dependence of exponential terms in Equation (3.1) ( $c_0 = c_Q = 2000$ ). b) Dependence of  $\gamma$  function from triplet energy for  $\alpha = 0.01$  at constant  $\Delta_O = 1145 \text{ cm}^{-1}$ . c) Effect of  $\Delta_B$  (triplet energy) and  $\Delta_O$  (OH stretching frequency) on  $\gamma$  (values given by the colour bar). The horizontal red lines correspond to the frequency of the centroid of OH stretching band (Figure S7) for ethanol and water. The label BE nT and MP highlight the regions where only back energy transfer and MP quenching are active, respectively.

obtained with  $\alpha = 0.01$  to which corresponds a  $\gamma$  of 0.43 for Eu3E. In Figure 3c, the map of  $\gamma$  values as function of  $\Delta_B$  and  $\Delta_O$  parameters is plotted. Moving along the  $\Delta_O = 1145 \text{ cm}^{-1}$  isoline (red continuous line in Figure 3c), it is possible to notice that, considering our model (where  $c_B = c_Q$ ), if  $\Delta_B \leq \Delta_O = 1145 \text{ cm}^{-1}$ , the luminescence quenching will not explicitly show its dependence on the presence (or absence) of MP processes. Hence, a sort of “shadow region” for MP quenching is generated. This is the case of compound Eu3E (Figure 3a), where the two deactivation channels are competing, masking the effect of MP process. The effect will become more evident when  $\Delta_B \ll \Delta_O$  and back energy transfer to the triplet level is activated at lower temperatures becoming the primary deactivation pathway (Figure 3c, yellow zone). If, instead of EtOH, the quencher is water ( $\Delta_O = 1253 \text{ cm}^{-1}$ , red dashed line in Figure 3c), similar results are obtained, but the MP shadow region is shifted of ca.  $100 \text{ cm}^{-1}$  up to  $\Delta_B \approx 1253 \text{ cm}^{-1}$ . On the other hand, if  $\Delta_B \gg \Delta_O$ , most of the deactivation will go through the MP channel, if present, regardless of the triplet energy (Figure 3c, blue zone). This is the case of complexes Eu1E and Eu2E

when compared to Eu1T and Eu2T, where the presence of coordinated ethanol molecules dramatically quenches the emission intensity, but at the same time improves the thermometric response. It is worthy to note that many widely used antenna ligands, including  $\beta$ -diketones, feature triplet levels higher than  $18700 \text{ cm}^{-1}$ . In these cases, therefore, the introduction of MP quenching molecules in europium coordination sphere can be used to enhance and tune the thermometric response of the systems.

### 2.3.3. Determination of $c_D$ , $A_D$ and Definition of the Model

At this point, all the terms of  $M(T)$ , Eq 3.1, have been defined. To understand the need for  $L(T)$  and its origin, we need to compare the experimental and calculated (Eq. (3.1),  $M(T)$ )  $\Delta$  vs.  $T$  (Figure 4a and 4c and S13) and  $S_f$  vs.  $T$  (Figure S13 and S14) curves for the EUnE and EUnT complexes. Even if there are some discrepancies, the agreement between experimental and calculated data is already fairly good. The agreement between



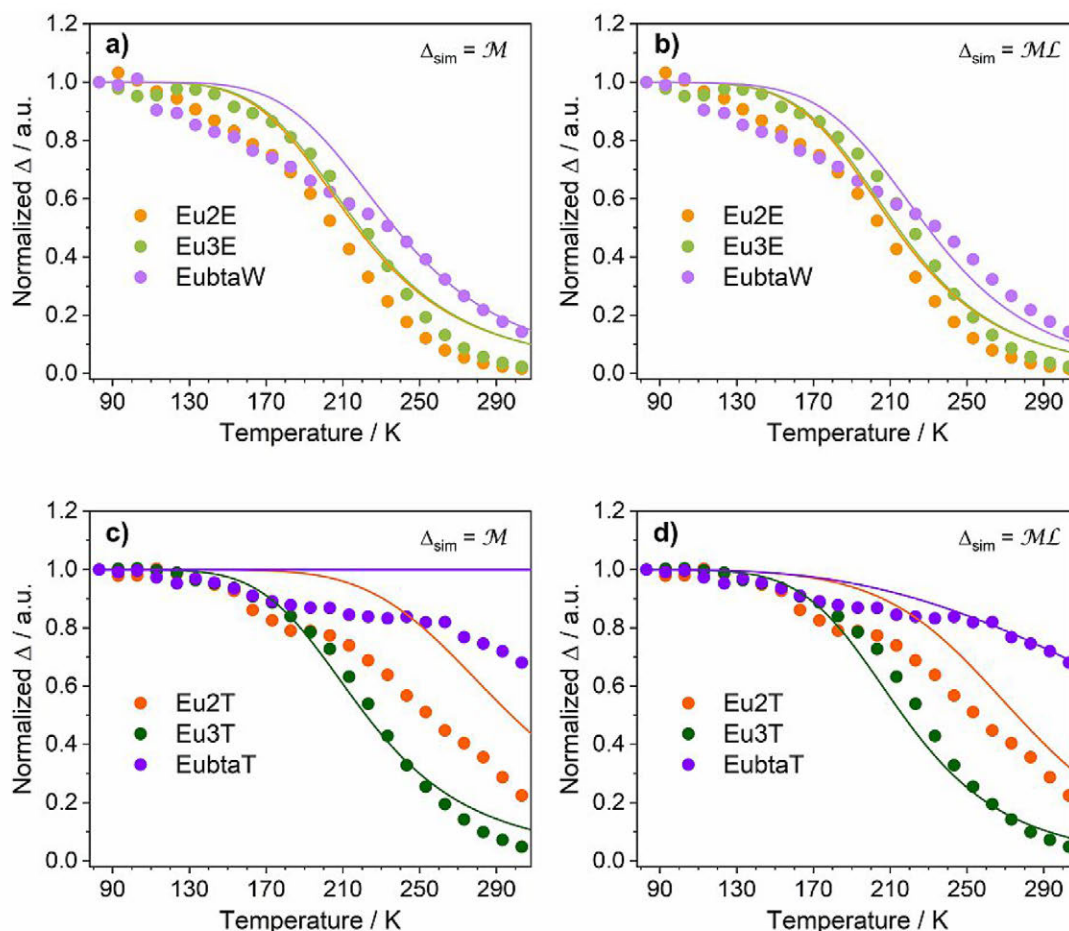


**Figure 4.** Comparison between experimental and simulated thermometric parameter  $\Delta$  calculated using the M(T) (a, c) or M(T)L(T) (b, d) equations. Since complexes with L1 and L2 have similar behaviour, only the data for compounds **Eu2E** and **Eu2T** are reported. Data for **Eu1E** and **Eu1T** are displayed in Figure S13.

simulated and experimental results is in general better for the **EunE** than **EunT** complexes, with **Eu1T** being the most challenging system. It appears that, under the hypothesis above adopted, BEnT and MP quenching are not enough to quantitatively account for the observed emission intensity decrease from 83 to 303 K. To improve model performance and to increase its versatility, we tested the proposed model with  $\text{Eu}^{3+}$ -benzoyltrifluoroacetone (bta) complexes, a ligand widely employed to prepare highly emissive europium complexes thanks to the high energy triplet excited state ( $21470 \text{ cm}^{-1}$ ).<sup>[30]</sup> We prepared  $[\text{Eu}(\text{bta})_3(\text{H}_2\text{O})_2]$  (**EubtaW**) starting from the commercial ligand and  $[\text{Eu}(\text{bta})_3(\text{TPPO})_2]$  (**EubtaT**) by exchanging water with TPPO. According to the M(T) model only BEnT is active for the **EubtaT** complex. Since  $\Delta_b = 4243 \text{ cm}^{-1}$ , the  $\Delta$  vs. T curve for **EubtaT** should be a straight line in the 83–303 K range. However, the measured emission spectra of **EubtaT**, embedded in polystyrene films and recorded in this temperature range, show an intensity decrease of ca. 30% as the temperature increases (Figure 4c). This points-out the existence

of other non-radiative deactivation processes besides BEnT and MP. These processes are likely to be present also in the **EunE** and **EunT** compounds but, depending on the activation energy, BEnT and MP can mask them.

Until now, in the M(T) equation, we have only considered metal-centred deactivation channels without taking into account that thermally driven processes can also affect the population of the antenna triplet. It is important to note that this would only affect the emission intensity without modifying the lifetime.<sup>[31]</sup> To explore this further path, we recorded the emission spectra of the **Gd3E** complex at different temperatures, between 83 and 303 K, and plotted the intensity of the phosphorescence bands vs. the temperature. The resulted S-shaped curve (Figure S15) was fitted using a one term Mott-Seitz equation ( $\Delta E = 670 \pm 50 \text{ cm}^{-1}$ ). To define the L(T) term [Eq. (3.2)], we set  $\Delta_D = 670 \text{ cm}^{-1}$  and the  $c_D$  parameter was determined by fitting the  $\Delta$  vs. T curve for **EubtaT** at the now fixed  $\Delta_D$  value. A value of 7.45 was hence obtained for  $c_D$ .

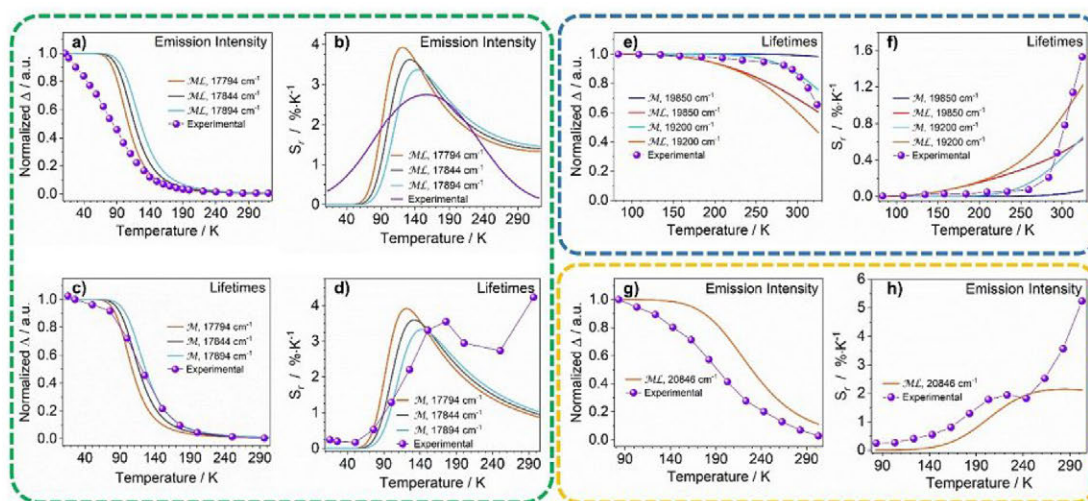
The results obtained in the simulations of *EunE*, *EunT*, *EubtaW* and *EubtaT* by applying first the partial model, metal-centred deactivation processes (M(T) term, Eq. (3.1)), and then the final model with the multiplicative (M(T)L(T) terms, Eq. (3)) are reported in Figure 4. The introduction of a ligand-related term in the model improved the quantitative agreement with experimental results for both  $\Delta$  (Figure 4b and 4d, S13) and  $S_r$  (Figure S13 and S14). The effect of L(T) becomes visible starting from 180 K and is more pronounced for systems in which BEnT is the primary non-radiative deactivation path (Figure S16). In fact, in the absence of quencher molecules, L(T) is the only active process for systems featuring large values of  $\Delta_B$  as for instance in *EubtaT* ( $\Delta_B = 4243 \text{ cm}^{-1}$ ).

Figure 4b and 4d suggest that the model may be further improved in order to increase the agreement between experimental and simulated data. Nevertheless the function M(T)L(T) succeeds in calculating  $\Delta$  (Figure 4) and  $S_r$  (Figure S14) trends, locating very precisely the range of applicability of the thermometers. The simulated  $S_r$  values surpasses the edge-value  $1\% \cdot \text{K}^{-1}$  in the same temperature intervals observed for the experimental data for all the compounds, proving that the model may be used to help the search and the design of new Eu(III)-based optical temperature probes. The modular nature of the model allows for a dynamical range of applicability. For example, excited state lifetimes are tied only to metal-centred deactivation pathways, while the variations in emission intensity can also depend on ligand-based processes.<sup>[31]</sup> The proposed model can therefore be used not only to predict the temperature dependence of emission intensity – including both L(T) and M(T) terms – but also the trend of the lifetimes if only M(T) is considered.

## 2.4. Extending the Model to Other Systems

To prove the applicability of the model, we tested it with other europium-based thermometers from the literature. Before discussing a few examples of systems found in the literature, there are some general aspects which should be tackled. *i)* Usually, when experimental  $\Delta(T)$  curves are fitted with the Mott-Seitz equation, the energy terms obtained can differ from the experimental values to a large extent, up to 10–40%.<sup>[17,25–27,29,32]</sup> *ii)* The determination of triplet energies from phosphorescence spectra of gadolinium complexes can give different results depending on the approach used. In particular, the two most frequently adopted methods are: drawing a tangent line in the highest energy edge of the phosphorescence spectra, or locating the phosphorescence zero-zero phonon energy by taking the maximum of the highest energy vibronic band.<sup>[26,33]</sup> The values obtained in the two cases can differ by several hundreds of  $\text{cm}^{-1}$  and, in certain conditions (see below), this can lead to very large differences in the simulated emission trend.<sup>[26,33]</sup> *iii)* The precise determination of the –OH stretching frequency needed for the calculation of  $\Delta_0$  is not straightforward since the IR bands of coordinated –OH groups are often broad and of low intensity.<sup>[34,35]</sup> *iv)* In the proposed model, we use the free-ion energy levels for  $\text{Eu}^{3+}$ , however the energy of  $^5\text{D}_0 \rightarrow ^7\text{F}_0$  transitions can vary as much as  $450 \text{ cm}^{-1}$  ranging from ca. 17550 to ca. 17100  $\text{cm}^{-1}$ , leading to different values of  $\Delta_B$  and  $\Delta_0$ .

Five representative examples of the simulations of literature data are reported. In Figure 5a–d, the  $\Delta(T)$  (in the form of both intensities and lifetimes) and  $S_r$  curves for the LOF  $(\text{Me}_2\text{NH}_2)_3[\text{Eu}_3(\text{FDC})_4(\text{NO}_3)_4] \cdot 4\text{H}_2\text{O}$  ( $\text{H}_2\text{FDC} = 9\text{-fluorenone-2,7-dicarboxylic acid}$ )<sup>[24]</sup> are reported. This system is challenging since it contains two independent and different Eu centres both with FDC ligand



**Figure 5.** (a–d) Comparison between literature data<sup>[24]</sup> and simulations for  $(\text{Me}_2\text{NH}_2)_3[\text{Eu}_3(\text{FDC})_4(\text{NO}_3)_4] \cdot 4\text{H}_2\text{O}$  system: emission intensity (a,b) and  $^5\text{D}_0$  lifetimes (c,d). (e,f) Comparison between literature data<sup>[36]</sup> and simulations for  $^5\text{D}_0$  lifetime vs. T in  $[\text{Eu}(\text{tta})_3(\text{pyphen})]$  complex. Simulations have been performed using the M(T) or M(T)L(T) terms. (g,h)  $[\text{Eu}(\text{bzac})_3(\text{H}_2\text{O})_2]$  data,<sup>[26]</sup> bzac = benzoylacetate. The numbers reported in the panels are the energies of the ligand triplet level used for the simulations.

(the antenna) and with nitrate anion coordinated. The intensity-based data, Figures 5a and 5b, are modelled with a good agreement for  $T > 100$  K. This is not surprising since the modelling of two different  $\text{Eu}^{3+}$  centres, at the present time, is beyond the capabilities of the proposed model. The high temperature tail of the curve is well reproduced, since this effect is mainly given by BEnT, which is included in the model. The numerical agreement is much better when using lifetimes as thermometric parameter (Figures 5c and 5d). In this case, the authors<sup>[24]</sup> were able to experimentally discriminate the two contributions and the lifetime data refer to a single  $\text{Eu}^{3+}$  centre (see Figure 5 of reference<sup>[24]</sup>). It is interesting to note how the profile of  $\Delta(T)$  and  $S_i$  curves for the lifetimes changes by varying the triplet energy with an increase of only  $50 \text{ cm}^{-1}$  *i.e.* ca. 0.3%. For this system  $\Delta_0$  is always the leading non-radiative deactivation channel, therefore the eventual presence of a high energy oscillator as quencher or the effects of L(T) cannot be appreciated.

Conversely, the second example (Figure 5e,f), which concerns the {tris(thenoyltrifluoroacetone)pyrazino[2,3-f][1,10]phenanthroline}europium(III) complex<sup>[36]</sup>  $[\text{Eu}(\text{tta})_3(\text{pyphen})]$ , allows to evidence the role of L(T) term. In this compound, europium is 8-coordinated by three  $\beta$ -diketone ligands (tta, the antenna) and a *N,N*-donor chelate (pyphen). For the simulation of lifetimes vs.  $T$  curves, we started using the triplet literature value<sup>[36]</sup> ( $19850 \text{ cm}^{-1}$ ), Figure 5e and 5f. However, the best simulation is obtained using an energy of  $19200 \text{ cm}^{-1}$  (ca. 3.3%

lower). Indeed, it has been previously showed<sup>[37]</sup> that the tta ligand lowest triplet level shows a vibronic progression with three main peaks, centred around  $20492 \text{ cm}^{-1}$ ,  $19305 \text{ cm}^{-1}$ , and  $17986 \text{ cm}^{-1}$ . When L(T) is enabled,  $\Delta(T)$ , *i.e.* lifetime values, decreases too quickly and the curve shape does not reproduce the trend of experimental data. If only BEnT is considered,  $M(T)$  term, the experimental data are well reproduced. In fact, lifetimes are only related to metal-centred deactivation processes, hence in this case, L(T) should not be taken into account.

Another example is related to the compound  $[\text{Eu}(\text{bzac})_3(\text{H}_2\text{O})_2]$ , bzac = benzoylacetone,<sup>[26]</sup> Figure 5g,h. In this compound, europium is 8-coordinated by three  $\beta$ -diketone ligands (bzac, the antenna) and two water molecules. The simulation of the emission intensity experimental data reproduces very well the trend of the curves  $\Delta(T)$  and  $S_i$ . In particular, the model well-simulates the thermometer working region ranging from 180 to 300 K, Figure 5h.

A further very intriguing example to test the model is the molecular thermometer  $[\text{Eu}(\text{keto})_3(\text{H}_2\text{O})]$ ,<sup>[33]</sup> where keto is ketoprofen and the Eu centre is 7-coordinated by three carboxylate units (keto) and one water molecule (Figure 6a,b). A complicated energy level diagram characterizes this system as evidenced by Lahoud *et al.*<sup>[33]</sup> The triplet state extends from 400 ( $25000 \text{ cm}^{-1}$ ) to 570 nm ( $17543 \text{ cm}^{-1}$ ), being the zero phonon line at 430 nm ( $23255 \text{ cm}^{-1}$ ).<sup>[33]</sup> The variation of the emission intensity with temperature was rationalized<sup>[33]</sup> taking into account the large overlap between ligand-centred triplet

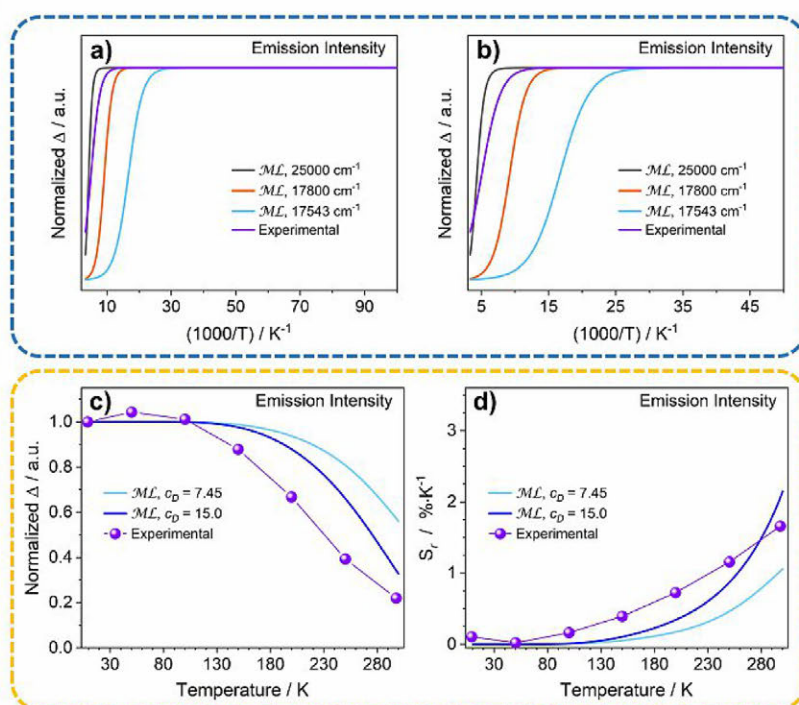


**Figure 6.** a) Simulations for  $[\text{Eu}(\text{keto})_3(\text{H}_2\text{O})]$  molecular thermometer data.<sup>[33]</sup> b) Magnified region. The numbers reported in the panels are the energies of the ligand triplet level used for the simulations. (c, d) Simulations for the Tb–Eu dyad cycTb-phEu data<sup>[38]</sup> with a triplet energy of  $19100 \text{ cm}^{-1}$  and varying the  $c_D$  parameter.

state and the low-energy intra- $4f^6$  excited states ( $^5D_{0-3}$ ), evidencing the relevant role of the  $^5D_1$ ,  $^5D_2$  and  $^5D_3$  levels. Emission intensity vs. temperature curves were modelled, in the original reference,<sup>[33]</sup> with a two-terms Mott-Seitz equation giving the following values for the activation energies:  $\Delta E_1 = 494 \text{ cm}^{-1}$  and  $\Delta E_2 = 3.8 \text{ cm}^{-1}$ . If treated taking into account all these levels, this system is beyond the current capability of our model. Nevertheless, interesting results may be achieved by using few approximations. The shape of  $I(T)$  curve, Figure 6a, is mainly determined by  $\Delta E_1$  for  $1000/T < 12 \text{ K}^{-1}$  ( $T > 83 \text{ K}$ ) and by  $\Delta E_2$  for  $1000/T > 12 \text{ K}^{-1}$ . To analyse this system with our model we focused the attention on the  $\Delta E_1$  term. This term determines the behaviour in the temperature range where the proposed model has been developed ( $80 < T < 350 \text{ K}$ ). We calculated  $I(T)$  using  $M(T)L(T)$  with the following values for triplet energy: *i*)  $25000 \text{ cm}^{-1}$  starting and *ii*)  $17543 \text{ cm}^{-1}$  ending point of the triplet emission<sup>[33]</sup> and *iii*)  $17800 \text{ cm}^{-1} = E(^5D_0 \rightarrow ^7F_0, \text{ free-ion}) + \Delta E_1$ . Results reported in Figure 6a,b show that simulation *iii*) better succeeds in determining the temperature range where the major emission intensity variation occurs in strong agreement with the results of the Mott-Seitz fitting performed by the authors.

As last example (Figure 6c,d), we report another challenging case to test the model with a system where the europium ion has a chemical environment very different compared to that of the **EunE** and **EunT** compounds. The compound is a hetero-dinuclear Tb–Eu dyad named **cycTb–phEu**: the Tb ion is complexed by a modified tetraazacyclododecane unit linked to a phenanthroline moiety that binds the Eu ion.<sup>[38]</sup> The coordination sphere of the europium is completed by three *N*, *N*-dithiocarbamate ligands. Thus, the Eu ion is 8-coordinated by two nitrogen and six sulfur atoms. Despite this great diversity of the coordinating sites, the model well reproduces the trend of the thermal parameters. Authors report<sup>[38]</sup> that the europium lifetimes are only moderately modified by temperature variations, reaching a decrease of 20% at 300 K, that is the same result we obtained in the simulation with a triplet energy of  $19100 \text{ cm}^{-1}$  (Figure S17a). The emission intensity trend vs. temperature is well reproduced even if its values are slightly underestimated, Figure 6c,d. The numerical agreement can be satisfactorily improved by varying the  $c_D$  parameter as shown in Figure 6c and 6d imposing a  $c_D$  value of 15 instead of the usual 7.45. Figure S17 reports simulations with different  $c_D$  values. This variation is fully justified since the  $c_D$  parameter weights the contribution of the ligand-centred  $L(T)$  term. In this compound the antenna ligand is a 1,10-phenanthroline unit with very different features from the tested  $\beta$ -diketones.

### 3. Conclusions

The model has been developed and tested using the two compound families **EunE** and **EunT** and then extended to other literature systems. The goal is to provide a tool capable to predict the thermometric behaviour ( $\Delta(T)$  and  $S_f(T)$ ) of europium-based molecular thermometers using easily available experimental data. In general, in the simulation of  $\Delta(T)$  and  $S_f$

( $T$ ), under the tight constraints imposed by the model, both a well reproduced trend and a good numerical agreement may be obtained. The model proved to be very effective in describing the interplay between back energy transfer and MP deactivation channels. It correctly predicts the range of applicability of the thermometer and, in particular, the shape of the relative thermal sensitivity curve  $S_r$ . The key points used to develop the model are here summarized. *i*) Only BEnT from  $\text{Eu}^{3+}$ -centered to the ligand triplet levels, MP relaxations and a ligand related path were considered as deactivation channels. *ii*) The pre-exponential factor were set to a fixed value independent of the nature of the ligand. *iii*) EtOH or  $\text{H}_2\text{O}$  were used to quantify the effect of MP quenching. *iv*) Only the 4<sup>th</sup> harmonic of the oscillator in the computation of MP quenching was taken into account. *v*)  $\text{Eu}^{3+}$  free-ion energy values were used to calculate  $\Delta_Q$  and  $\Delta_B$ . *vi*) The final optimized values of the numerical constants in Equations (3.1), (3.2) and (4) are:  $c_B = c_Q = 2000$ ,  $c_D = 7.45$ ,  $\Delta_Q = 1145 \text{ (R-OH)}$  or  $1253 \text{ cm}^{-1} \text{ (H}_2\text{O)}$ ,  $\Delta_D = 670 \text{ cm}^{-1}$ , and  $\alpha = 0.01$ .

The triplet energy is the most important required input parameter. In the previous examples, it has been strongly highlighted that variations smaller than 1% of this parameter induce drastic effects on both  $\Delta(T)$  and  $S_f(T)$  curves. Another important point is the value of the  $c_D$  parameter. This quantity is strongly related to the antenna ligand. The obtained value (7.45) is particularly suited for  $\beta$ -diketone ligands and other oxygen donors such as carboxylates. The model can well reproduce the  $S_r$  trends of systems not featuring only  $\beta$ -diketones as antenna ligands and is applicable to  $\text{Eu}^{3+}$  systems bearing ligands such as carboxylates, nitrogen and sulfur donors. Of course, better numerical agreement can be obtained by changing the  $c_D$  parameter if the antenna ligand is very different to those used to develop the model. An incoming improvement will be the development of specific  $c_D$  values for specific antenna ligand classes such as: carboxylates, *N,N*-donor ligands (for instance bipyridine, phenanthroline, etc.) or *N,O*-donor ligands (for instance hydroquinoline and hydroxyisophthalamide derivatives). Moreover, the modular nature of the model grants an easy way to expand it in order to include other deactivation channels simply by adding more terms in the equation. For instance, metal-metal energy transfer is a possible candidate for a future implementation. Other types of quenchers such as  $-\text{NH}$  and  $-\text{CH}$  oscillators can be easily parametrised and validated the same way  $-\text{OH}$  quencher has been. We envisage that, in the future, other metal centres will also be treated. The model was built with  $\text{Eu}^{3+}$  complexes, but its principles have a general validity.

These observations should serve as a warning on the judicious use of the proposed model, which is based on a quite simple description of the temperature dependent phenomena with well-defined limits of applicability and predictive capabilities, as above stated and explained. As a final general rule of thumb on the model performances: it will tend to provide the correct temperature range for the maximum sensitivity of the thermometer and hence, its range of applicability, with the numerical values of  $S_r$  being usually underestimated. This underestimation will be useful for the final user since, in the

worst-case scenario, the real thermometer will show  $S_r$  values at least as predicted by the model.

## Experimental Section

The details of complexes synthesis, characterizations (NMR, mass spectrometry and XRD), thin films preparation, DFT calculations, PL and thermometric studies are reported in the Supporting Information. All the simulations were performed in the framework of the ThesEuS program. ThesEuS can be freely downloaded at the following link: <http://www.disc.chimica.unipd.it/FMNLab/theseus.html>

## Acknowledgements

Authors thank the University of Padova for the grant P-DISC #CARL-SID17 BIRD2017-UNIPD, project CHIRoN. Dr. E. F. Campana (INM-CNR) is acknowledged for helpful discussions.

## Conflict of Interest

The authors declare no conflict of interest.

**Keywords:** europium · molecular thermometers · temperature dependence · thermometry

- [1] C. D. S. Brites, P. P. Lima, N. J. O. Silva, A. Millán, V. S. Amaral, F. Palacio, L. D. Carlos, *New J. Chem.* **2011**, *35*, 1177.
- [2] K. Okabe, N. Inada, C. Gota, Y. Harada, T. Funatsu, S. Uchiyama, *Nat. Commun.* **2012**, *3*, 705.
- [3] M. Mecklenburg, W. A. Hubbard, E. R. White, R. Dhall, S. B. Cronin, S. Aloni, B. C. Regan, *Science* **2015**, *347*, 629.
- [4] L. Aigouy, G. Tessier, M. Mortier, B. Charlot, *Appl. Phys. Lett.* **2005**, *87*, 184105.
- [5] S. Arai, M. Suzuki, S. J. Park, J. S. Yoo, L. Wang, N. Y. Kang, H. H. Ha, Y. T. Chang, *Chem. Commun.* **2015**, *51*, 8044.
- [6] S. A. Wade, S. F. Collins, G. W. Baxter, *J. Appl. Phys.* **2003**, *94*, 4743.
- [7] C. D. S. Brites, A. Millán, L. D. Carlos, in *Handb. Phys. Chem. Rare Earths*, Elsevier, **2016**, pp. 339–427.
- [8] C. D. S. Brites, S. Balabhadra, L. D. Carlos, *Adv. Opt. Mater.* **2019**, *7*, 1801239.
- [9] J. Rocha, C. D. S. Brites, L. D. Carlos, *Chem. Eur. J.* **2016**, *22*, 14782.
- [10] T. Liu, J. P. Sullivan, *Pressure and Temperature Sensitive Paints*, Springer, **2005**.
- [11] M. Miozzi, A. Capone, F. Di Felice, C. Klein, T. Liu, *Phys. Fluids* **2016**, *28*, 124101.
- [12] N. F. Mott, *Proc. R. Soc. London Ser. A* **1938**, *167*, 384.
- [13] F. Seitz, *Trans. Faraday Soc.* **1939**, *35*, 74.
- [14] M. T. Berry, P. Stanley May, H. Xu, *J. Phys. Chem.* **1996**, *100*, 9216.
- [15] Y. An, G. E. Schramm, M. T. Berry, *J. Lumin.* **2002**, *97*, 7.
- [16] M. D. Dramičanin, *Methods Appl. Fluoresc.* **2016**, *4*, 042001.
- [17] A. Kovalenko, V. V. Utochnikova, S. Z. Vatsadze, A. M. Magerramov, A. A. Vashchenko, A. S. Burlov, P. O. Rublev, N. G. Shikhaliyev, L. S. Lepnev, L. O. Tcelykh, A. S. Goloveshkin, Ł. Marciniak, *Chem. Mater.* **2019**, *31*, 759.
- [18] K. Binnemans, *Handb. Phys. Chem. Rare Earths* **2005**, *35*, 107.
- [19] L. Armelao, S. Quici, F. Barigelletti, G. Accorsi, G. Bottaro, M. Cavazzini, E. Tondello, *Coord. Chem. Rev.* **2010**, *254*, 487.
- [20] V. Ondrus, R. J. Meier, C. Klein, U. Henne, M. Schäferling, U. Beifuss, *Sensors* **2015**, *233*, 434.
- [21] L. Armelao, A. Carlotto, F. Mian, J. Tessarolo, G. Bottaro, M. Rancan, *Can. J. Chem.* **2017**, *95*, 1183.
- [22] Y. Hasegawa, Y. Kitagawa, T. Nakanishi, *NPG Asia Mater.* **2018**, *10*, 52.
- [23] K. Binnemans, *Coord. Chem. Rev.* **2015**, *295*, 1.
- [24] L. Li, Y. Zhu, X. Zhou, C. D. S. Brites, D. Ananias, Z. Lin, F. A. A. Paz, J. Rocha, W. Huang, L. D. Carlos, *Adv. Funct. Mater.* **2016**, *26*, 8677.
- [25] D. A. Gállico, E. R. Souza, I. O. Mazali, F. A. Sigoli, *J. Lumin.* **2019**, *210*, 397.
- [26] D. A. Gállico, I. O. Mazali, F. A. Sigoli, *J. Lumin.* **2017**, *192*, 224.
- [27] C. D. S. Brites, P. P. Lima, N. J. O. Silva, A. Millán, V. S. Amaral, F. Palacio, L. D. Carlos, *Adv. Mater.* **2010**, *22*, 4499.
- [28] J. F. C. B. Ramalho, S. F. H. Correia, L. Fu, L. L. F. António, C. D. S. Brites, P. S. André, R. A. S. Ferreira, L. D. Carlos, *Adv. Sci.* **2019**, *6*, 1900950.
- [29] A. M. Kaczmarek, Y. Y. Liu, C. Wang, B. Laforce, L. Vincze, P. Van Der Voort, R. Van Deun, *Dalton Trans.* **2017**, *46*, 12717.
- [30] P. P. Lima, R. A. Sá Ferreira, R. O. Freire, F. A. Almeida Paz, L. Fu, S. Alves, L. D. Carlos, O. L. Malta, *ChemPhysChem* **2006**, *7*, 735.
- [31] M. L. Bhaumik, *J. Chem. Phys.* **1964**, *40*, 3711.
- [32] J. F. C. B. Ramalho, S. F. H. Correia, L. Fu, L. L. F. António, C. D. S. Brites, P. S. André, R. A. S. Ferreira, L. D. Carlos, *Adv. Sci.* **2019**, *6*, 1900950.
- [33] M. G. Lahoud, R. C. G. Frem, D. A. Gállico, G. Bannach, M. M. Nolasco, R. A. S. Ferreira, L. D. Carlos, *J. Lumin.* **2016**, *170*, 357.
- [34] J. Coates, Interpretation of infrared spectra, a practical approach. In: RA Meyers, ed. *Encyclopedia of analytical chemistry*. Chichester, New Jersey: John Wiley & Sons Ltd; **2006**; p. 10815–10837.
- [35] R. M. Silverstein, F. X. Webster, D. J. Kiemle, *Microchem. J.* **2005**, *21*, 496.
- [36] F. M. Cabral, D. A. Gállico, I. O. Mazali, F. A. Sigoli, *Inorg. Chem. Commun.* **2018**, *98*, 29.
- [37] N. S. Baek, M. K. Nah, Y. H. Kim, H. K. Kim, *J. Lumin.* **2007**, *127*, 707.
- [38] G. Bao, K. L. Wong, D. Jin, P. A. Tanner, *Light Sci. Appl.* **2018**, *7*, 96.

Manuscript received: July 7, 2020

Revised manuscript received: July 8, 2020

Accepted manuscript online: July 8, 2020

Version of record online: July 30, 2020



# ChemPhotoChem

Supporting Information

## **Luminescent Thermometers: From a Library of Europium (III) $\beta$ -Diketonates to a General Model for Predicting the Thermometric Behaviour of Europium-Based Coordination Systems**

Alice Carlotto<sup>+</sup>, Luca Babetto<sup>+</sup>, Silvia Carlotto, Massimo Miozzi, Roberta Seraglia, Maurizio Casarin, Gregorio Bottaro,<sup>\*</sup> Marzio Rancan,<sup>\*</sup> and Lidia Armelao

# Index

<b>1. Syntheses</b> .....	<b>2</b>
1.1 Ligands syntheses .....	2
1.2 Complexes syntheses .....	6
<b>2. Single crystal X-ray diffraction</b> .....	<b>9</b>
<b>3. Geometry optimizations – computational details</b> .....	<b>11</b>
<b>4. Mass spectrometry analysis</b> .....	<b>12</b>
<b>5. FTIR Spectroscopy</b> .....	<b>14</b>
<b>6. Thin polystyrene film</b> .....	<b>15</b>
<b>7. Absorption and Photoluminescence data</b> .....	<b>16</b>
7.1 UV-Vis Absorption Spectroscopy .....	16
7.2 Photoluminescence Spectroscopy .....	16
<b>8. Model development</b> .....	<b>20</b>
<b>References</b> .....	<b>24</b>



# 1. Syntheses

Reagents were purchased from Aldrich and used as received. The elemental analyses were carried out with a Flash 2000 Thermo Scientific Analyzer at the Department of Chemical Sciences of the University of Padova.

## 1.1 Ligands syntheses

**Synthesis of 1,3-di(thien-2-yl)propane-1,3-dione (L1).** The ligand **L1** was synthesized following the literature procedure reported by Armelao *et al.*<sup>1</sup>

**Synthesis of 1-(naphthalen-3-yl)-3-(thiophen-2-yl)propane-1,3-dione (L2).** The Claisen condensation was performed under argon in dry THF. Potassium *tert*-butoxide (1.44 g, 13 mmol) was added to a THF (25 ml) solution of 2-acetonaphthone (1.72 g, 10 mmol) and ethyl-2-thiophenecarboxylate (2.32 g, 15 mmol). The resulting solution turned to dark-bordeaux and was stirred at 80 °C for 4 hours. After cooling, the crude was acidified with 20 ml of 10% HCl. The product was extracted with dichloromethane to give a yellow solution and dried over MgSO<sub>4</sub>. The crude product was purified by recrystallization (5 times) from n-hexane/dichloromethane (1:1), obtaining yellow-orange crystals. Yield: 86%.

Elemental analysis for C<sub>17</sub>H<sub>12</sub>O<sub>2</sub>S: calculated C 72.83 %, H 4.31 %, S 11.44 %; found: C 72.25 %, H 4.20 %, S 11.78 %.

ESI-MS (negative ions, MeOH): *m/z* 279.23 [L2-H]<sup>-</sup>



**Figure S1.** Ligand **L2**, keto enol (left) and diketone (right) tautomers.

$^1\text{H}$  NMR ( $\text{CDCl}_3$ , 400 MHz,  $T = 25\text{ }^\circ\text{C}$ ) Keto enol tautomer ( $\sim 93\%$ ),  $\delta$  [ppm] = 6.82 (1H, s,  $\text{H}_2$ ), 7.19 (1H, dd,  $^3J_{\text{H}_6,\text{H}_7} = 4.9\text{ Hz}$ ,  $^3J_{\text{H}_6,\text{H}_5} = 3.9\text{ Hz}$ ,  $\text{H}_6$ ), 7.52-7.61 (ov, 2H, m,  $\text{H}_{12}$ ,  $\text{H}_{13}$ ), 7.65 (1H, dd,  $^3J_{\text{H}_7,\text{H}_6} = 4.9\text{ Hz}$ ,  $^4J_{\text{H}_7,\text{H}_5} = 1.0\text{ Hz}$ ,  $\text{H}_7$ ), 7.86 (ov, 1H, dd,  $^3J_{\text{H}_5,\text{H}_6} = 3.9\text{ Hz}$ ,  $^4J_{\text{H}_5,\text{H}_7} = 1.0\text{ Hz}$ ,  $\text{H}_5$ ), 7.87-7.99 (ov, 4H, m,  $\text{H}_{11}$ ,  $\text{H}_{14}$ ,  $\text{H}_{16}$ ,  $\text{H}_{17}$ ), 8.50 (1H, s,  $\text{H}_9$ ), 16.24 (br, 1H, s, OH). Diketone tautomer ( $\sim 7\%$ ),  $\delta$  [ppm] = 4.68 (2H, s,  $\text{H}_2$ ), 7.15 (1H, dd,  $^3J_{\text{H}_6,\text{H}_7} = 5.0\text{ Hz}$ ,  $^3J_{\text{H}_6,\text{H}_5} = 3.9\text{ Hz}$ ,  $\text{H}_6$ ), 7.53-7.62 (ov, 2H,  $\text{H}_{12}$ ,  $\text{H}_{13}$ ), 7.69 (1H, dd,  $^3J_{\text{H}_7,\text{H}_6} = 5.0\text{ Hz}$ ,  $^4J_{\text{H}_7,\text{H}_5} = 1.1\text{ Hz}$ ,  $\text{H}_7$ ), 7.84-8.0 (ov, 5H,  $\text{H}_5$ ,  $\text{H}_{11}$ ,  $\text{H}_{14}$ ,  $\text{H}_{16}$ ,  $\text{H}_{17}$ ), 8.59 (1H, s,  $\text{H}_9$ ).

$^{13}\text{C}$ -NMR ( $\text{CDCl}_3$ , 100 MHz,  $T = 25\text{ }^\circ\text{C}$ ) Keto enol tautomer,  $\delta$  [ppm] = 93.64, 123.09, 126.95, 127.90, 128.08, 128.21, 128.47, 128.56, 129.44, 130.53, 132.77 (CH), 131.79, 132.93, 135.36, 142.49 (C), 180.71, 183.10 ( $\text{C}=\text{O}$ ,  $\text{C}-\text{OH}$ )

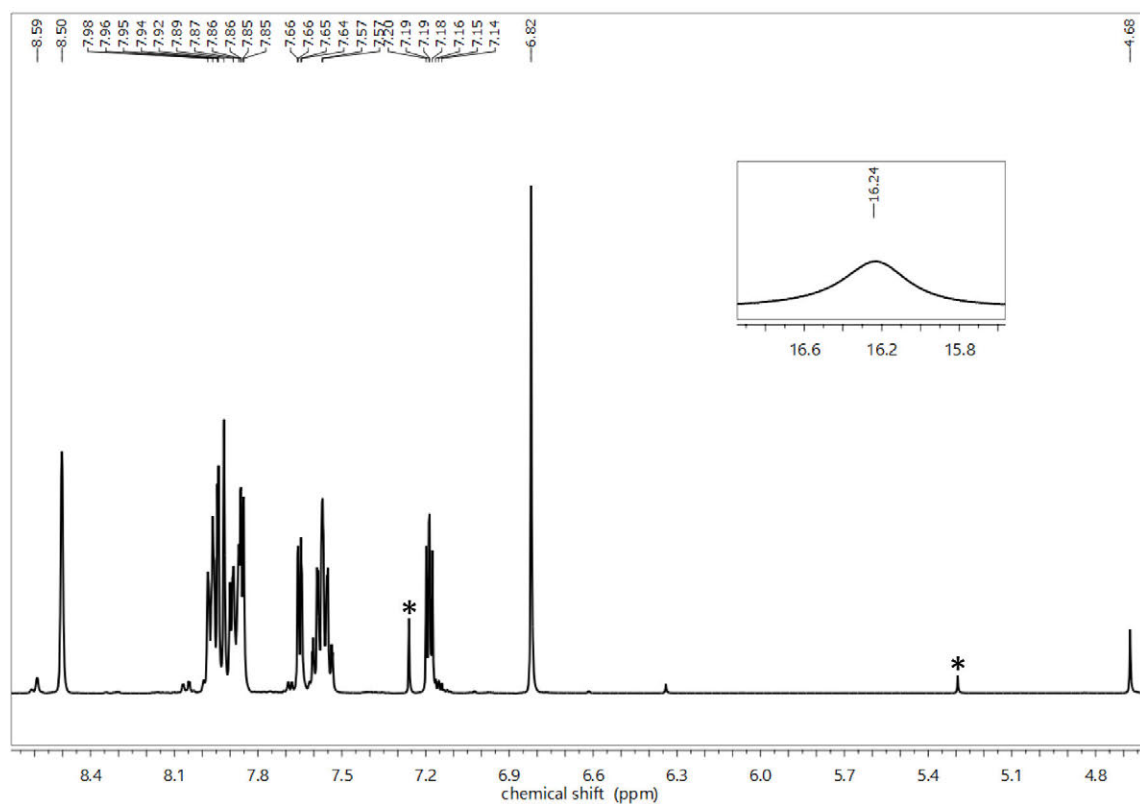


**Figure S2.**  $^1\text{H}$ -NMR of ligand **L2** in  $\text{CDCl}_3$ . Inset: OH signal. Solvent signals are marked with an asterisk.

**Synthesis of 1-(phenanthren-3-yl)-3-(thiophen-2-yl)propane-1,3-dione (L3).** The Claisen condensation was performed under argon in dry THF. Potassium *tert*-butoxyde (1.45 g, 13 mmol) was added to a THF (25 ml) solution of 3-acetylphenanthrene (2.24 g, 10 mmol) and ethyl-2-thiophenecarboxylate (2.3 g, 15 mmol). The resulting solution turned to dark-red and was stirred for 24 hours at 55°C. After cooling, the crude was acidified with 20 ml of 10% HCl. The product was extracted with dichloromethane to give an orange-red solution and dried over MgSO<sub>4</sub>. The crude product was purified by recrystallization (5 times) from DCM/hexane (1:2). Yield: 77%.

Elemental analysis for C<sub>21</sub>H<sub>14</sub>O<sub>2</sub>S: calculated C 76.34 %, H 4.27 %, S 9.70 %; found: C 76.20 %, H 4.36 %, S 9.82 %.

ESI-MS (negative ions, MeOH): *m/z* 329.25 [L3-H]<sup>-</sup>

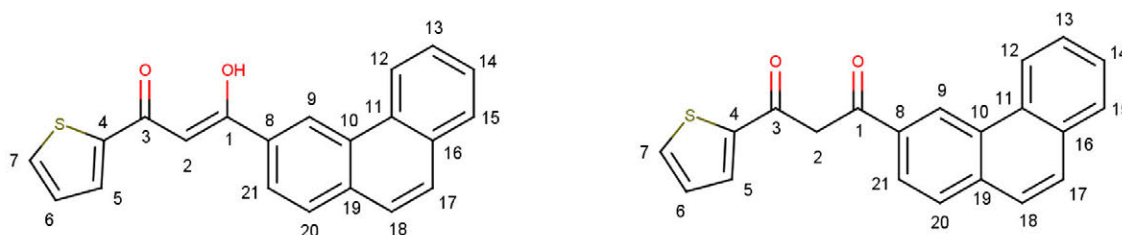


**Figure S3.** Ligand L3, keto enol (left) and diketone (right) tautomers.

<sup>1</sup>H NMR (CDCl<sub>3</sub>, 400 MHz, T = 25 °C) Keto enol tautomer (~94%), δ [ppm] = 6.89 (1H, s, H<sub>2</sub>), 7.21 (1H, dd, <sup>3</sup>J<sub>H<sub>6</sub>,H<sub>7</sub></sub> = 5.0 Hz, <sup>3</sup>J<sub>H<sub>6</sub>,H<sub>5</sub></sub> = 3.8 Hz, H<sub>6</sub>), 7.58-8.02 (ov, 9H, m, H<sub>5</sub>, H<sub>7</sub>, H<sub>13</sub>, H<sub>14</sub>, H<sub>15</sub>, H<sub>17</sub>, H<sub>18</sub>, H<sub>20</sub>), 8.08 (1H, dd, <sup>3</sup>J<sub>H<sub>21</sub>,H<sub>20</sub></sub> = 8.4 Hz, <sup>4</sup>J<sub>H<sub>21</sub>,H<sub>9</sub></sub> = 1.5 Hz, H<sub>21</sub>) 8.82 (1H, d, <sup>3</sup>J<sub>H<sub>12</sub>,H<sub>13</sub></sub> = 8.2 Hz, H<sub>12</sub>), 9.34 (br, 1H, s, H<sub>9</sub>), 16.51 (1H, s, OH). Diketone tautomer (~6%), δ [ppm] = 4.75 (2H, s, H<sub>2</sub>), 7.18 (1H, dd, <sup>3</sup>J<sub>H<sub>6</sub>,H<sub>7</sub></sub> = 5.0 Hz, <sup>3</sup>J<sub>H<sub>6</sub>,H<sub>5</sub></sub> = 3.9 Hz, H<sub>6</sub>), 7.58-8.02 (ov, 9H, m, H<sub>5</sub>, H<sub>7</sub>, H<sub>13</sub>, H<sub>14</sub>, H<sub>15</sub>, H<sub>17</sub>, H<sub>18</sub>, H<sub>20</sub>) 8.20 (1H, dd, <sup>3</sup>J<sub>H<sub>21</sub>,H<sub>20</sub></sub> = 8.2 Hz, <sup>4</sup>J<sub>H<sub>21</sub>,H<sub>9</sub></sub> = 1.5 Hz, H<sub>21</sub>) 8.78 (1H, d, <sup>3</sup>J<sub>H<sub>12</sub>,H<sub>13</sub></sub> = 8.2 Hz, H<sub>12</sub>) 9.48 (1H, s, H<sub>9</sub>).

<sup>13</sup>C-NMR (CDCl<sub>3</sub>, 100 MHz, T = 25 °C) Keto enol tautomer δ [ppm] = 93.72, 122.36, 123.00, 124.22, 126.46, 127.35, 127.38, 128.51, 128.96, 129.07, 129.51, 130.58, 132.83 (CH), 130.23, 130.65, 132.26, 132.38, 134.72, 142.52 (C), 180.93, 183.16 (C=O, C-OH)

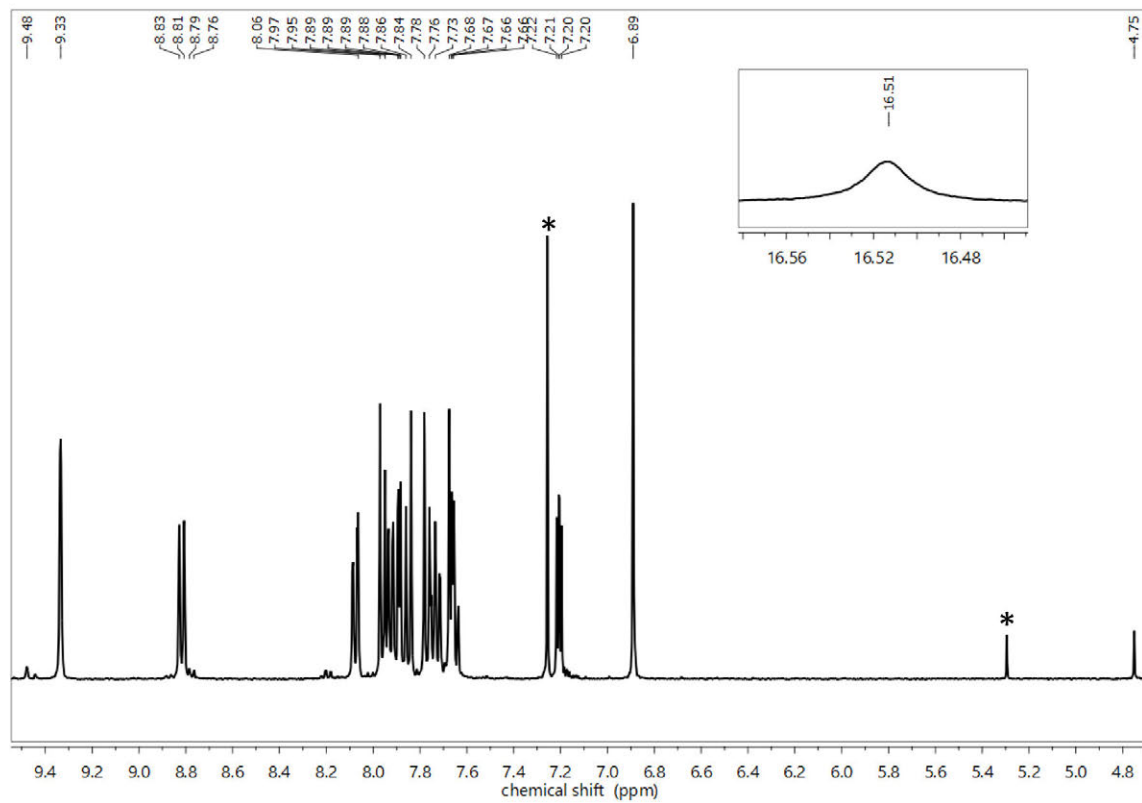


**Figure S4.**  $^1\text{H-NMR}$  of ligand L3 in  $\text{CDCl}_3$ . Inset: OH signal. Solvent signals are marked with an asterisk.

## 1.2 Complexes syntheses

**Synthesis of [EuL1<sub>3</sub>(EtOH)<sub>2</sub>] (Eu1E).** The compound **Eu1E** was synthesized following the literature procedure reported by Armelao *et al.*<sup>1</sup>

**Synthesis of [Eu(L1)<sub>3</sub>(TPPO)<sub>2</sub>] (Eu1T).** **Eu1E** (55 mg, 0.05 mmol) was dissolved in THF (5.0 ml) with TPPO (34 mg, 0.12 mmol) and stirred at 50 °C overnight. The solvent was evaporated and the compound **Eu1T** was obtained as a yellow powder after precipitation from n-hexane/dichloromethane (10:1) and removing the organic solvent. Yield: 82 %.

LDI-MS (positive ions):  $m/z$  900.98 [Eu(L1)<sub>2</sub>TPPO]<sup>+</sup>, 622.90 [Eu(L1)<sub>2</sub>]<sup>+</sup>

Elemental analysis for EuC<sub>69</sub>H<sub>51</sub>O<sub>8</sub>P<sub>2</sub>S<sub>6</sub>: calculated C 58.59 %, H 3.63 %, S 13.60 %; found: C 58.49 %, H 3.70 %, S 13.71 %.

**Synthesis of [Gd(L1)<sub>3</sub>(TPPO)<sub>2</sub>] (Gd1T).** An ethanol solution (2.5 ml) of Gd(NO<sub>3</sub>)<sub>3</sub>·6H<sub>2</sub>O (45.2 mg, 0.10 mmol) was added dropwise to a hot ethanol solution (3.0 ml) of **L1** (72.8 mg, 0.31 mmol) and NaOH (16.9 mg, 0.4 mmol). A yellow powder precipitated and the mixture was stirred and heated at 50 °C for 2 hours. The solid was recovered by filtration and washed with ethanol. Then the powder was dissolved in THF with TPPO (65.7 mg, 0.24 mmol) and stirred at 80 °C overnight. The solvent was evaporated and the compound **Gd1T** was obtained as a yellow powder after precipitation from n-hexane/dichloromethane (10:1) and removing the organic solvent. Yield: 75 %.

LDI-MS (positive ions):  $m/z$  905.99 [Gd(L1)<sub>2</sub>TPPO]<sup>+</sup>, 627.90 [Gd(L1)<sub>2</sub>]<sup>+</sup>

Elemental analysis for GdC<sub>69</sub>H<sub>51</sub>O<sub>8</sub>P<sub>2</sub>S<sub>6</sub>: calculated C 58.37 %, H 3.62 %, S 13.55 %; found: C 58.43 %, H 3.66 %, S 13.50 %.

**Synthesis of [Eu(L2)<sub>3</sub>(EtOH)<sub>2</sub>] (Eu2E).** An ethanol solution (2.5 ml) of EuCl<sub>3</sub>·6H<sub>2</sub>O (37.7 mg, 0.10 mmol) was added dropwise to a hot ethanol solution (2.5 ml) of **L2** (88.2 mg, 0.30 mmol) and NaOH (20.4 mg, 0.50 mmol). A yellow powder precipitated, the mixture was stirred and heated at 75 °C for 1 hour. The yellow powder was recovered by filtration, dissolved in acetone and filtered on celite® to remove NaCl. Then the solvent was evaporated and the yellow solid dissolved in dichloromethane to give a yellow solution. The compound **Eu2E** was obtained as a yellow powder after precipitation from n-hexane/dichloromethane (10:1) and removing the organic solvent. Yield: 81 %.

LDI-MS (positive ions):  $m/z$  1029.03 [Eu(L2)<sub>3</sub>+K]<sup>+</sup>, 1013.06 [Eu(L2)<sub>3</sub>+Na]<sup>+</sup>, 711.02 [Eu(L2)<sub>2</sub>]<sup>+</sup>.

Elemental analysis for EuC<sub>55</sub>H<sub>45</sub>O<sub>8</sub>S<sub>3</sub>: calculated C 61.05 %, H 4.19 %, S 8.89 %; found: C 61.16 %, H 4.24 %, S 8.80 %.

**Synthesis of [Eu(L2)<sub>3</sub>(TPPO)<sub>2</sub>] (Eu2T).** An ethanol solution (2.5 ml) of EuCl<sub>3</sub>·6H<sub>2</sub>O (38.0 mg, 0.10 mmol) was added dropwise to a hot ethanol solution (2.5 ml) of **L2** (90.2 mg, 0.30 mmol) and NaOH (18.6 mg, 0.50 mmol). A yellow powder precipitated, and the mixture was stirred and heated at 50 °C for 40 min. The solid was recovered by decantation and dissolved in dichloromethane. The solution was extracted with deionized water to remove NaCl and then, MgSO<sub>4</sub> was added to the organic solution. The solution was filtered, and a yellow powder was obtained after removing the organic solvent. Yield: 77 %. It was dissolved in chloroform with TPPO (54.7 mg, 0.20 mmol) and stirred at 50 °C overnight. The compound **Eu2T** was obtained as a yellow powder after precipitation from n-hexane/chloroform (10:1) and removing the organic solvent. Yield: 69 %.

LDI-MS (positive ions): *m/z* 989.10 [Eu(L2)<sub>2</sub>TPPO]<sup>+</sup>, 711.02 [Eu(L2)<sub>2</sub>]<sup>+</sup>.

Elemental analysis for EuC<sub>87</sub>H<sub>63</sub>O<sub>8</sub>P<sub>2</sub>S<sub>3</sub>: calculated C 67.57 %, H 4.11 %, S 6.22 %; found: C 67.48 %, H 4.06 %, S 6.28 %.

**Synthesis of [Gd(L2)<sub>3</sub>(TPPO)<sub>2</sub>] (Gd2T).** An ethanol solution (2.5 ml) of Gd(NO<sub>3</sub>)<sub>3</sub>·6H<sub>2</sub>O (45.4 mg, 0.10 mmol) was added dropwise to a hot ethanol solution (2.5 ml) of **L2** (89.6 mg, 0.30 mmol) and NaOH (17.2 mg, 0.40 mmol). A yellow powder precipitated, and the mixture was stirred and heated at 50 °C for 2 hours. The solid was recovered by decantation and dissolved in dichloromethane. The solution was extracted with deionized water to remove NaCl and then, MgSO<sub>4</sub> was added to the organic solution. The solution was filtered, and a yellow powder was obtained after removing the organic solvent. Yield: 98 %. It was dissolved in chloroform with TPPO (69.4 mg, 0.25 mmol) and stirred at 50 °C overnight. The compound **Gd2T** was obtained as a yellow powder after precipitation from n-hexane/chloroform (10:1) and removing the organic solvent. Yield: 78 %.

LDI-MS (positive ions): *m/z* 994.11 [Gd(L2)<sub>2</sub>TPPO]<sup>+</sup>, 716.02 [Gd(L2)<sub>2</sub>]<sup>+</sup>

Elemental analysis for GdC<sub>87</sub>H<sub>63</sub>O<sub>8</sub>P<sub>2</sub>S<sub>3</sub>: calculated C 67.34 %, H 4.09 %, S 6.20 %; found: C 67.25 %, H 4.08 %, S 6.26 %.

**Synthesis of [Eu(L3)<sub>3</sub>(EtOH)<sub>2</sub>] (Eu3E).** An ethanol solution (2.5 ml) of EuCl<sub>3</sub>·6H<sub>2</sub>O (37.2 mg, 0.10 mmol) was added dropwise to a hot ethanol solution (2.5 ml) of **L3** (107.5 mg, 0.30 mmol) and TEAOH solution 25 % wt (280 μl, 0.41 mmol). A yellow powder precipitated, the mixture was stirred and heated at 75 °C for overnight. The yellow powder was recovered by centrifugation and washed with cold EtOH. Yield: 67 %.

LDI-MS (positive ions): *m/z* 1179.20 [Eu(L3)<sub>3</sub>+K]<sup>+</sup>, 1163.25 [Eu(L3)<sub>3</sub>+Na]<sup>+</sup>, 811.20 [Eu(L3)<sub>2</sub>]<sup>+</sup>.

Elemental analysis for EuC<sub>67</sub>H<sub>51</sub>O<sub>8</sub>S<sub>3</sub>: calculated C 65.30 %, H 4.17 %, S 7.81 %; found: C 65.40 %, H 4.11 %, S 7.89 %.

**Synthesis of [Eu(L3)<sub>3</sub>(TPPO)<sub>2</sub>] (Eu3T).** An ethanol solution (2.5 ml) of EuCl<sub>3</sub>·6H<sub>2</sub>O (36.8 mg, 0.10 mmol) was added dropwise to a hot ethanol solution (3.5 ml) of **L3** (99.2 mg, 0.30 mmol) and TEAOH solution 25 % wt (300 μl, 0.44 mmol). A yellow powder precipitated, and the mixture was stirred and heated at 50 °C overnight. The yellow powder was recovered by centrifugation and washed with cold EtOH. Yield: 99 %. It was dissolved in chloroform/acetonitrile mixture (1:1) with TPPO (61.7 mg, 0.25 mmol) and stirred at 50 °C overnight. The compound **Eu3T** was obtained as a yellow powder after precipitation from n-hexane/chloroform (10:1) and removing the organic solvent. Yield: 65 %. LDI-MS (positive ions): *m/z* 1179.20 [Eu(L3)<sub>3</sub>+K]<sup>+</sup>, 1163.25 [Eu(L3)<sub>3</sub>+Na]<sup>+</sup>, 1089.30 [Eu(L3)<sub>2</sub>+TPPO]<sup>+</sup>, 811.20 [Eu(L3)<sub>2</sub>]<sup>+</sup>. Elemental analysis for EuC<sub>99</sub>H<sub>69</sub>O<sub>8</sub>P<sub>2</sub>S<sub>3</sub>: calculated C 70.08 %, H 4.10 %, S 5.67 %; found: C 69.95 %, H 4.01 %, S 5.73 %.

**Synthesis of [Gd(L3)<sub>3</sub>(EtOH)<sub>2</sub>] (Gd3E).** An ethanol solution (2.5 ml) of Gd(NO<sub>3</sub>)<sub>3</sub>·6H<sub>2</sub>O (28.5 mg, 0.06 mmol) was added dropwise to a hot ethanol solution (3.5 ml) of **L3** (61.2 mg, 0.19 mmol) and TEAOH solution 25 % wt (230 μl, 0.34 mmol). A yellow powder precipitated, the mixture was stirred and heated at 75 °C overnight. The yellow powder was recovered by centrifugation and washed with cold EtOH. Yield: 61 %. LDI-MS (positive ions): *m/z* 1184.32 [Gd(L3)<sub>3</sub>+K]<sup>+</sup>, 1168.36 [Gd(L3)<sub>3</sub>+Na]<sup>+</sup>, 816.31 [Gd(L3)<sub>2</sub>]<sup>+</sup>. Elemental analysis for GdC<sub>67</sub>H<sub>51</sub>O<sub>8</sub>S<sub>3</sub>: calculated C 65.02 %, H 4.15 %, S 7.77 %; found: C 64.97 %, H 4.10 %, S 7.81 %.

**Synthesis of [Eu(bta)<sub>3</sub>(H<sub>2</sub>O)<sub>2</sub>] (EubtaW).** A water/ethanol solution 50% v/v (2.0 ml) of sodium hydroxide (24.0 mg, 0.60 mmol) was added dropwise, over 30 min, to a stirred solution of EuCl<sub>3</sub>·6H<sub>2</sub>O (73.6 mg, 0.20 mmol) and benzoyltrifluoroacetone (136.2 mg, 0.60 mmol) in 15 ml of a water/ethanol mixture (50 % v/v). The ethanol was evaporated and the white powder obtained was recrystallized from chloroform/petroleum spirit. Yield: 80 % LDI-MS (positive ions): *m/z* 837.00 [Eu(bta)<sub>3</sub>+K]<sup>+</sup>, 821.00 [Eu(bta)<sub>3</sub>+Na]<sup>+</sup> Elemental analysis for EuC<sub>30</sub>H<sub>22</sub>O<sub>8</sub>F<sub>9</sub>: calculated C 43.23 %, H 2.66 %; found: C 43.18 %, H 2.62 %.

**Synthesis of [Eu(bta)<sub>3</sub>(TPPO)<sub>2</sub>] (EubtaT).** [Eu(bta)<sub>3</sub>(H<sub>2</sub>O)<sub>2</sub>] (32.1 mg, 0.04 mmol) was dissolved in chloroform/toluene mixture (1:1) with TPPO (33.0 mg, 0.12 mmol) and stirred at 50 °C overnight. The compound **EubtaT** was obtained as a white powder after precipitation from n-pentane/toluene (10:1) and removing the organic solvent. Yield: 70 %.

LDI-MS (positive ions):  $m/z$  861.10 [Eu(bta)<sub>2</sub>TPPO]<sup>+</sup>

Elemental analysis for EuC<sub>66</sub>H<sub>48</sub>O<sub>8</sub>F<sub>9</sub>P<sub>2</sub>: calculated C 58.55 %, H 3.57 %; found: C 58.47 %, H 3.65 %.

## 2. Single crystal X-ray diffraction

A suitable single crystal of Eu1T covered with Paratone-N oil was fastened on the top of a Lindemann glass capillary and centred on the head of a four-circle kappa goniometer Oxford Diffraction Gemini E diffractometer, equipped with a 2K × 2K EOS CCD area detector and sealed-tube Enhance Mo and Cu X-ray sources. Mo K $\alpha$  ( $\lambda = 0.71070 \text{ \AA}$ ) radiation was used. Data were collected at room temperature by means of the  $\omega$  - scans technique using graphite-monochromated radiation. The diffraction intensities were corrected for Lorentz and polarization effects and were also optimized with respect to absorption. Empirical multi-scan absorption corrections using equivalent reflections were performed with the scaling algorithm SCALE3 ABSPACK. Data collection, data reduction and finalization were carried out through the CrysAlisPro software. Structures were solved with the ShelXT<sup>2</sup> program by Intrinsic Phasing and refined with the ShelXL<sup>3</sup> package using least squares minimisation, in the framework of Olex2 software.<sup>4</sup> In the last cycles of refinement, non-hydrogen atoms were refined anisotropically. For some thienyl rings the rotation of the ring by 180° could not be neglected. These fragments were splitted in two parts the occupancies of which were constrained to sum to 1. Also a phenyl ring of a TPPO molecule was splitted in two parts. DFIX, DANG, SADI and FLAT restrains have been applied to better model the disordered fragments. EADP constrain has been applied to selected atoms. Reflections (17) with error/esd > 10 have been omitted. Hydrogen atoms were included in idealised positions and a riding model was used for their refinement. Finally an inspection of the crystal packing revealed void regions. The mask routine of OLEX2 was applied. The program calculated a total solvent accessible volume/cell of 347.0 Å<sup>3</sup> and a total electron-count/cell of 48.7 electrons all located in a single void of 246.5 Å<sup>3</sup>. Such value perfectly fits the presence of a dichloromethane molecule (48 electrons) in the unit cell. Crystallographic data and refining details are available in the CIF files deposited with the Cambridge Crystallographic Data Centre as supplementary publication (CCDC 1993313).



**Table S1.** Crystal data and structure refinement for **Eu1T**.

Identification code	Eu1T
Empirical formula	(C <sub>69</sub> H <sub>50</sub> EuO <sub>8</sub> P <sub>2</sub> S <sub>6</sub> )·0.5(CH <sub>2</sub> Cl <sub>2</sub> )
Formula weight	1456.82
Temperature/K	296.4(8)
Crystal system	triclinic
Space group	P-1
a/Å	13.1921(5)
b/Å	14.0451(4)
c/Å	20.8487(5)
α/°	83.325(2)
β/°	80.241(3)
γ/°	64.273(3)
Volume/Å <sup>3</sup>	3425.7(2)
Z	2
ρ <sub>calc</sub> /cm <sup>3</sup>	1.412
μ/mm <sup>-1</sup>	1.237
F(000)	1478.0
Crystal size/mm <sup>3</sup>	0.13 × 0.1 × 0.01
Radiation	MoKα (λ = 0.71073)
2θ range for data collection/°	4.878 to 52.744
Index ranges	-16 ≤ h ≤ 16, -17 ≤ k ≤ 17, -26 ≤ l ≤ 25
Reflections collected	40041
Independent reflections	13889 [R <sub>int</sub> = 0.0410, R <sub>sigma</sub> = 0.0475]
Data/restraints/parameters	13889/910/930
Goodness-of-fit on F <sup>2</sup>	1.025
Final R indexes [I ≥ 2σ (I)]	R <sub>1</sub> = 0.0343, wR <sub>2</sub> = 0.0751
Final R indexes [all data]	R <sub>1</sub> = 0.0429, wR <sub>2</sub> = 0.0795
Largest diff. peak/hole / e Å <sup>-3</sup>	0.94/-0.74
CCDC	1993313

### 3. Geometry optimizations – computational details

DFT calculations were carried out using the Amsterdam Density Functional (ADF) package (version 2013.01).<sup>5,6</sup> The generalized gradient approximation (GGA) PBE<sup>7-10</sup> functional was employed, with a triple- $\zeta$  quality Slater-type orbital basis set with two polarization functions (TZ2P) for all atoms. Core shells up to level  $4d$  for Eu,  $2p$  for P and S, and  $1s$  for O and C were kept frozen. Scalar relativistic effects were included by means of a two-component Hamiltonian with the zeroth-order regular approximation (ZORA).<sup>11-13</sup> All geometries were optimized via the analytical energy gradient method implemented by Versluis and Ziegler<sup>14</sup> starting from crystallographic geometries where available. In all cases, frequency calculations were performed to ensure the geometry optimization had reached a minimum in the potential energy surface.

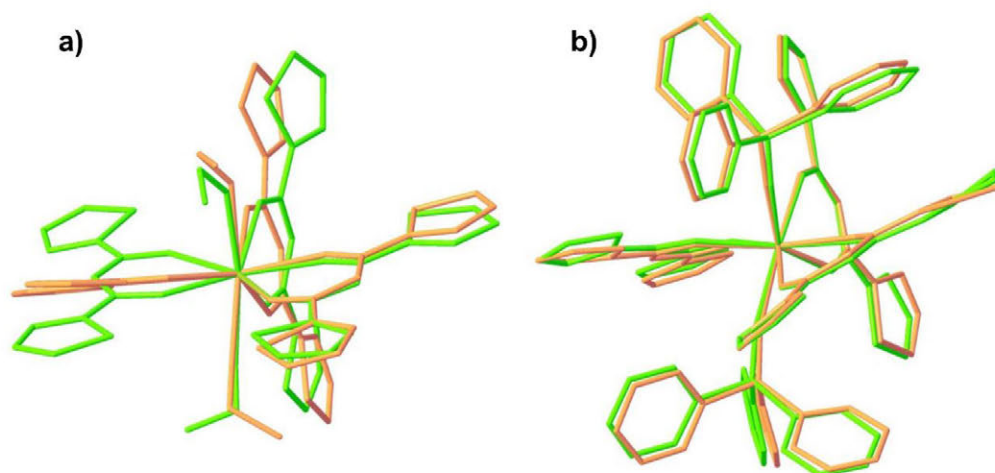


**Figure S5.** Overlay of the XRD (green) and DFT-optimized (orange) structures for compounds a) **Eu1E** and b) **Eu1T**. The overlay shows that optimized structures are in very good agreement with the experimental ones.

## 4. Mass spectrometry analysis

### *Electrospray ionization (ESI) mass spectrometric measurements – instrumental setup*

ESI-MS were performed using a LCQ Fleet ion trap instrument (ThermoFisher), operating in negative ion mode. The entrance capillary temperature and voltage were 280°C and 4 kV, respectively. Sample (**L2**, **L3**) solutions ( $10^{-6}$  M in methanol) was introduced by direct infusion using a syringe pump at a flow rate of  $8 \mu\text{L}\times\text{min}^{-1}$

### *Laser desorption ionization (LDI) mass spectrometric measurements – instrumental setup*

LDI-MS measurements were performed using a MALDI/TOF/TOF UltrafleXtreme instrument (Bruker Daltonics, Bremen, Germany), equipped with a 1 kHz smartbeam II laser ( $\lambda = 355$  nm) and operating in the reflectron positive ion mode. The instrumental conditions were: IS1 = 25 kV; IS2 = 22.4 kV; reflectron potential = 26.3 kV; delay time = 120 ns.

External mass calibration (Peptide Calibration Standard) was based on monoisotopic values of  $[\text{M}+\text{H}]^+$  of angiotensin II, angiotensin I, substance P, bombesin, ACTH clip (1-17), ACTH clip (18-39), somatostatin 28 at  $m/z$  1046.5420, 1296.6853, 1347.7361, 1619.8230, 2093.0868, 2465.1990 and 3147.4714, respectively.

1  $\mu\text{L}$  of dichlorometane (**Eu1E**, **Eu1T**, **Gd1T**, **Eu2E**, **Eu2T**, **Gd2T**) or acetonitrile (**Eu3E**, **Eu3T**, **Gd3E**, **EubtaW**, **EubtaT**) sample solution was deposited on the stainless steel sample holder and allowed to dry before introducing into the mass spectrometer.

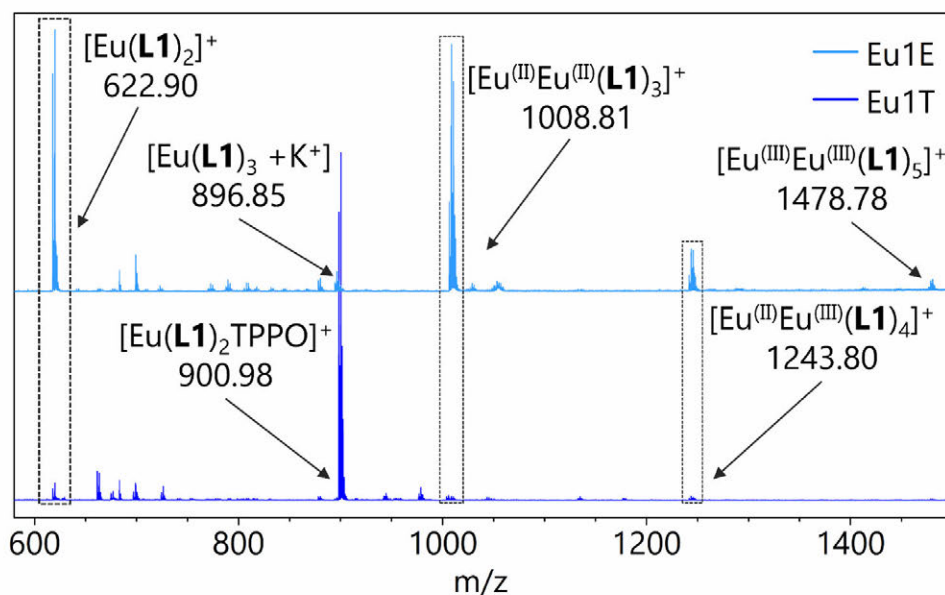


Figure S6. LDI-MS spectra for compounds **Eu1E** (light blue) and **Eu1T** (blue).

LDI-MS analyses show similar spectra for all the compounds of the **Eu***n***E** and **Eu***n***T** families, respectively. For illustrative purposes, Figure S6 shows the MS spectra of **Eu1** and **Eu1T**. The intense peak (1008.81 *m/z*) generated by **Eu1E** is related to a monocharged species  $[\text{Eu}_2(\text{L1})_3]^+$ , in which both the Eu atoms are in oxidation state 2+ as a consequence of the ionization promoted by the laser irradiation. In **Eu1T**, the most intense peak is related to the  $[\text{Eu}(\text{L1})_2\text{TPPO}]^+$  species. In Table S2 are reported the most significant LDI-MS peaks for the Ln complexes.

**Table S2.** Principal peaks in the LDI-MS spectra of the Ln complexes

	$[\text{Ln}(\text{L})_2]^+$	$[\text{Ln}(\text{L})_3+\text{Na}]^+$	$[\text{Ln}(\text{L})_3+\text{K}]^+$	$[\text{Ln}(\text{L})_2\text{TPPO}]^+$
<b>Eu1E</b>	$[\text{Eu}(\text{L1})_2]^+$ 622.90 <i>m/z</i>	$[\text{Eu}(\text{L1})_3+\text{Na}]^+$ 880.88 <i>m/z</i>	$[\text{Eu}(\text{L1})_3+\text{K}]^+$ 896.85 <i>m/z</i>	
<b>Eu1T</b>	$[\text{Eu}(\text{L1})_2]^+$ 622.90 <i>m/z</i>			$[\text{Eu}(\text{L1})_2\text{TPPO}]^+$ 900.98 <i>m/z</i>
<b>Eu2E</b>	$[\text{Eu}(\text{L2})_2]^+$ 711.02 <i>m/z</i>	$[\text{Eu}(\text{L2})_3+\text{Na}]^+$ 1013.06 <i>m/z</i>	$[\text{Eu}(\text{L2})_3+\text{K}]^+$ 1029.03 <i>m/z</i>	
<b>Eu2T</b>	$[\text{Eu}(\text{L2})_2]^+$ 711.02 <i>m/z</i>			$[\text{Eu}(\text{L2})_2\text{TPPO}]^+$ 989.10 <i>m/z</i>
<b>Eu3E</b>	$[\text{Eu}(\text{L3})_2]^+$ 811.20 <i>m/z</i>	$[\text{Eu}(\text{L3})_3+\text{Na}]^+$ 1163.25 <i>m/z</i>	$[\text{Eu}(\text{L3})_3+\text{K}]^+$ 1179.20 <i>m/z</i>	
<b>Eu3T</b>	$[\text{Eu}(\text{L3})_2]^+$ 811.20 <i>m/z</i>	$[\text{Eu}(\text{L3})_3+\text{Na}]^+$ 1163.25 <i>m/z</i>	$[\text{Eu}(\text{L3})_3+\text{K}]^+$ 1179.20 <i>m/z</i>	$[\text{Eu}(\text{L3})_2\text{TPPO}]^+$ 1089.30 <i>m/z</i>
<b>EubtaW</b>		$[\text{Eu}(\text{bta})_3+\text{Na}]^+$ 821.00 <i>m/z</i>	$[\text{Eu}(\text{bta})_3+\text{K}]^+$ 837.00 <i>m/z</i>	
<b>EubtaT</b>				$[\text{Eu}(\text{bta})_2\text{TPPO}]^+$ 861.10 <i>m/z</i>
<b>Gd1T</b>	$[\text{Gd}(\text{L1})_2]^+$ 627.90 <i>m/z</i>			$[\text{Gd}(\text{L1})_2\text{TPPO}]^+$ 905.99 <i>m/z</i>
<b>Gd2T</b>	$[\text{Gd}(\text{L2})_2]^+$ 716.02 <i>m/z</i>			$[\text{Gd}(\text{L2})_2\text{TPPO}]^+$ 994.11 <i>m/z</i>
<b>Gd3E</b>	$[\text{Gd}(\text{L3})_2]^+$ 816.31 <i>m/z</i>	$[\text{Gd}(\text{L3})_3+\text{Na}]^+$ 1168.36 <i>m/z</i>	$[\text{Gd}(\text{L3})_3+\text{K}]^+$ 1184.32 <i>m/z</i>	

## 5. FTIR Spectroscopy

FTIR measurements were performed with a Nicolet Nexus 870 FTIR equipped with an Attenuated Total Reflectance (ATR) accessory using a diamond ATR crystal. FTIR spectra were acquired in the 4000-500  $\text{cm}^{-1}$  range, collecting 32 scans with a spectral resolution of 2  $\text{cm}^{-1}$ .

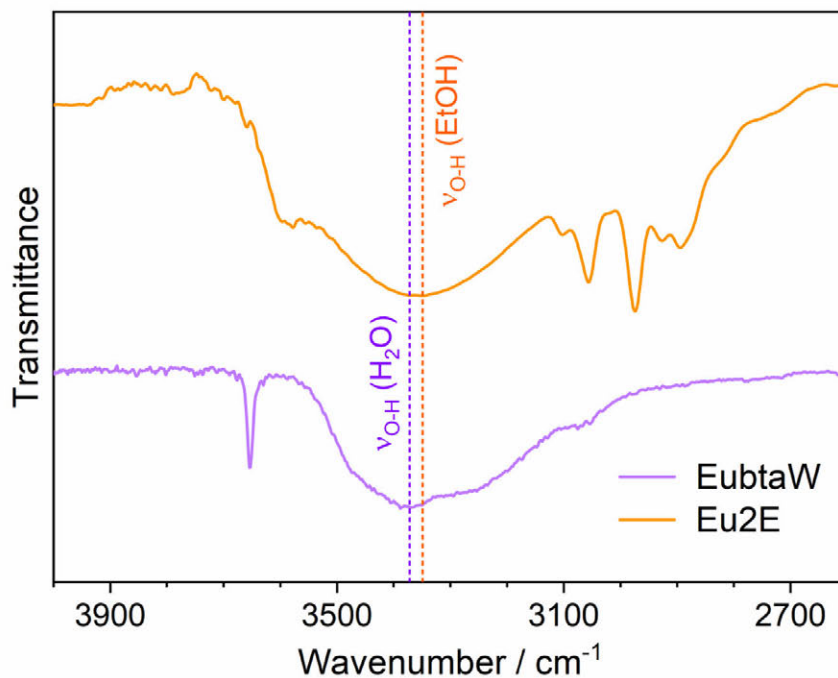


**Figure S7.** FTIR spectra of **Eu2E** and **EubtaW** complexes, in the region of O-H stretching (4000-2600  $\text{cm}^{-1}$ ). The dashed lines highlight the wavenumber associate with the O-H stretching for ethanol (orange) and water (violet).

## 6. Thin polystyrene film

Deposition of the polymer/complex blends on fused silica slides was performed using spin-coating technique. All the depositions were performed with the following parameters: polymer concentration 60 mg/ml and only one deposition at 6000 rpm. A complex/polymer ratio w/w of 1/20 was adopted. The thickness of the deposited films is around 2  $\mu\text{m}$  and was determined from the interference fringes present in the non-absorption region of the transmittance spectrum using the following equation:

$$\nu = \frac{n \left( \frac{1}{\lambda_1} - \frac{1}{\lambda_2} \right)}{N_{cyc}}$$

$$FT = (2\nu)^{-1}$$

Where  $FT$  is the film thickness,  $n$  is the refraction index of the film (1.59, bulk value for polystyrene),  $N_{cyc}$  is the number of cycles between two wavelength  $\lambda_1$  and  $\lambda_2$  ( $\lambda_1 < \lambda_2$ ) and  $\nu$  is the period of a single cycle.<sup>15</sup>

## **7. Absorption and Photoluminescence data**

### **7.1 UV-Vis Absorption Spectroscopy**

Absorption spectra were recorded on a CARY5000 double-beam spectrophotometer in the 300-800 nm range, with a spectral bandwidth of 1 nm. The contribution due to the solvent was subtracted.

### **7.2 Photoluminescence Spectroscopy**

Room temperature luminescence spectra were recorded with a Horiba JobinYvon Fluorolog-3 spectrofluorimeter equipped with double-grating monochromator in both the excitation and emission sides coupled to a R928P Hamamatsu photomultiplier and a 450 W Xe arc lamp as the excitation source. Emission spectra were corrected for detection and optical spectral response of the spectrofluorimeter supplied by the manufacturer. The excitation spectra were corrected for the spectral distribution of the lamp intensity using a photodiode reference detector.

The luminescence lifetimes in the microsecond–millisecond scales were measured by a pulsed Xe lamp with variable repetition rate or a Horiba SpectraLed (370 nm) and elaborated with standard software fitting procedures. The reported lifetimes are the average values and the experimental uncertainty on lifetimes values is  $\pm 10\%$ . Absolute photoluminescence quantum yields (PLQY) were calculated by corrected emission spectra obtained with an apparatus consisting of a Spectralon coated Integrating Sphere accessory (4", F-3018, Horiba Jobin Yvon), fitted in the fluorimeter sample chamber. For each compound, three independent measurements were carried out, with an estimated error of  $\pm 20\%$

Temperature dependent experiments (83–303 K) were carried out in backscattering geometry using a Horiba T64000 triple spectrometer equipped with a Peltier-cooled charge-coupled device detector (Horiba Synapse). A Xe arc lamp (450 W) has been used as excitation source. The scattered radiation was collected through a 10× microscope objective (Olympus MPLAN, 10×/0.25). The spectrograph, equipped with 300 lines/mm gratings was used as a single stage imaging monochromator. Temperature dependent experiments were performed by means of a Linkam THMS600 heating/freezing microscope stage having temperature stability  $< 0.1$  °C over 83-873 K temperature range.

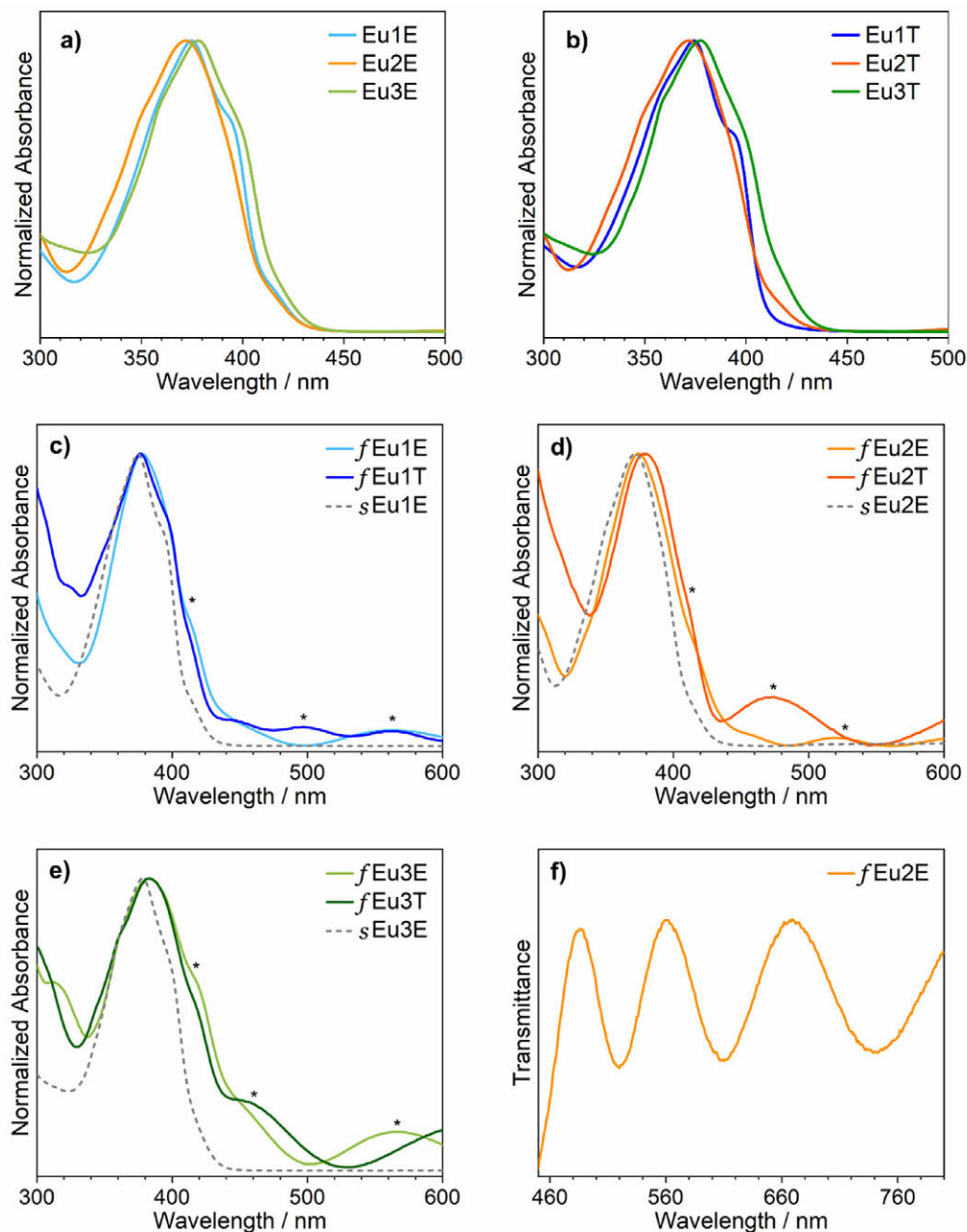


**Figure S8.** a, b) The absorption spectra of the six complexes dissolved in toluene (*ca.* 10<sup>-5</sup> M), show an intense band in the 320-440 nm region, associated to the singlet–singlet electronic transition typical of  $\beta$ -diketonates (antenna ligands). The absorption maxima slightly shift towards lower energies upon moving from **L1**- to **L3**-based complexes due to the increasing size of the conjugate system. Each component of the two families **Eu<sub>n</sub>E** and **Eu<sub>n</sub>T** ( $n = 1, 2, 3$ ) has similar spectra. The substitution of the EtOH molecules with TPPO does not induce relevant variations in the absorption spectra of the complexes as the transitions are fully localized on the antenna ligands. c-f) Absorption spectra of polystyrene thin films (*f*) **Eu1E**/**Eu1T** (c), **Eu2E**/**Eu2T** (d) and **Eu3E**/**Eu3T** (e), compared with the analogous **Eu<sub>n</sub>E** complex in solution (*s*). Interference fringes are marked with an asterisk. f) Transmittance spectrum of **Eu2E** in polystyrene thin film in the region where the interference fringes are more visible (450-800 nm).



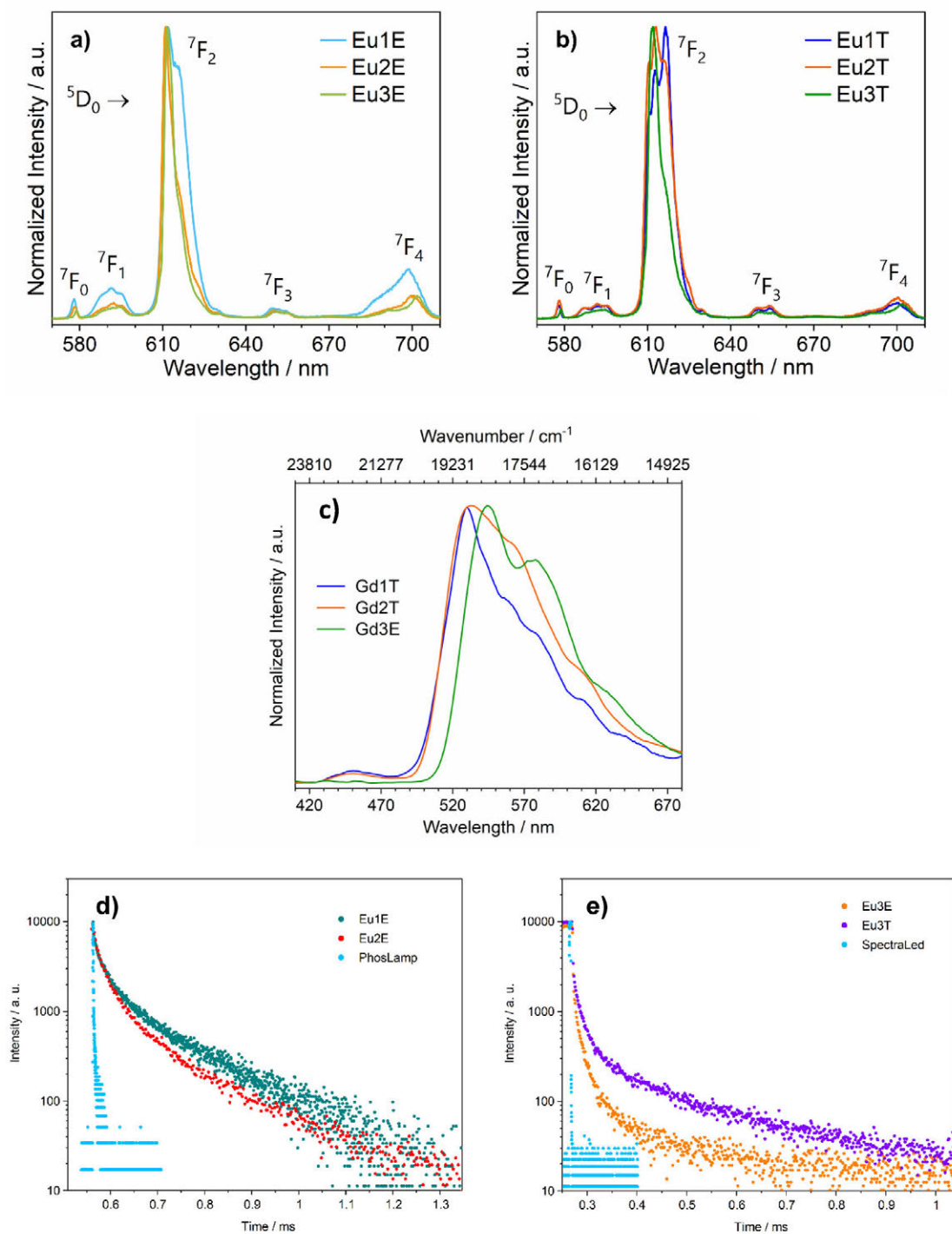


**Figure S9.** a, b) Room temperature emission spectra ( $\lambda_{\text{exc}} = 370$  nm) of **Eu1E** (a) and **Eu1T** (b) complexes embedded in polystyrene thin films. The shape of the  ${}^5D_0 \rightarrow {}^7F_2$  transition and the relative intensities of the other emission lines  ${}^5D_0 \rightarrow {}^7F_J$  ( $J = 1, 4$ ) change with the different antenna ligands due to small variations in the coordination geometry, induced by the progressive increase in the steric hindrance of the  $\beta$ -diketonato ligands going from **L1** to **L3**. For the same reason, similar variations of the emission spectra are also observed when europium coordinates TPPO instead of EtOH. c)

Phosphorescence spectra ( $\lambda_{\text{exc}} = 370$  nm) recorded at 77 K with a 300  $\mu\text{s}$  delay after the excitation pulse of gadolinium complexes **Gd1T**, **Gd2T**, and **Gd3E** embedded in polystyrene thin film (*ca.* 2  $\mu\text{m}$  thick). The ligand triplet energies were estimated from the maximum of the highest energy vibronic band in phosphorescence spectra of the  $\text{Gd}^{3+}$  complexes, measured at 77 K. The  $T_1$  state energies were found to be 18900  $\text{cm}^{-1}$  for **L1**, 18800  $\text{cm}^{-1}$  for **L2**, and 18400  $\text{cm}^{-1}$  for **L3**. As expected, this family of ligands features low lying  $T_1$  levels, and the energy can be tuned by modifying the PAH substituent. d-e) Decay curves acquired with Xe flash lamp (d) and with 370 nm SpectraLed (e) for selected samples.

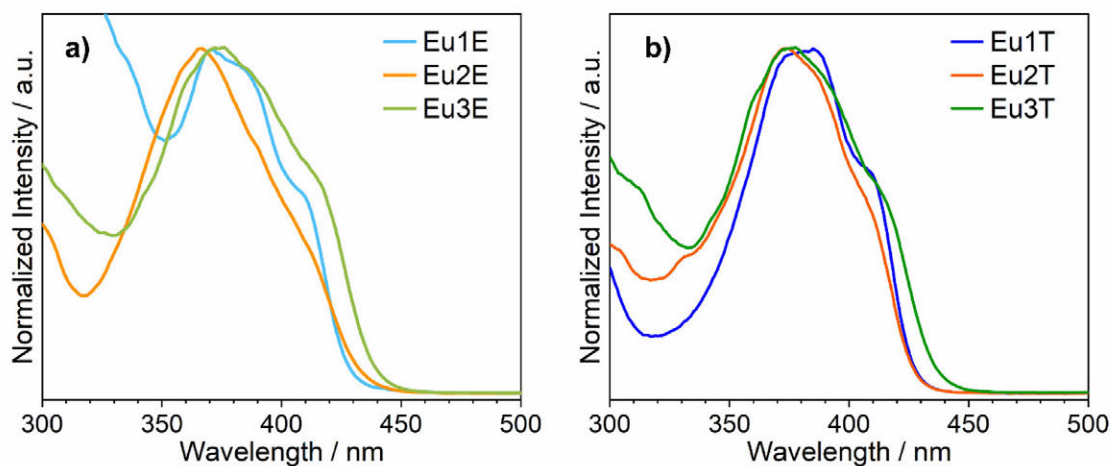


**Figure S10.** Photoluminescence excitation spectra of europium complexes a) **Eu1E**, **Eu2E**, **Eu3E** and b) **Eu1T**, **Eu2T**, **Eu3T** embedded in polystyrene thin film (*ca.* 2 thick).

**Table S3.** Absorption and emission data of the Eu complexes

	<b>Eu1E</b>	<b>Eu2E</b>	<b>Eu3E</b>	<b>Eu1T</b>	<b>Eu2T</b>	<b>Eu3T</b>
Triplet energy ( $\text{cm}^{-1}$ )	18900	18800	18400	18900	18800	18400
$\lambda_{\text{max}}$ (nm)	375	372	378	375	372	378
$\epsilon$ ( $10^4 \text{ M}^{-1} \text{ cm}^{-1}$ )	8.7	6.6	7.8	7.5	7.8	9.2
$\tau$ ( $\mu\text{s}$ )	60.7	49.3	9.0	170.8	153.0	40.2
PLQY (%)	0.4	1	< 1%	5	7	1.7

## 8. Model development

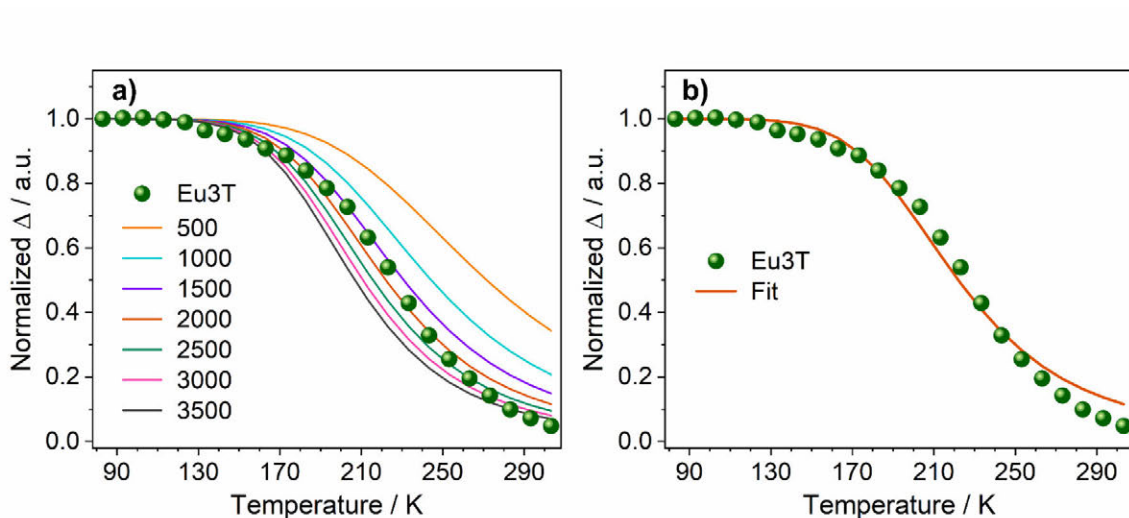


**Figure S11.** Determination of  $c_B$  value: a) effect of  $c_B$  variation and b) experimental  $\Delta(T)$  for **Eu3T** (dots) and best fit ( $c_B = 2000$ , continuous line). The fit was used to determine the value of  $c_B$ .

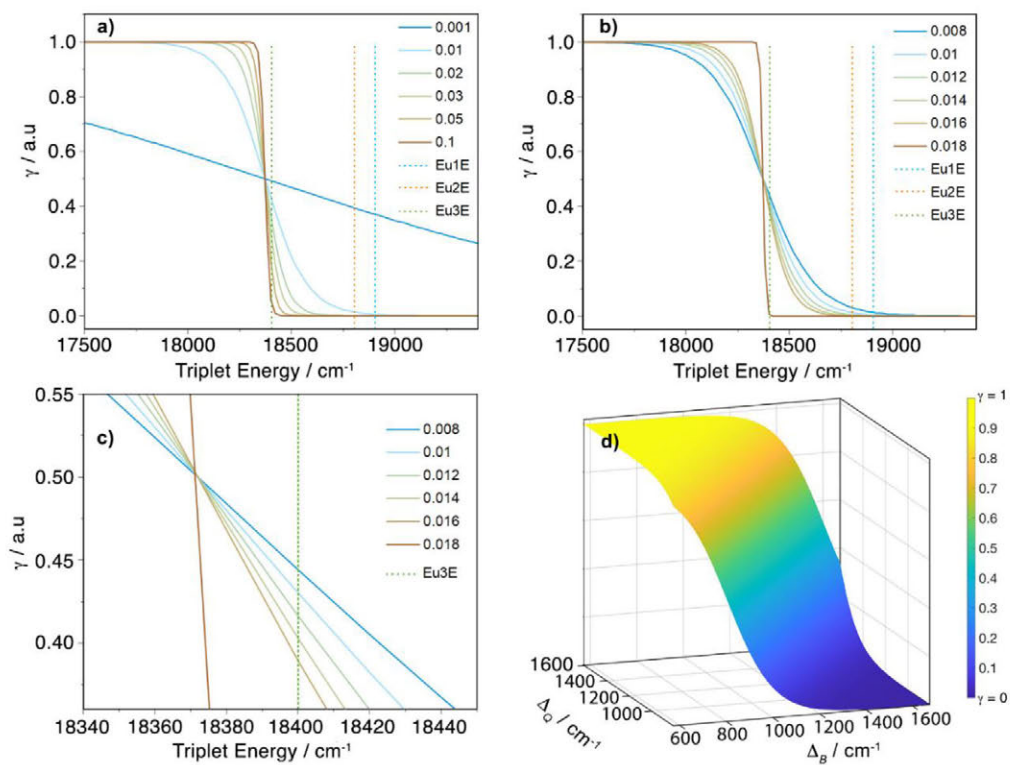


**Figure S12.** a), b), and c) plots of  $\gamma$  function vs triplet energy at constant  $\Delta_Q = 1145 \text{ cm}^{-1}$  (the value for Et-OH) for different  $\alpha$  values. The vertical dotted lines highlight  $T_1$  energy of **Eu1E**, **Eu2E** and **Eu3E**. d)  $\gamma(\Delta_B, \Delta_Q)$  surface at  $\alpha = \text{constant} = 0.01$ . The colour bar gives  $\gamma$  values.

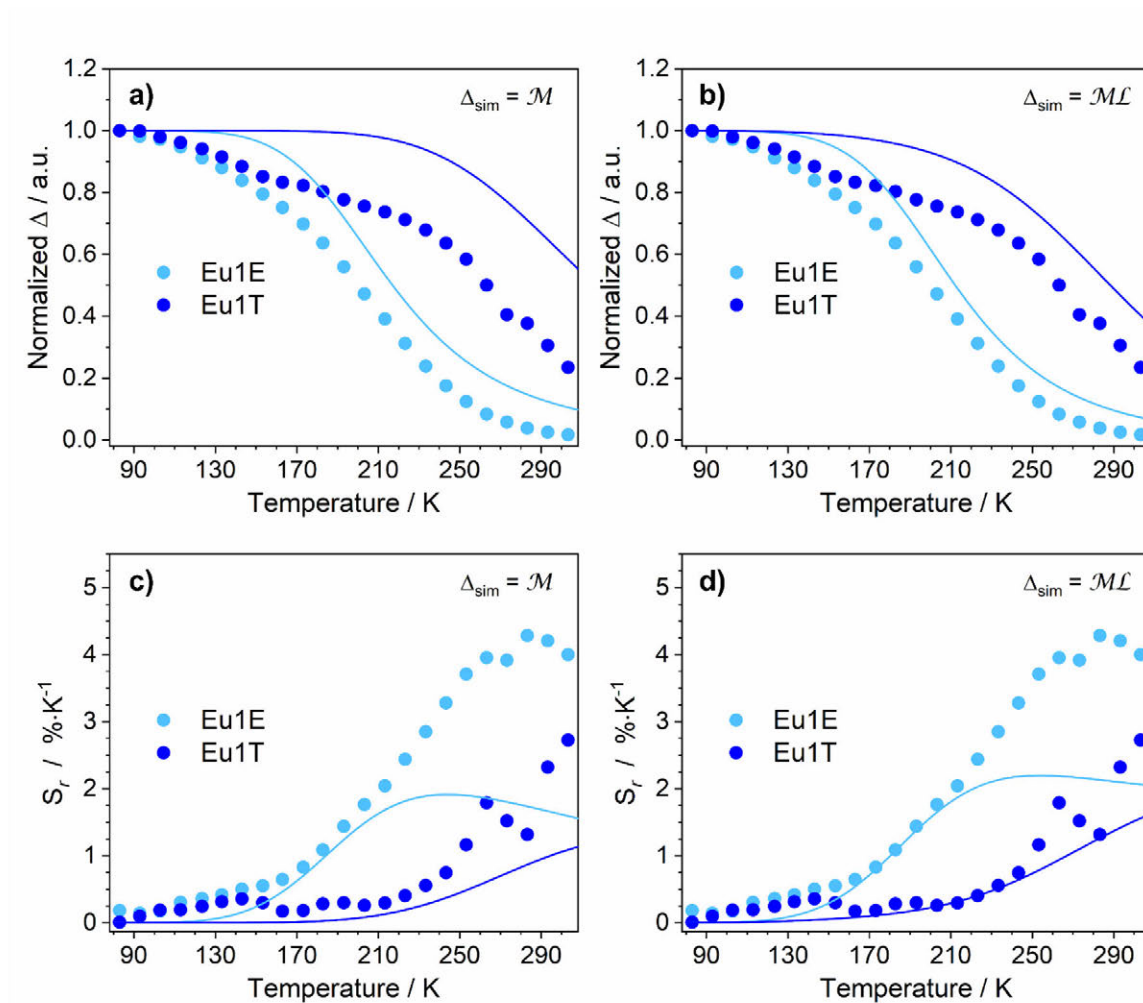


**Figure S13.** Comparison between experimental and simulated thermometric parameters  $\Delta$  and relative thermal sensitivity  $S_r$  calculated using  $\mathcal{M}(T)$  (a, c) or  $\mathcal{M}(T) \cdot \mathcal{L}(T)$  (b, d) for **Eu1E** and **Eu1T**.

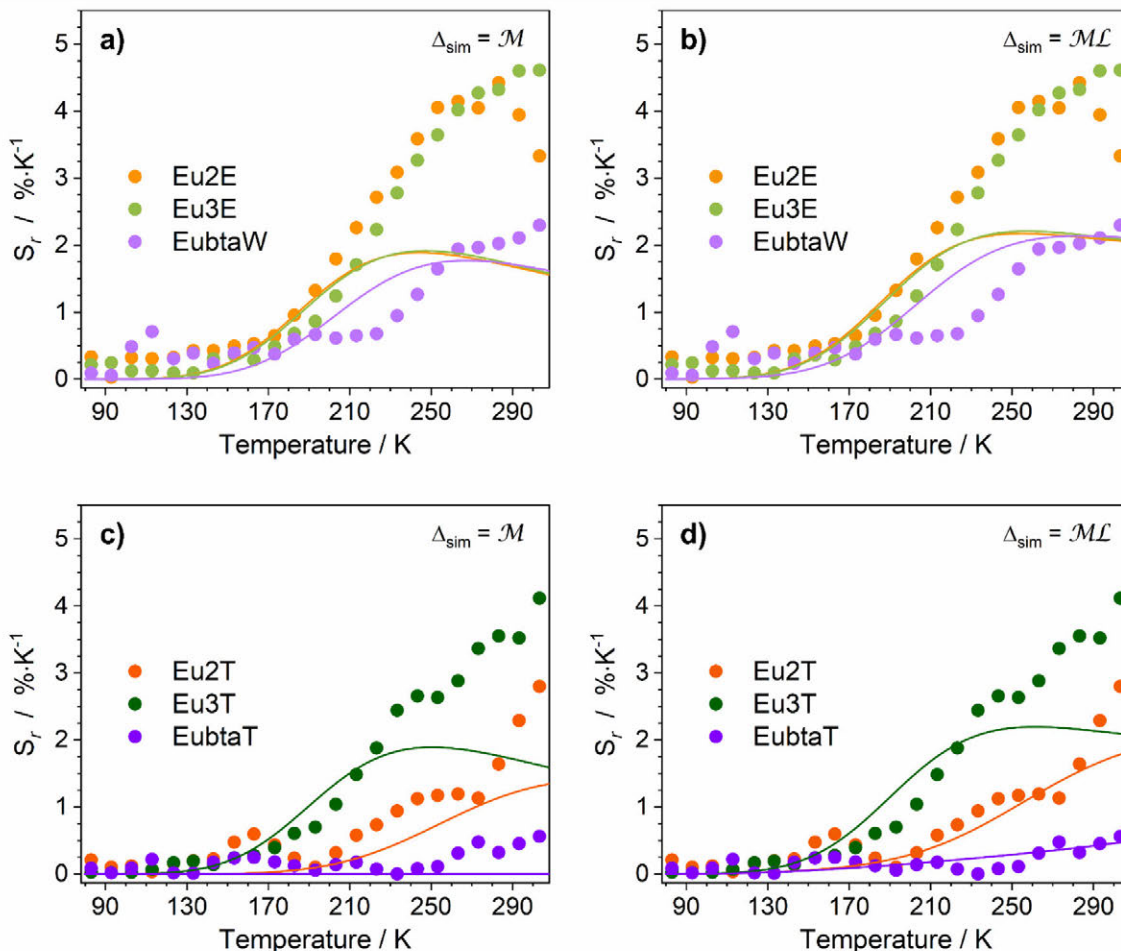


**Figure S14.** Comparison between experimental and simulated relative thermal sensitivity  $S_r$  calculated using  $\mathcal{M}(T)$  (a, c) or  $\mathcal{M}(T) \cdot \mathcal{L}(T)$  (b, d). Since complexes with ligands **L1** and **L2** have similar behaviour, only the data for compounds **Eu2E** and **Eu2T** are reported. Data for **Eu1E** and **Eu1T** are displayed in Figure S13 (c, d).

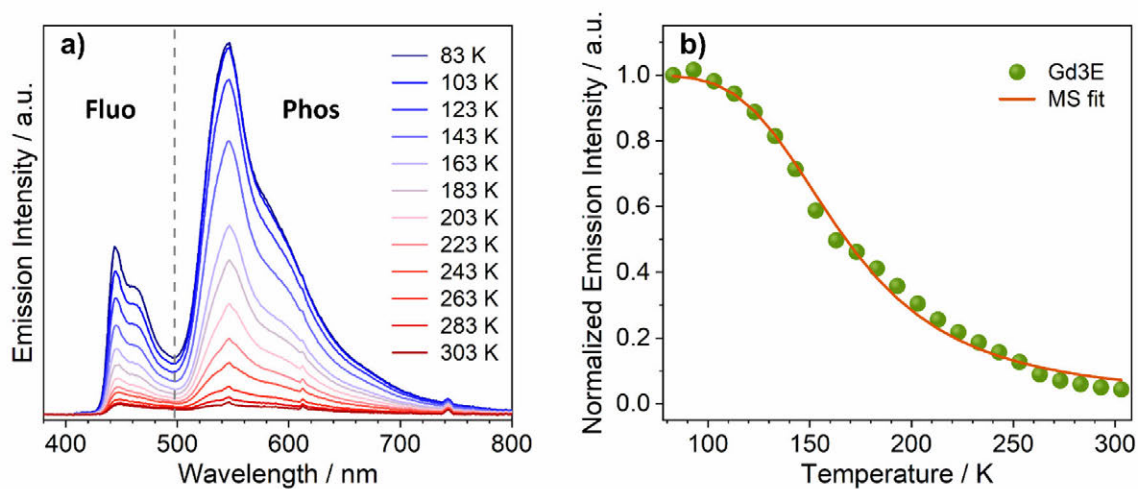


**Figure S15.** a) Emission spectra of **Gd3E** complex at different temperatures between 83 and 303 K and b) the intensity of the phosphorescence bands vs T with the relative MS fit (orange line).

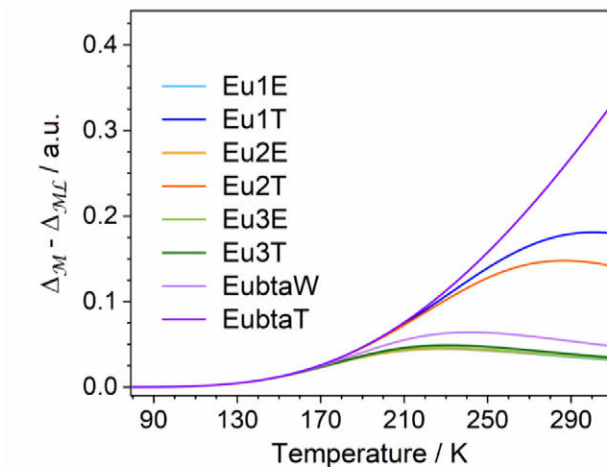


**Figure S16.** Residuals ( $\Delta_M - \Delta_{ML}$ ) plots for the compounds synthesized to define and test the model where  $\Delta_M$  and  $\Delta_{ML}$  are the  $\Delta$  curves simulated using  $\mathcal{M}(T)$  or  $\mathcal{M}(T) \cdot \mathcal{L}(T)$ , respectively.

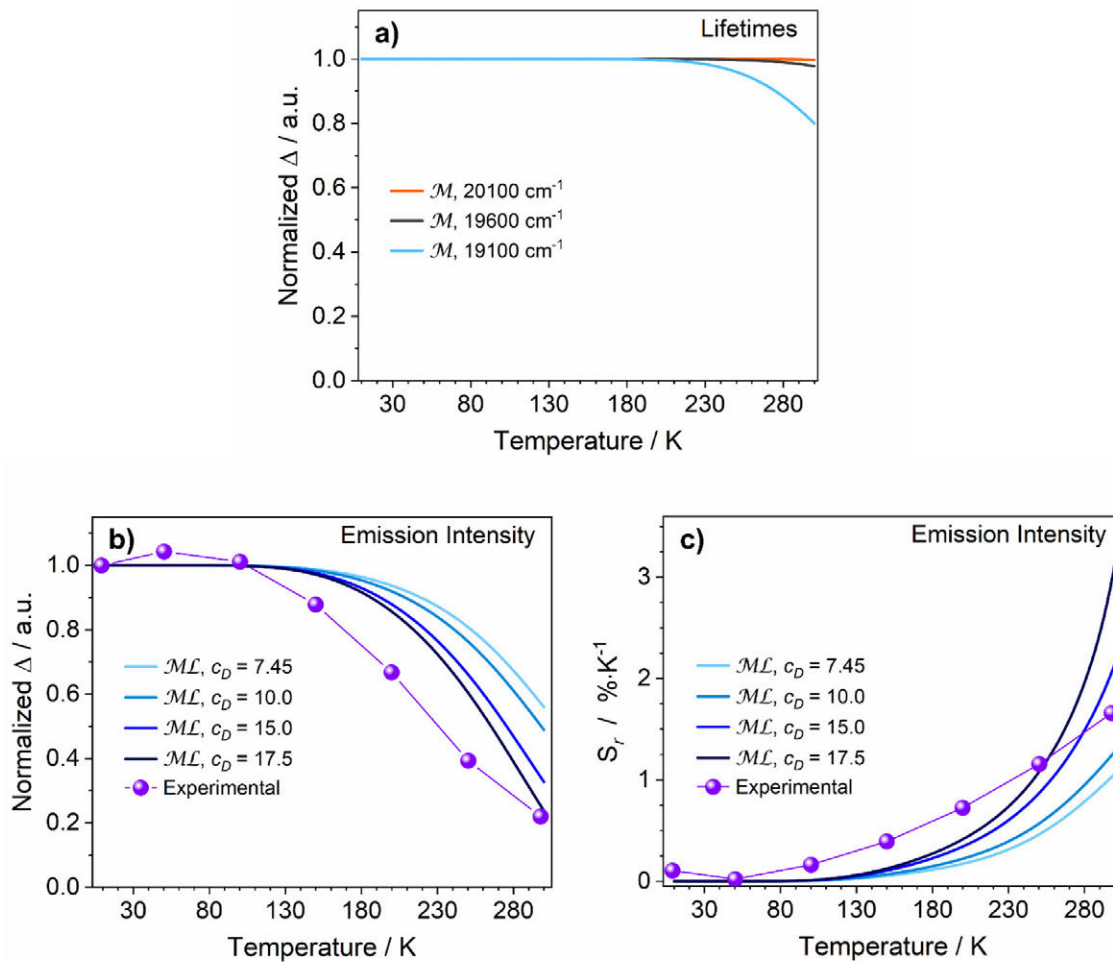









**Figure S17.** Simulations for the Tb-Eu dyad cycTb-phEu complex data<sup>16</sup>. a)  $^5D_0$  lifetime  $\Delta$  vs T (numbers reported in the panels are the energies of the ligand triplet level used for the simulations). b) Emission intensity  $\Delta$  vs T and c) relative thermal sensitivity  $S_r$  vs T, considering a triplet energy of 19100  $\text{cm}^{-1}$  and varying the  $c_D$  parameter.

## References

- (1) L. Armelao, A. Carlotto, F. Mian, J. Tessarolo, G. Bottaro, M. Rancan, *Can. J. Chem.* **2017**, *95* (11), 1183.
- (2) G. M. Sheldrick, *Acta Cryst.* **2015**, *A71*, 3.
- (3) G. M. Sheldrick, *Acta Cryst.* **2015**, *C71*, 3.
- (4) O. V. Dolomanov, L. J. Bourhis, R. J. Gildea, J. A. K. Howard, H. Puschmann, *J. Appl. Crystallogr.* **2009**, *42*, 339.
- (5) G. te Velde, F. M. Bickelhaupt, E. J. Baerends, C. Fonseca Guerra, S. J. A. van Gisbergen, J. G. Snijders, T. Ziegler, *J. Comput. Chem.* **2001**, *22* (9), 931.
- (6) C. Fonseca Guerra, J. G. Snijders, G. te Velde, E. J. Baerends, *Theor. Chem. Acc.* **1998**, *99* (6), 391.
- (7) J. P. Perdew, K. Burke, M. Ernzerhof, *Phys. Rev. Lett.* **1996**, *77* (18), 3865.
- (8) J. P. Perdew, Y. Wang, *Phys. Rev. B* **1992**, *45* (23), 13244.
- (9) J. C. Slater, *Phys. Rev.* **1951**, *81* (3), 385.
- (10) P. A. M. Dirac, *Proc. R. Soc. Lond. A* **1929**, *123* (792), 714.
- (11) E. van Lenthe, E. J. Baerends, J. G. Snijders, *J. Chem. Phys.* **1994**, *101* (11), 9783.
- (12) E. van Lenthe, A. Ehlers, E. J. Baerends, *J. Chem. Phys.* **1999**, *110* (18), 8943.
- (13) E. van Lenthe, E. J. Baerends, J. G. Snijders, *J. Chem. Phys.* **1993**, *99* (6), 4597.
- (14) L. Versluis, T. Ziegler, *J. Chem. Phys.* **1988**, *88* (1), 322.
- (15) P. D. T. Huibers, D. O. Shah, *Langmuir*, **1997**, *13*, 5995.
- (16) G. Bao, K.-L. Wong, D. Jin, P. A. Tanner, *Light Sci. Appl.* **2018**, *7* (1), 96.





Cite this: *Dalton Trans.*, 2020, **49**,  
14556Antenna triplet DFT calculations to drive the  
design of luminescent Ln<sup>3+</sup> complexes†Luca Babetto, <sup>a</sup> Silvia Carlotto, <sup>\*†a,b</sup> Alice Carlotto, <sup>a</sup> Marzio Rancan, <sup>b</sup>  
Gregorio Bottaro, <sup>b</sup> Lidia Armelao <sup>a,b</sup> and Maurizio Casarin <sup>\*a,b</sup>

Density functional theory-based methods have been exploited to look into the structural, vibrational and electronic properties of antenna ligands, all of them being crucial factors for the reliable design of customized luminescent lanthanide (Ln<sup>3+</sup>) complexes. The X-ray structures, UV-Vis absorption spectra and triplet (T<sub>1</sub>) energies of three novel β-diketone ligands with a thienyl group and naphthyl (**L1**), phenanthryl (**L2**), and pyrenyl (**L3**) polycyclic aromatic hydrocarbons as substituents have been modelled. Vibronic progressions provide a strong contribution to the **L1** and **L2** absorption spectra, while the **L3** absorption spectrum needs the assumption of different conformational isomers in solution. T<sub>1</sub> energies have been estimated either through the vertical- or the adiabatic-transition approach. The comparison with the phosphorescence spectra of Gd<sup>3+</sup> complexes allowed us to infer that the latter approach is the most suitable one, in particular when sizable ligands are involved. Results obtained for the isolated antennas can be directly compared with those of the corresponding Ln<sup>3+</sup> complexes, due to the unanimously accepted assumption that the excitation is ligand-centred.

Received 25th July 2020,  
Accepted 21st September 2020

DOI: 10.1039/d0dt02624g

rsc.li/dalton

## Introduction

As a consequence of their peculiar optical properties, lanthanide (Ln)-based luminescent systems have found applications in a variety of fields ranging from the detection of cancer biomarkers<sup>1</sup> to drug delivery monitoring,<sup>2</sup> thermometry,<sup>3</sup> LEDs<sup>4–6</sup> and sensors, and many others.<sup>7</sup> Ln<sup>3+</sup>-based emission lines are narrow, easily recognisable and maintain their characteristic spectral fingerprint even in very different environments. Nevertheless, the direct excitation of the Ln<sup>3+</sup> centre *via* light absorption is very inefficient; as a matter of fact, the 4f–4f transitions are parity-forbidden, according to the Laporte rule;<sup>8</sup> the emitter state usually has a different spin multiplicity than the ground state (GS), thus making the transition spin-forbidden;<sup>8</sup> for some Lns, such as Eu<sup>3+</sup>, the transition (<sup>7</sup>F<sub>0</sub> → <sup>5</sup>D<sub>0</sub>) is also forbidden by the standard Judd–Ofelt theory.<sup>9</sup> To efficiently populate the emitting level and sensitize the Ln<sup>3+</sup>-based luminescence, the so-called “antenna effect” is usually

exploited. After light irradiation, the antenna (often used as a ligand) is excited to a higher energy singlet state, and relaxation to the first excited singlet state (S<sub>1</sub>) subsequently takes place (Kasha’s rule).<sup>10</sup> Intersystem crossing then promotes the population of the lowest-lying excited triplet state (T<sub>1</sub>) of the antenna and an energy transfer to the emitter state of the Ln<sup>3+</sup> centre subsequently occurs (Fig. S1 in the ESI†). The Ln<sup>3+</sup>-based luminescence then occurs.

T<sub>1</sub> energy plays a critical role in tailoring luminescent Ln<sup>3+</sup> complexes; for instance, when Ln<sup>3+</sup>-based coordination compounds are used as luminescent molecular thermometers, high thermal sensitivities are usually achieved if the energy difference between T<sub>1</sub> and the Ln<sup>3+</sup> emitting levels is small (*ca.* 20–1000 cm<sup>−1</sup>).<sup>11–13</sup> Conversely, when very bright emission is required (lighting or biomedical applications) energy gaps of 2000–3000 cm<sup>−1</sup> are usually required.<sup>14,15</sup> A reliable prediction of the T<sub>1</sub> energy might then be useful for the experimental community to design novel Ln<sup>3+</sup> systems. Suitable theoretical techniques devoted to this goal are consequently mandatory.

It is commonly accepted that, in Ln<sup>3+</sup>-antenna complexes, the excitation is mainly localized on the ligand and this assumption is supported by several experimental and theoretical studies.<sup>16–18</sup> Indeed, different Ln<sup>3+</sup> complexes with the same ligands show excitation and emission bands almost in the same positions.<sup>19,20</sup> This suggests that it should be possible to adopt accurate theoretical methodologies to investigate the electronic properties of isolated ligands and then extend

<sup>a</sup>Dipartimento di Scienze Chimiche, Università degli Studi di Padova, Via F. Marzolo 1, 35131 Padova, Italy. E-mail: silvia.carlotto@unipd.it, maurizio.casarin@unipd.it

<sup>b</sup>Institute of Condensed Matter Chemistry and Technologies for Energy (ICMATE), National Research Council (CNR), c/o Department of Chemistry, University of Padova, via F. Marzolo 1, 35131 Padova, Italy

† Electronic supplementary information (ESI) available. CCDC 1998680–1998682. For ESI and crystallographic data in CIF or other electronic format see DOI: 10.1039/D0DT02624G

‡ These authors equally contributed to this work.

the obtained results to their  $\text{Ln}^{3+}$  complexes with a much lower computational cost.

A widespread agreement on how to carry out ligands'  $T_1$  energy calculations has not yet been reached in the literature, and the current state-of-the-art consists of two distinct approaches, both based on time-dependent density functional theory (TD-DFT): (i) the vertical transition (VT) approach, where  $T_1$  and the GS share the same geometry;<sup>21–27</sup> (ii) the adiabatic transition (AT) approach, corresponding to the energy difference between  $T_1$  and the GS both of them in their optimised geometry.<sup>20,28–30</sup> To the best of our knowledge, only one study<sup>27</sup> considered a direct comparison between the two methods; nevertheless, the corresponding calculations were carried out by considering the whole complexes. Before going on, it has to be noticed that higher level methods such as complete active space self-consistent field (CASSCF) calculations have been shown to provide essentially equivalent results to those of the much cheaper and less challenging DFT calculations.<sup>19</sup> For this reason, the forthcoming discussion will be limited to DFT numerical experiments.

To properly describe the chromophore electronic properties, the  $S_0 \rightarrow S_1$  transition ( $S_0$  corresponds to the electronic GS) must also be considered. Experimental information about it can be gained from the absorption spectra, traditionally modelled by taking into account only VTs and neglecting vibronic effects<sup>31,32</sup> whose relevance in luminescent  $\text{Ln}^{3+}$  complexes has been started to be considered only recently.<sup>33</sup> Moreover, when a molecular system may have different conformational isomers, the theoretical investigation is usually limited to one of them.<sup>34,35</sup> These assumptions are usually acceptable in many cases; however, ligand size and nature may strongly affect these simplifications. In fact, the smaller the chromophore is, the greater the relevant vibronic contributions are as a consequence of the large overlap between the GS and excited state vibronic wavefunctions.<sup>36</sup> Conversely, experimental data suggest that the more sizable is the chromophore, the higher is the possibility for conformational isomers to contribute their own absorption properties to the overall spectrum.<sup>35</sup>

The main aim of this study is therefore to present a general and comprehensive theoretical protocol based on DFT calculations to rationalize and possibly drive the design of luminescent  $\text{Ln}^{3+}$  complexes through the precise *ab initio* determination of the sole antenna electronic properties. The outcomes obtained for the ligands will be then directly transferred to the corresponding  $\text{Ln}^{3+}$  complexes. Even though these principles are valid for any  $\text{Ln}^{3+}$ -based complex, this protocol has been validated herein for a series of  $\text{Gd}^{3+}$  tris( $\beta$ -diketonate) complexes whose coordination chemistry and photo-physics are well established.<sup>37,38</sup> The  $\beta$ -diketones we considered feature a thienyl group and different polycyclic aromatic hydrocarbons (PAH, naphthyl for **L1**, phenanthryl for **L2**, and pyrenyl for **L3**, see Fig. 1). These ligands have been previously employed in an ongoing study on luminescent molecular thermometers to prepare a small library of  $\text{Eu}^{3+}$  tris( $\beta$ -diketonate) that served as a base to develop a predictive strategy for thermometric appli-

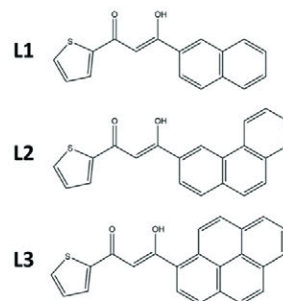


Fig. 1 Ligands **L1**, **L2**, and **L3**.

cations.<sup>39</sup> The used  $\beta$ -diketones with PAH fragments allow achieving a small energy gap between the  $\text{Eu}^{3+}$  emitting level ( $^5D_0$ ) and  $T_1$ . As stated above, this enhances the system response to temperature variations. The presence of PAH fragments such as naphthyl, phenanthryl and pyrenyl is also interesting since the substitution of this moiety allows a steady variation of the system properties. This tuneable behaviour is crucial to test the accuracy of the proposed protocol.

The forthcoming discussion of the theoretical outcomes is organized in three sections: (i) the first one is devoted to the modelling of the structural properties of the **L1**, **L2**, and **L3** GS in comparison with single crystal X-ray diffraction (SCXRD) data; (ii) the second one examines and rationalises the shapes and origins of the **L1**, **L2**, and **L3** absorption spectra and (iii) the third one is focused on the VT and AT approaches to estimate the ligand  $T_1$  energies. The obtained results are then compared with  $\text{Gd}^{3+}$  complexes' phosphorescence measurements.

## Experimental and computational details

### Experimental details

**L1**, **L2**, and **L3** have been synthesised *via* Claisen condensation, purified, and fully characterized by SCXRD (see Table S1 of the ESI<sup>†</sup>),  $^1\text{H}$ - and  $^{13}\text{C}$ -NMR (see Fig. S2 and S3 of the ESI<sup>†</sup>), and ESI-MS as described in the ESI<sup>†</sup>. The  $\text{Gd}^{3+}$  complexes have general formula  $\text{GdL}_3\text{S}_2$ , where **L** is a  $\beta$ -diketone and **S** is the coordinated solvent molecule (EtOH). The ligands have been reacted with  $\text{Gd}(\text{NO}_3)_3$  in the presence of a stoichiometric amount of base in ethanol at 50 °C, leading to the formation of  $[\text{GdL}_3(\text{EtOH})_2]$  compounds (see the ESI<sup>†</sup> for details). LDI-MS analyses show similar spectra for all the complexes.<sup>39</sup> Absorption spectra were recorded on a CARY5000 double-beam spectrophotometer in the 300–800 nm range, with a spectral bandwidth of 1 nm. The contribution due to the solvent was subtracted. Phosphorescence spectra at 83 K were acquired using a Horiba Fluorolog 3 coupled *via* optical fibres to a Linkam THMS600 heating and freezing stage.

### Computational details

DFT calculations have been carried out by using the Amsterdam density functional (ADF) package (version 2013.01).<sup>40–42</sup> The hybrid exchange–correlation (XC) functional B3LYP<sup>43–46</sup> has been employed to optimise the L1, L2, and L3 geometries. An all-electron triple- $\zeta$  quality Slater-type orbital basis set with one polarization function (TZP) has been adopted for all the atoms. L1, L2, and L3 may have four possible rotamers (A, B, C, and D in Fig. 2) according to the relative orientation of the substituent rings. If we assume rotamer A, the predominant form in the crystal structure, as a reference, B and C may be obtained by flipping either the thienyl moiety (B) or the polycyclic fragment (C). If the thienyl group and the PAH fragment are both flipped, rotamer D is generated. The geometries of  $S_0$ ,  $S_1$ , and  $T_1$  have been optimised for each rotamer. The  $S_1$  structural parameters have been evaluated by exploiting the ExcitedGO<sup>47</sup> keyword in ADF, where the gradients of the chosen electronic excitation and of the GS are combined to give the gradients of the excited state. As far as the  $T_1$  geometries are concerned, they have been estimated by carrying out a GS geometry optimization on a triplet electronic state, as  $T_1$  is the lowest-lying electronic state with that spin multiplicity.

All geometries have been optimised by using the analytical energy gradient method implemented by Versluis and Ziegler<sup>48</sup> and starting from crystallographic data. As such, frequency calculations have been systematically performed to confirm the absence of imaginary frequencies and to then be sure that the optimised geometry corresponds to a minimum on the potential energy hypersurface. Rotational energy barriers for the 180° fragment flips have been obtained by performing a 100-point linear transit (LT) calculation between the two rotamers and relaxing the geometry of the molecule at each step by means of a constrained geometry optimization. Solvent effects were taken into account by adopting the COSMO model implemented in ADF, with the default parameters for toluene.<sup>49</sup> Dispersion corrections were included as implemented by Grimme.<sup>50</sup>

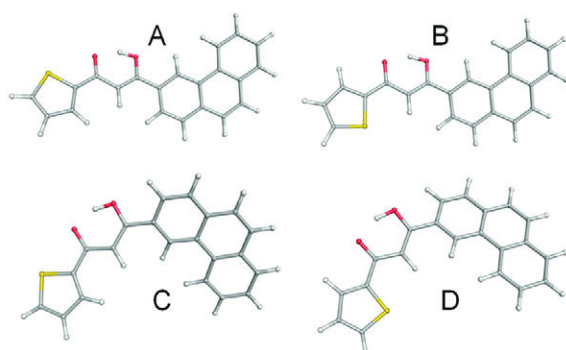


Fig. 2 A ball and stick representation of the optimised B3LYP/TZP structures for the L2 A, B, C, and D rotamers. Grey, red, yellow and white spheres are representative of C, O, S and H atoms, respectively.

Optical properties have been estimated by employing time-dependent density functional theory (TD-DFT)<sup>51,52</sup> coupled to the asymptotically correct statistical average of orbital potentials (SAOP)<sup>53,54</sup> XC functional and by using an all-electron triple- $\zeta$  quality Slater-type orbital basis set with two polarization functions (TZ2P) for all the atoms. LB94<sup>55</sup> and B3LYP<sup>43–46</sup> functionals have also been tested for the calculation of the absorption spectra. Franck–Condon factors<sup>55–58</sup> for the simulation of vibrationally resolved spectra were calculated with the ADF fcf module.<sup>55</sup> The excited state has been chosen as the most intense TD-DFT transition; as already mentioned, the  $S_1$  geometry has been optimised by using the ADF ExcitedGO keyword and a frequency analysis has been carried out after the geometry optimization. A Lorentzian broadening factor of 0.1 eV has been applied for the plot of the absorption spectra when considering the electronic transitions, while a 0.05 eV broadening has been applied on the vibronic components.

The study of the energy transfer pathways associated with the antenna effect in  $\text{Ln}^{3+}$  complexes implies the precise determination of the excited state energies.  $S_1$  is assumed to be too short-lived to allow for nuclear relaxation: its energy has then been determined from the most intense low energy transition calculated *via* TD-DFT in the GS  $S_0$  geometry. At variance to that, the  $T_1$  energy has been evaluated in two ways: either considering a vertical singlet–triplet transition calculated *via* TD-DFT in the GS  $S_0$  geometry, or as the energy difference between  $T_1$  and  $S_0$  in their optimised geometry, thus simulating an adiabatic transition. Incidentally, the former way implicitly assumes that  $T_1$  does not possess a lifetime long enough to allow for nuclear relaxation – as the transition is calculated in the GS geometry – while the opposite is true for the latter.

## Results and discussion

The electronic properties of the fragments composing the  $\text{Ln}^{3+}$  complex – ligands and  $\text{Ln}^{3+}$  – are: (i) surrounding-independent and (ii) substantially unaffected upon moving from the isolated fragments to the complex.<sup>59–61</sup> This is an approximation, but this assumption allows us to extend to the coordination complexes the results obtained for the ligands.

### GS geometries

The L1, L2, and L3 B3LYP/TZP optimised GS geometries are in excellent agreement with SCXRD experimental evidences (see Fig. S4 and S5 of the ESI†). The dihedral angle between the diketone moiety and the polycyclic aromatic fragment – the structural parameter showing largest variations along the series – has been used as a gauge for such an agreement. The B3LYP/TZP outcomes slightly overestimate this angle because of crystal packing effects, which would favour its decrease (experimental/calculated; L1: 17.9°/20.5°; L2: 20.7°/23.2°; L3: 50.2°/55.9°). Crystallographic data pertinent to L2 and L3 are consistent with the mere presence of rotamers A and B due to

the disorder derived from the rotation of 180° of the thienyl moiety (see Fig. 2 and Fig. S4 of the ESI†) and, even though neither form C nor form D have been experimentally revealed, the ligands' geometries have been optimised for all the possible conformers. This has been done because the absence of the C and D forms in the solid state does not necessarily rule out their presence in solution. As a matter of fact, the inspection of Table 1 – in which the conformer theoretical abundance estimated by assuming a Boltzmann population at 298.15 K and the energies of the optimised structures are reported – reveals that the relative stability of the rotamers could be different in different phases. For L3, the GS calculated structure corresponds to the C form even if the A form has been found in the solid state (SCXRD structure). However, it has to be highlighted that the calculated energy difference between the two forms is negligible (0.51 kcal mol<sup>-1</sup>).

The calculated rotational energy barriers between different rotamers are 7.85 kcal mol<sup>-1</sup> for the thienyl fragment (the average value of the thienyl rotation for L1 = 8.25 kcal mol<sup>-1</sup>, L2 = 7.90 kcal mol<sup>-1</sup>, and L3 = 7.40 kcal mol<sup>-1</sup>), 5.57, 5.65, and 2.19 kcal mol<sup>-1</sup> for naphthyl (L1), phenanthryl (L2), and pyrenyl (L3) fragments, respectively. Their relatively low values thus suggest a substantially free rotation of rings in solution.

The addition of solvent effects slightly changes the percentage of the different rotamers (see Table S2 of the ESI†), but the relative stabilities are maintained for all ligands. The influence of the dispersion corrections on the different rotamers was also evaluated in a vacuum and the results are reported in Table S3 of the ESI.† The percentages of the different rotamers show small variations (below 4%) but, similarly to the

inclusion of solvent effects, the relative stabilities are preserved.

### Absorption spectra

Antenna ligands are used to harvest energy through light absorption and to sensitize the Ln<sup>3+</sup> centre emission. Diverse factors concur to determine the shape of the absorption spectra: (i) the presence of different structural isomers of the free ligand (keto–enol tautomerism in β-diketone ligands); (ii) the presence of different geometrical isomers of the ligand (different rotamers/stereoisomers) and (iii) the presence of a vibronic progression based on the Franck–Condon principle. All these factors have been individually considered *via* DFT-based methods for each ligand. The experimental absorption spectra of L1 and L2 show their maximum at ~380 nm, with lower intensity shoulders at ~400 and ~350 nm (see Fig. 3, dashed lines), while the highest intensity peak of L3 lies at ~400 nm, with a shoulder at ~380 nm (Fig. 3). TD-DFT calculations have been performed on different functionals: SAOP, LB94 and B3LYP (see Fig. S6 of the ESI†). The relative intensities and positions, and the absolute positions of the vertical transitions show that the SAOP functional shows the best agreement with the experimental spectra for all ligands. Only one high intensity TD-DFT transition (~400 nm, see Tables S4–S6 of the ESI†) characterizes the UV-Vis region of the predominant L1, L2, and L3 rotamers (A). This is obviously not enough to account for the shape of the spectrum of any ligand, hence the different factors illustrated above and their influence on the absorption spectrum need to be considered.

DFT calculations regarding the presence of structural isomers (point (i)) found that the transition for the keto form of each free ligand falls in the far UV region, at λ < 300 nm, therefore it cannot contribute to the shape of the spectrum. The solvent effects on keto–enol equilibria are negligible for all ligands, where the enol form accounts for > 99% of the total.

As far as the presence of different geometric isomers is concerned (point (ii)), the transitions for the diverse rotamers of L1 and L2 fall at similar energies, and the resulting spectrum

**Table 1** Theoretical abundance of the diverse rotamers in L1, L2, and L3 in a vacuum. The energy differences (kcal mol<sup>-1</sup>) with respect to the most stable rotamer are reported in parentheses

	A	B	C	D
L1	50%	19% (+0.58)	22% (+0.50)	9% (+1.03)
L2	49%	24% (+0.42)	19% (+0.57)	8% (+1.06)
L3	23% (+0.51)	7% (+1.20)	56%	14% (+0.81)

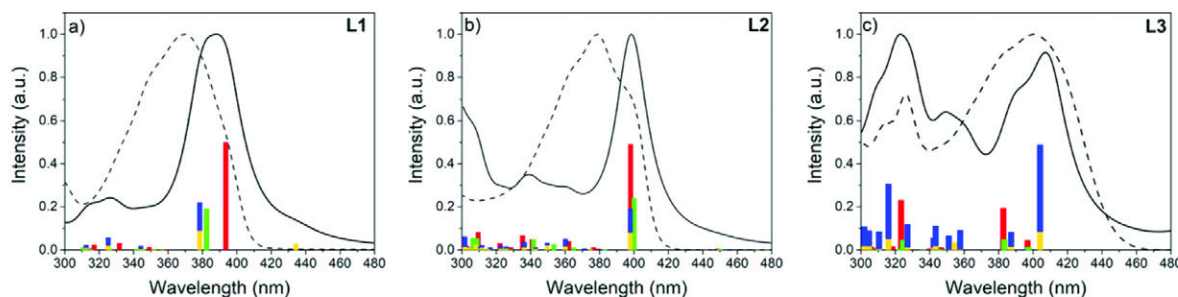


**Fig. 3** Experimental (dashed lines) and simulated electronic absorption spectra (solid lines) for the L1 (a), L2 (b), and L3 (c) ligands, calculated at the SAOP/TZ2P level. The coloured bars represent the weighted contributions of the different rotamers (A = red, B = green, C = blue, and D = yellow). The calculated spectra of L2 and L3 have been shifted by +25 nm and –5 nm, respectively. Transition intensities are scaled by the relative abundance (see Table 1) of each rotamer. Experimental spectra are obtained in toluene at a ligand concentration of 5 × 10<sup>-6</sup> M.

still shows a featureless single band in the region around 400 nm (Fig. 3a and b, Tables S4 and S5 of the ESI†); however, the opposite is true when L3 is considered. Different L3 rotamers show markedly diversified transitions and the combined spectrum reproduces the experimental data very well (see Fig. 3c and Table S6 of the ESI†). The inclusion of solvent effects causes an average red-shift of 13 nm and the effects on each ligand are reported in Fig. S7 of the ESI†.

A comparison between the molecular orbitals (MOs) involved in the most relevant electronic transitions for each ligand better highlights the similarity between L1 and L2. The most relevant electronic transition for L1 (rotamer A, red bar in Fig. 3a) primarily involves a HOMO-1  $\rightarrow$  LUMO transition,<sup>62</sup> with HOMO-1 delocalized on the whole molecule and the LUMO mainly concentrated on the thienyl/diketone portion of the molecule (see Fig. 4, top). Similar considerations were observed for the most relevant electronic transition of L2 (rotamer A, red bar in Fig. 3b), which involves a HOMO-2  $\rightarrow$  LUMO excitation, with HOMO-2 delocalized on the whole molecule and the LUMO once again predominantly localized on the thienyl/diketone fragment (see Fig. 4, centre). The electronic transition for the most relevant rotamer of L3 (C) is between HOMO-2 and the LUMO with both MOs delocalized on the whole molecule (see Fig. 4, bottom).

Point (iii), corresponding to the vibronic progression, seems then to be crucial only for the L1 and L2 spectra. As a matter of fact, the simulated vibronic progression for the A rotamer of L1 and L2 (the most stable) well reproduces the experimental evidence (Fig. 5). In particular, the relative positions of the shoulders with respect to the main peaks are quantitatively in agreement with the experimental evidence: the calculated (experimental) energy variations between the main peak and the shoulder in L1 and L2 are 16 (20 nm) and 18 (18 nm), respectively.

Interestingly, the L3 Franck-Condon factors are all zero. Such a result can be straightforwardly rationalized by referring

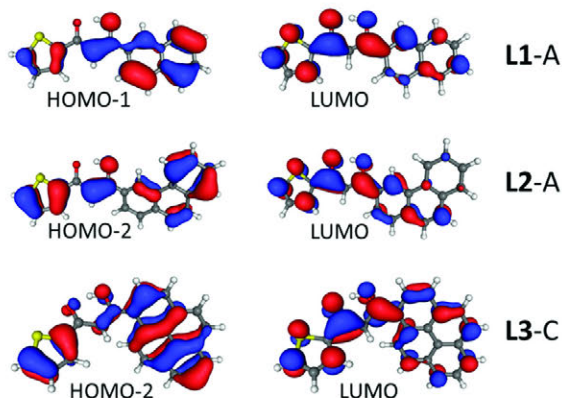


Fig. 4 MOs involved in the most relevant electronic transitions for ligands L1, L2, and L3. For each ligand, only the most stable rotamer MOs are reported (A for L1 and L2; C for L3).

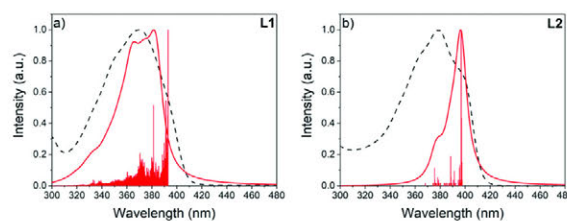


Fig. 5 L1 and L2 vibrationaly-resolved absorption spectra (solid red line) vs. experimental evidence (the dashed black line). Vibronic components have been calculated at the B3LYP level of theory. The L2 spectrum has been shifted by +25 nm to match the energy of the experimental 0-0 transition.

to the  $S_0$  and  $S_1$  geometries.  $S_0$  and  $S_1$  substantially share the same structural arrangement in L1 and L2 (see Fig. S8 of the ESI†), while the opposite is true for L3. Here, the pyrenyl fragment in  $S_1$  is, with respect to  $S_0$ , rotated by  $\sim 90^\circ$  and the overlap integrals between the  $S_0$  and  $S_1$  vibronic wavefunctions are then zero (see Fig. S8 of the ESI†). As a whole, the overview on the three ligands highlights that the absorption spectrum shapes of L1/L2 and L3 have different origins.

#### T<sub>1</sub> energies

The  $T_1$  energy can be estimated through two distinct paths: (i) as the lowest energy  $S_0$ - $T_1$  TD-DFT vertical transition in the GS geometry (the already mentioned VT approach);<sup>63</sup> (ii) as the energy difference between  $T_1$  and  $S_0$  each of them in their optimised geometries, see Fig. 6 (the adiabatic transition - AT approach).<sup>19</sup>

Experimentally, the  $T_1$  energies have been determined by phosphorescence measurements on  $Gd^{3+}$  complexes.<sup>37</sup> As a matter of fact, the  $^6P_{7/2}$  state of the  $Gd^{3+}$  ion is too high in energy ( $32\,150\text{ cm}^{-1}$ ) to allow the energy transfer from  $T_1$  and the observed luminescence has to be then attributed to the ligand. The  $T_1$  energies calculated by exploiting either the VT or the AT approach are reported in Table 2. As such, it has to be noticed that the comparison between the SCXRD data and optimized geometries reveals that rotamer A is the most stable one for both L1 and L2; only the  $T_1$  energies for rotamer A are then included in Table 2. At variance to that, the L3 GS structure corresponds to the C form, while the A form is found in the solid state (see above). As already mentioned, the C and A

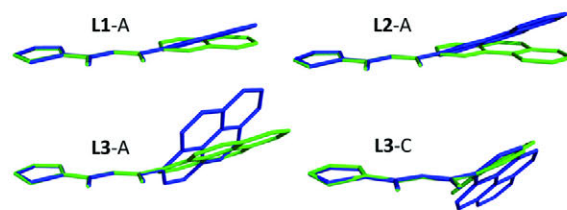


Fig. 6 Comparison between the ground state  $S_0$  (blue) and excited triplet state  $T_1$  (green) of ligands L1, L2, and L3 calculated at the B3LYP level of theory. The labels A and C refer to forms A and C.

**Table 2**  $T_1$  energies (in  $\text{cm}^{-1}$ ) estimated with the VT and the AT approaches on the isolated ligands. Experimental data are obtained from the  $\text{Gd}^{3+}$  spectra displayed in Fig. S9 of the ESI.† **L1** and **L2**  $T_1$  energies are reported for rotamer A, while the **L3**  $T_1$  energy is reported for both C and A (in parenthesis) rotamers

	VT method isolated L	AT method isolated L	Experimental $\text{GdL}_3(\text{EtOH})_2$
<b>L1</b>	18 786	18 990	18 800
<b>L2</b>	19 029	18 695	18 400
<b>L3</b>	16 633 (17 144)	15 163 (15 075)	15 181

forms are very close in energy; for this reason, the  $T_1$  energies for both A and C rotamers are reported in Table 2.

Notably, the **L3**  $T_1$  energies of the A and C rotamers are quite different, especially the VT values. In addition to what already said on the **L3** absorption spectrum modelling, differences affecting the  $T_1$  energies further confirm the relevance of considering all possible rotamers. Moreover, it has to be mentioned that, although the AT values are generally in better numerical agreement with the experimental evidence (Table 2), the **L1** and **L2** theoretical outcomes are useless to determine the most appropriate approach. However, the **L3** VT and AT results are significantly different and, for both A and C rotamers, the AT approach provides a definitely better agreement between the theory and experiment. Incidentally, this is consistent with a benchmark of similar nature carried out on  $\text{Pt}(\text{II})/\text{Pd}(\text{II})$  complexes, which also found the VT approach to generally overestimate  $T_1$  energies.<sup>27</sup>

A further point to be stressed concerns the agreement between the experimental and calculated  $T_1$  energies, which becomes progressively worse upon moving from **L1** to **L3** when the VT approach is adopted. The inspection of Fig. 6 reveals that as the PAH fragment increases in size (naphthyl, phenanthryl and pyrenyl for **L1**, **L2**, and **L3**, respectively) the overlap between the  $S_0$  and  $T_1$  geometries decreases. This suggests that as the ligand size increases, the assumption that the  $S_0$  and  $T_1$  geometries are the same (VT approach) becomes progressively less reliable. For this reason, the AT method shows the best agreement independently of the ligand nature (see Table 2) and hence should be preferred.

## Conclusions

This paper aims at presenting a comprehensive set of calculations for a rigorous and thorough theoretical investigation of the electronic properties of organic chromophores to be used as sensitizers for luminescent  $\text{Ln}^{3+}$  complexes. Numerical experiments have been performed on the sole ligands and compared with the experimental data of  $\text{Gd}^{3+}$  coordination complexes. In particular, the absorption spectra and the  $T_1$  energies have been investigated *via* DFT-based methods for three novel  $\beta$ -diketone ligands, in which a thienyl group and the following PAH are present as substituents: naphthyl (**L1**), phenanthryl (**L2**) and pyrenyl (**L3**). The B3LYP geometries and

modelled absorption spectra are in excellent agreement with the X-ray crystallographic data and UV-Vis measurements, respectively. Calculations show that the nature of the absorption spectra is significantly different for **L1**, **L2**, and **L3** thus highlighting the need to consider both the vibronic contribution (**L1** and **L2**) and the presence of different rotational isomers (**L3**). Two distinct TD-DFT approaches (VT and AT) have been compared to estimate the  $T_1$  energies. The VT and AT pathways provide essentially indistinguishable results for **L1** and **L2**, while a marked difference characterizes the **L3** outcomes, *i.e.*, when the overlap between the  $S_0$  and  $T_1$  geometries significantly decreases.

The outcomes herein reported have been obtained for the isolated ligands but they can be straightforwardly extended to their  $\text{Ln}^{3+}$  complexes. The assumption of considering the  $T_1$  energy being substantially unaffected upon moving from the isolated ligand to the complex is crucial from both a computational and an experimental point of view. In fact, it must be noted that calculating a ligand-centred triplet state in a complex featuring a lanthanide ion with many unpaired electrons can prove to be extremely challenging with DFT-based methods. The possibility of reducing the complexity of the problem allows us to carry out these calculations with more accurate methods. Thus, in principle, the relative simplicity of DFT calculations on small molecules will allow us to easily determine and screen the triplet energies of several antenna ligands. In this way, experimentalists would have access to valuable information in order to design and then drive synthetic efforts towards luminescent systems with well-tailored and tuneable properties.

## Conflicts of interest

There are no conflicts to declare.

## Acknowledgements

The Computational Chemistry Community (C3P) of the University of Padova is kindly acknowledged. This work was supported by the University of Padova (Grant P-DISC#CARL-SID17 BIRD2017-UNIPD, Project CHIRON). Dr R. Seraglia is acknowledged for mass spectrometry measurements of the  $\text{Gd}^{3+}$  sample.

## Notes and references

- V. Fernández-Moreira, B. Song, V. Sivagnanam, A. S. Chauvin, C. D. B. Vandevyver, M. Gijls, I. Hemmilä, H. A. Lehr and J. C. G. Bünzli, *Analyst*, 2010, **135**, 42–52.
- J. C. G. Bünzli and S. V. Eliseeva, *Chem. Sci.*, 2013, **4**, 1939–1949.
- Y. Zhu, W. Huang, J. Rocha, Z. Lin, L. D. Carlos, L. Li, D. Ananias, X. Zhou, C. D. S. Brites and F. A. A. Paz, *Adv. Funct. Mater.*, 2016, **26**, 8677–8684.

- 4 R. Boddula, K. Singh, S. Giri and S. Vaidyanathan, *Inorg. Chem.*, 2017, **56**, 10127–10130.
- 5 K. Singh, R. Boddula and S. Vaidyanathan, *Inorg. Chem.*, 2017, **56**, 9376–9390.
- 6 R. Devi, K. Singh and S. Vaidyanathan, *J. Mater. Chem. C*, 2020, **8**, 8643–8653.
- 7 R. Devi and S. Vaidyanathan, *Dalton Trans.*, 2020, **49**, 6205–6219.
- 8 E. U. Condon and G. H. Shortley, *The theory of atomic spectra*, Cambridge University Press, 1951.
- 9 B. G. Wybourne and L. Smentek, *Optical spectroscopy of lanthanides: magnetic and hyperfine interactions*, CRC press, 2007.
- 10 J. L. McHale, *Molecular spectroscopy*, CRC Press, 2017.
- 11 C. D. S. Brites, P. P. Lima, N. J. O. Silva, A. Millán, V. S. Amaral, F. Palacio and L. D. Carlos, *Nanoscale*, 2012, **4**, 4799–4829.
- 12 J. Rocha, C. D. S. Brites and L. D. Carlos, *Chem. – Eur. J.*, 2016, **22**, 14782–14795.
- 13 C. Bradac, S. F. Lim, H. C. Chang and I. Aharonovich, *Adv. Opt. Mater.*, 2020, **2000183**, 1–29.
- 14 S. V. Eliseeva and J. C. G. Bünzli, *Chem. Soc. Rev.*, 2010, **39**, 189–227.
- 15 J. C. G. Bünzli, *Coord. Chem. Rev.*, 2015, **293–294**, 19–47.
- 16 S. Tobita, M. Arakawa and I. Tanaka, *J. Phys. Chem.*, 1985, **89**, 5649–5654.
- 17 G. A. Crosby, R. E. Whan and J. J. Freeman, *J. Phys. Chem.*, 1962, **66**, 2493–2499.
- 18 W. M. Faustino, O. L. Malta, E. E. S. Teotonio, H. F. Brito, A. M. Simas and G. F. De Sa, *J. Phys. Chem. A*, 2006, **110**, 2510–2516.
- 19 F. Gutierrez, C. Tedeschi, L. Maron, J. P. Daudey, R. Poteau, J. Azema, P. Tisnès and C. Picard, *J. Chem. Soc., Dalton Trans.*, 2004, **4**, 1334–1347.
- 20 F. Gutierrez, C. Tedeschi, L. Maron, J.-P. Daudey, J. Azema, P. Tisnès, C. Picard and R. Poteau, *J. Mol. Struct.: THEOCHEM*, 2005, **756**, 151–162.
- 21 X. Yi, P. Yang, D. Huang and J. Zhao, *Dyes Pigm.*, 2013, **96**, 104–115.
- 22 A. B. Kajjam and S. Vaidyanathan, *J. Photochem. Photobiol., A*, 2018, **350**, 130–141.
- 23 B. Rajamouli, C. S. Dwaraka Viswanath, S. Giri, C. K. Jayasankar and V. Sivakumar, *New J. Chem.*, 2017, **41**, 3112–3123.
- 24 I. V. Krauklis, K. I. Reshetova, O. Y. Podkopaeva and Y. V. Chizhov, *J. Photochem. Photobiol., A*, 2018, **354**, 112–118.
- 25 A. Zhao, W. Cai, X. Yan, H. Zhang, J. Wang and W. Shen, *Photochem. Photobiol. Sci.*, 2019, **18**, 2421–2429.
- 26 T. Biet, T. Cauchy, Q. Sun, J. Ding, A. Hauser, P. Oulevey, T. Bürgi, D. Jacquemin, N. Vanthuyne, J. Crassous and N. Avarvari, *Chem. Commun.*, 2017, **53**, 9210–9213.
- 27 H. Brahim, *J. Lumin.*, 2019, **210**, 96–103.
- 28 S. yeol Baek, S. Y. Kwak, S. T. Kim, K. Y. Hwang, H. Koo, W. J. Son, B. Choi, S. Kim, H. Choi and M. H. Baik, *Nat. Commun.*, 2020, **11**, 1–7.
- 29 A. A. Farcas and A. Bende, *AIP Conf. Proc.*, 2020, **2206**, 030001.
- 30 C. Greco, G. Moro, L. Bertini, M. Biczysko, V. Barone and U. Cosentino, *J. Chem. Theory Comput.*, 2014, **10**, 767–777.
- 31 F. Gutierrez, C. Rabbe, R. Poteau and J. P. Daudey, *J. Phys. Chem. A*, 2005, **109**, 4325–4330.
- 32 W. A. Rabanal-León, D. Páez-Hernández and R. Arratia-Pérez, *Phys. Chem. Chem. Phys.*, 2014, **16**, 25978–25988.
- 33 M. J. Beltrán-Leiva, E. Solis-Céspedes and D. Páez-Hernández, *Dalton Trans.*, 2020, **49**, 7444–7450.
- 34 H. Ullah, A. Rauf, Z. Ullah, Fazl-I-Sattar, M. Anwar, A. H. A. Shah, G. Uddin and K. Ayub, *Spectrochim. Acta, Part A*, 2014, **118**, 210–214.
- 35 K. S. Min, Y. J. Kim, H. J. Ko, D. H. Kwak, T. W. Kim, J. W. Shin and B. G. Kim, *J. Phys. Org. Chem.*, 2014, **27**, 960–966.
- 36 G. Pescitelli, V. Barone, L. Di Bari, A. Rizzo and F. Santoro, *J. Org. Chem.*, 2013, **78**, 7398–7405.
- 37 K. Binnemans, *Handb. Phys. Chem. Rare Earths*, 2005, **35**, 107.
- 38 J. G. Bünzli, *Coord. Chem. Rev.*, 2015, **293–294**, 19–47.
- 39 A. Carlotto, L. Babetto, S. Carlotto, M. Miozzi, R. Seraglia, M. Casarin, G. Bottaro, M. Rancan and L. Armelao, *ChemPhotoChem*, 2020, **4**, 674–684.
- 40 ADF2013.01 Program, SCM, Theoretical Chemistry, Vrije Universiteit, Amsterdam, The Netherlands, <http://www.scm.com>.
- 41 G. te Velde, F. M. Bickelhaupt, E. J. Baerends, C. Fonseca Guerra, S. J. A. van Gisbergen, J. G. Snijders and T. Ziegler, *J. Comput. Chem.*, 2001, **22**, 931–967.
- 42 C. Fonseca Guerra, J. G. Snijders, G. te Velde and E. J. Baerends, *Theor. Chem. Acc.*, 1998, **99**, 391–403.
- 43 C. Lee, W. Yang and R. G. Parr, *Phys. Rev. B: Condens. Matter Mater. Phys.*, 1988, **37**, 785–789.
- 44 S. H. Vosko, L. Wilk and M. Nusair, *Can. J. Phys.*, 1980, **58**, 1200–1211.
- 45 P. J. Stephens, F. J. Devlin, C. F. N. Chabalowski and M. J. Frisch, *J. Phys. Chem.*, 1994, **98**, 11623–11627.
- 46 A. D. Becke, *J. Chem. Phys.*, 1993, **98**, 5648–5652.
- 47 M. Seth, G. Mazur and T. Ziegler, *Theor. Chem. Acc.*, 2011, **129**, 331–342.
- 48 L. Versluis and T. Ziegler, *J. Chem. Phys.*, 1988, **88**, 322–328.
- 49 C. C. Pye and T. Ziegler, *Theor. Chem. Acc.*, 1999, **101**, 396–408.
- 50 S. Grimme, S. Ehrlich and L. Goerigk, *J. Comput. Chem.*, 2011, **32**, 1456–1465.
- 51 S. J. A. van Gisbergen, J. G. Snijders and E. J. Baerends, *Comput. Phys. Commun.*, 1999, **118**, 119–138.
- 52 A. Rosa, E. J. Baerends, S. J. A. van Gisbergen, E. van Lenthe, J. A. Groeneveld and J. G. Snijders, *J. Am. Chem. Soc.*, 1999, **121**, 10356–10365.
- 53 O. V. Gritsenko, P. R. T. Schipper and E. J. Baerends, *Chem. Phys. Lett.*, 1999, **302**, 199–207.
- 54 P. R. T. Schipper, O. V. Gritsenko, S. J. A. van Gisbergen and E. J. Baerends, *J. Chem. Phys.*, 2000, **112**, 1344–1352.

- 55 J. S. Seldenthuis, H. S. J. van der Zant, M. A. Ratner and J. M. Thijssen, *ACS Nano*, 2008, **2**, 1445–1451.
- 56 J. Franck and E. G. Dymond, *Trans. Faraday Soc.*, 1926, **21**, 536–542.
- 57 E. Condon, *Phys. Rev.*, 1926, **28**, 1182–1201.
- 58 E. U. Condon, *Phys. Rev.*, 1928, **32**, 858–872.
- 59 M. J. Beltrán-Leiva, P. Cantero-López, C. Zúñiga, A. Bulhões-Figueira, D. Páez-Hernández and R. Arratia-Pérez, *Inorg. Chem.*, 2017, **56**, 9200–9208.
- 60 M. J. Beltrán-Leiva, D. Páez-Hernández and R. Arratia-Pérez, *Inorg. Chem.*, 2018, **57**, 5120–5132.
- 61 Z. Abbas, S. Dasari, M. J. Beltrán-Leiva, P. Cantero-López, D. Páez-Hernández, R. Arratia-Pérez, R. J. Butcher and A. K. Patra, *New J. Chem.*, 2019, **43**, 15139–15152.
- 62 HOMO and LUMO acronyms stand for Highest Occupied MO and Lowest Unoccupied MO, respectively.
- 63 D. Jacquemin, E. A. Perpète, I. Ciofini and C. Adamo, *J. Chem. Theory Comput.*, 2010, **6**, 1532–1537.



# Antenna triplet DFT calculations to drive the design of luminescent Ln<sup>3+</sup> complexes.

Luca Babetto,<sup>a</sup> Silvia Carlotto<sup>a,b\*</sup> Alice Carlotto,<sup>a</sup> Marzio Rancan,<sup>b</sup> Gregorio Bottaro,<sup>b</sup> Lidia Armelao<sup>a,b</sup> and Maurizio Casarin<sup>a,b\*</sup>

<sup>a</sup>Dipartimento di Scienze Chimiche, Università degli Studi di Padova, via F. Marzolo 1, 35131 Padova, Italy.

<sup>b</sup> Institute of Condensed Matter Chemistry and Technologies for Energy (ICMATE), National Research Council (CNR), c/o Department of Chemistry, University of Padova, via F. Marzolo 1, 35131 Padova, Italy

## 1. ANTENNA EFFECT

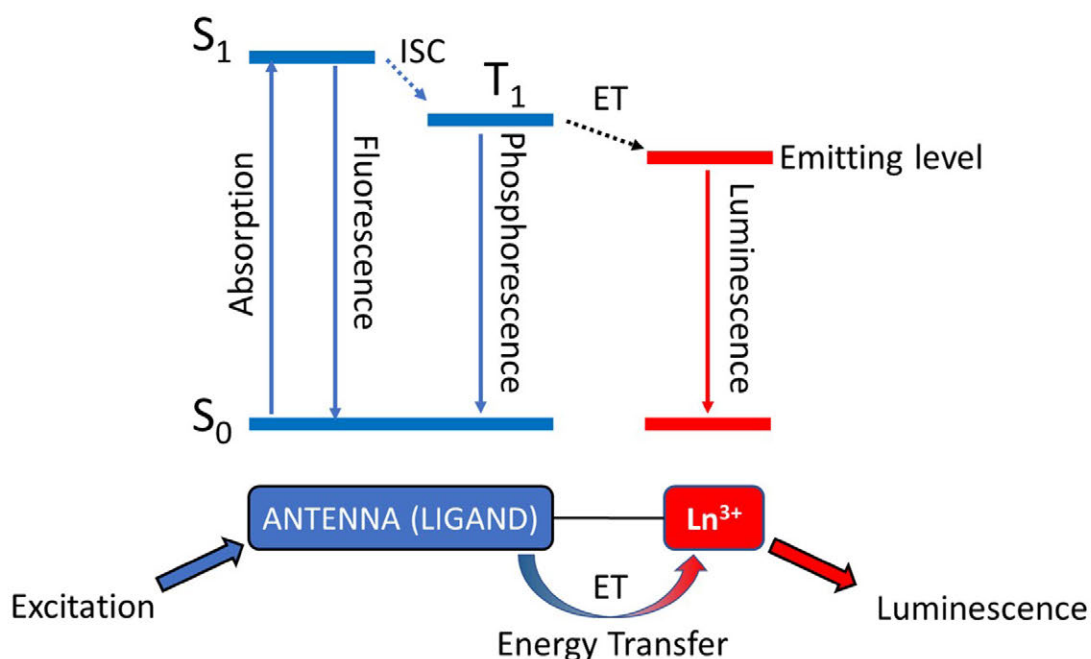


**Figure S1.** Energy level diagram illustrating the antenna effect. In blue the antenna processes and in red the Ln<sup>3+</sup> one. ISC is the intersystem crossing process. S and T designates levels with singlet and triplet multiplicity, respectively.

## 2. SYNTHESSES

Reagents were purchased from Aldrich and used as received. The elemental analyses were carried out with a Flash 2000 Thermo Scientific Analyzer at the Department of Chemical Sciences of the University of Padova.

**Syntheses of L1 and L2.** The ligands 1-(naphthalen-3-yl)-3-(thiophen-2-yl)propane-1,3-dione (**L1**) and 1-(phenanthren-3-yl)-3-(thiophen-2-yl)propane-1,3-dione (**L2**) were synthesized and characterized as reported in literature.<sup>1</sup>

**Synthesis of (2Z)-3-hydroxy-3-(pyren-1-yl)-1-(thiophen-2-yl)prop-2-en-1-one (L3).** The Claisen condensation was performed under argon in dry THF. Potassium *tert*-butoxide (1.12 g, 10 mmol) was added to a THF (22 ml) solution of 1-acetylpyrene (1.85 g, 7.5 mmol) and ethyl-2-thiophenecarboxylate (1.74 g, 11 mmol). The resulting solution turned to dark-red and was stirred for 18 days at 40-50°C. After cooling, the crude was acidified with 30 ml of 10% HCl. The product was extracted with dichloromethane to give a red-brown solution and dried over MgSO<sub>4</sub>. The crude product was purified by recrystallization (6 times) from DCM/hexane (1:3). Yield: 48%. ESI-MS (negative ions, MeOH): *m/z* 353.23 [L3-H]

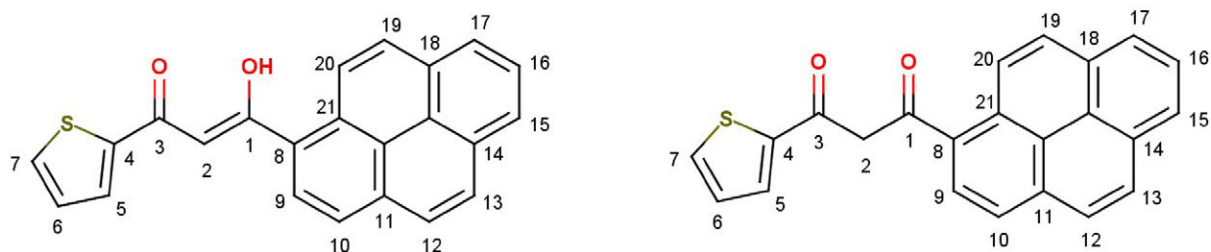


**Figure S2.** Ligand L3, keto enol (left) and diketone (right) tautomers.

<sup>1</sup>H NMR (CDCl<sub>3</sub>, 400 MHz, T = 25 °C) Keto enol tautomer (~96%), δ [ppm] = 6.69 (1H, s, H<sub>2</sub>), 7.17 (1H, dd, <sup>3</sup>J<sub>H<sub>6</sub>,H<sub>7</sub></sub> = 5.1 Hz, <sup>3</sup>J<sub>H<sub>6</sub>,H<sub>5</sub></sub> = 3.9 Hz, H<sub>6</sub>), 7.65 (1H, dd, <sup>3</sup>J<sub>H<sub>7</sub>,H<sub>6</sub></sub> = 5.0 Hz, <sup>4</sup>J<sub>H<sub>7</sub>,H<sub>5</sub></sub> = 1.1 Hz, H<sub>7</sub>), 7.81 (1H, dd, <sup>3</sup>J<sub>H<sub>5</sub>,H<sub>6</sub></sub> = 3.9 Hz, <sup>4</sup>J<sub>H<sub>5</sub>,H<sub>7</sub></sub> = 1.1 Hz, H<sub>5</sub>) 7.99-8.32 (ov, 8H, m, H<sub>10</sub>, H<sub>12</sub>, H<sub>13</sub>, H<sub>15</sub>, H<sub>16</sub>, H<sub>17</sub>, H<sub>19</sub>, H<sub>20</sub>), 8.79 (1H, d, <sup>3</sup>J<sub>H<sub>20</sub>,H<sub>19</sub></sub> = 9.2 Hz, H<sub>9</sub>), 16.55 (1H, s, OH). Diketone tautomer (~4%), δ [ppm] = 4.83 (2H, s, H<sub>2</sub>), 7.13 (1H, dd, <sup>3</sup>J<sub>H<sub>6</sub>,H<sub>7</sub></sub> = 5.0 Hz, <sup>3</sup>J<sub>H<sub>6</sub>,H<sub>5</sub></sub> = 3.8 Hz, H<sub>6</sub>), 7.63 (1H, dd, <sup>3</sup>J<sub>H<sub>7</sub>,H<sub>6</sub></sub> = 5.0 Hz, <sup>4</sup>J<sub>H<sub>7</sub>,H<sub>5</sub></sub> = 1.2 Hz, H<sub>7</sub>), 7.88 (1H, dd, <sup>3</sup>J<sub>H<sub>5</sub>,H<sub>6</sub></sub> = 3.8 Hz, <sup>4</sup>J<sub>H<sub>5</sub>,H<sub>7</sub></sub> = 1.2 Hz, H<sub>5</sub>) 7.99-8.34 (ov, 9H, m, H<sub>9</sub>, H<sub>10</sub>, H<sub>12</sub>, H<sub>13</sub>, H<sub>15</sub>, H<sub>16</sub>, H<sub>17</sub>, H<sub>19</sub>, H<sub>20</sub>). <sup>13</sup>C-NMR (CDCl<sub>3</sub>, 100 MHz, T = 25 °C) Keto enol tautomer δ [ppm] = 99.33, 124.83, 124.99, 126.30, 126.46, 126.53, 126.73, 127.54, 128.74, 129.26, 129.52, 130.89, 133.12 (CH), 124.80, 125.26, 129.41, 130.66, 130.98, 131.52, 133.64, 142.30 (C), 182.37, 185.51 (C=O, C-OH)

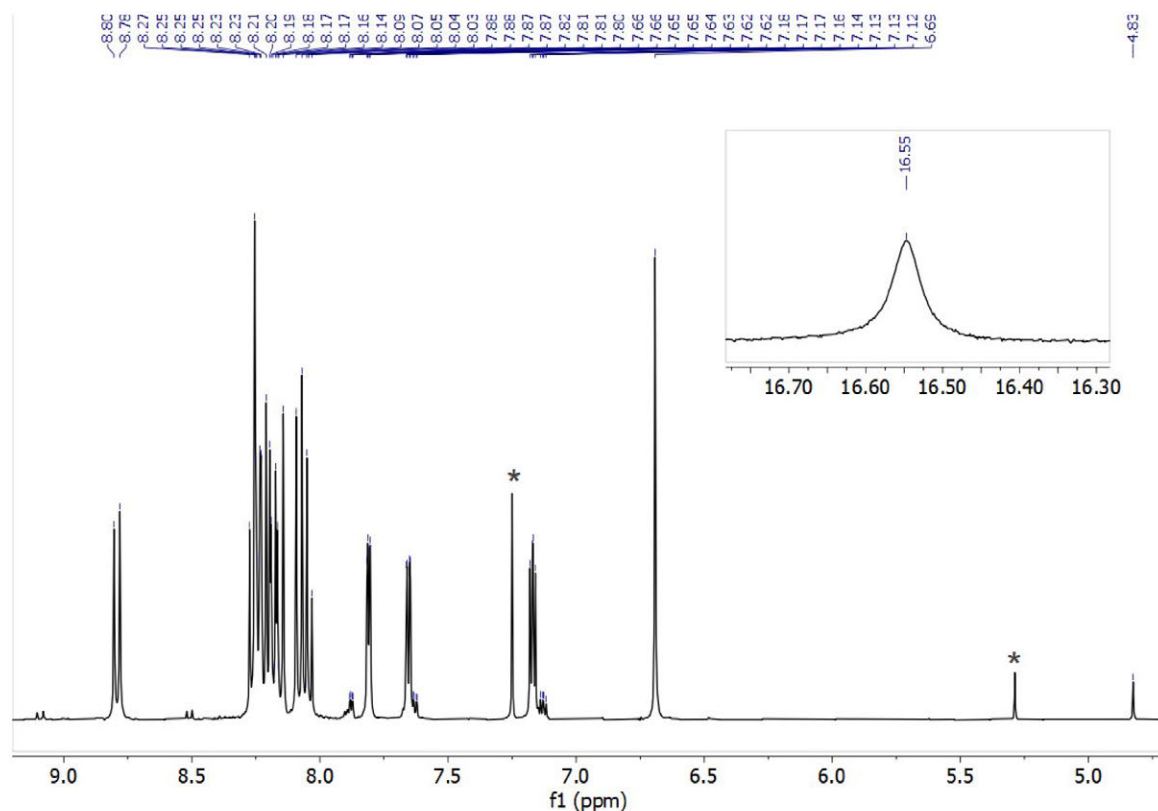


**Figure S3.** <sup>1</sup>H-NMR of ligand L3 in CDCl<sub>3</sub>. Inset: OH signal. Solvent signals are marked with an asterisk.

## 2.2 Complexes syntheses.

**Synthesis of [Gd(L3)<sub>3</sub>(EtOH)<sub>2</sub>] (Gd3).** An ethanol solution (2.5 ml) of Gd(NO<sub>3</sub>)<sub>3</sub>·6H<sub>2</sub>O (32.6 mg, 0.07 mmol) was added dropwise to a hot ethanol solution (3.5 ml) of L3 (77.4 mg, 0.22 mmol) and TEAOH solution 25 % wt (170 μl, 0.26 mmol). A yellow powder precipitated, the mixture was stirred and heated at 75 °C for overnight. The yellow powder was recovered by centrifugation and washed with cold EtOH. Yield: 60 %. LDI-MS (positive ions): *m/z* 1256.43 [Gd(L3)<sub>3</sub>+K]<sup>+</sup>, 1240.49 [Gd(L3)<sub>3</sub>+Na]<sup>+</sup>. Elemental analysis for GdC<sub>73</sub>H<sub>51</sub>O<sub>8</sub>S<sub>3</sub>: calculated C 66.95 %, H 3.93 %, S 7.35 %; found: C 67.02 %, H 3.99 %, S 7.42 %.

## 3. MASS SPECTROMETRY ANALYSIS

### *Electrospray mass spectrometric measurements – instrumental setup*

Electrospray mass spectrometric measurements (ESI/MS) were performed using a LCQ Fleet ion trap instrument (ThermoFisher), operating in negative ion mode. The entrance capillary temperature and voltage were 280°C and 4 kV, respectively. Sample (L3) solutions (10<sup>-6</sup> M in methanol) was introduced by direct infusion using a syringe pump at a flow rate of 8 μL×min<sup>-1</sup>.

### *LDI mass spectrometric measurements – instrumental setup*

LDI/MS measurements were performed using a MALDI/TOF/TOF UltrafleXtreme instrument (Bruker Daltonics, Bremen, Germany), equipped with a 1 kHz smartbeam II laser (λ= 355 nm) and operating in the reflectron positive ion mode. The instrumental conditions were: IS1 = 25 kV; IS2 = 22.4 kV; reflectron potential = 26.3 kV; delay time = 120 nsec.

External mass calibration (Peptide Calibration Standard) was based on monoisotopic values of [M+H]<sup>+</sup> of angiotensin II, angiotensin I, substance P, bombesin, ACTH clip (1-17), ACTH clip (18-39), somatostatin 28 at *m/z* 1046.5420, 1296.6853, 1347.7361, 1619.8230, 2093.0868, 2465.1990 and 3147.4714, respectively.

1 mL of acetonitrile (Gd3) sample solution was deposited on the stainless-steel sample holder and allowed to dry before introducing into the mass spectrometer.

## 4. SINGLE CRYSTAL X-RAY DIFFRACTION

Mo Kα (λ = 0.71073 Å) radiation was used for L1 and Cu Kα (λ = 1.54184 Å) for L2 and L3. Data were collected at room temperature by means of the ω - scans technique using graphite–monochromated radiation. The diffraction intensities were corrected for Lorentz and polarization effects and were also optimized with respect to absorption. Empirical multi-scan absorption corrections using equivalent reflections were performed with the scaling algorithm SCALE3 ABSPACK. Data collection, data reduction and finalization were carried out through the CrysAlisPro software. Structures were solved with the ShelXT<sup>2</sup> program by Intrinsic Phasing and refined with the ShelXL<sup>3</sup> package using least squares minimisation, in the framework of Olex2 software.<sup>4</sup> In the last cycles of refinement, non-hydrogen atoms were refined anisotropically.

L1 was treated as an inversion twin with TWIN instruction of SHELX was applied (BASf 0.2). For L2 and L3 in the thienyl moiety the rotation of the ring by 180° could not be neglected. These fragments were splitted in two parts the occupancies of which were constrained to sum to 1. DFIX, SADI and FLAT restrains have been applied to better model the fragments. EADP constrain has been applied to selected atoms. Crystallographic data and refining details are available in Table S1 in the CIF files deposited with the Cambridge Crystallographic Data Centre as supplementary publication (CCDC 1998680-1998682).

**Table S1.** Crystal data and structure refinement for L1, L2 and L3.

Identification code	L1	L2	L3
Empirical formula	C <sub>17</sub> H <sub>12</sub> O <sub>2</sub> S	C <sub>21</sub> H <sub>14</sub> O <sub>2</sub> S	C <sub>23</sub> H <sub>14</sub> O <sub>2</sub> S
Formula weight	280.33	330.38	354.40
Temperature/K	299.3(2)	297.3(5)	297.6(6)
Crystal system	orthorhombic	orthorhombic	triclinic

Space group	Pca2 <sub>1</sub>	P2 <sub>1</sub> 2 <sub>1</sub> 2 <sub>1</sub>	P-1
a/Å	8.7457(4)	6.32131(13)	9.1371(3)
b/Å	6.3938(2)	12.7658(3)	10.1916(3)
c/Å	23.9293(9)	20.1479(5)	10.4736(3)
α/°	90	90	78.929(3)
β/°	90	90	65.508(3)
γ/°	90	90	71.717(3)
Volume/Å <sup>3</sup>	1338.08(9)	1625.87(6)	840.58(5)
Z	4	4	2
ρ <sub>calc</sub> /cm <sup>3</sup>	1.392	1.350	1.400
μ/mm <sup>-1</sup>	0.239	1.839	1.821
F(000)	584.0	688.0	368.0
Crystal size/mm <sup>3</sup>	0.3 × 0.25 × 0.15	0.35 × 0.23 × 0.02	0.3 × 0.2 × 0.15
Radiation	MoKα (λ = 0.71073)	CuKα (λ = 1.54184)	CuKα (λ = 1.54184)
2θ range for data collection/°	6.372 to 56.56	8.2 to 145.486	9.162 to 145.616
Index ranges	-11 ≤ h ≤ 11, -8 ≤ k ≤ 8, -31 ≤ l ≤ 31	-7 ≤ h ≤ 7, -15 ≤ k ≤ 15, -24 ≤ l ≤ 24	-10 ≤ h ≤ 11, -12 ≤ k ≤ 12, -12 ≤ l ≤ 12
Reflections collected	15330	13259	9770
Independent reflections	3308 [R <sub>int</sub> = 0.0219, R <sub>sigma</sub> = 0.0170]	3233 [R <sub>int</sub> = 0.0241, R <sub>sigma</sub> = 0.0209]	3339 [R <sub>int</sub> = 0.0193, R <sub>sigma</sub> = 0.0217]
Data/restraints/parameters	3308/1/183	3233/28/226	3339/54/255
Goodness-of-fit on F <sup>2</sup>	1.068	1.042	1.062
Final R indexes [I ≥ 2σ (I)]	R <sub>1</sub> = 0.0329, wR <sub>2</sub> = 0.0876	R <sub>1</sub> = 0.0358, wR <sub>2</sub> = 0.0993	R <sub>1</sub> = 0.0433, wR <sub>2</sub> = 0.1276
Final R indexes [all data]	R <sub>1</sub> = 0.0357, wR <sub>2</sub> = 0.0899	R <sub>1</sub> = 0.0387, wR <sub>2</sub> = 0.1022	R <sub>1</sub> = 0.0486, wR <sub>2</sub> = 0.1344
Largest diff. peak/hole / e Å <sup>-3</sup>	0.18/-0.21	0.17/-0.20	0.21/-0.18
Flack parameter	Inversion Twin (BASF 0.2)	0.014(9)	---
CCDC	1998680	1998681	1998682

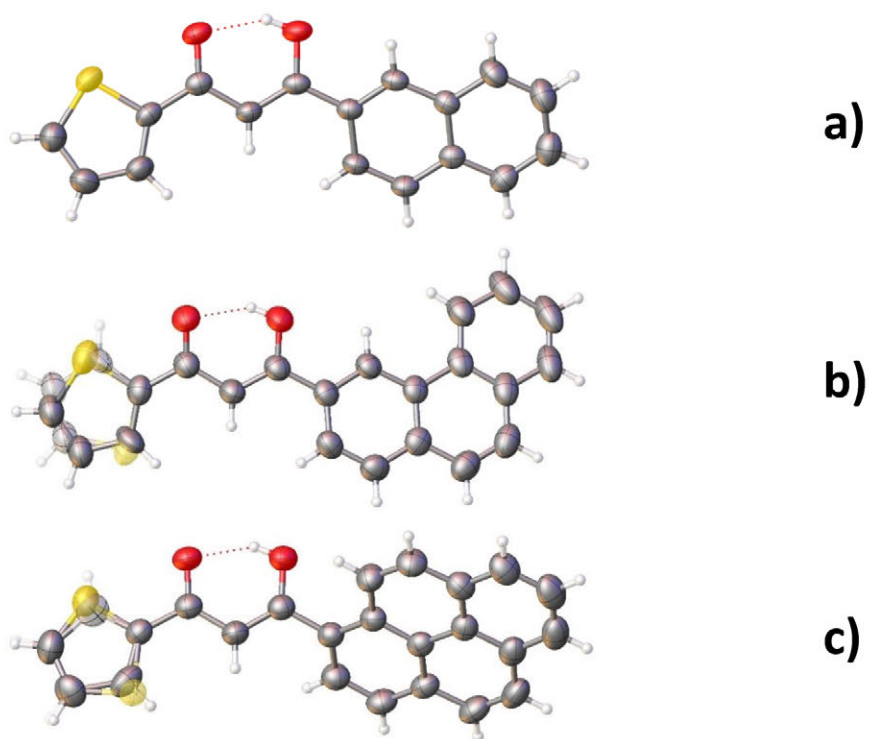


**Figure S4.** SCXRD structure of **L1** (a), **L2** (b) and **L3** (c). Colour code: C grey, O red, S yellow. Thermal ellipsoids are drawn at the 50% probability level. Disordered parts translucent.

## 5. LIGAND GEOMETRIES

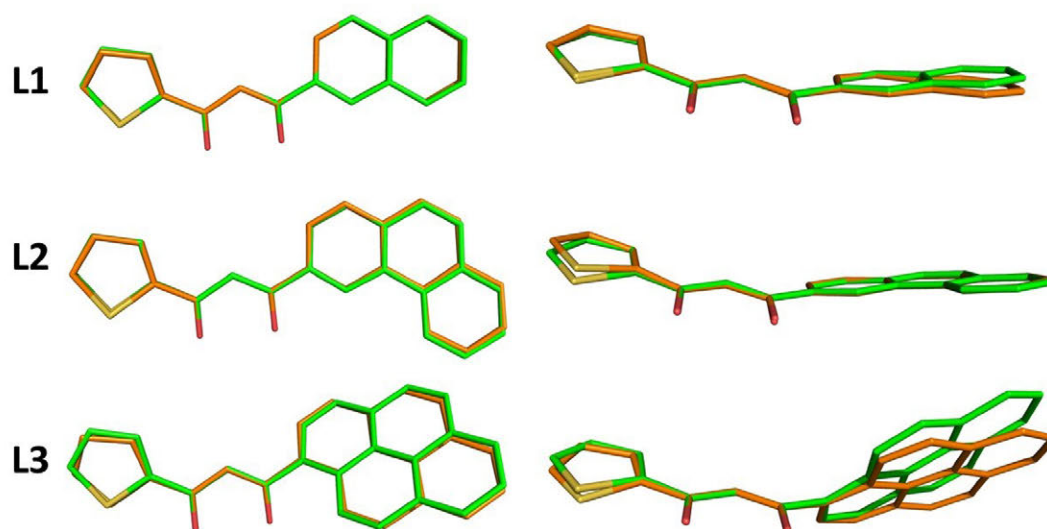


**Figure S5.** Comparison between the B3LYP (green) and experimental (orange) structures of the ligands.

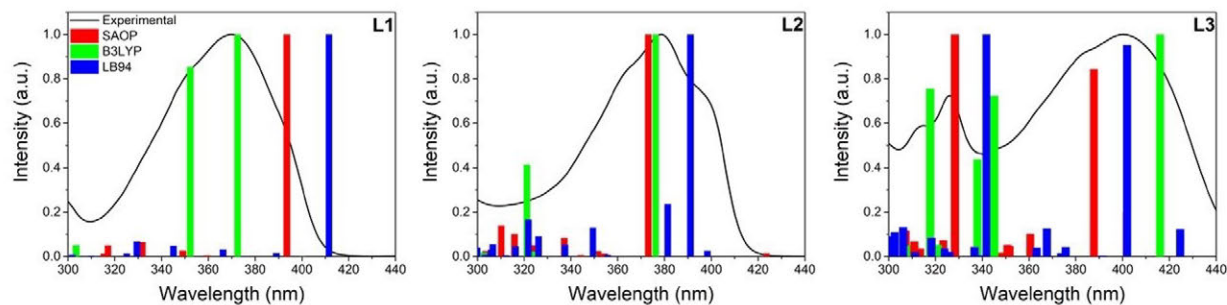
**Table S2.** Theoretical abundance of the diverse rotamers in **L1**, **L2**, and **L3** in toluene. The energy differences (kcal/mol) with respect to the most stable rotamer are reported in parentheses.

	A	B	C	D
<b>L1</b>	61%	12% (+0.96)	21% (+0.62)	5% (+1.43)
<b>L2</b>	62%	17% (+0.77)	17% (+0.78)	4% (+1.56)
<b>L3</b>	33% (+0.25)	7% (+1.15)	50%	10% (+0.95)

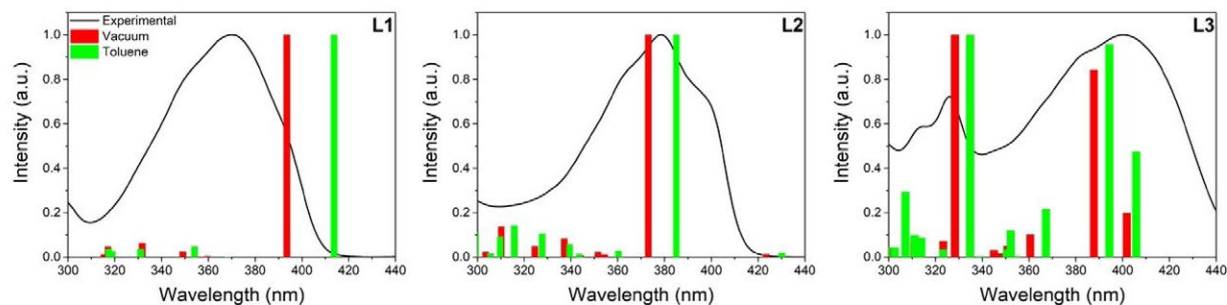
**Table S3.** Theoretical abundance of the diverse rotamers in **L1**, **L2**, and **L3** with the inclusion of dispersion corrections in vacuum. The energy differences (kcal/mol) with respect to the most stable rotamer are reported in parentheses.

	A	B	C	D
<b>L1</b>	51%	21% (+0.53)	19% (+0.59)	10% (+0.97)
<b>L2</b>	42%	26% (+0.28)	21% (+0.41)	11% (+0.78)
<b>L3</b>	13% (+0.94)	5% (+1.47)	62%	21% (+0.65)

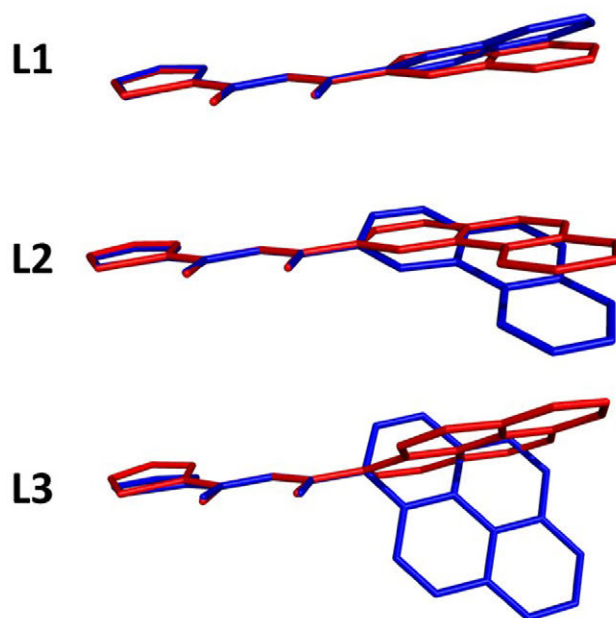
## 6. UV-VIS ABSORPTION AND PHOTOLUMINESCENCE SPECTROSCOPIES



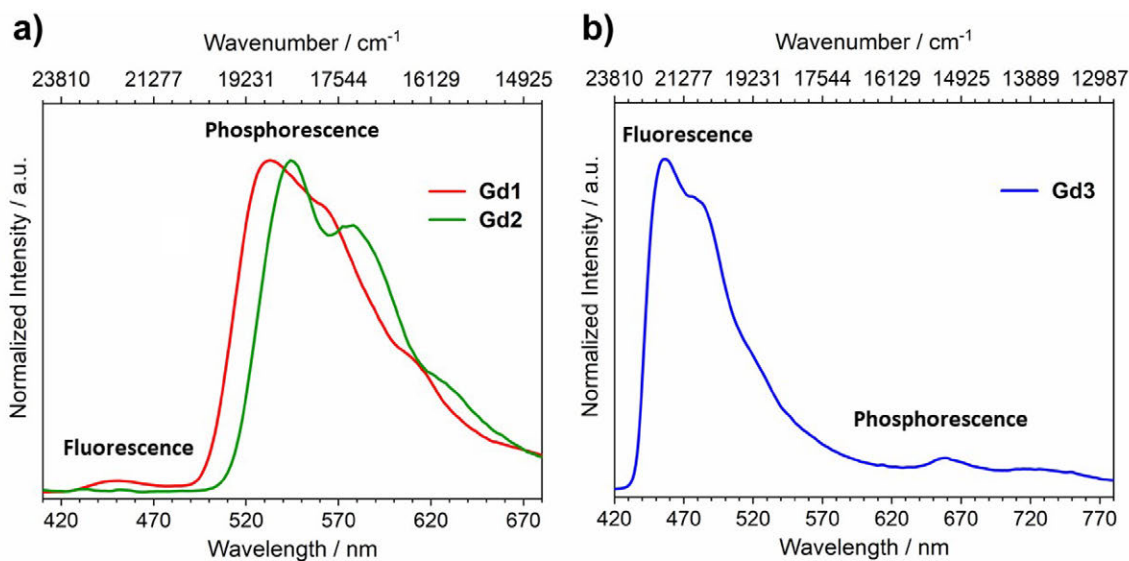
**Figure S6.** Comparison between calculated vertical excitation energies on the rotamer A for **L1** (a), **L2** (b) and **L3** (c) with different functionals (SAOP, LB94, B3LYP). The ground state geometries have been optimized at B3LYP level of theory.



**Figure S7.** Comparison between calculated vertical excitation energies on the rotamer A for **L1** (a), **L2** (b) and **L3** (c) with SAOP in vacuum and in solvent (toluene). The ground state geometries have been optimized at B3LYP level of theory.



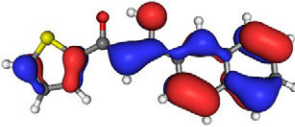
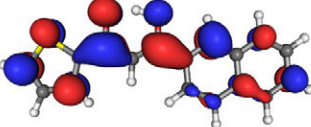
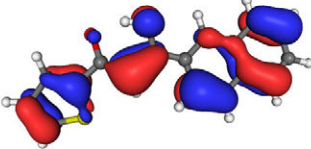
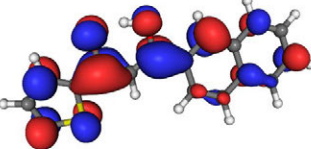
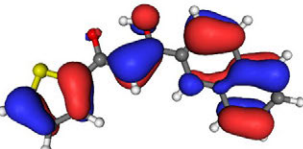
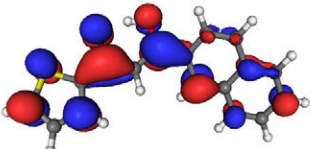
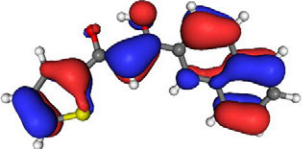
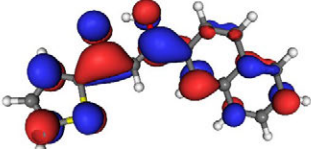
**Figure S8.** Comparison between the ground state  $S_0$  (blue) and excited singlet state  $S_1$  (red) structures of the ligands **L1**, **L2**, and **L3** calculated at the B3LYP level of theory for rotamer A. For **L3** the calculated Franck-Condon factors are zero due to the significantly different geometries of the two states.



**Figure S9.** Phosphorescence spectra recorded at 77 K of gadolinium complexes embedded in polystyrene thin film (*ca.* 2  $\mu\text{m}$  thick): a) **Gd1** and **Gd2** with a 300  $\mu\text{s}$  delay after the excitation pulse ( $\lambda_{\text{ex}}$  = 370 nm); b) **Gd3** ( $\lambda_{\text{ex}}$  = 380 nm) recorded using a continuous light source (Xe lamp). Inset: zoom of the spectrum in the phosphorescence region (610-730 nm).

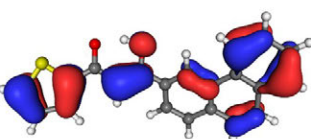
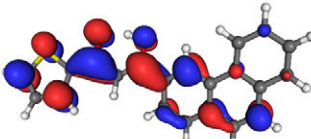
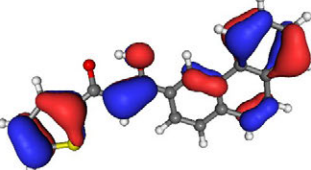
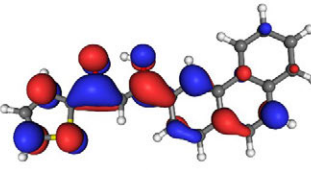
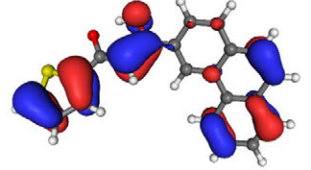
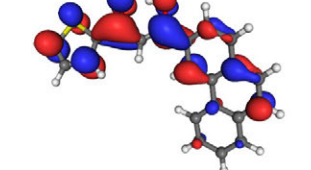
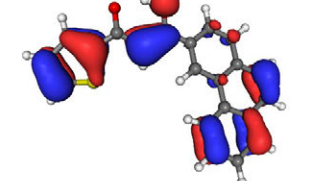
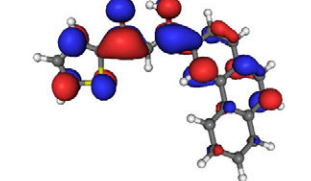
## 7. TD-DFT ABSORPTION SPECTRA

**Table S4.** Most relevant TD-DFT/SAOP UV-Vis electronic transitions for the rotamers A, B, C, and D of ligand **L1**. Intensities are weighted by the relative abundance of the rotamer. Only transitions in the 300 – 480 nm range with normalized intensities higher than 20% of the most intense transition for each form have been included.  $MO_i$  and  $MO_f$  are the initial and the final MOs involved in the transition. Components accounting for less than 10% are neglected. Graphical representations of the orbitals involved in the predominant transition are reported.

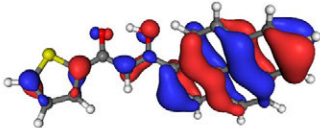
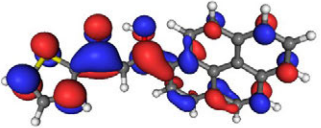
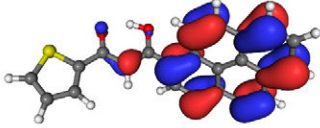
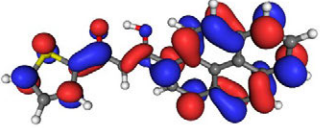
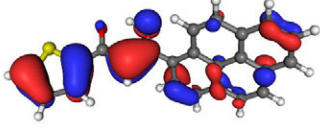
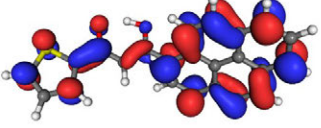
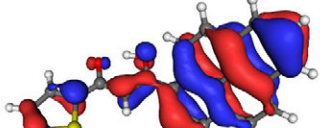
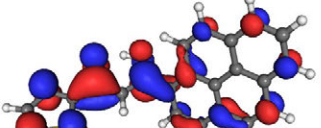
transition	wavelength (nm)	weighted intensity	$MO_i \rightarrow MO_f$	$MO_i$	$MO_f$
2A	394	0.50	H-1 $\rightarrow$ L (52%) H $\rightarrow$ L (38%)		
2B	382	0.19	H-1 $\rightarrow$ L (63%) H $\rightarrow$ L (27%)		
2C	378	0.22	H-1 $\rightarrow$ L (62%) H $\rightarrow$ L (22%)		
2D	380	0.09	H-1 $\rightarrow$ L (66%) H $\rightarrow$ L (20%)		

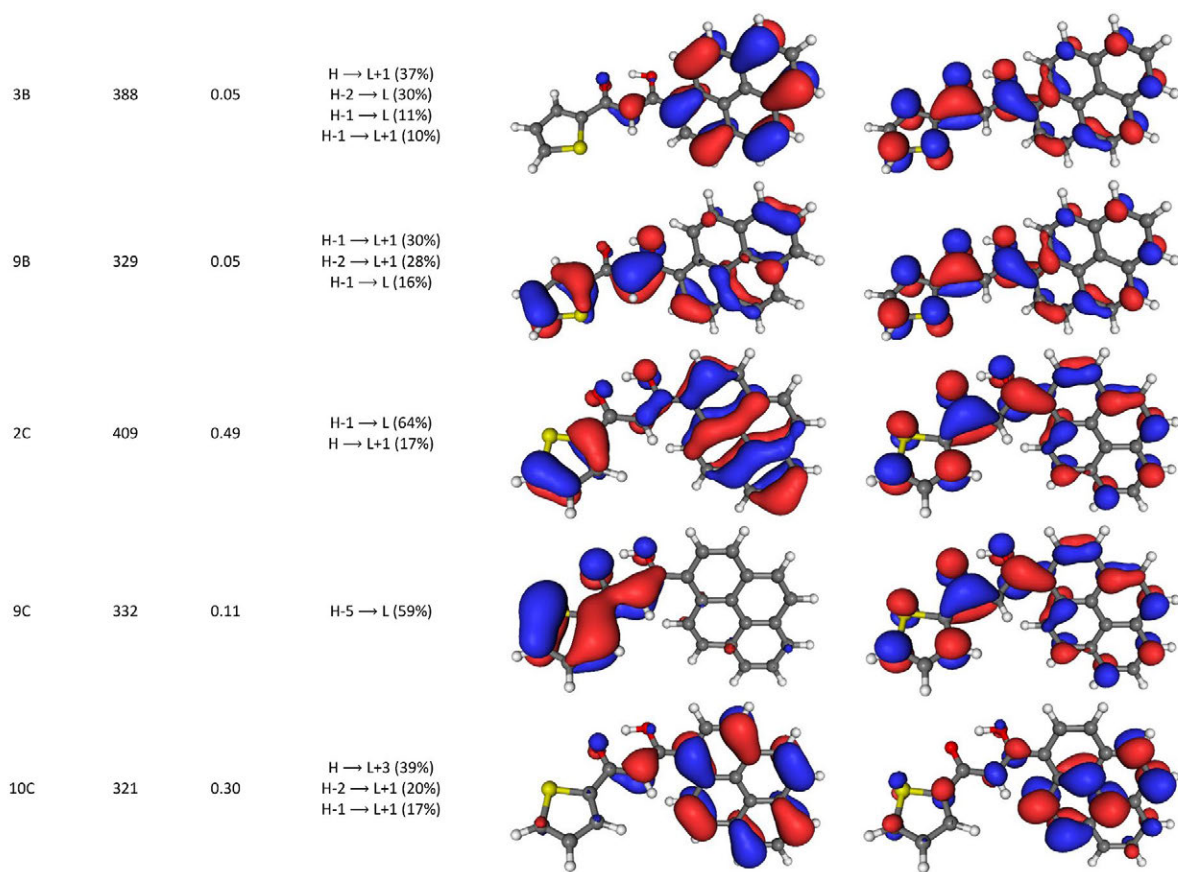


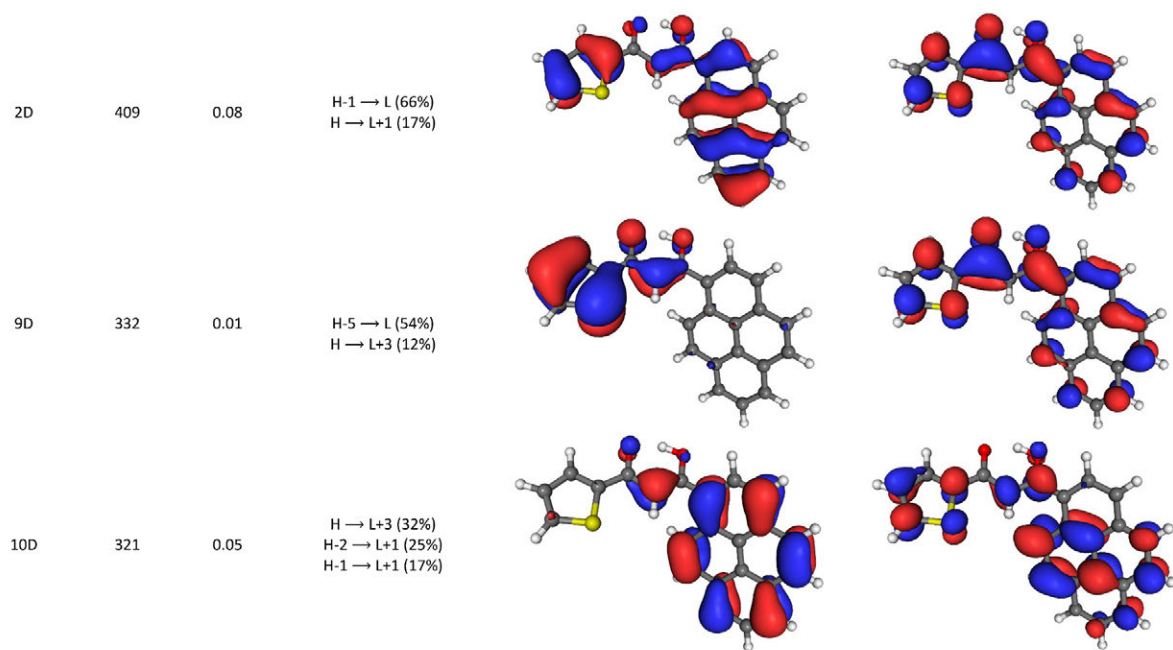
**Table S5.** Most relevant TD-DFT/SAOP UV-Vis electronic transitions for the rotamers A, B, C, and D of ligand **L2**. Intensities are weighted by the relative abundance of the rotamer. Only transitions in the 300 – 480 nm range with normalized intensities higher than 20% of the most intense transition for each form have been included.  $MO_i$  and  $MO_f$  are the initial and the final MOs involved in the transition. Components accounting for less than 10% are neglected. Graphical representations of the orbitals involved in the predominant transition are reported.

transition	wavelength (nm)	weighted intensity	$MO_i \rightarrow MO_f$	$MO_i$	$MO_f$
3A	398	0.49	H-2 $\rightarrow$ L (66%) H $\rightarrow$ L+1 (12%) H $\rightarrow$ L (10%)		
3B	400	0.24	H-2 $\rightarrow$ L (70%) H $\rightarrow$ L (10%)		
3C	398	0.19	H-2 $\rightarrow$ L (66%) H $\rightarrow$ L+1 (16%) H $\rightarrow$ L (10%)		
3D	399	0.08	H-2 $\rightarrow$ L (70%) H $\rightarrow$ L+1 (15%)		

**Table S6.** Most relevant TD-DFT/SAOP UV-Vis electronic transitions for the rotamers A, B, C, and D of ligand **L3**. Intensities are weighted by the relative abundance of the rotamer. Only transitions in the 300 – 480 nm range with normalized intensities higher than 20% of the most intense transition for each form have been included.  $MO_i$  and  $MO_f$  are the initial and the final MOs involved in the transition. Components accounting for less than 10% are neglected. Graphical representations of the orbitals involved in the predominant transition are reported.

transition	wavelength (nm)	weighted intensity	$MO_i \rightarrow MO_f$	$MO_i$	$MO_f$
2A	402	0.05	H-2 $\rightarrow$ L (61%) H-1 $\rightarrow$ L (28%)		
3A	388	0.23	H $\rightarrow$ L+1 (37%) H-2 $\rightarrow$ L (23%) H-1 $\rightarrow$ L (17%) H-1 $\rightarrow$ L+1 (13%)		
9A	328	0.27	H-1 $\rightarrow$ L+1 (28%) H-1 $\rightarrow$ L (25%) H-2 $\rightarrow$ L+1 (15%) H-6 $\rightarrow$ L (11%)		
2B	402	0.01	H-2 $\rightarrow$ L (48%) H-1 $\rightarrow$ L (38%)		





## 8. REFERENCES

1. Carlotto, A.; Babetto, L.; Carlotto, S.; Miozzi, M.; Seraglia, R.; Casarin, M.; Bottaro, G.; Rancan, M.; Armelao, L., *ChemPhotoChem*, **2020**, *4*, 674–684.
2. G. M. Sheldrick, *Acta Cryst.* **2015**, *A71*, 3.
3. G. M. Sheldrick, *Acta Cryst.* **2015**, *C71*, 3.
4. O. V. Dolomanov, L. J. Bourhis, R. J. Gildea, J. A. K. Howard, H. Puschmann, *J. Appl. Crystallogr.* **2009**, *42*, 339.

# Multireference *Ab Initio* Investigation on Ground and Low-Lying Excited States: Systematic Evaluation of $J$ – $J$ Mixing in a $\text{Eu}^{3+}$ Luminescent Complex

Luca Babetto, Silvia Carlotto,\* Alice Carlotto, Marzio Rancan, Gregorio Bottaro, Lidia Armelao, and Maurizio Casarin\*

Cite This: *Inorg. Chem.* 2021, 60, 315–324

Read Online

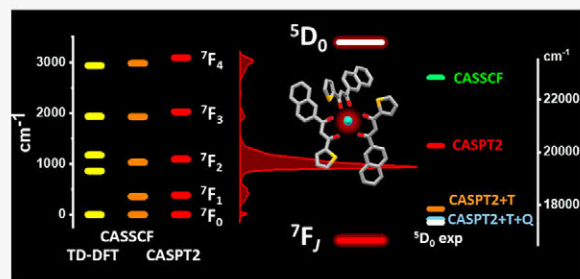
ACCESS |

Metrics & More

Article Recommendations

Supporting Information

**ABSTRACT:** A theoretical protocol combining density functional theory (DFT) and multireference (CAS) calculations is proposed for a  $\text{Eu}^{3+}$  complex. In the complex, electronic levels of the central  $\text{Eu}^{3+}$  ion are correctly calculated at the CASPT2 level of theory, and the effect of introducing different numbers of states in the configuration interaction matrices is highlighted as well as the shortcomings of DFT methods in the treatment of systems with high spin multiplicity and strong spin–orbit coupling effects. For the  $^5\text{D}_0$  state energy calculation, the inclusion of states with different multiplicity and the number of states considered for each multiplicity are crucial parameters, even if their relative weight is different. Indeed, the addition of triplet and singlets is important, while the number of states is relevant only for the quintets. The herein proposed protocol enables a rigorous, full *ab initio* treatment of  $\text{Eu}^{3+}$  complex, which can be easily extended to other  $\text{Ln}^{3+}$  ions.



## 1. INTRODUCTION

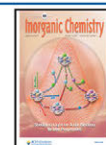
In recent decades, lanthanides have been employed in a wide variety of applications spreading from energy production to life sciences.<sup>1</sup> They are a fundamental element in light-emitting diodes, displays, lasers, telecommunications, sensors, molecular thermometers, lighting systems, and biological immunoassays and imaging.<sup>2–4</sup> Among lanthanides, the  $\text{Eu}^{3+}$  ion has had an increasingly relevant role as a luminescent activator in different classes of materials due to its high efficiency as a red light emitter.<sup>5</sup> Moreover, its energy level structure is relatively simple, and the ground ( $^7\text{F}_0$ ) and the emitting ( $^5\text{D}_0$ ) states are not degenerate; hence, it is possible to monitor  $\text{Eu}^{3+}$  emission and excitation transitions also in a host lattice.<sup>6,7</sup> Some  $^5\text{D}_0 \rightarrow ^7\text{F}_j$  electronic transitions are very sensitive to the local environment surrounding the ion; therefore,  $\text{Eu}^{3+}$  can be used as a spectroscopic probe for investigating structural properties of the material in which it is embedded.<sup>8,9</sup> This characteristic results in the extensive use of this ion to determine the local symmetry of an ion site,<sup>10,11</sup> to test the crystal defects, to evaluate the crystal field strength,<sup>12</sup> and to rationalize the thermal treatment effects on oxides.<sup>13</sup> Literature highlights the importance of accurate determination of the electronic states of the  $\text{Eu}^{3+}$ ; hence, the development of new methods and the nonstandard application of the existent theoretical tools to correctly include the not always negligible effects of the ligand field on  $4f$  states are the new frontier in the *ab initio* treatment of this ion.

Theoretical studies on  $\text{Eu}^{3+}$  complexes consist of two main approaches: (i) semiempirical methods often parametrized for a single class of compounds (e.g., the LUMPAC<sup>14,15</sup> program) and (ii) density functional theory (DFT) and multireference *ab initio* methods.<sup>16–18</sup> Only the latter approaches allow in principle to tackle a wide range of systems, but there is not a general consensus on how to carry out these high-level calculations on molecular systems, especially when multireference methods such as complete active space self-consistent field (CASSCF) and complete active space second-order perturbation theory (CASPT2) are considered.<sup>17,19–23</sup>

Some work has been done in investigating the effect of including different electronic states on the energy of low-lying excited states in isolated  $\text{Eu}^{3+}$  ion, but without a thorough and systematic procedure and neglecting the effects of the surrounding environment.<sup>24</sup> CASSCF/CASPT2 methods have been also applied to disordered systems, such as  $\text{Eu}^{3+}$ -

Received: October 6, 2020

Published: December 15, 2020



doped glasses.<sup>25–27</sup> In these works, the environment is treated implicitly through the use of a model potential.

In the case of molecular systems, for which the chemical environment needs to be treated explicitly, there is still uncertainty on where to focus the attention: some authors evaluate the influence of excited states with different spin but neglect the effects of second-order perturbations;<sup>17</sup> others recognize the importance of dynamic correlation and employ a reasoned number of quintet states, but they do not include states with different spin multiplicity such as triplets and singlets.<sup>19</sup> As a whole, in most cases in the literature it can be seen that the energy of the <sup>5</sup>D<sub>0</sub> emitter is not correctly reproduced.<sup>17,19,20,22,23,28</sup>

Recently, hybrid approaches combining the computationally efficient qualities of semiempirical methods and the accuracy of full *ab initio* calculations—the CERES<sup>29</sup> program is one prime example—have started to catch on. In these suites of programs, a specific *ab initio* protocol is optimized and set up for the determination of certain observables. The CERES program, for instance, focuses on calculations of magnetic properties of lanthanide complexes, also limited to Eu<sup>3+</sup>, in an efficient way by employing some approximations in the description of the electronic states, which are perfectly valid if we limit the attention to the magnetic properties. In particular, magnetic properties are not significantly influenced by higher energy excited states and are mostly attributed to the ground state (GS) manifold. The program therefore does not include second-order perturbations (CASPT2), which are only relevant when excited states are considered.

Literature<sup>18,30,31</sup> demonstrated that when considering excited states, dynamic correlation in the form of second-order perturbation theory needs to be introduced, but the role of the mixing and the choice of the relevant states is still under discussion. The main aim of this contribution is to present a general theoretical protocol based on a combination of DFT and multireference methods to gain detailed information about electronic states of the Eu<sup>3+</sup> ion, with the possibility to extend the results to other lanthanides. The protocol has been validated for a Eu<sup>3+</sup> complex, general formula EuL<sub>3</sub>(EtOH)<sub>2</sub>, where L is a  $\beta$ -diketone (see Figure 1).

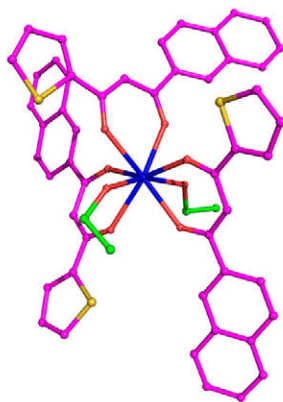


**Figure 1.** A ball and stick representation of the Eu complex with the antenna ligands (three) in magenta and the ancillary ligands (two) in green. The coordination number of the Eu<sup>3+</sup> ion (the central blue sphere) amounts to 8. Magenta, red, yellow, and blue spheres are C, O, S, and Eu atoms, respectively.

The main aim of the study is the calculation of the excited (<sup>5</sup>D<sub>0</sub>) and ground (<sup>7</sup>F<sub>J</sub>) energy levels for Eu complex. The role played by the number of excited states adopted in the multireference calculations and the relevance of the mixing of states with the same *J* value will be rationalized for different computational approaches. Moreover, the absorption spectrum will be simulated to understand how the electronic properties of the complex depend on the Eu<sup>3+</sup> and ligand fragments. Because of the relatively simple electronic structure where the ground (<sup>7</sup>F<sub>0</sub>) and the emitting (<sup>5</sup>D<sub>0</sub>) states are not degenerate, Eu<sup>3+</sup> will be then herein considered as a case study to showcase the effect of including different states, with the awareness that the obtained results will have a general validity and could be straightforwardly transferred to whatever Ln<sup>3+</sup> ion.

## 2. METHODS

**Experimental Details.** The studied complex has the general formula EuL<sub>3</sub>(EtOH)<sub>2</sub>, where L is a  $\beta$ -diketone which features a thienyl and a naphthyl group as substituents. The ligand and [EuL<sub>3</sub>(EtOH)<sub>2</sub>] compounds were prepared as previously reported.<sup>32</sup> Absorption spectra were recorded on a CARY5000 double-beam spectrophotometer in the 300–800 nm range, with a spectral bandwidth of 1 nm. The contribution due to the toluene solvent was subtracted. Photoluminescence spectrum was acquired with a Horiba Fluorolog 3-22 spectrofluorometer.

**Computational Details.** DFT calculations have been performed by using the Amsterdam Density Functional (ADF) package (ver. 2013.01),<sup>33–35</sup> while multireference *ab initio* calculations have been run by exploiting the OpenMolcas package.<sup>36–38</sup>

The generalized gradient approximation (GGA) PBE<sup>39–42</sup> functional coupled to a TZ2P basis set has been employed to optimize the Eu complex geometry. Core–shells up to level 4d for Eu, 2p for P and S, and 1s for O and C have been kept frozen throughout the calculations. Scalar relativistic effects have been included by adopting a two-component Hamiltonian with the zeroth-order regular approximation (ZORA).<sup>43–45</sup> Once again, frequency calculations have been performed to ensure the geometry optimization had reached a minimum in the potential energy hypersurface. The complex absorption spectrum has been simulated at the same level of theory of the free ligands by using the statistical average of orbital potential (SAOP) with a TZ2P basis set, as the transitions are ligand-centered in nature (see the Results and Discussion section).

Complete active space self-consistent field (CASSCF) calculations have been performed on a model system that maintains the same coordination sphere as the full complex at the DFT optimized geometry (see details in the discussion) by using the all-electron Gaussian-type atomic natural orbital-relativistic core-correlated basis set contracted to TZP quality (ANO-RCC-VTZP).<sup>46,47</sup> Scalar relativistic effects have been included by means of the two-component second-order Douglas–Kroll–Hess (DKH) Hamiltonian in its scalar form.<sup>48</sup> Spin–orbit coupling (SOC) has been treated by state interaction between the CASSCF wave functions by using the restricted active space state interaction (RASSI) program.<sup>49</sup> The SOC operator matrix has been calculated from the atomic mean-field (AMF1) approximation,<sup>50</sup> while dynamic correlation has been included by using the complete active space second-order perturbation theory (CASPT2) method.<sup>51,52</sup> The active space has been selected by including six electrons in the seven 4f orbitals, equating to a CAS(6,7) calculation. A multitude of states for each spin multiplicity have been evaluated, and further details are reported in the Results and Discussion section. As far as the correlation orbital space for the CASPT2 calculation is concerned, it has been limited to the central Eu<sup>3+</sup> ion and the ligand donor atoms (AFREeze keyword). Just for comparison, the Eu<sup>3+</sup> emitter state <sup>5</sup>D<sub>0</sub> has been also calculated by considering the lowest energy spin-flip<sup>53,54</sup> TD-DFT/LB94<sup>55</sup> transition between the GS characterized by six unpaired electrons and a state with four unpaired electrons; the <sup>7</sup>F<sub>J</sub> states

energies have also been evaluated at the TD-DFT/LB94 level of theory.

The specific influence of the solvent effects and of the dispersion corrections on this ligand was investigated in detail in a previous study.<sup>56</sup> The negligible variations with respect to the gas phase calculations for toluene allows us to avoid including the solvent in the calculations.

### 3. RESULTS AND DISCUSSION

**GS Geometry.** The crystal structure of the Eu complex is not available, which makes DFT calculations the only source of information about structural properties. As such, the accuracy of DFT has been recently tested on similar Eu complexes characterized by the presence of two thienyl groups substituents,<sup>32</sup> where the PBE XC functional coupled to a TZ2P basis set accurately reproduced the crystal structure geometry. The same level of theory has been then herein used to optimize the Eu complex. The ligand symmetry implies that the complex may assume *cis* and *trans* configurations depicted in Figure 2 and defined as follows: in the former, the polyaromatic hydrocarbon moieties of the two almost coplanar ligands are on the same side, while in the latter they are opposed.

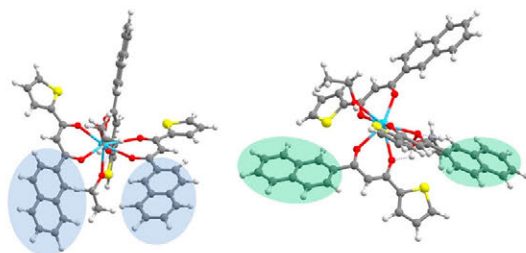


**Figure 2.** *Cis* (left) and *trans* (right) isomers of the Eu complex. Gray, white, red, yellow, and blue spheres are C, H, O, S, and Eu atoms, respectively.

To obtain the optimized geometries of both stereoisomers, we started from *cis* or *trans* configurations. Independently from the starting configuration, the final geometry converged toward the *trans* one, probably due to the significant steric hindrance between the aromatic fragments in the *cis* form. The impossibility to achieve the *cis* form suggests that this form is not stable enough to provide any contribution to experimental measurements.

**Absorption Spectra.** To understand the role of the ligand and the Eu<sup>3+</sup> ion on the electronic properties and to follow the variation from the isolated fragments to the complex, the absorption spectra of isolated ligands and the Eu complex are compared. Figure 3 reports the overlap between the ligand and Eu complex absorption spectra. Even though similar, the two UV–vis spectral patterns are not identical. Such evidence suggests that light absorption in the complex is almost completely localized on the ligand, and a detailed analysis of the ligand absorption spectra and the role of the vibronic progression is reported in our previous investigation.<sup>56</sup>

The main difference in the two experimental spectra is a weak but clearly visible shoulder at ~420 nm, which is missing from the ligand pattern (Figure 3). The efforts are then focused on elucidating the nature of this mismatch; as such SAOP vertical transitions have been calculated for the Eu complex (colored bars in the Figure 3). Unsurprisingly, the

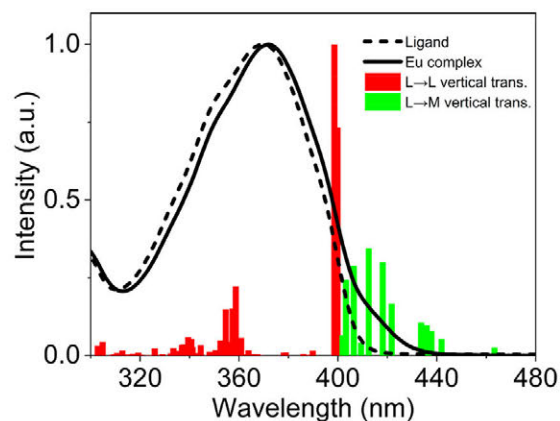


**Figure 3.** Calculated SAOP vertical transitions (bars) for the Eu complex. The red and the green bars represent the ligand centered and the ligand-to-metal-charge-transfer vertical transitions, respectively. The experimental spectra for the Eu complex (solid line) and the isolated ligand (dashed line) are reported. Ligand and complex absorption spectra are obtained in toluene with a concentration of  $5 \times 10^{-6}$  and  $3 \times 10^{-6}$  M, respectively.

UV–vis spectrum of the complex is dominated by ligand-based transitions of the same nature as that of the free ligand (red bars in Figure 3), as highlighted by molecular orbital analysis (see Table S1 in the Supporting Information). A direct comparison between the isolated ligand and the Eu complex main transitions further highlights the similarity of the initial and final molecular orbitals (see Figure S1) and that the complex spectrum is only weakly affected by the presence of the central Eu<sup>3+</sup>. Other than that, there are several weak transitions lying at lower energies (~420 nm) with a ligand-to-metal-charge-transfer (LMCT) character (green bars in the Figure 3). The weak shoulder characterizing the complex spectra can therefore be assigned to LMCT transitions (see Table S1). These results confirm that the ligand maintains the electronic properties of the isolated condition; hence, the ligand and the metal center can be considered practically independent.<sup>56</sup> Even if independent, these two fragments can interact, and new properties arise from this interaction, such as the shoulder in the complex spectrum due to the LMCT transitions. A clear trace of this interaction is also observed in the variation of the Eu<sup>3+</sup> ground state (<sup>7</sup>F<sub>J</sub>) energies going from the Eu<sup>3+</sup> isolated ion to the Eu complex.

**TD-DFT Calculations for <sup>5</sup>D<sub>0</sub> and <sup>7</sup>F<sub>J</sub> Levels.** As for the Eu<sup>3+</sup>-centered transitions, it has to be kept in mind that DFT, a *single-determinant* method, is not well suited to investigate the Ln<sup>3+</sup> electronic properties, and the adopted software package (ADF) does not currently allow for a *self-consistent* treatment of spin–orbit coupling in open-shell systems, which is the leading perturbation term for rare earths after electron repulsion. Furthermore, conventional TD-DFT cannot calculate transitions between terms with different spin multiplicities in open-shell systems; a variation of the method called *spin-flip* TD-DFT is required, in which electrons initially located in  $\alpha$  orbitals are only excited to  $\beta$  orbitals, and vice versa. At a first glance, TD-DFT transitions calculated by exploiting the LB94 functional in which only scalar relativistic effects have been included seem to be in good agreement with experimental evidence (Table 1).

**Table 1.**  ${}^7F_J$  and  ${}^5D_0$  State Energies (in  $\text{cm}^{-1}$ ) Calculated at the Scalar Relativistic TD-DFT/LB94 and the RASSI-CAS(6,7)PT2 Level for the  $\text{Eu}^{3+}$  Model Complex<sup>a</sup>

	TD-DFT	CAS(6,7)	CAS(6,7) PT2	Eu complex exp.	$\text{Eu}^{3+}$ free ion exp. <sup>5</sup>
Ground State					
${}^7F_0$	0	0	0	0	0
${}^7F_1$	860	359	384	392	379
${}^7F_2$	1171	1029	1091	1119	1043
${}^7F_3$	1935	1929	2025	1955	1896
${}^7F_4$	2934	2977	3088	2898	2869
${}^7F_5$	3995	4110	4214	//	3912
${}^7F_6$	6440	5294	5370	//	4992
Excited State					
${}^5D_0$	16339	22789	20214	17302	17227

<sup>a</sup>Each  ${}^7F_J$  term for CASSCF calculations is taken as the barycenter of the respective manifold generated by crystal field splitting.

Table 1 reports  ${}^7F_J$  and  ${}^5D_0$  state energies for both  $\text{Eu}^{3+}$  free ion and Eu complex to demonstrate that the variation between them is small but not negligible. The coordination environment influences the  $\text{Eu}^{3+}$  energy levels, and this effect has to be considered.

To allow a direct and reliable comparison between experimental and calculated data, the experimental energy of the different  ${}^7F_J$  manifolds are obtained as arithmetic mean of the initial and final energy of each  ${}^5D_0 \rightarrow {}^7F_J$  multiplets ( $J = 0, 1, 2, 3,$  and  $4$ , Figure 4, dotted lines), deduced from the

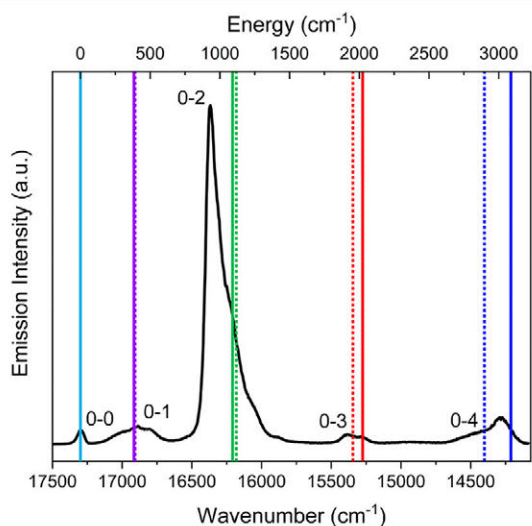


**Figure 4.** The solid black line is the experimental emission spectrum of the Eu complex. The solid and dotted lines are the  ${}^7F_J$  CAS(6,7)PT2 and experimental values (see Table 1), respectively. Details for the experimental values are reported in the text.

emission spectrum (Figure 4, solid black line). The calculation of the average wavenumber of the transitions using the intensity of experimental spectrum as weight factor<sup>5</sup> is not a good choice in our case because the calculated values cannot be correlated to any oscillator strength and hence cannot be weighted.

When looking at the first column of Table 1, it must be remembered that experimental lines arise from transitions

between the different  ${}^7F_J$  states generated by the SOC interaction, which is not taken into account in TD-DFT calculations<sup>57</sup> and TD-DFT calculations performed for the Eu complex are only purely  $4f-4f$  in nature. To appropriately describe the electronic states of the  $\text{Eu}^{3+}$  ion, higher level calculations are therefore necessary.

#### Multireference Calculations for ${}^5D_0$ and ${}^7F_J$ Levels.

The valence electrons for  $\text{Eu}^{3+}$  ions reside in orbitals which are shielded from the environment by the closed  $5s^2$  and  $5p^6$  outer shells: the intensity of crystal field effects, which lift the degeneracy of the electronic terms originated from the  $4f^n$  configuration, is then greatly mitigated by comparison with transition metal ion complexes. Moreover, SOC scales with the fourth power of the atomic number  $Z$ , thus overwhelming, in heavy elements such as lanthanides, effects associated with the crystal field splitting.  $\text{Eu}^{3+}$ -based transitions are therefore expected to be almost in the same energy range even for a significantly different environment, as widely confirmed by the literature.<sup>58–60</sup> All of this allows to carry out multireference calculations by focusing on the  $\text{Eu}^{3+}$  center and modeling the antenna ligands in a simplified fashion, that is, by maintaining the actual complex coordination sphere with the antenna ligands only featuring the fragment directly coordinated to the  $\text{Eu}^{3+}$  ion. The Eu complex has been then modeled by substituting the ligand with a much simpler one, but with a similar structure (malondialdehyde) to preserve the  $\text{Eu}^{3+}$  coordination sphere geometry (Figure 5). The positions for

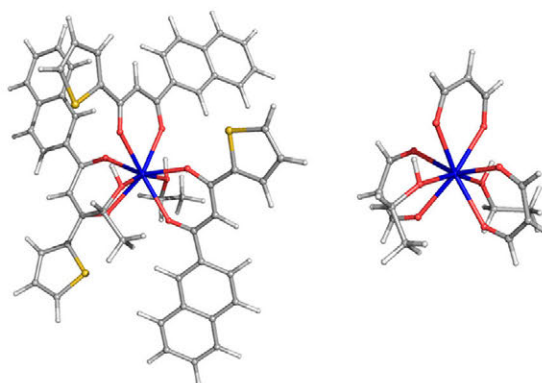


**Figure 5.** Eu complex (left) and its simplified model (right) obtained by substituting the ligand with malondialdehyde. Gray, red, yellow, white, and blue spheres are C, O, S, H, and Eu atoms, respectively.

the atoms that are taken from the full complex are kept fixed, while the hydrogen atoms replacing the aromatic fragments have been reoptimized at the same level of theory.

The static correlation, arising from the multideterminant nature of the wave function, has been recovered via spin-adapted state-averaged CASSCF followed by state interaction with spin-orbit coupling. Such a procedure, able to properly describe the GS manifold, yields a series of electronic states linkable to Russell–Saunders terms. Besides static correlation, the evaluation of the excited state energies needs the inclusion of dynamic correlation as well in the form of second-order perturbation theory on the CASSCF wave function (CASPT2). As such, it is necessary to define two parameters in CASSCF/CASPT2 calculations: (i) the active space and (ii) the dimensions of the configuration interaction (CI) matrices, that is, the number of electronic states taken into account for



each spin multiplicity. The former assessment is quite trivial: the appropriate active space will include all the  $\text{Ln}^{3+}$   $n$  4f electrons distributed among the seven 4f orbitals; that is, a CAS(6,7) calculation needs to be performed in the present case regarding  $\text{Eu}^{3+}$ . As far as the latter point is concerned, this is usually not discussed in detail in the literature,<sup>61–63</sup> and even if so, it is done in a rather heuristic fashion.<sup>17,19</sup>

Differently from the TD-DFT black-box approach, the setup of a multireference numerical experiment is not at all a matter of routine. In fact, both the active space choice and the selection of the CI matrices dimensions imply, *a priori*, a rather deep understanding of the electronic properties of the investigated system. The  $\text{Eu}^{3+}$  4f<sup>6</sup> electronic configuration implies 3003 possible microstates, that is, ways of distributing six electrons in 14 spin-orbitals. This nominal degeneracy is lifted by the electron repulsion, SOC, and the crystal field in order of decreasing intensity. In the Russell–Saunders coupling scheme,<sup>64</sup> the electron repulsion generates the  $2S+1L(\tau)$  terms with  $S$  and  $L$  corresponding to the total spin angular momentum and total orbital angular momentum quantum numbers, respectively ( $\tau$  is an additional identifier discriminating between states with the same  $S$  and  $L$  quantum numbers). According to Hund's rules,<sup>65</sup> the free-ion ground state term for  $\text{Eu}^{3+}$  is the  ${}^7F_0$ . The crystal field eventually present further reduce the  $2J + 1$  degeneracy of the  $2S+1L(\tau)$  states according to the symmetry of the  $\text{Ln}^{3+}$  chemical environment.

A RASSI-CAS(6,7) calculation featuring a CI matrix of dimension  $7 \times 7$  for electronic states with a spin multiplicity of 7 should describe appropriately the  ${}^7F_J$  terms of the GS manifold. Moreover, the dynamic correlation inclusion (at the CASPT2 level) is unessential because we are not focusing on the  ${}^5D_J$  excited states energies. In Table 1, the energies for the  ${}^7F_J$  states calculated including seven septets as well as five quintets for tracking the  ${}^5D$  term are reported. Each  ${}^7F_J$  free-ion state is split in  $2J + 1$  crystal field levels in the complex due to its low symmetry ( $C_1$ ); therefore, its energy has been taken as the barycenter of the manifold of levels within the same energy range. This is probably the most appropriate way to treat the electronic GS term, not only for the better agreement between theory and experiments but also for the lack of ambiguity compared to the TD-DFT calculations. The number and character of the output states are directly assignable to the expected theoretical levels. The comparison of CASSCF and CASPT2 results reveals minor differences for the  ${}^7F_J$  states while the opposite is true for the  ${}^5D_0$  state where, as expected, dynamic correlation plays a relevant role. Indeed, in the CASPT2 framework, the reference state (i.e., the CASSCF wave function) directly interacts only with states differing by a single or double excitation.<sup>18</sup> In a septet state only a limited number of single excitations preserve  $S = 3$ ; at variance to that the CASSCF wave function may interact with a definitely larger number of states when a quintet is involved. In Figure 4 is reported the comparison between the experimental energy of the different  ${}^7F_J$  manifolds (Figure 4, dotted lines) and the corresponding CAS(6,7)PT2 ones (Figure 4, solid lines). All these values are in Table 1. The inspection of Figure 4 testified the good agreement between experimental and CAS(6,7)PT2 values, especially low  $J$  values. This is consistent with results from Ungur and Chibotaru,<sup>66</sup> who found that the appropriate description of the  $\text{Er}^{3+}$  complex ground state manifold actually requires the inclusion of second-order perturbations, and the CASPT2 results are significantly different from the CASSCF

ones. These outcomes cannot be translated directly to our  $\text{Eu}^{3+}$  system because the ground state of  $\text{Er}^{3+}$  (4f<sup>11</sup> configuration) is represented by a quartet term ( ${}^4I$ ), for which the number of possible single and double excitations is much larger than for our septet ground state.

The comparison between the diverse methods herein considered is schematically represented in Figure 6. Despite

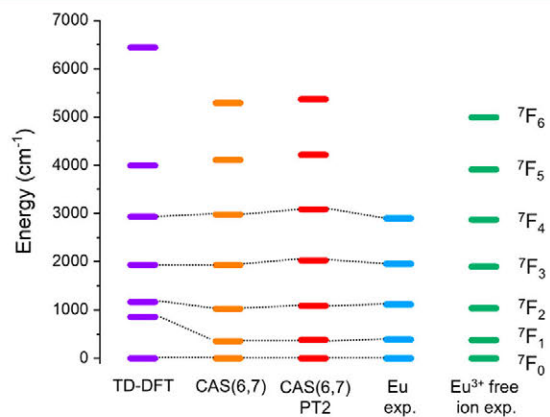


**Figure 6.** TD-DFT (violet bars), CAS(6,7) (orange bars), and CAS(6,7)PT2 (red bars)  ${}^7F_J$  calculated energies for the  $\text{Eu}^{3+}$  model complex (see Table 1 for details).  $\text{Eu}^{3+}$  free ion experimental values (green bars) are also included for comparison with the  $\text{Eu}$  complex (blue bars).

a slight overestimation of the energy of  ${}^7F_J$  states with increasing  $J$ , multireference calculations provide satisfactory results. As far as the TD-DFT approach is concerned, the numerical agreement between experiment and theory is better for certain  $J$  values but worse for others. Once more, we emphasize that these TD-DFT calculations do not include spin-orbit effects, which are the leading term of interaction for these electronic states after electron repulsion. Finally, to definitively test the importance of the  $\text{Eu}^{3+}$  coordination sphere geometry, CASSCF and CASPT2 calculations are also performed on the  $\text{Eu}^{3+}$  isolated ion (see Table S2). In this case, there is a poor agreement between calculated values and the experimental ones obtained from the  $\text{Eu}^{3+}$  dopant in crystalline host matrices.<sup>5,67</sup> The disagreement between experimental values and CASPT2 calculations is probably due to the fact that the energy terms acquired from data in crystalline matrices cannot be fully considered as “isolated ion” terms. Indeed, the effects of the surrounding chemical environment are indirectly included in the determination of the term energies. On the contrary, the CASPT2 calculations are performed on a truly isolated ion (Table S2), and the influence of the surrounding environment can be directly evidenced by comparison between CASPT2 outcomes on the  $\text{Eu}^{3+}$  isolated ion (Table S2) and on a molecular complex (Table 1).

When  $\text{Eu}^{3+}$ -based luminescence is considered, transitions between the lowest-lying excited state ( ${}^5D_0$ ) and the ground state manifold ( ${}^7F_J$ ) are the most relevant. Therefore, it might be tempting to limit the states considered in the multireference calculation to the  ${}^7F_J$  seven septets and the  ${}^5D_J$  five quintets. This would be simply wrong because SOC allows the mixing of states with different (same)  $L$  and  $S$  ( $J$ ) values. For instance, the  ${}^7F_0$  GS wave function includes the following main

contributions:<sup>68</sup> 93.4%  ${}^7F_0$  + 3.5%  ${}^5D_0(1)$  + 2.8%  ${}^5D_0(3)$  + 0.12%  ${}^3P_0(6)$ . Similarly, the wave function of the  ${}^5D_0$  emitter state has contributions from other states with  $J = 0$ . The inclusion of all possible states with  $J = 0$  able to mix with  ${}^5D_0$  would imply, besides the seven septets, the presence of 140 quintets, 588 triplets, and 490 singlets. This is not only unrealistic but also unnecessary; in fact, the interaction we are dealing with is related to second-order perturbation theory,<sup>18</sup> and it is well-known that the closer in energy the interacting states are the larger their mixing will be. We then do expect, knowing the layout of the lowest lying electronic terms,<sup>5</sup> that  ${}^5D_0$  will strongly mix with septet states, other quintet states, and eventually low-lying triplet/singlet states, while its mixing with the high energy triplet/singlet states should be negligible. To quantify the mixing between  ${}^5D_0$  and other states, a series of RASSI-CAS(6,7)PT2 calculations have been performed on the Eu complex (see Table 2).

**Table 2.**  ${}^5D_0$  State Energies Calculated at the RASSI-CAS(6,7)PT2 Level for the  $\text{Eu}^{3+}$  Model Complex<sup>a</sup>

no.	no. of states (2S + 1)	${}^5D_0/\text{cm}^{-1}$
States with Different Multiplicities		
1	7(7) + 5(5)	20214
2	7(7) + 5(5) + 3(3)	17810
3	7(7) + 5(5) + 3(3) + 1(1)	17794
States with Different Multiplicities and Different Number of States		
4	7(7) + 5(5)	20214
5	7(7) + 31(5)	20055
6	7(7) + 42(5)	20018
7	7(7) + 49(5)	19987
8	7(7) + 62(5)	19947
9	7(7) + 77(5)	19895
10	7(7) + 140(5)	19676
11	7(7) + 140(5) + 3(3)	17504
12	7(7) + 140(5) + 31(3)	17506
13	7(7) + 140(5) + 3(3) + 1(1)	17313
14	7(7) + 140(5) + 31(3) + 1(1)	17311
15	7(7) + 140(5) + 31(3) + 20(1)	17315

<sup>a</sup>The labels identifying the calculations are reported in the first column. In the second column, the number of states included for each spin (in parentheses) are reported. The experimental value for Eu complex  ${}^5D_0$  is  $17302\text{ cm}^{-1}$ .<sup>5</sup>

In the first set of calculations, the role of states with different multiplicities (quintets, triplets, and singlets) is considered (from run 1 to run 3 in Table 2). The base calculation (run 1 in Table 2) only features seven septets and five quintets, which is equivalent to taking into account the ground  ${}^7F$  and the excited  ${}^5D$  states. The  ${}^5D_0$  state is calculated at  $20214\text{ cm}^{-1}$ , definitely too high with respect to the experimental  ${}^5D_0$  energy, which is found at  $17302\text{ cm}^{-1}$  for the Eu complex. Such a result ultimately testifies the poor description of the excited state. The mixing with other electronic terms with  $J = 0$ , for which Binnemans<sup>5</sup> reports all the energies for levels below  $40000\text{ cm}^{-1}$ , seems to be a crucial factor. The lowest lying triplet state is  ${}^3P$ .<sup>5</sup> Its inclusion in run 2 through the addition of three triplet states drops the  ${}^5D_0$  energy to  $17810\text{ cm}^{-1}$ , thus confirming the importance of this mixing. The addition of one singlet state (run 3) further improves the agreement, even if only marginally. States with different multiplicities contribute differently to the result. In particular, the inclusion of triplet states is more important than the singlet

one. The reason is probably due to the higher energy of the singlet (above  $40000\text{ cm}^{-1}$ ) that disadvantages, but not prevents, direct mixing with the  ${}^5D_0$  state. A graphical representation of the trend in these calculations can be found in Figure 7 (red path). An uncertainty of around  $3\text{ cm}^{-1}$  has been found for these calculations by running them multiple times.

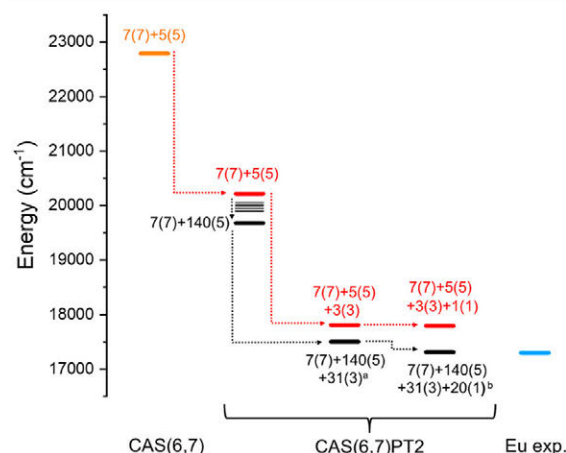


**Figure 7.** CAS(6,7) and CAS(6,7)PT2  ${}^5D_0$  calculated energies for states with different multiplicities (red path) and for states with different multiplicities and a different number of states (black path). Calculations are performed on the  $\text{Eu}^{3+}$  model complex. The blue line is the experimental value for the Eu complex. <sup>a</sup>Energies for 7(7) + 140(5) + 31(3) and 7(7) + 140(5) + 3(3) are equal (see Table 2, runs 10 and 11). <sup>b</sup>Energies for 7(7) + 140(5) + 31(3) + 20(1) and 7(7) + 140(5) + 31(3) + 1(1) are very similar (see Table 2, runs 13 and 14) and are not distinguishable in the graph.

In the second set of calculations, in addition to states with different multiplicities, also the role of the number of states within the same spin multiplicity is investigated (from run 4 to run 14 in Table 2). The progressive addition of quintets up to the inclusion of all possible states with this multiplicity (140) significantly changes the  ${}^5D_0$  energy with an improvement of over  $500\text{ cm}^{-1}$  (see Table 2, from run 4 to run 9). This trend is almost linear.<sup>69</sup> As already demonstrated in the first set of calculations (run 2 in Table 2), the addition of triplets allows a better agreement with experimental value (a jump of around  $2100\text{ cm}^{-1}$ , run 10), but the inclusion of a larger number of triplets (the  ${}^3K$  (15) and  ${}^3I$  (13) terms, run 11 in Table 2) does not change significantly the  ${}^5D_0$  energy. This is likely due to the fact that the  ${}^3K_0$  and  ${}^3I_0$  levels are too high in energy (the lowest-lying levels for  ${}^3K$  and  ${}^3I$  are  ${}^3K_6$  ( $38780\text{ cm}^{-1}$ ) and  ${}^3I_6$  ( $38780\text{ cm}^{-1}$ ), respectively, while the terms with  $J = 0$  are found well above  $40000\text{ cm}^{-1}$ ),<sup>5</sup> whereas the lowest lying  ${}^3P$  state ( ${}^3P_0$ ,  $32790\text{ cm}^{-1}$ )<sup>5</sup> is more easily accessible. These energy differences lead to a poor energy match with the  ${}^5D_0$  state for second-order perturbation mixing. Similarly to triplets, adding a singlet reduces the  ${}^5D_0$  energy by around  $200\text{ cm}^{-1}$  (run 12 in Table 2).

This is an interesting difference with respect to the run 3, in which the addition of the singlet state did not produce an effect of this magnitude. However, the inclusion of a larger number of singlet states (run 14 in Table 2) does not change the energy of the  ${}^5D_0$  state in any meaningful way. We could

suppose that the  $^1S_0$  state associated with the inclusion of this singlet does not mix directly with the  $^5D_0$  state but rather mixes with other states (other quintet states,  $^3P_0$ ), which in turn mix with the  $^5D_0$  state, contributing indirectly to the determination of its energy. Other high-energy triplets do not seem to mix with this singlet state significantly (runs 12 and 13). A graphical representation of the trend in these calculations can be found in Figure 7 (black path). Figure 7 clearly resumes from one side the role of the triplets, singlets, and quintets and from the other side the effects of a number of states involved in the  $^5D_0$  value calculations for the CAS(6,7)PT2.

Considering the data in Table 2 and Figure 7, it is possible to infer that: (i) the inclusion of the triplets ( $^3P$ ) strongly improves the agreement with the experimental value, as they mix directly with the  $^5D_0$  state; (ii) differently from the triplets, the addition of the singlet ( $^1S$ ) to the calculations with quintets and triplets only slightly affects the agreement with experimental value via an indirect mechanism; and (iii) the number of states is significant only for the quintets, while it is almost negligible for triplets and singlets, as only the lowest-lying term has an effect on the  $^5D_0$  state. A very good agreement between experimental and calculated values can be obtained considering all quintets and a minimal number of triplets (3) and singlet (1).

#### 4. CONCLUSIONS

This study features advanced applications of *ab initio* quantum chemistry methods in the form of the nonroutine use of density functional theory based techniques as well as employment of multireference methods (CASSCF/CASPT2) for the rigorous treatment of the  $\text{Eu}^{3+}$  molecular complex. In particular, in the former point the absorption properties of the complex are studied; in the latter we address a number of inconsistencies in the literature regarding technical parameters in multireference calculations on  $\text{Ln}^{3+}$  ions, outlining the appropriate options on the base of theoretical arguments and calculated results.

The literature demonstrates the importance of second-order perturbation theory when considering excited states. Nevertheless, the role of the mixing and the choice of the relevant states are still under discussion. In this contribution, a general protocol based on a combination of DFT and multireference methods is presented to gain detailed information about  $\text{Eu}^{3+}$  electronic states. The shortcomings of DFT have been highlighted as well as some general guidelines for carrying out CASPT2 calculations. For the description of the GS manifold, static correlation is the leading term; therefore, a CASSCF calculation is enough, and CASPT2 is not necessary for the  $\text{Eu}^{3+}$  ion. When considering excited states, dynamic correlation in the form of second-order perturbation theory needs to be introduced. Because an electronic state can in principle mix with any other state with the same value of  $J$ , a series of benchmark calculations were performed to illustrate how significant this mixing is and to frame the appropriate way to carry out these calculations, since the literature is not in clear agreement on this point.

In particular, we have shown that for the  $^5D_0$  state energy calculation, two parameters are important: (i) the inclusion of states with different multiplicity and (ii) the number of states considered for each multiplicity. The relative weight of these parameters in improving the agreement with the experimental value is different. The inclusion of triplet and singlet states is

crucial. The inclusion of a large number of states is necessary only for the quintets, while it is practically negligible for triplets and singlets.

To summarize, the finalized protocol for the determination of  $\text{Eu}^{3+}$ -based emission properties in molecular complexes (the protocol evaluating ligand-based properties can be found in our previous study)<sup>56</sup> consists of the following steps: (i) geometry optimization of the whole complex at the DFT/PBE level; (ii) evaluation of LMCT transitions at the TDDFT/SAOP level; and (iii) CAS(6,7)PT2 calculations on a model system which maintains the coordination sphere of the original complex, limited to 7 septet states without second-order perturbation effects for the  $^7F_j$  ground state manifold and 7 septets, 140 quintets, 3 triplets, and 1 singlet for the accurate determination of the  $^5D_0$  emitter level.

The outcomes to this  $\text{Eu}^{3+}$  case study can be extended to other  $\text{Ln}^{3+}$  ions as well. As a rule of thumb, all states that can reasonably mix with the emitter level should be considered. In the absence of experimental data for the possible spectroscopic terms to be included in the CASPT2 calculation for the determination of the  $^5D_0$  state energy, a series of prescreening calculations on an isolated  $\text{Ln}^{3+}$  ion can be performed because its excited electronic levels are not expected to be greatly influenced by the presence of ligands. The appropriate configuration interaction (CI) matrices size can then be set from these preliminary calculations (Table S3).

#### ■ ASSOCIATED CONTENT

##### Supporting Information

The Supporting Information is available free of charge at <https://pubs.acs.org/doi/10.1021/acs.inorgchem.0c02956>.

Comparison between the ligand and the  $\text{Eu}^{3+}$  complex MOs in SAOP/TD-DFT transitions (Figure S1); most intense relevant SAOP/TD-DFT UV–vis electronic transitions for the  $\text{Eu}^{3+}$  complex (Table S1);  $^7F_j$  and  $^5D_0$  state energies calculated at the RASSI-CAS(6,7)PT2 level for the  $\text{Eu}^{3+}$  free ion (Table S2) and  $^5D_0$  state energies calculated at the RASSI-CAS(6,7)PT2 level for the  $\text{Eu}^{3+}$  free ion (Table S3) (PDF)

#### ■ AUTHOR INFORMATION

##### Corresponding Authors

**Silvia Carlotto** – Dipartimento di Scienze Chimiche, Università degli Studi di Padova, 35131 Padova, Italy; Institute of Condensed Matter Chemistry and Technologies for Energy (ICMATE), National Research Council (CNR), c/o Department of Chemistry, University of Padova, 35131 Padova, Italy; [orcid.org/0000-0003-0043-3538](https://orcid.org/0000-0003-0043-3538); Email: [silvia.carlotto@unipd.it](mailto:silvia.carlotto@unipd.it)

**Maurizio Casarin** – Dipartimento di Scienze Chimiche, Università degli Studi di Padova, 35131 Padova, Italy; Institute of Condensed Matter Chemistry and Technologies for Energy (ICMATE), National Research Council (CNR), c/o Department of Chemistry, University of Padova, 35131 Padova, Italy; [orcid.org/0000-0002-3347-8751](https://orcid.org/0000-0002-3347-8751); Email: [maurizio.casarin@unipd.it](mailto:maurizio.casarin@unipd.it)

##### Authors

**Luca Babetto** – Dipartimento di Scienze Chimiche, Università degli Studi di Padova, 35131 Padova, Italy; [orcid.org/0000-0003-3898-4765](https://orcid.org/0000-0003-3898-4765)

Alice Carlotto – Dipartimento di Scienze Chimiche, Università degli Studi di Padova, 35131 Padova, Italy; [orcid.org/0000-0001-5048-6537](https://orcid.org/0000-0001-5048-6537)

Marzio Rancan – Institute of Condensed Matter Chemistry and Technologies for Energy (ICMATE), National Research Council (CNR), c/o Department of Chemistry, University of Padova, 35131 Padova, Italy; [orcid.org/0000-0001-9967-5283](https://orcid.org/0000-0001-9967-5283)

Gregorio Bottaro – Institute of Condensed Matter Chemistry and Technologies for Energy (ICMATE), National Research Council (CNR), c/o Department of Chemistry, University of Padova, 35131 Padova, Italy; [orcid.org/0000-0001-6196-8638](https://orcid.org/0000-0001-6196-8638)

Lidia Armelao – Dipartimento di Scienze Chimiche, Università degli Studi di Padova, 35131 Padova, Italy; Institute of Condensed Matter Chemistry and Technologies for Energy (ICMATE), National Research Council (CNR), c/o Department of Chemistry, University of Padova, 35131 Padova, Italy

Complete contact information is available at:

<https://pubs.acs.org/10.1021/acs.inorgchem.0c02956>

### Author Contributions

L.B. and S.C. equally contributed to this work.

### Notes

The authors declare no competing financial interest.

### ACKNOWLEDGMENTS

The Computational Chemistry Community (C<sub>3</sub>P) of the University of Padova is kindly acknowledged. This work was supported by the University of Padova (Grant P-DISC #CARL-SID17 BIRD2017-UNIPD, Project CHIRoN).

### REFERENCES

- (1) Pallares, R. M.; Abergel, R. J. Transforming Lanthanide and Actinide Chemistry with Nanoparticles. *Nanoscale* **2020**, *12* (3), 1339–1348.
- (2) Bünzli, J. C. G. Benefiting from the Unique Properties of Lanthanide Ions. *Acc. Chem. Res.* **2006**, *39* (1), 53–61.
- (3) Bünzli, J. C. G. Rising Stars in Science and Technology: Luminescent Lanthanide Materials. *Eur. J. Inorg. Chem.* **2017**, *2017* (44), 5058–5063.
- (4) Bünzli, J.-C. G.; Piguet, C. Taking Advantage of Luminescent Lanthanide Ions. *Chem. Soc. Rev.* **2005**, *34* (12), 1048–1077.
- (5) Binnemans, K. Interpretation of Europium(III) Spectra. *Coord. Chem. Rev.* **2015**, *295*, 1–45.
- (6) Armelao, L.; Bottaro, G.; Bovo, L.; Maccato, C.; Pascolini, M.; Sada, C.; Soini, E.; Tondello, E. Luminescent Properties of Eu-Doped Lanthanum Oxyfluoride Sol-Gel Thin Films. *J. Phys. Chem. C* **2009**, *113* (32), 14429–14434.
- (7) Sudarsan, V.; Van Veggel, F. C. J. M.; Herring, R. A.; Raudsepp, M. Surface Eu<sup>3+</sup> Ions Are Different than “Bulk” Eu<sup>3+</sup> Ions in Crystalline Doped LaF<sub>3</sub> Nanoparticles. *J. Mater. Chem.* **2005**, *15* (13), 1332–1342.
- (8) Bünzli, J. C. G. Review: Lanthanide Coordination Chemistry: From Old Concepts to Coordination Polymers. *J. Coord. Chem.* **2014**, *67*, 3706–3733.
- (9) Canu, G.; Bottaro, G.; Buscaglia, M. T.; Costa, C.; Condurache, O.; Curecheriu, L.; Mitoseriu, L.; Buscaglia, V.; Armelao, L. Ferroelectric Order Driven Eu<sup>3+</sup> Photoluminescence in BaZr<sub>x</sub>Ti<sub>1-x</sub>O<sub>3</sub> Perovskite. *Sci. Rep.* **2019**, *9* (1), 1–11.
- (10) Serna-Gallén, P.; Beltrán-Mir, H.; Cordocillo, E.; West, A. R.; Balda, R.; Fernández, J. Site-Selective Symmetries of Eu<sup>3+</sup>-Doped BaTiO<sub>3</sub> Ceramics: A Structural Elucidation by Optical Spectroscopy. *J. Mater. Chem. C* **2019**, *7* (44), 13976–13985.
- (11) Kaczkan, M.; Kowalczyk, M.; Szostak, S.; Majchrowski, A.; Malinowski, M. Transition Intensity Analysis and Emission Properties of Eu<sup>3+</sup>:Bi<sub>2</sub>ZnOB<sub>2</sub>O<sub>6</sub> Acentric Biaxial Single Crystal. *Opt. Mater. (Amsterdam, Neth.)* **2020**, *107*, 110045.
- (12) Malta, O. L.; Antic-Fidancev, E.; Lemaitre-Blaise, M.; Milicic-Tang, A.; Taibi, M. The Crystal Field Strength Parameter and the Maximum Splitting of the <sup>7</sup>F<sub>1</sub> Manifold of the Eu<sup>3+</sup> Ion in Oxides. *J. Alloys Compd.* **1995**, *228* (1), 41–44.
- (13) Costa Macedo, W.; Germano Bispo Junior, A.; de Oliveira Rocha, K.; de Souza Albas, A. E.; Pires, A. M.; Rainho Teixeira, S.; Longo, E. Photoluminescence of Eu<sup>3+</sup>-Doped CaZrO<sub>3</sub> Red-Emitting Phosphors Synthesized via Microwave-Assisted Hydrothermal Method. *Mater. Today Commun.* **2020**, *24*, 100966.
- (14) Dutra, J. D. L.; Bispo, T. D.; Freire, R. O. LUMPAC Lanthanide Luminescence Software: Efficient and User Friendly. *J. Comput. Chem.* **2014**, *35* (10), 772–775.
- (15) Dutra, J. D. L.; Freire, R. O. Theoretical Tools for the Calculation of the Photoluminescent Properties of Europium Systems - A Case Study. *J. Photochem. Photobiol., A* **2013**, *256*, 29–35.
- (16) Ferbinteanu, M.; Stroppa, A.; Scarozza, M.; Humelnicu, I.; Maftai, D.; Frecus, B.; Cimpoesu, F. On the Density Functional Theory Treatment of Lanthanide Coordination Compounds: A Comparative Study in a Series of Cu-Ln (Ln = Gd, Tb, Lu) Binuclear Complexes. *Inorg. Chem.* **2017**, *56* (16), 9474–9485.
- (17) Beltrán-Leiva, M. J.; Cantero-López, P.; Zúñiga, C.; Bulhões-Figueira, A.; Páez-Hernández, D.; Arratia-Pérez, R. Theoretical Method for an Accurate Elucidation of Energy Transfer Pathways in Europium(III) Complexes with Dipyrrophenazine (Dppz) Ligand: One More Step in the Study of the Molecular Antenna Effect. *Inorg. Chem.* **2017**, *56* (15), 9200–9208.
- (18) Dolg, M. *Computational Methods in Lanthanide and Actinide Chemistry*; John Wiley & Sons: 2015.
- (19) Janicki, R.; Kędziorski, A.; Mondry, A. The First Example of: Ab Initio Calculations of *ff* Transitions for the Case of [Eu(DOTP)]<sup>5-</sup> Complex - Experiment versus Theory. *Phys. Chem. Chem. Phys.* **2016**, *18* (40), 27808–27817.
- (20) Holzer, C.; Wernbacher, A. M.; Senekowitsch, J. M.; Gatterer, K.; Kelterer, A. M. A Theoretical Study on Trivalent Europium: From the Free Ion to the Water Complex. *J. Phys. Chem. A* **2014**, *118* (49), 11499–11511.
- (21) Marmodée, B.; Jahn, K.; Ariese, F.; Gooijer, C.; Kumke, M. U. Direct Spectroscopic Evidence of 8- and 9-Fold Coordinated Europium(III) Species in H<sub>2</sub>O and D<sub>2</sub>O. *J. Phys. Chem. A* **2010**, *114* (50), 13050–13054.
- (22) Abbas, Z.; Dasari, S.; Beltrán-Leiva, M. J.; Cantero-López, P.; Páez-Hernández, D.; Arratia-Pérez, R.; Butcher, R. J.; Patra, A. K. Luminescent Europium(III) and Terbium(III) Complexes of β-Diketonate and Substituted Terpyridine Ligands: Synthesis, Crystal Structures and Elucidation of Energy Transfer Pathways. *New J. Chem.* **2019**, *43* (38), 15139–15152.
- (23) Gendron, F.; Moore, B.; Cador, O.; Pointillart, F.; Autschbach, J.; Le Guennic, B. Ab Initio Study of Circular Dichroism and Circularly Polarized Luminescence of Spin-Allowed and Spin-Forbidden Transitions: From Organic Ketones to Lanthanide Complexes. *J. Chem. Theory Comput.* **2019**, *15* (7), 4140–4155.
- (24) Freidzon, A. Y.; Kurbatov, I. A.; Vovna, V. I. Ab Initio Calculation of Energy Levels of Trivalent Lanthanide Ions. *Phys. Chem. Chem. Phys.* **2018**, *20* (21), 14564–14577.
- (25) Qin, X.; Liu, X.; Huang, W.; Bettinelli, M.; Liu, X. Lanthanide-Activated Phosphors Based on 4*f*-5*d* Optical Transitions: Theoretical and Experimental Aspects. *Chem. Rev.* **2017**, *117* (5), 4488–4527.
- (26) de Jong, M.; Meijerink, A.; Seijo, L.; Barandiarán, Z. Energy Level Structure and Multiple 4*f*<sup>2</sup>5*d*<sup>1</sup> Emission Bands for Tm<sup>2+</sup> in Halide Perovskites: Theory and Experiment. *J. Phys. Chem. C* **2017**, *121* (18), 10095–10101.
- (27) Seijo, L.; Barandiarán, Z. The Ab Initio Model Potential Method: A Common Strategy for Effective Core Potential and Embedded Cluster Calculations. *Comput. Chem. Rev. CURR. TRENDS* **1999**, *4*, 55–152.

- (28) Hidalgo-Rosa, Y.; Treto-Suárez, M. A.; Schott, E.; Zarate, X.; Páez-Hernández, D. Sensing Mechanism Elucidation of a Europium(III) Metal–Organic Framework Selective to Aniline: A Theoretical Insight by Means of Multiconfigurational Calculations. *J. Comput. Chem.* **2020**, *41* (22), 1956–1964.
- (29) Calvello, S.; Piccardo, M.; Rao, S. V.; Soncini, A. CERES: An Ab Initio Code Dedicated to the Calculation of the Electronic Structure and Magnetic Properties of Lanthanide Complexes. *J. Comput. Chem.* **2018**, *39* (6), 328–337.
- (30) Becke, A. D. Density Functionals for Static, Dynamical, and Strong Correlation. *J. Chem. Phys.* **2013**, *138* (7), 074109.
- (31) Barandiarán, Z.; Seijo, L. Radial Correlation Effects on Interconfigurational Excitations at the End of the Lanthanide Series: A Restricted Active Space Second Order Perturbation Study of  $\text{Yb}^{2+}$  and  $\text{SrCl}_2:\text{Yb}^{2+}$ . *J. Chem. Phys.* **2013**, *138* (7), 074102.
- (32) Carlotto, A.; Babetto, L.; Carlotto, S.; Miozzi, M.; Seraglia, R.; Casarin, M.; Bottaro, G.; Rancan, M.; Armelao, L. Luminescent Thermometers: From a Library of Europium(III)  $\beta$ -Diketonates to a General Model for Predicting the Thermometric Behaviour of Europium-Based Coordination Systems. *ChemPhotoChem.* **2020**, *4* (9), 674–684.
- (33) ADF201 3.01 Program, SCM, Theoretical Chemistry, Vrije Universiteit, Amsterdam, The Netherlands, <http://www.scm.com>.
- (34) te Velde, G.; Bickelhaupt, F. M.; Baerends, E. J.; Fonseca Guerra, C.; van Gisbergen, S. J. A.; Snijders, J. G.; Ziegler, T. Chemistry with ADF. *J. Comput. Chem.* **2001**, *22* (9), 931–967.
- (35) Fonseca Guerra, C.; Snijders, J. G.; te Velde, G.; Baerends, E. J. Towards an Order-N DFT Method. *Theor. Chem. Acc.* **1998**, *99* (6), 391–403.
- (36) Veryazov, V.; Widmark, P. O.; Serrano-Andrés, L.; Lindh, R.; Roos, B. O. 2MOLCAS as a Development Platform for Quantum Chemistry Software. *Int. J. Quantum Chem.* **2004**, *100*, 626–635.
- (37) Aquilante, F.; Pedersen, T. B.; Veryazov, V.; Lindh, R. MOLCAS—a Software for Multiconfigurational Quantum Chemistry Calculations. *Wiley Interdiscip. Rev. Comput. Mol. Sci.* **2013**, *3* (2), 143–149.
- (38) Aquilante, F.; Autschbach, J.; Carlson, R. K.; Chibotaru, L. F.; Delecy, M. G.; De Vico, L.; Fdez. Galván, I.; Ferré, N.; Frutos, L. M.; Gagliardi, L.; Garavelli, M.; Giussani, A.; Hoyer, C. E.; Li Manni, G.; Lischka, H.; Ma, D.; Malmqvist, P. Å.; Müller, T.; Nenov, A.; Olivucci, M.; Pedersen, T. B.; Peng, D.; Plasser, F.; Pritchard, B.; Reiher, M.; Rivalta, I.; Schapiro, I.; Segarra-Martí, J.; Stenrup, M.; Truhlar, D. G.; Ungur, L.; Valentini, A.; Vancoillie, S.; Veryazov, V.; Vysotskiy, V. P.; Weingart, O.; Zapata, F.; Lindh, R. Molcas 8: New Capabilities for Multiconfigurational Quantum Chemical Calculations across the Periodic Table. *J. Comput. Chem.* **2016**, *37* (5), 506–541.
- (39) Perdew, J. P.; Burke, K.; Ernzerhof, M. Generalized Gradient Approximation Made Simple. *Phys. Rev. Lett.* **1996**, *77* (18), 3865–3868.
- (40) Perdew, J. P.; Wang, Y. Accurate and Simple Analytic Representation of the Electron-Gas Correlation Energy. *Phys. Rev. B: Condens. Matter Mater. Phys.* **1992**, *45* (23), 13244–13249.
- (41) Slater, J. C. A Simplification of the Hartree-Fock Method. *Phys. Rev.* **1951**, *81* (3), 385–390.
- (42) Dirac, P. A. M. Quantum Mechanics of Many-Electron Systems. *Proc. R. Soc. London A* **1929**, *123* (792), 714–733.
- (43) van Lenthe, E.; Baerends, E. J.; Snijders, J. G. Relativistic Total Energy Using Regular Approximations. *J. Chem. Phys.* **1994**, *101* (11), 9783–9792.
- (44) van Lenthe, E.; Ehlers, A.; Baerends, E.-J. Geometry Optimizations in the Zero Order Regular Approximation for Relativistic Effects. *J. Chem. Phys.* **1999**, *110* (18), 8943–8953.
- (45) van Lenthe, E.; Baerends, E. J.; Snijders, J. G. Relativistic Regular Two-component Hamiltonians. *J. Chem. Phys.* **1993**, *99* (6), 4597–4610.
- (46) Roos, B. O.; Lindh, R.; Malmqvist, P. Å.; Veryazov, V.; Widmark, P. O. Main Group Atoms and Dimers Studied with a New Relativistic ANO Basis Set. *J. Phys. Chem. A* **2004**, *108* (15), 2851–2858.
- (47) Roos, B. O.; Lindh, R.; Malmqvist, P. Å.; Veryazov, V.; Widmark, P. O.; Borin, A. C. New Relativistic Atomic Natural Orbital Basis Sets for Lanthanide Atoms with Applications to the Ce Diatom and  $\text{LuF}_3$ . *J. Phys. Chem. A* **2008**, *112* (45), 11431–11435.
- (48) Hess, B. A. Relativistic Electronic-Structure Calculations Employing a Two-Component No-Pair Formalism with External-Field Projection Operators. *Phys. Rev. A: At., Mol., Opt. Phys.* **1986**, *33* (6), 3742–3748.
- (49) Malmqvist, P. Å.; Roos, B. O.; Schimmelpfennig, B. The Restricted Active Space (RAS) State Interaction Approach with Spin-Orbit Coupling. *Chem. Phys. Lett.* **2002**, *357* (3–4), 230–240.
- (50) Heß, B. A.; Marian, C. M.; Wahlgren, U.; Gropen, O. A Mean-Field Spin-Orbit Method Applicable to Correlated Wavefunctions. *Chem. Phys. Lett.* **1996**, *251* (5–6), 365–371.
- (51) Finley, J.; Malmqvist, P. Å.; Roos, B. O.; Serrano-Andrés, L. The Multi-State CASPT2 Method. *Chem. Phys. Lett.* **1998**, *288* (2–4), 299–306.
- (52) Ghigo, G.; Roos, B. O.; Malmqvist, P. Å. A Modified Definition of the Zeroth-Order Hamiltonian in Multiconfigurational Perturbation Theory (CASPT2). *Chem. Phys. Lett.* **2004**, *396* (1–3), 142–149.
- (53) Wang, F.; Ziegler, T. The Performance of Time-Dependent Density Functional Theory Based on a Noncollinear Exchange-Correlation Potential in the Calculations of Excitation Energies. *J. Chem. Phys.* **2005**, *122* (7), 074109.
- (54) Wang, F.; Ziegler, T. Time-Dependent Density Functional Theory Based on a Noncollinear Formulation of the Exchange-Correlation Potential. *J. Chem. Phys.* **2004**, *121* (24), 12191–12196.
- (55) van Leeuwen, R.; Baerends, E. J. Exchange-Correlation Potential with Correct Asymptotic Behavior. *Phys. Rev. A: At., Mol., Opt. Phys.* **1994**, *49* (4), 2421–2431.
- (56) Babetto, L.; Carlotto, S.; Carlotto, A.; Rancan, M.; Bottaro, G.; Armelao, L.; Casarin, M. Antenna Triplet DFT Calculations to Drive the Design of Luminescent  $\text{Ln}^{3+}$  Complexes. *Dalt. Trans.* **2020**, *49* (41), 14556–14563.
- (57) From the ADF manual: spin–orbit coupling can be included, in a self-consistent way, in the TD-DFT calculation of excitation energies for closed-shell molecules. Excitation energies can be obtained for open-shell systems in a spin-unrestricted TD-DFT calculation including spin–orbit coupling in a perturbative way. This approximate method uses a single determinant for the open shell ground state. Note that the approximations made in this approximate method are much worse than for spin–orbit coupled TD-DFT for closed shell systems.
- (58) Reddy, M. L. P.; Divya, V.; Pavithran, R. Visible-Light Sensitized Luminescent Europium(III)- $\beta$ -Diketonate Complexes: Bioprobes for Cellular Imaging. *Dalt. Trans.* **2013**, *42* (43), 15249–15262.
- (59) Martins, J. P.; Martín-Ramos, P.; Chamorro-Posada, P.; Pereira Silva, P. S.; Martín-Gil, J.; Hernández-Navarro, S.; Ramos Silva, M. Experimental and Theoretical Studies on the Structure and Photoluminescent Properties of New Mononuclear and Homodinuclear Europium(III)  $\beta$ -Diketonate Complexes. *Adv. Condens. Matter Phys.* **2015**, *2015*, 1.
- (60) Raj, D. B. A.; Francis, B.; Reddy, M. L. P.; Butorac, R. R.; Lynch, V. M.; Cowley, A. H. Highly Luminescent Poly(Methyl Methacrylate)-Incorporated Europium Complex Supported by a Carbazole-Based Fluorinated  $\beta$ -Diketonate Ligand and a 4,5-Bis-(Diphenylphosphino)–9,9-Dimethylxanthene Oxide Co-Ligand. *Inorg. Chem.* **2010**, *49* (d), 9055–9063.
- (61) Tsuchiya, T.; Taketsugu, T.; Nakano, H.; Hirao, K. Theoretical Study of Electronic and Geometric Structures of a Series of Lanthanide Trihalides  $\text{LnX}_3$  ( $\text{Ln} = \text{La-Lu}$ ;  $\text{X} = \text{Cl, F}$ ). *J. Mol. Struct.: THEOCHEM* **1999**, *461–462*, 203–222.
- (62) Tsukamoto, S.; Mori, H.; Tatewaki, H.; Miyoshi, E. CASSCF and CASPT2 Calculations for Lanthanide Trihalides  $\text{LnX}_3$  Using Model Core Potentials. *Chem. Phys. Lett.* **2009**, *474* (1–3), 28–32.
- (63) Marx, R.; Moro, F.; Dörfel, M.; Ungur, L.; Waters, M.; Jiang, S. D.; Orlita, M.; Taylor, J.; Frey, W.; Chibotaru, L. F.; Van Slageren, J.

Spectroscopic Determination of Crystal Field Splittings in Lanthanide Double Deckers. *Chem. Sci.* **2014**, *5* (8), 3287–3293.

(64) Roemelt, M.; Neese, F. Excited States of Large Open-Shell Molecules: An Efficient, General, and Spin-Adapted Approach Based on a Restricted Open-Shell Ground State Wave Function. *J. Phys. Chem. A* **2013**, *117* (14), 3069–3083.

(65) Hund, F. Zur Deutung Verwickelter Spektren. II. *Eur. Phys. J. A* **1925**, *34* (1), 296–308.

(66) Ungur, L.; Chibotaru, L. F. Ab Initio Crystal Field for Lanthanides. *Chem. - Eur. J.* **2017**, *23* (15), 3708–3718.

(67) Binnemans, K. A Comparative Spectroscopic Study of  $\text{Eu}^{3+}$  in Crystalline Host Matrices. *Bull. Soc. Chim. Belg.* **1996**, *105* (12), 793–798.

(68) Tanner, P. A. Some Misconceptions Concerning the Electronic Spectra of Tri-Positive Europium and Cerium. *Chem. Soc. Rev.* **2013**, *42* (12), 5090–5101.

(69) The largest  $\Delta E$  corresponds to the inclusion of the  $^5L$  and  $^5G$  terms (run 4): the  $^5D_4$  state is not contiguous to the other  $^5D_J$  ( $J \neq 4$ ) states, and it is found among the states originated from  $^5L$  and  $^5G$  terms. Their inclusion is then needed not only because the  $^5L_0$  and  $^5G_0$  states directly mix with  $^5D_0$  one but also to obtain an appropriate description of the  $^5D$  term before the SOC is taken into account. The addition of the remaining quintet terms lowers the  $^5D_0$  energy from  $20055 \text{ cm}^{-1}$  to  $19676 \text{ cm}^{-1}$ . However, this was paid for with a significantly heavier computational effort (the CASPT2 module took 11 times longer than the one with only the  $^5D$ ,  $^5L$ , and  $^5G$  terms, while the RASSI module spent 21.5 times longer). The choice of considering the tradeoff of a small accuracy loss for significantly lower computational resources ultimately resides with the user.

# Multireference *ab initio* investigation on ground and low-lying excited states: systematic evaluation of J-J mixing in a $\text{Eu}^{3+}$ luminescent complex.

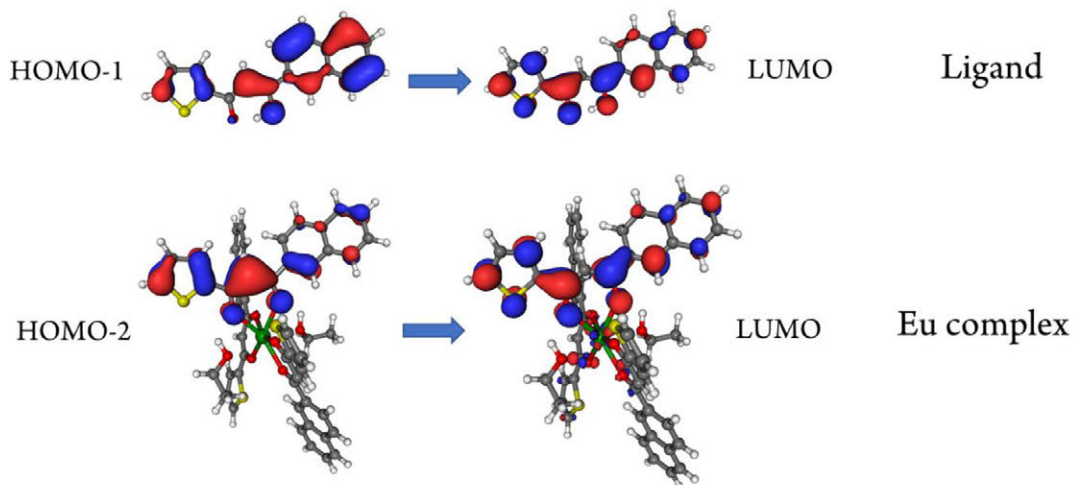
Luca Babetto,<sup>a</sup> Silvia Carlotto,<sup>a,b\*</sup> Alice Carlotto,<sup>a</sup> Marzio Rancan,<sup>b</sup> Gregorio Bottaro,<sup>b</sup> Lidia Armelao<sup>a,b</sup> and Maurizio Casarin<sup>a,b\*</sup>

<sup>a</sup>Dipartimento di Scienze Chimiche, Università degli Studi di Padova, via F. Marzolo 1, 35131 Padova, Italy.

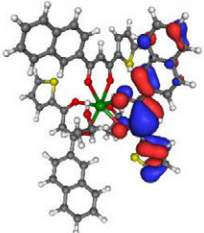
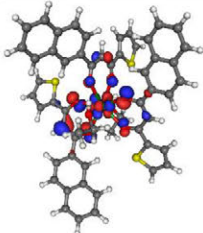
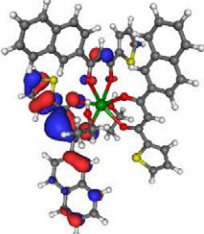
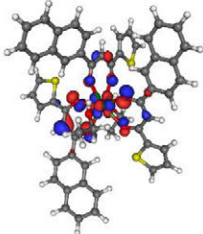
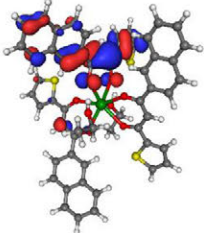
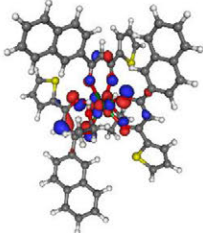
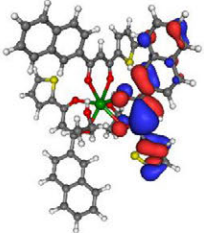
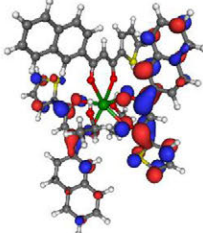
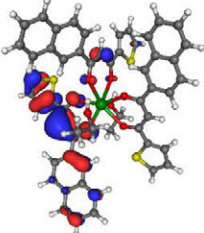
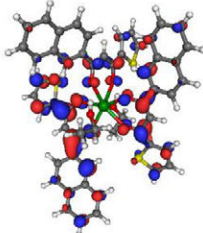
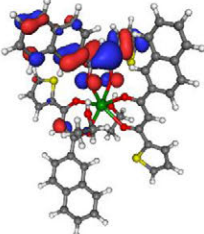
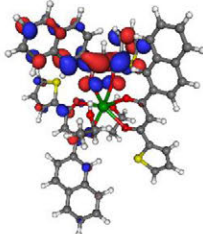
<sup>b</sup>Institute of Condensed Matter Chemistry and Technologies for Energy (ICMATE), National Research Council (CNR), c/o Department of Chemistry, University of Padova, via F. Marzolo 1, 35131 Padova, Italy

Correspondence: [silvia.carlotto@unipd.it](mailto:silvia.carlotto@unipd.it); [maurizio.casarin@unipd.it](mailto:maurizio.casarin@unipd.it)

**Figure S1.** Comparison between the orbitals involved in the most intense SAOP/TD-DFT transition for the ligand (top) and the Eu complex (bottom). Even in the complex the transitions are still fully localized on the ligand, and the nature of the orbitals involved is analogue as that of the isolated form.



**Table S1.** Most relevant SAOP/TD-DFT UV-Vis electronic transitions for the Eu complex. Only transitions in the 300 – 480 nm range with normalized intensities higher than 20% of the most intense transition have been included.

wavelength (nm)	normalised intensity	MO <sub>i</sub> → MO <sub>f</sub> (character)	MO <sub>i</sub>	MO <sub>f</sub>
418	0.30	HOMO → LUMO+6 (LMCT)		
412	0.34	HOMO-1 → LUMO+6 (LMCT)		
406	0.29	HOMO-2 → LUMO+6 (LMCT)		
403	0.24	HOMO → LUMO+1 (L-centred)		
400	0.73	HOMO-1 → LUMO+2 (L-centred)		
398	1	HOMO-2 → LUMO (L-centred)		



**Table S2.**  ${}^7F_j$  and  ${}^5D_0$  state energies (in  $\text{cm}^{-1}$ ) calculated at the RASSI-CAS(6,7)PT2 level for the  $\text{Eu}^{3+}$  free ion. Each  ${}^7F_j$  term for CAS calculations is taken as the barycentre of the respective manifold generated by crystal field splitting. Unfortunately, scalar relativistic TD-DFT/LB94 calculations systematically converge to fractional occupation numbers which are incompatible with the calculation of excitation energies in ADF. Forcing integer occupation numbers causes the SCF to not converge.

	CAS(6,7)	CAS(6,7)PT2	$\text{Eu}^{3+}$ free ion exp. <sup>5</sup>
Ground state			
${}^7F_0$	0	0	0
${}^7F_1$	382	406	379
${}^7F_2$	1104	1168	1043
${}^7F_3$	2099	2206	1896
${}^7F_4$	3292	3431	2869
${}^7F_5$	4625	4780	3912
${}^7F_6$	6062	6219	4992
Excited state			
${}^5D_0$	22778	20441	17227

**Table S3.**  ${}^5D_0$  state energies calculated at the RASSI-CAS(6,7)PT2 level for the  $\text{Eu}^{3+}$  free ion. The labels identifying the calculations are reported in the first column. In the second column, the number of states included for each spin (in parentheses) are reported. Experimental value for the  ${}^5D_0$  state energy is  $17227 \text{ cm}^{-1}$ .<sup>5</sup>

#	number of states (2S+1)	${}^5D_0 / \text{cm}^{-1}$
States with different multiplicities		
1	$7(7) + 5(5)$	20441
2	$7(7) + 5(5) + 3(3)$	18265
3	$7(7) + 5(5) + 3(3) + 1(1)$	18086
States with different multiplicities and different number of states		
1	$7(7) + 5(5)$	20441
4	$7(7) + 31(5)$	20383
5	$7(7) + 42(5)$	20354
6	$7(7) + 49(5)$	20325
7	$7(7) + 62(5)$	20296
8	$7(7) + 77(5)$	20253
9	$7(7) + 140(5)$	20081
10	$7(7) + 140(5) + 3(3)$	18019
11	$7(7) + 140(5) + 31(3)$	18018
12	$7(7) + 140(5) + 3(3) + 1(1)$	17850
13	$7(7) + 140(5) + 31(3) + 1(1)$	17852
14	$7(7) + 140(5) + 31(3) + 20(1)$	17852



## Nature of the Ligand-Centered Triplet State in $Gd^{3+}$ $\beta$ -Diketonate Complexes as Revealed by Time-Resolved EPR Spectroscopy and DFT Calculations

Silvia Carlotto,\* Luca Babetto, Marco Bortolus,\* Alice Carlotto, Marzio Rancan, Gregorio Bottaro, Lidia Armelao, Donatella Carbonera, and Maurizio Casarin

Cite This: *Inorg. Chem.* 2021, 60, 15141–15150

Read Online

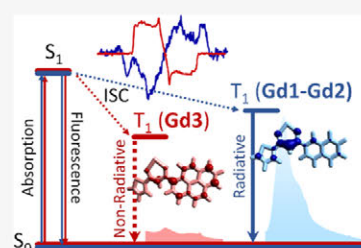
ACCESS |

Metrics & More

Article Recommendations

Supporting Information

**ABSTRACT:** A series of  $Gd^{3+}$  complexes ( $Gd1$ – $Gd3$ ) with the general formula  $GdL_3(EtOH)_2$ , where  $L$  is a  $\beta$ -diketonate ligand with polycyclic aromatic hydrocarbon substituents of increasing size (1–3), was studied by combining time-resolved electron paramagnetic resonance (TR-EPR) spectroscopy and DFT calculations to rationalize the anomalous spectroscopic behavior of the bulkiest complex ( $Gd3$ ) through the series. Its faint phosphorescence band is observed only at 80 K and it is strongly red-shifted ( $\sim 200$  nm) from the intense fluorescence band. Moreover, the TR-EPR spectral analysis found that triplet levels of  $3/Gd3$  are effectively populated and have smaller  $|D|$  values than those of the other compounds. The combined use of zero-field splitting and spin density delocalization calculations, together with spin population analysis, allows us to explain both the large red shift and the low intensity of the phosphorescence band observed for  $Gd3$ . The large red shift is determined by the higher delocalization degree of the wavefunction, which implies a larger energy gap between the excited  $S_1$  and  $T_1$  states. The low intensity of the phosphorescence is due to the presence of C–H groups which favor non-radiative decay. These groups are present in all complexes; nevertheless, they have a relevant spin density only in  $Gd3$ . The spin population analysis on NaL models, in which  $Na^+$  is coordinated to a deprotonated ligand, mimicking the coordinative environment of the complex, confirms the outcomes on the free ligands.



### INTRODUCTION

Excited triplet states of chromophore units play an important role in several photophysical and reactive phenomena. Among processes involving them, triplets are of paramount importance in the so-called antenna effect for the sensitization of lanthanide (Ln) ion emission,<sup>1</sup> as the energy gap between triplet and  $Ln^{3+}$  emitter levels is one of the key factors ruling the emission properties.<sup>1</sup> For instance, lanthanide luminescence-based thermometric features are tightly bound to the triplet state energy, in particular when the back-energy transfer is considered.<sup>2–7</sup> Besides its energy, the design of novel luminescent systems with tailored properties requires a detailed knowledge of the triplet spin distribution over the molecular skeleton. Indeed, energy transfer pathways are sometimes directly influenced by the specific spatial distribution of the spin density in the sensitizer ligand and by the triplet energy.<sup>8–10</sup> Moreover, the delocalization of the triplet state spin density can be related to the phosphorescence quantum yield, whose control is crucial in technological applications such as organic light-emitting diodes.<sup>11</sup>

To investigate the triplet formation mechanism, its population, the spin density distribution, time-resolved electron paramagnetic resonance (TR-EPR) spectroscopy, and quantum mechanical modeling have been herein combined. In general, the TR-EPR technique can be used to

monitor the evolution of short-lived spin states induced by light excitation<sup>12,13</sup> and can be applied to triplet,<sup>14</sup> quartet, and quintet states,<sup>15,16</sup> spin correlated radical pairs,<sup>17</sup> and charge-separated states.<sup>18,19</sup> More specifically, the triplet state TR-EPR spectroscopy provides information about (i) the triplet formation mechanisms from the sub-level populations, (ii) the delocalization and the symmetry of the triplet wavefunction through the zero-field splitting (ZFS) parameters, and (iii) the orientation of the transition dipole moment from magneto-photo selection effects.<sup>20</sup> Conversely, triplet formation and decay kinetics are not straightforwardly obtained from TR-EPR spectroscopy, being often overshadowed by the faster spin-relaxation.<sup>21</sup> It is well known that density functional theory (DFT) calculations are suitable for estimating EPR parameters such as the  $g$ -tensor.<sup>22</sup> However, the evaluation of ZFS parameters ( $D$  and  $E$ ) has proven to be much more challenging. As a matter of fact, the spin contamination has a

Received: April 12, 2021

Published: October 6, 2021



deep impact on the calculation accuracy, and spin-unrestricted DFT calculations are therefore advised against. The restricted open-shell (RO) approach does not suffer from spin contamination and, even though the wavefunction description might not be as accurate as with the unrestricted formalism, the resulting ZFS parameters are usually in better agreement with the experiment.<sup>23,24</sup> Furthermore, only spin–spin coupling needs to be taken into account for organic triplets as the spin–orbit contribution is negligible for these systems.<sup>23,24</sup> Before going on, it has to be remarked that DFT can reproduce trends in *D* and *E* parameters for a series of homologue molecules, but their absolute values are usually underestimated relative to the experimental ones.<sup>23,24</sup> Multi-reference methods such as complete active space self-consistent field (CASSCF) are a possible alternative to DFT, but they become impractical as the molecular size, and consequently the active space size, increases. Moreover, CASSCF and DFT calculations provide quite similar results on a wide variety of organic systems.<sup>23</sup>

In this work, a series of Gd<sup>3+</sup> complexes with the general formula GdL<sub>3</sub>(EtOH)<sub>2</sub>, where L is a  $\beta$ -diketone ligand with polycyclic aromatic hydrocarbon (PAH) substituents of increasing size (1–3, see Figure 1), have been investigated

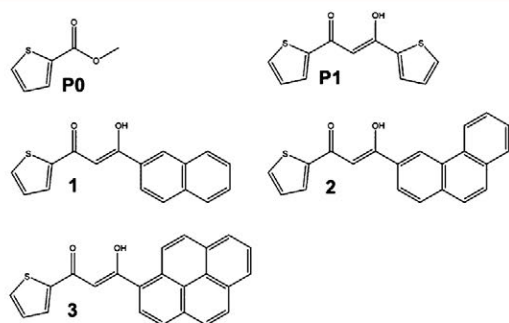


**Figure 1.** Chemical structures for precursors **P0** and **P1** bearing one and two thienyl rings, respectively, and ligands **1**, **2**, and **3** containing a thienyl ring and a PAH substituent of increasing size (naphthyl, phenanthryl, and pyrenyl).

along with two precursors (**P0** and **P1**, see Figure 1) bearing one and two thienyl rings, respectively, which were considered for assessing the contribution of the thienyl group to the triplet properties.

We started from the observation of the anomalous phosphorescence emission of the bulkiest complex (**Gd3**) compared to **Gd1** and **Gd2**. Indeed, the **Gd3** phosphorescence band is barely observed only at 80 K and red-shifted by  $\sim$ 200 nm from the most intense fluorescence band. Such a red shift decreases to  $\sim$ 100 nm in **Gd1** and **Gd2**, whose phosphorescence spectra are clearly visible also at room temperature (RT). Since the origin of the anomalous spectroscopic behavior of **3/Gd3** compared to the other compounds might be due to the nature of the triplet states, TR-EPR spectroscopy and DFT calculations have been exploited in an integrated fashion to look into this matter.

## RESULTS AND DISCUSSION

Structural, vibrational, and electronic properties of ligands 1–3 have been recently investigated by combining DFT-based methods with X-ray crystallographic data and UV–Vis

absorption spectra.<sup>2</sup> In particular, the analysis of X-ray structures revealed, in agreement with DFT outcomes, the presence of different rotational isomers for the ligands. Triplet energies<sup>2</sup> were theoretically estimated and the corresponding results compared with the phosphorescence spectra of Gd<sup>3+</sup> complexes. Further investigations on the emission spectra of **GdP1** and **Gd1–Gd3** complexes reveal relevant differences through the series (from **GdP1** to **Gd1–Gd3**). Indeed, both fluorescence and phosphorescence bands are present at RT for **GdP1**, **Gd1**, and **Gd2** (Figure 2). The polystyrene films in which the complexes were embedded provided a sufficiently rigid matrix to hamper vibrational motion, thus allowing the observation of phosphorescence bands even at RT. Cooling the sample down to 80 K strongly modifies the relative intensity of fluorescence and phosphorescence bands, with the latter becoming the dominant contribution in the photoluminescence spectra of **GdP1**, **Gd1**, and **Gd2**. Conversely, the **Gd3** 80 K phosphorescence emission is barely observable at wavelengths longer than 630 nm and it appears red-shifted by approximately 200 nm from the intense fluorescence band. For the other complexes, this shift is approximately 100 nm. This evidence cannot be explained by simply considering the emission data and the calculations of the energy of the ground (singlet) and triplet states.<sup>2</sup> Insights into such a peculiar behavior may be gained by combining TR-EPR spectroscopy with DFT calculations.

TR-EPR spectra of **P1**, 1–3 and **GdP1**, **Gd1–Gd3** in frozen solutions (80 K) are reported in Figure 3, while simulated TR-EPR spectra for ligands and complexes are displayed in Figures S1 and S2 of the Supporting Information. As far as the simulation parameters are concerned, they are collected in Table 1. Spectra simulations allowed us to obtain: (i) ZFS parameters of the triplet states; (ii) populations of the triplet sublevels (spin polarizations); and (iii) the relative amount of different triplet spectral contributions when more than one is present. Only relative spectral contributions can be evaluated since the absolute intensity of a TR-EPR spectrum depends on spin polarization, on the extinction coefficient of different species at the excitation wavelength (see Figure S3 in the Supporting Information), and on several hard to control experimental parameters. Moreover, absolute values of ZFS parameters are reported in Table 1 because the direct experimental determination of the *D* and *E* signs was beyond the scope of this work and far from trivial.<sup>25</sup> Nevertheless, as the software package employed for simulations needs the sign for the ZFS parameters, a negative sign for *D* and *E* has been adopted based on the results of DFT calculations (*vide infra*); thus, the three triplet sublevels in order of increasing energy are  $T_y$ ,  $T_x$ , and  $T_z$  (see also Figure 4).

The lineshape analysis of the **GdP1** and **Gd1–Gd3** TR-EPR spectra suggests that triplet states are populated *via* intersystem crossing (ISC) from the first excited singlet state rather than singlet fission or recombination of a radical pair as these would both lead to drastically different polarizations (and thus lineshapes).<sup>13,25</sup> The **GdP1** TR-EPR spectrum is dominated by a single triplet species (only the wings of a second larger species are visible as highlighted by the green bands in Figure 3), while the **Gd1** and **Gd2** ones are consistent with the presence of two triplet species (the simulations of the individual species are reported in Figure S2 of the Supporting Information). The **Gd3** spectrum is characterized by the presence of a single triplet state. The presence of multiple triplet species for **Gd1** and **Gd2** cannot be attributed to the

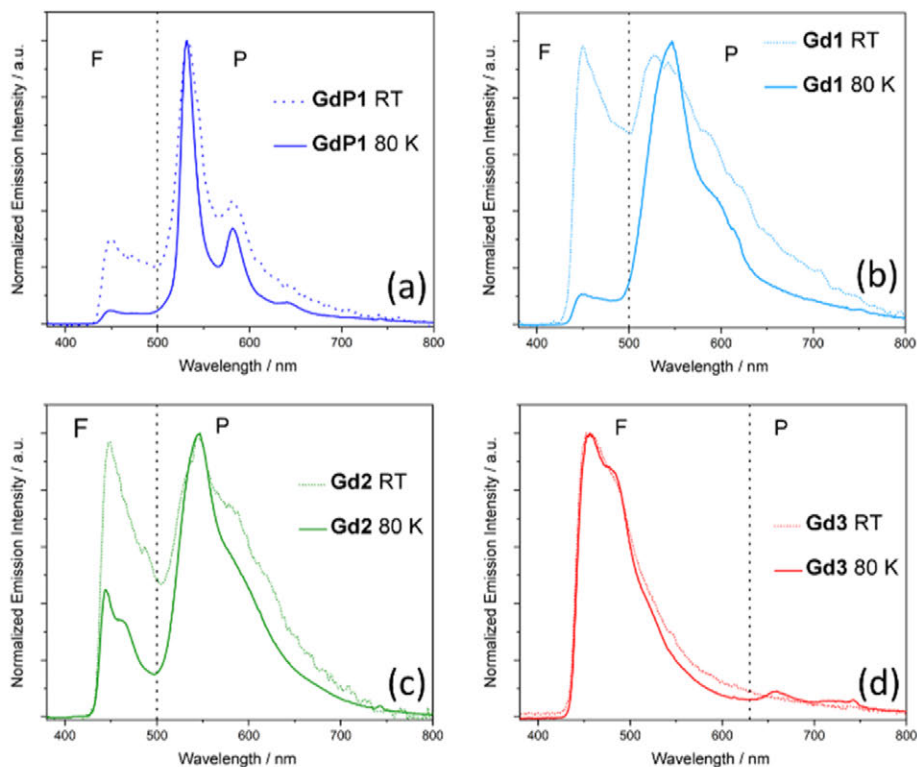


**Figure 2.** Emission spectra of (a) GdP1 and (b–d) Gd1–Gd3 complexes at RT and at 80 K. Vertical dashed lines are a guide to the eye to better visualize the region in which the most intense fluorescence (F) and phosphorescence (P) bands are located.

contributions from higher excited triplet states ( $T_2$ ,  $T_3$ , ...) since these would relax to  $T_1$  too quickly to be detected by TR-EPR. They may be ascribed to different rotamers—whose presence was previously observed from the X-ray structures<sup>2</sup>—with a different delocalization of the triplet wavefunction and thus different ZFS parameters.

To disentangle the role of the  $Gd^{3+}$  ion on the observed triplet states properties, TR-EPR spectra of the free ligand have also been recorded. The P1/GdP1, 1/Gd1, and 2/Gd2 spectra and parameters are very similar, thus indicating a marginal role played by the  $Ln^{3+}$  ion. The largest variations involve the triplet sublevel population ratios, thus suggesting that the metal ion modifies only the triplet sublevel population, that is, it affects the ISC process. Since the presence of  $Gd^{3+}$  does not perturb the ZFS parameters of the triplet state and only the relative amounts of the rotamers are possibly affected, their conformation (and thus spin distribution) remains unchanged in the complexes. On the contrary, when the 3/Gd3 pair is considered, markedly different spectra and parameters are observed (*vide infra*), suggesting a structural conformational change induced by the complex formation.

Energies of the triplet sublevels ( $T_x$ ,  $T_y$ , and  $T_z$ ) relative to the triplet state energy (dashed line) are displayed for P1, 1–3 in Figure 4, where black bars refer to the main species, while orange bars refer to the minority species. Both Figure 4 and Table 1 highlight that  $|D|$  values decrease upon increasing the PAH size (P1, 1  $\rightarrow$  3), while a clear trend is not evident for  $E$ . As such, the decrease of  $D$  along the series accounts for a progressively broader delocalization of the triplet wavefunction over the molecular skeleton (see the spin densities for the main

species on the top of Figure 4). The trend in the ZFS parameters can be analyzed in terms of the  $E/D$  ratio (see Table 1), which indicates the symmetry of the spin distribution, from purely axial ( $E/D = 0$ ) to fully rhombic ( $E/D = 1/3$ ). The main spectral species show a clear reduction of the  $E/D$  ratio moving along the series, indicating a progressively more axial distribution, from P0/P1 to 1/2 (and the corresponding complexes), but again the 3/Gd3 pair deviates from this trend. Further information about the roles played by the thienyl and PAH fragments has been gained by recording and simulating the TR-EPR spectra of P0, a precursor only bearing the thienyl moiety. Experimental and simulated spectra of P0 are reported in Figure S1 of the Supporting Information, while the relative ZFS parameters are reported in Table 1. The triplet species of 1 is narrower ( $|D| = 0.098 \text{ cm}^{-1}$ ) than that observed for P0, thus indicating a larger delocalization; however,  $|D|$  for P1 is not greatly reduced compared to P0 as it could be expected if the triplet state were fully delocalized from one thienyl ring to the other in P1. Such evidence necessarily implies that the two thienyl rings of P1 are not equivalent. In this regard, it is worth mentioning that the reduction of the ZFS in conjugated structures with progressively increasing repeating units depends not only on the extent of the delocalization but also on the ZFS axes' direction.<sup>26</sup> Moreover,  $|D|$  values pertaining to the main triplet species in 1 ( $|D| = 0.092 \text{ cm}^{-1}$ ) and 2 ( $|D| = 0.090 \text{ cm}^{-1}$ ) and to the only species in 3 ( $|D| = 0.073 \text{ cm}^{-1}$ ) are similar but slightly smaller than those of the corresponding PAH<sup>27</sup> (naphthalene,  $|D| = 0.101 \text{ cm}^{-1}$ , for 1; phenanthrene,  $|D| = 0.105 \text{ cm}^{-1}$ , for 2; pyrene,  $|D| = 0.086 \text{ cm}^{-1}$ , for 3). Such a

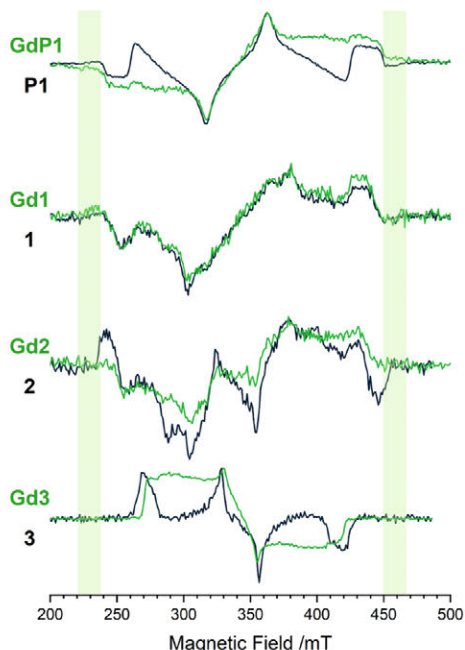


**Figure 3.** TR-EPR spectra ( $\lambda_{\text{exc}} = 355$  nm) of the precursor **P1** and ligands **1–3** (black lines) and  $\text{Gd}^{3+}$  complexes **GdP1**, **Gd1–Gd3** (green lines) in frozen toluene solution at the X-band ( $\nu = 9.705$  GHz),  $T = 80$  K. The green side-bands correspond to the maximum width of the spectra of **GdP1**, **Gd1**, and **Gd2** (equal to  $2|D| \times h/g\mu_B$ ) and highlight the progressive narrowing of the EPR spectra.

**Table 1.** Triplet Parameters Obtained from the Simulations of the TR-EPR Spectra when Two Species are Present; Each Row Reports Two Sets of Parameters<sup>a</sup>

	$ D $	$ E $	$ E/D $	$P_x/P_y/P_z$	%
<b>P0</b>	0.111	0.030	0.270	0.80:0.00:0.20	100
<b>P1</b>	0.098	0.019	0.194	0.00:0.49:0.51	>95
	0.111	n.d.	n.d.	n.d.	n.d.
<b>GdP1</b>	0.098	0.019	0.194	0.00:0.39:0.61	>95
	0.111	n.d.	n.d.	n.d.	n.d.
<b>1 &amp; Gd1</b>	0.092	0.017	0.185	0.00:0.00:1.00	63
	0.111	0.013	0.117	1.00:0.00:0.00	37
<b>2</b>	0.090	0.008	0.089	0.07:0.00:0.93	62
	0.100	0.024	0.240	0.93:0.07:0.00	38
<b>Gd2</b>	0.090	0.008	0.089	0.00:0.02:0.98	73
	0.100	0.024	0.240	0.90:0.00:0.10	27
<b>3</b>	0.074	0.016	0.216	0.79:0.21:0.00	100
<b>Gd3</b>	0.070	0.016	0.229	0.49:0.51:0.00	100

<sup>a</sup>Absolute values of the ZFS parameters  $|D|$  and  $|E|$  ( $\text{cm}^{-1}$ );  $|E/D|$  ratio; triplet sublevel population ( $P_x$ ,  $P_y$ , and  $P_z$ ); relative amount of each spectral component (%). The  $g$  tensor for all is  $g_{xx} = 2.006$ ,  $g_{yy} = g_{zz} = 2.009$ . n.d. = not determined.

result seems to indicate that in the main species of the asymmetric ligands, the wavefunction is delocalized on both the  $\beta$ -diketone part and the PAH moiety without any involvement of the thienyl ring. Note that a triplet state delocalized over most of the ligand molecules represents a prolate spin density distribution, which implies a negative  $D$  parameter as found by the DFT calculations (*vide infra*).<sup>25</sup>

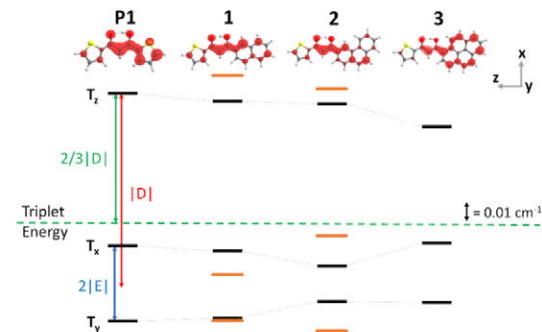


**Figure 4.** Top, the spin delocalization of the triplet state in the main conformer of the precursor **P1** and ligands **1–3**. The axes describe the orientation of the main ZFS reference frame relative to the molecular skeleton for all the molecules (see Figure S4 of the Supporting Information for details). Gray, yellow, red, and white spheres are C, S, O, and H atoms, respectively. Bottom, energies of the triplet sublevels ( $T_x$ ,  $T_y$ , and  $T_z$ ) relative to the triplet energy (green dashed line) based on the  $|D|$  and  $|E|$  experimental values for the precursor **P1** and all ligands (in  $\text{cm}^{-1}$ ). The scheme has been drawn using the signs of the ZFS parameters obtained from the calculations ( $D < 0$ ;  $E < 0$ ). Black and orange bars represent the different species where the former is the species with the highest spectral percentage.

TR-EPR spectra and their analysis also provide useful information to rationalize the **GdP1** and **Gd1–Gd3** fluorescence and phosphorescence measurements. In this regard, (i) the **3/Gd3** spectra confirm that the corresponding triplet levels are effectively populated; hence, the low phosphorescence cannot be associated with the difficulty of populating the triplet state; (ii) the lowest  $|D|$  values in **3/Gd3** clearly indicate the largest delocalization among the ligands. As a whole, TR-EPR spectra of **3/Gd3** do not show any evidence that may justify the very weak phosphorescence emission, even in a rigid matrix, at 80 K.

Taking these results as a starting point, we performed a series of DFT numerical experiments to investigate the triplet states through the evaluation of ZFS parameters and to gain insights into the spin delocalization. The latter aspect is crucial because the delocalization of the triplet state spin density provides information about the possible regions of the molecules where the spin–orbit coupling may occur.<sup>11</sup> The large similarity observed between the ZFS parameters of the complexes and those of the free ligands supports the commonly accepted assumption that in  $\text{Ln}^{3+}$  antenna complexes, the excitation is localized on the ligands and the emission on the lanthanide. This implies that the central metal and the ligands are mostly independent, and electronic properties are substantially unaffected upon moving from the isolated fragments to the complex.<sup>2,28,29</sup> Thus, the smaller size of the free ligand compared to that of the corresponding complex allows the estimation of ligand ZFS parameters through more accurate calculations, and the results can be then transferred to their  $\text{Gd}^{3+}$  complexes.

Before discussing the results of the ZFS calculations pertaining to ligands, it is crucial to underline the similarities and the differences of the optimized structures for the **P1**, **1–3/GdP1**, and **Gd1–Gd3** pairs. Experimental crystal structures of **P1** and **1–3** are reported in the literature.<sup>6</sup> The comparison between ground-state optimized geometries for **P1**, **1–3** and **GdP1**, **Gd1–Gd3** reveals that, in **P1**, **1** and **2** and **GdP1**, **Gd1**, and **Gd2**, the PAH groups have almost the same orientation.

Indeed, the **GdP1**, **Gd1**, and **Gd2** average dihedral angles  $\Phi$  (defined as C1–C2–C3–C4, Figure 5) are 4, 20, and 27°,

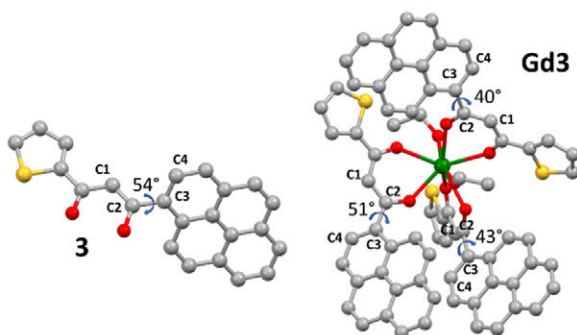


**Figure 5.** Comparison between the pyrenyl group orientations in **3** and **Gd3**. Gray, yellow, red, and green spheres are C, S, O, and La atoms, respectively. H atoms are omitted for clarity. Dihedral angles are given in degrees.

respectively, and are very close to the values of **P1**, **1**, and **2** ( $\Phi = 0, 20,$  and  $23^\circ$ , respectively). At variance to that, the bulky pyrenyl group in **Gd3** and **3** is characterized by significantly different twist angles (average  $\Phi = 45^\circ$  in the former,  $\Phi = 54^\circ$  in the latter) to favor the coordination of three ligands to the  $\text{Gd}^{3+}$  (see Figure 5). Different  $|D|$  values in **3** and **Gd3** are then tentatively ascribed to the diverse  $\Phi$  angles upon moving from **3** and **Gd3**.

To evaluate ZFS parameters, triplet geometries for **P0/P1** and **1–3** have been optimized. Experimental crystal structures of **P1** and **1–3** are consistent with the presence of multiple rotamers differing for the relative orientation of the aromatic rings.<sup>2</sup> Triplet geometries needed for ZFS parameters have therefore been optimized for all four possible rotamers, herein labeled A, B, C, and D (see Figure S5 of the Supporting Information). B and C rotamers may be obtained by flipping either the thienyl moiety (B) or the PAH fragment (C) of the predominant species A. Rotamer D is generated by flipping both the thienyl group and the PAH fragment. Relative energies of optimized structures are systematically within 2 kcal/mol of the most stable rotamer. The relatively low energy barriers for the rotation of the aromatic fragment around the bond with the diketone moiety suggest a substantially free ring rotation in solution and thus the presence of all possible

rotamer configurations.<sup>30</sup> The detailed description of the calculations for rotational barriers and their values have been reported in a previous work.<sup>2</sup> Experimental and theoretical  $|D|$  and  $|E|$  triplet values for all possible rotamers of **P0/P1** and **1–3** are reported in Table 2.

Two different functionals, GGA-(BP86) (in Table 2) and hybrid (B3LYP), have been tested and the results are very similar (Table S2 of the Supporting Information). In agreement with the literature,<sup>23</sup> theoretical calculations of  $D$  and  $E$  underestimate the experimental values by  $\sim 30\text{--}40\%$ ; nevertheless, the  $|D|$  trend through the series, similar values for **P1**, **1**, and **2** and a much lower value for **3**, is satisfactorily reproduced. The experimental trend of the  $E/D$  ratio is not well reproduced moving along the series, but interestingly it shows that A/B conformers, in general, have a more axial distribution, whereas C/D conformers have a more rhombic distribution. A similar behavior has been observed experimentally when two species are present, that is, the main species is more axial while the minor species is more rhombic. It has already been mentioned that TR-EPR spectra of **1** and **2** suggest the presence of two species, while those of **P0/P1** and **3** are consistent with the occurrence of a single species. This perfectly matches the RO-BP86 results (see Table 2): in **P0**, **P1**, and **3**,  $D$  and  $E$  values corresponding to the relevant species of **P0/P1** and **3** are very close; meanwhile, for **1** and **2**, the ZFS parameters of A/B rotamers significantly differ from those of the C/D ones, consistent with the presence of two magnetically active species. The hypothesis that different rotamers with different spin delocalizations<sup>31</sup> and ZFS parameters contribute to the TR-EPR spectra is then fully supported by DFT calculations.

The different  $D$  and  $E/D$  parameters in A/B and C/D rotamers imply different spin densities (whose 3D plot are displayed in Figure 6). More specifically, the spin density analysis of the **P0/P1**, **1–3** rotamer A reveals that: (i) the spin density on the thienyl moiety decreases upon increasing the PAH size; (ii) the diketone fragment of all but one ligand (**3**) is always populated; and (iii) the spin density values are only slightly affected by the PAH size. Despite the fact that the  $|D|$  trend is properly reproduced for **P1**, **1–3**, we cannot be silent about a minor discrepancy between experiment ( $|D(\text{P1})| > |D(\text{1})|$ ) and theory ( $|D(\text{P1})| \approx |D(\text{1})|$ ). Indeed, the spin density on the thienyl ring (enol side) in **P1** appears too high compared to the other ring.

**Table 2.** ZFS Parameters  $D$  and  $E/D$  for All Rotamers of **P0**, **P1**, and **1–3**<sup>a</sup>

		RO-BP86		experimental	
		$D$ (%)	$E/D$	$ D $ (%)	$ E/D $
<b>P0</b>	A/B	−0.070(21)/−0.071(79)	0.329/0.324	0.111	0.270
<b>P1</b>	A/B	−0.067(42)/−0.068(27)	0.209/0.206	0.098	0.194
	C <sup>b</sup> /D	−0.068(27)/−0.080(4)	0.206/0.125		
<b>1</b>	A/B	−0.071(5)/−0.081(3)	0.085/0.062	0.092(63)	0.185
	C/D	−0.048(56)/−0.048(36)	0.292/0.208	0.111(37)	0.117
<b>2</b>	A/B	−0.070(20)/−0.070(13)	0.100/0.100	0.090(62)	0.089
	C/D	−0.050(41)/−0.049(26)	0.280/0.286	0.100(38)	0.240
<b>3</b>	A/B	−0.039(20)/−0.039(17)	0.128/0.179	0.074	0.216
	C/D	−0.031(36)/−0.031(27)	−0.226/0.226		

<sup>a</sup> $D$  parameter is given in  $\text{cm}^{-1}$ . Calculated RO-BP86% are taken on the optimized triplet-state geometries considering the energy difference between the rotamers (A/B/C/D) according to a Boltzmann population at 298.15 K and are reported in parentheses in the  $D$  column. <sup>b</sup>For **P1**, with two thienyl rings, the B and C rotamers are equal.

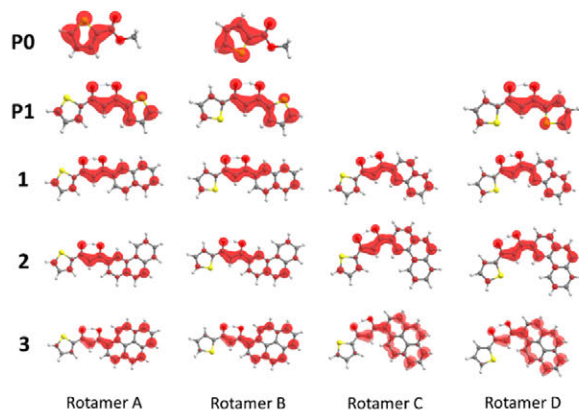


**Figure 6.** Spin densities of all rotamers for **P0**, **P1**, and **1–3** calculated at the RO-BP86 level. The displayed isosurfaces correspond to  $0.003 \times 10^{1/2} \times \text{\AA}^{-3/2}$  values. Gray, white, yellow, and red spheres are C, H, S, and O atoms, respectively. For **P1** with two thienyl rings, the B and C rotamers are equal.

Spin density differences can be qualitatively evaluated by considering Lüdwin<sup>32</sup> or Mulliken<sup>33</sup> spin populations. The spin density is a function of the three-dimensional space and the spin populations simply correspond to the spin density breakdowns onto the atoms, making it possible to assign percentage values (see Table S3 of the Supporting Information) to different fragments. The spin population is mainly localized on the diketone moiety in **P1**, **1**, and **2**, while a pronounced spin density shift on the PAH fragment takes place in **3**. More specifically, the spin density % localization on the diketone decreases from ~50 to ~20% upon moving from **P1**, **1**, and **2** to **3** while on the PAH fragment, it increases from ~40 to >70%. These outcomes are consistent with both the larger phosphorescence red shift observed for **Gd3** and its lower phosphorescence yield. As far as the former point is concerned, a higher degree of delocalization in the wavefunction with respect to the other ligands (see Figure 6) results in a higher stabilization for the corresponding triplet state and therefore a larger energy gap between the excited  $S_1$  and  $T_1$  states, that is, a larger shift between the fluorescence and phosphorescence bands.<sup>34,35</sup> Indeed, while paired electrons mostly repel each other *via* Coulomb interaction, the exchange term, which characterizes electrons with the same spin, is less pronounced as the delocalization of the wavefunction increases, therefore stabilizing the corresponding triplet states for a relatively more delocalized triplet (pyrene) compared to a more localized one (diketone). Moving to the latter point, the low intensity of the phosphorescence band can be associated with relevant non-radiative triplet decay pathways. The efficiency of the non-radiative decay processes is tied to two quantities: the energy gap between the two electronic states of interest (in our case  $T_1$  and  $S_0$ ) and the presence of high-energy oscillators. This relation<sup>36</sup> has been successfully applied to several systems to explain the phosphorescence trend of a series of conjugated polymers and monomers<sup>37</sup> or the luminescence efficiencies of transition-metal complexes.<sup>38</sup>

High-energy oscillators such as the C–H stretching mode have already been proven to cause lower phosphorescence yields and excited state lifetimes in similar organic compounds.<sup>39,40</sup> However, our DFT outcomes demonstrate that the mere presence of a high-energy oscillator is not enough to

explain this behavior. Indeed, the **P1** precursor and all ligands **1–3** feature C–H groups able to contribute to non-radiative decay, but they have different phosphorescence yields. This is because in **P1**, **1**, **2/GdP1**, **Gd1**, and **Gd2** the spin density is primarily localized on the diketone fragment, where only a single C–H oscillator is present (Figure 6 and Table S3 of the Supporting Information), whereas in **3/Gd3**, the triplet is localized on the C–H oscillator of the pyrenyl moiety. In our case, therefore, the combination of a more stable triplet state in **3/Gd3** and the presence of a high number of C–H oscillators in the pyrenyl fragment bearing the spin density contributes to significantly more efficient non-radiative decay processes compared to **P1**, **1**, **2/GdP1**, **Gd1**, and **Gd2**.

Results so far obtained provide information about the origin of the anomalous behavior of the **Gd3** phosphorescence spectra, both in terms of intensity and red shift. Aimed to better model the  $\text{Gd}^{3+}$  coordinative environment and to obtain also a quantitative agreement with experimental data, the deprotonated ligand ( $L^-$ ) has been coordinated to a  $\text{Na}^+$  ion (see Figure S7 of the Supporting Information where the **Na1** model is displayed) for a further series of numerical experiments. The triplet geometries of the **NaP1** and **Na1–Na3** models have been optimized for all rotamers. *D* and *E/D* values for rotamer A are reported in Table 3, while values for all the rotamers are collected in Table S4 of the Supporting Information.

**Table 3.** Calculated ZFS Parameters *D* and *E/D* for **P1**, **1–3**, for **NaP1**, **Na1–Na3** Models (Rotamer A) and **GdP1**, **Gd1–Gd3** in the Lowest Energy Triplet State<sup>4</sup>

	<i>D</i> ( <i>E/D</i> )			<i>D</i>   ( <i>E/D</i> )	
	calculated			experimental	
	L	NaL model	$\text{Gd}^{3+}$ complex	L	$\text{Gd}^{3+}$ complex
<b>P1</b>	−0.067 (0.209)	−0.078 (0.137)	−0.072 (0.111)	0.098 (0.194)	0.098 (0.194)
<b>1</b>	−0.071 (0.085)	−0.080 (0.114)	−0.072 (0.107)	0.092 (0.185)	0.092 (0.185)
<b>2</b>	−0.070 (0.100)	−0.072 (0.097)	−0.073 (0.068)	0.090 (0.089)	0.090 (0.089)
<b>3</b>	−0.039 (0.128)	−0.040 (0.118)	−0.036 (0.117)	0.074 (0.216)	0.070 (0.229)

<sup>a</sup>*D* parameter is given in  $\text{cm}^{-1}$ . Absolute experimental values for ligand and  $\text{Gd}^{3+}$  complexes are reported for comparison. Level of theory: RO-BP86.

The inspection of Table 3 highlights a better agreement between experiment and theory, particularly evident for the smallest models (**NaP1** and **Na1**), suggesting that the constraints induced by the sodium coordination are sufficient to improve the agreement. The poorer enhancement characterizing bulkier models, especially **Na3**, is probably due to the larger geometrical variations between the isolated and the coordinated ligand in the whole complex, which is not captured by the simplified model. This assumption was demonstrated for singlet ground-state  $\text{Gd}^{3+}$  complex geometries, where the dihedral angles are compared (see above). The comparison between the rotamer spin densities for **P1**, **1–3** (Figure 6) and **NaP1**, **Na1–Na3** optimized triplet states (Figure S8 of the Supporting Information) reveals that the **NaP1** and **Na1** spin density is more localized on the diketone moiety with respect to the free ligand one. Negligible variations are instead found for larger models (**Na2** and **Na3**). Spin



population analysis was also performed for the NaP1 and Na1–Na3 models and the outcomes are very similar to the ligand ones. Not only the trend is the same, but the percentage values themselves are close (see Table S3 of the Supporting Information).

Calculations of ZFS parameters have been extended to the deprotonated ligands ( $L^-$ , rotamer A) as well in order to evaluate the effect of the counterion ( $H^+$  or  $Na^+$ ).  $D$  values of  $L$  and  $L^-$  clearly indicate a better agreement for the former species (see Table S5 of the Supporting Information). As such, it is noteworthy that the deprotonated species 3 has the highest  $|D|$  value, while, according to the experiments, the protonated form 3 has the lowest  $|D|$  value. Analogous considerations hold for spin densities (see Figure S9 of the Supporting Information). The presence/absence of the proton slightly affects the spin density distribution of P1 and 1, whereas it strongly influences that of 2 and 3. Similar trends can be drawn by comparing  $L^-$  and NaL. The  $H^+/Na^+$  coordination to the O atom is then crucial for reproducing the experimental trend.

The last computational step concerned the evaluation of GdP1 and Gd1–Gd3 ZFS parameters. Optimized geometries of the lowest energy triplet states have been obtained and the corresponding ZFS relative parameters are collected in Table 3. The comparison between the calculated and the experimental ZFS values of GdP1, Gd1–Gd3/NaP1, and Na1–Na3 reveals that the best qualitative and quantitative agreement is obtained for NaP1 and Na1–Na3 models. This suggests that calculations on the  $Gd^{3+}$  complexes are unnecessary, and a simpler model, able to correctly mimic the ligand coordination to a central ion, is more than sufficient.

## CONCLUSIONS

A series of  $\beta$ -diketone ligands featuring a thienyl ring and a PAH fragment of varying size and their  $Gd^{3+}$  complexes has been investigated to rationalize the different behavior of the emission spectra for the largest system (Gd3). Indeed, its phosphorescence band is only barely observed at 80 K and a large red shift with respect to the fluorescence band is revealed. To gain information on the triplet states and to explain the spectral trend, all ligands and complexes have been investigated both experimentally and theoretically by combining TR-EPR spectroscopy and DFT calculations. TR-EPR spectra of the  $Gd^{3+}$  tris- $\beta$ -diketonate complexes for P1, 1, and 2 are similar to those of the free species, ultimately stating that the triplet nature is unchanged upon complexation. The different behavior of the 3/Gd3 pair is attributed to a different twist of the pyrenyl group in the free ligand compared to the coordinated one, as highlighted by DFT outcomes. Moreover, TR-EPR spectra found that the triplet populations in 3 and Gd3 are significant; hence, the low phosphorescence intensities observed are not due to the low triplet yield. The smallest  $|D|$  values of 3 and Gd3 found by TR-EPR analysis suggested a broader electron spin density delocalization on the ligands.

Starting from these results, DFT calculations for estimating the ZFS parameters have been performed on (i) free ligands; (ii) a model with the deprotonated ligands coordinated to a  $Na^+$  ion; (iii) the deprotonated ligands; and (iv) the  $Gd^{3+}$  complexes. Calculated ZFS parameters confirmed the smallest  $D$  values for 3 and Gd3 and also a larger delocalization on the PAH moiety. The combination of ZFS calculations, spin density delocalization, and spin population analysis clearly shows the different behavior of 3 and Gd3 with respect to the

other ligands and complexes, which can explain the low intensity of the phosphorescence band and the large red shift of Gd3. Indeed, the latter derives from the high degree of delocalization of the wavefunction of Gd3. An extended delocalization implies a larger triplet state stabilization and hence a larger energy gap between the excited  $S_1$  and  $T_1$  states. The low intensity of the phosphorescence band suggests the presence of very relevant non-radiative triplet decay, which is favored by the lower energy of the  $T_1$  state and the presence of C–H groups. All  $Gd^{3+}$  complexes have a relevant number of C–H groups in the aromatic fragments, but DFT spin density calculations found that only in Gd3, the spin density is localized on these groups, hence contributing to the non-radiative decay process. Results concerning the spin density and spin populations analysis on the different fragments of the ligand show that (i) high energy oscillators (i.e., C–H groups) may play a significant role in the non-radiative decay process, but (ii) the mere presence of these groups is not a sufficient condition to rationalize their behavior since they must also carry a relevant spin density. These outcomes could be relevant to drive the design of novel systems in which the non-radiative decay paths from the triplet states can be tuned and controlled.

## EXPERIMENTAL SECTION

**Synthesis and Characterization.** Synthesis and characterization of the precursor P1 and ligands 1 and 2 (see Figure 1) and corresponding  $Gd^{3+}$  complexes (GdP1, Gd1, and Gd2) are reported in ref 6, while those of 3 and Gd3 are thoroughly described in ref 2. Emission spectra were collected with a Horiba Fluorolog 3 spectrofluorometer. GdP1 and Gd1–Gd3 were embedded in polystyrene thin films and deposited via spin-coating on  $10 \times 10$  mm<sup>2</sup> fused silica slides.<sup>6</sup> Temperature was controlled by using a Linkam THMS600 heating/freezing microscope stage coupled with the spectrofluorometer *via* optical fibers. We determined the nature of the emission performing time-gated experiments at 80 K in which a 300  $\mu$ s delay after the excitation pulse was used to detect slow components (phosphorescence) of the emission spectra. This procedure is commonly employed to isolate the phosphorescence emission of  $Gd^{3+}$  complexes and to determine the energy of the triplet levels. We discussed these points in ref 2 where the complete energy level calculation is also reported. A calculation confirmed the nature of the observed transitions. In this work, we used a continuous source for a technical reason. Since the phosphorescence bands of 3 and Gd3 are faint, we needed high excitation intensity for their detection. The pulsed Xe lamp does not provide enough excitation intensity.

**EPR Spectroscopy.** All molecules were dissolved in toluene with a small addition of  $CH_3CN$  and/or  $CHCl_3$  for solubility; solutions were placed in quartz tubes (i.d. 3 mm), degassed, and sealed under vacuum. The concentration of all samples was approximately 300  $\mu$ M. TR-EPR experiments were performed at 80 K on a Bruker ELEXSYS E580 spectrometer equipped with an ER 4118X-MDS dielectric cavity, an Oxford CF935 liquid helium flow cryostat, and an Oxford ITC4 temperature controller. The microwave frequency was measured by a frequency counter, HPS342A. An Nd:YAG laser (Quantel Brilliant) was used for photoexcitation: the laser was equipped with second and third harmonic generators for laser pulses at 355 nm; laser pulses were 5 ns long with an average energy of 5 mJ. TR-EPR experiments were carried out by recording the time evolution of the EPR signal after the laser pulse with a LeCroy LT344 digital oscilloscope. At each magnetic field position, an average of about 1000 transient signals was usually recorded; 300 points on the magnetic field axis were recorded, with a sweep width of 310.0 mT. The microwave power for TR-EPR experiments was set to be low enough (20–25 dB attenuation, i.e. 1.5 mW or less) to be in a low-power regime and avoid Torrey oscillations on the time trace. The time versus field surfaces were processed using a home-written MATLAB program that removes the background signal before the

laser pulse (signal vs magnetic field) and the intrinsic response of the cavity to the laser pulse (signal vs time). The TR-EPR spectra shown in the main text were extracted from the surface at 1500 ns from the laser flash, about 100 ns after the maximum in the transient to avoid potential distortions. TR-EPR spectral simulations were performed with EasySpin version 6.0.0—dev34.<sup>41</sup> The ZFS parameters have been estimated directly from the spectra; the populations and relative amounts of the different spectral components (and, when needed, the anisotropic linewidths) have been obtained by automated fitting using a Levenberg–Marquardt algorithm within the EasySpin package (esfit function). The *g* and ZFS tensors have been assumed to be collinear. All parameters are reported in Table S1 of the Supporting Information.

**Computational Details.** DFT calculations were carried out by using the Orca suite of programs (version 4.2.1).<sup>42</sup> The hybrid PBE0 functional<sup>43,44</sup> coupled to an all-electron triple- $\zeta$  quality Ahlrichs basis set with one polarization function (def2-TZVP<sup>45</sup>) for all atoms was employed to optimize the molecular structures of singlet ( $S = 0$ ) ground and excited states and the triplet ( $S = 1$ ) excited state; for the optimization of the open-shell systems, spin-unrestricted DFT was employed. Coulomb and exchange integrals were approximated by using the Resolution of Identity approximation with the def2/JK auxiliary basis set.<sup>46</sup> Dispersion corrections were included by adopting Grimme's DFT-D3 method.<sup>47</sup> As the lanthanide primarily interacts with the ligands via electrostatic forces and the eventual 4f electrons do not actively take part in the complexation, Gd was substituted with La to obtain a closed-shell system and simplify the SCF convergence in the geometry optimization. The NaL models were obtained by taking the optimized complex geometry and eliminating everything but one ligand and the metal, substituting the lanthanide with a Na<sup>+</sup> atom, and finally carrying out the optimization on the model system. ZFS parameters were evaluated by using the approaches described in refs 23 and 24 and implemented in the Orca suite. Incidentally, only the spin–spin contribution to the *D* tensor was considered in DFT calculations as spin–orbit effects are negligible for organic systems.<sup>23,24</sup> As such, the GGA BP86<sup>48,49</sup> and the hybrid B3LYP<sup>50–52</sup> functionals in their RO formalism (RO-BP86 and RO-B3LYP) were used together with the def2-TZVP basis set.<sup>45</sup>

## ■ ASSOCIATED CONTENT

### Supporting Information

The Supporting Information is available free of charge at <https://pubs.acs.org/doi/10.1021/acs.inorgchem.1c01123>.

TR-EPR spectra and the relative simulations for all ligand and all complexes; absorption spectra for precursor **P1** and ligands 1–3; ZFS principal axes system for ligands and NaL models; comparison between PAH group orientations in ligand/Gd complex for singlet ground state; optimized structures for the different rotamers of **P1** and 1–3 for the triplet states; the NaL optimized model; comparison between the spin density of protonated and deprotonated forms for all ligands and rotamers; comparison between spin density of protonated and deprotonated forms for all ligands (rotamer A); comparison between DFT ZFS parameters *D* and *E* for **P0/P1** and 1–3, rotamer A; RO-BP86 Lüdwin (Mulliken) spin populations in % for the precursor **P1** and ligands 1–3 and in the NaL model (Na**P1** and Na1–Na3); RO-BP86 ZFS parameters *D* and *E* for all rotamers of optimized NaL models; and comparison between DFT ZFS parameters *D* and *E* for **P1** and 1–3 in protonated and deprotonated forms (rotamer A) (PDF)

## ■ AUTHOR INFORMATION

### Corresponding Authors

**Silvia Carlotto** – Department of Chemistry and Institute of Condensed Matter Chemistry and Technologies for Energy (ICMATE), National Research Council (CNR), c/o Department of Chemistry, University of Padova, 35131 Padova, Italy; [orcid.org/0000-0003-0043-3538](https://orcid.org/0000-0003-0043-3538); Email: [silvia.carlotto@unipd.it](mailto:silvia.carlotto@unipd.it)

**Marco Bortolus** – Department of Chemistry, University of Padova, 35131 Padova, Italy; [orcid.org/0000-0002-6033-6521](https://orcid.org/0000-0002-6033-6521); Email: [marco.bortolus@unipd.it](mailto:marco.bortolus@unipd.it)

### Authors

**Luca Babetto** – Department of Chemistry, University of Padova, 35131 Padova, Italy

**Alice Carlotto** – Department of Chemistry, University of Padova, 35131 Padova, Italy

**Marzio Rancan** – Institute of Condensed Matter Chemistry and Technologies for Energy (ICMATE), National Research Council (CNR), c/o Department of Chemistry, University of Padova, 35131 Padova, Italy; [orcid.org/0000-0001-9967-5283](https://orcid.org/0000-0001-9967-5283)

**Gregorio Bottaro** – Institute of Condensed Matter Chemistry and Technologies for Energy (ICMATE), National Research Council (CNR), c/o Department of Chemistry, University of Padova, 35131 Padova, Italy; [orcid.org/0000-0001-6196-8638](https://orcid.org/0000-0001-6196-8638)

**Lidia Armelao** – Department of Chemistry, University of Padova, 35131 Padova, Italy; Department of Chemical Sciences and Technology of Materials (DSCM), National Research Council (CNR), 00185 Roma, Italy

**Donatella Carbonera** – Department of Chemistry, University of Padova, 35131 Padova, Italy; [orcid.org/0000-0002-5499-1140](https://orcid.org/0000-0002-5499-1140)

**Maurizio Casarin** – Department of Chemistry, University of Padova, 35131 Padova, Italy; [orcid.org/0000-0002-3347-8751](https://orcid.org/0000-0002-3347-8751)

Complete contact information is available at: <https://pubs.acs.org/10.1021/acs.inorgchem.1c01123>

### Author Contributions

S.C. and L.B. contributed equally. The manuscript was written through contributions of all authors.

### Funding

This work was supported by the University of Padova (Grant P-DISC #CARL-SID17 BIRD2017-UNIPD, Project CHIRoN) and University of Padova Strategic Research Infrastructure Grant 2017: “CAPRI: Calcolo ad Alte Prestazioni per la Ricerca e l’Innovazione”.

### Notes

The authors declare no competing financial interest.

## ■ REFERENCES

- (1) Armelao, L.; Quici, S.; Barigelletti, F.; Accorsi, G.; Bottaro, G.; Cavazzini, M.; Tondello, E. Design of Luminescent Lanthanide Complexes: From Molecules to Highly Efficient Photo-Emitting Materials. *Coord. Chem. Rev.* **2010**, *254*, 487–505.
- (2) Babetto, L.; Carlotto, S.; Carlotto, A.; Rancan, M.; Bottaro, G.; Armelao, L.; Casarin, M. Antenna triplet DFT calculations to drive the design of luminescent Ln3+ complexes. *Dalt. Trans.* **2020**, *49*, 14556–14563.
- (3) Babetto, L.; Carlotto, S.; Carlotto, A.; Rancan, M.; Bottaro, G.; Armelao, L.; Casarin, M. Multireference Ab Initio Investigation on

- Ground and Low-Lying Excited States: Systematic Evaluation of J-J Mixing in a Eu<sup>3+</sup> Luminescent Complex. *Inorg. Chem.* **2021**, *60*, 315–324.
- (4) Brites, C. D. S.; Balabhadra, S.; Carlos, L. D. Lanthanide-Based Thermometers: At the Cutting-Edge of Luminescence Thermometry. *Adv. Opt. Mater.* **2019**, *7*, 1801239.
- (5) Brites, C. D. S.; Millán, A.; Carlos, L. D. Lanthanides in Luminescent Thermometry. In *Handbook on the Physics and Chemistry of Rare Earths*; Elsevier B.V., 2016; Vol. 49, pp 339–427.
- (6) Carlotto, A.; Babetto, G.; Carlotto, S.; Miozzi, M.; Seraglia, R.; Casarin, M.; Bottaro, G.; Rancan, M.; Armelao, L. Luminescent Thermometers: From a Library of Europium(III)  $\beta$ -Diketonates to a General Model for Predicting the Thermometric Behaviour of Europium-Based Coordination Systems. *ChemPhotoChem* **2020**, *4*, 674–684.
- (7) Rocha, J.; Brites, C. D. S.; Carlos, L. D. Lanthanide Organic Framework Luminescent Thermometers. *Chem.—Eur. J.* **2016**, *22*, 14782–14795.
- (8) Herbich, J.; Kapturkiewicz, A.; Nowacki, J. Phosphorescent Intramolecular Charge Transfer Triplet States. *Chem. Phys. Lett.* **1996**, *262*, 633–642.
- (9) Marazzi, M.; Gattuso, H.; Fumal, M.; Daniel, C.; Monari, A. Charge-Transfer versus Charge-Separated Triplet Excited States of [Re I (dmp)(CO) 3 (His124)(Trp122)] + in Water and in Modified Pseudomonas aeruginosa Azurin Protein. *Chem.—Eur. J.* **2019**, *25*, 2519–2526.
- (10) Siddique, Z. A.; Yamamoto, Y.; Ohno, T.; Nozaki, K. Structure-Dependent Photophysical Properties of Singlet and Triplet Metal-to-Ligand Charge Transfer States in Copper(I) Bis(Diimine) Compounds. *Inorg. Chem.* **2003**, *42*, 6366–6378.
- (11) Ratzke, W.; Schmitt, L.; Matsuoka, H.; Bannwarth, C.; Retegan, M.; Bange, S.; Klemm, P.; Neese, F.; Grimme, S.; Schiemann, O.; Lupton, J. M.; Höger, S. Effect of Conjugation Pathway in Metal-Free Room-Temperature Dual Singlet-Triplet Emitters for Organic Light-Emitting Diodes. *J. Phys. Chem. Lett.* **2016**, *7*, 4802–4808.
- (12) Roessler, M. M.; Salvadori, E. Principles and Applications of EPR Spectroscopy in the Chemical Sciences. *Chemical Society Reviews*; Royal Society of Chemistry, 2018; Vol. 47, pp 2534–2553.
- (13) Biskup, T. Structure-Function Relationship of Organic Semiconductors: Detailed Insights From Time-Resolved EPR Spectroscopy. *Front. Chem.* **2019**, *7*, 10.
- (14) Bortolus, M.; Prato, M.; Tol, J. v.; Maniero, A. L. Time-Resolved EPR Study of Fullerene C<sub>60</sub> Adducts at 240 GHz. *Chem. Phys. Lett.* **2004**, *398*, 228–234.
- (15) Bortolus, M.; Ribaud, G.; Toffoletti, A.; Carbonera, D.; Zagotto, G. Photo-Induced Spin Switching in a Modified Anthraquinone Modulated by DNA Binding. *Photochem. Photobiol. Sci.* **2019**, *18*, 2199–2207.
- (16) Franco, L.; Mazzoni, M.; Corvaja, C.; Gubskaya, V. P.; Berezhnaya, L. S.; Nuretdinov, I. A. TR-EPR of single and double spin labelled C<sub>60</sub>derivatives: observation of quartet and quintet excited states in solution. In *Molecular Physics*; Taylor and Francis Ltd., 2006; Vol. 104, pp 1543–1550.
- (17) Carbonera, D.; Di Valentin, M.; Corvaja, C.; Agostini, G.; Giacometti, G.; Liddell, P. A.; Kuciauskas, D.; Moore, A. L.; Moore, T. A.; Gust, D. EPR Investigation of Photoinduced Radical Pair Formation and Decay to a Triplet State in a Carotene–Porphyrin–Fullerene Triad. *J. Am. Chem. Soc.* **1998**, *120*, 4398–4405.
- (18) Wang, Z.; Sukhanov, A. A.; Toffoletti, A.; Sadiq, F.; Zhao, J.; Barbon, A.; Voronkova, V. K.; Dick, B. Insights into the Efficient Intersystem Crossing of Bodipy-Anthracene Compact Dyads with Steady-State and Time-Resolved Optical/Magnetic Spectroscopies and Observation of the Delayed Fluorescence. *J. Phys. Chem. C* **2019**, *123*, 265–274.
- (19) Hou, Y.; Zhang, X.; Chen, K.; Liu, D.; Wang, Z.; Liu, Q.; Zhao, J.; Barbon, A. Charge Separation, Charge Recombination, Long-Lived Charge Transfer State Formation and Intersystem Crossing in Organic Electron Donor/Acceptor Dyads. *J. Mater. Chem. C* **2019**, *7*, 12048–12074.
- (20) Toffoletti, A.; Wang, Z.; Zhao, J.; Tommasini, M.; Barbon, A. Precise Determination of the Orientation of the Transition Dipole Moment in a Bodipy Derivative by Analysis of the Magneto-photoselection Effect. *Phys. Chem. Chem. Phys.* **2018**, *20*, 20497–20503.
- (21) Hintze, C.; Steiner, U. E.; Drescher, M. Photoexcited Triplet State Kinetics Studied by Electron Paramagnetic Resonance Spectroscopy. *ChemPhysChem* **2017**, *18*, 6–16.
- (22) Neese, F. *Spin-Hamiltonian Parameters from First Principle Calculations: Theory and Application*; Springer: New York, NY, 2009, pp 175–229.
- (23) Sinnecker, S.; Neese, F. Spin–Spin Contributions to the Zero-Field Splitting Tensor in Organic Triplets, Carbenes and Biradicals A Density Functional and Ab Initio Study. *J. Phys. Chem. A* **2006**, *110*, 12267–12275.
- (24) Neese, F. Importance of Direct Spin–Spin Coupling and Spin-Flip Excitations for the Zero-Field Splittings of Transition Metal Complexes: A Case Study. *J. Am. Chem. Soc.* **2006**, *128*, 10213–10222.
- (25) Richert, S.; Tait, C. E.; Timmel, C. R. Delocalisation of Photoexcited Triplet States Probed by Transient EPR and Hyperfine Spectroscopy. *J. Magn. Reson.* **2017**, *280*, 103–116.
- (26) Tait, C. E.; Neuhaus, P.; Peeks, M. D.; Anderson, H. L.; Timmel, C. R. Transient EPR Reveals Triplet State Delocalization in a Series of Cyclic and Linear  $\pi$ -Conjugated Porphyrin Oligomers. *J. Am. Chem. Soc.* **2015**, *137*, 8284–8293.
- (27) Montalti, M.; Credi, A.; Prodi, L.; Gandolfi, M. T. *Handbook of Photochemistry*, 3rd ed.; CRC press, 2006.
- (28) Beltrán-Leiva, M. J.; Páez-Hernández, D.; Arratia-Pérez, R. Theoretical Determination of Energy Transfer Processes and Influence of Symmetry in Lanthanide(III) Complexes: Methodological Considerations. *Inorg. Chem.* **2018**, *57*, 5120–5132.
- (29) Beltrán-Leiva, M. J.; Cantero-López, P.; Zúñiga, C.; Bulhões-Figueira, A.; Páez-Hernández, D.; Arratia-Pérez, R. Theoretical Method for an Accurate Elucidation of Energy Transfer Pathways in Europium(III) Complexes with Dipyrrophenazine (Dppz) Ligand: One More Step in the Study of the Molecular Antenna Effect. *Inorg. Chem.* **2017**, *56*, 9200–9208.
- (30) Leroux, F. Atropisomerism, Biphenyls, and Fluorine: A Comparison of Rotational Barriers and Twist Angles. *ChemBioChem* **2004**, *5*, 644–649.
- (31) Brustolon, M.; Barbon, A.; Bortolus, M.; Maniero, A. L.; Sozzani, P.; Comotti, A.; Simonutti, R. Dynamics of Alkoxy–Oligothiophene Ground and Excited States in Nanochannels. *J. Am. Chem. Soc.* **2004**, *126*, 15512–15519.
- (32) Löwdin, P. O. On the Non-Orthogonality Problem Connected with the Use of Atomic Wave Functions in the Theory of Molecules and Crystals. *J. Chem. Phys.* **1950**, *18*, 365–375.
- (33) Mulliken, R. S. Electronic Population Analysis on LCAO-MO Molecular Wave Functions. I. *J. Chem. Phys.* **1955**, *23*, 1833–1840.
- (34) Juriček, M.; Ravat, P.; Šolomek, T.; Ribar, P. Biradicaloid with a Twist: Lowering the Singlet-Triplet Gap. *Synlett* **2016**, *27*, 1613–1617.
- (35) Monkman, A. P.; Burrows, H. D.; Hartwell, L. J.; Horsburgh, L. E.; Hamblett, I.; Navaratnam, S. Triplet Energies of  $\pi$ -Conjugated Polymers. *Phys. Rev. Lett.* **2001**, *86*, 1358–1361.
- (36) Pope, M.; Swenberg, C. E. *Electronic Processes in Organic Crystals and Polymers*, 2nd ed.; Oxford University Press, 1999.
- (37) Wilson, J. S.; Chawdhury, N.; Al-Mandhary, M. R. A.; Younus, M.; Khan, M. S.; Raithby, P. R.; Köhler, A.; Friend, R. H. The Energy Gap Law for Triplet States in Pt-Containing Conjugated Polymers and Monomers. *J. Am. Chem. Soc.* **2001**, *123*, 9412–9417.
- (38) Peng, Q.; Shi, Q.; Niu, Y.; Yi, Y.; Sun, S.; Li, W.; Shuai, Z. Understanding the efficiency drooping of the deep blue organometallic phosphors: a computational study of radiative and non-radiative decay rates for triplets. *J. Mater. Chem. C* **2016**, *4*, 6829–6838.

- (39) Martin, T. E.; Kalantar, A. H. Nonradiative Decay Processes of the Triplet State of Aromatic Compounds: Benzene. *J. Chem. Phys.* **1968**, *48*, 4996–5000.
- (40) Gacoin, P. Studies of the Triplet State of Carbonyl Compounds. I. Phosphorescence of  $\beta$ -Diketones. *J. Chem. Phys.* **1972**, *57*, 1418–1425.
- (41) Stoll, S.; Schweiger, A. EasySpin, a Comprehensive Software Package for Spectral Simulation and Analysis in EPR. *J. Magn. Reson.* **2006**, *178*, 42–55.
- (42) Neese, F. Software Update: The ORCA Program System, Version 4.0. *Wiley Interdiscip. Rev. Comput. Mol. Sci.* **2018**, *8*(1). DOI: DOI: 10.1002/wcms.1327.
- (43) Adamo, C.; Barone, V. Toward Reliable Density Functional Methods without Adjustable Parameters: The PBE0 Model. *J. Chem. Phys.* **1999**, *110*, 6158–6170.
- (44) Perdew, J. P. Density-Functional Approximation for the Correlation Energy of the Inhomogeneous Electron Gas. *Phys. Rev. B: Condens. Matter Mater. Phys.* **1986**, *33*, 8822–8824.
- (45) Weigend, F.; Ahlrichs, R. Balanced basis sets of split valence, triple zeta valence and quadruple zeta valence quality for H to Rn: Design and assessment of accuracy. *Phys. Chem. Chem. Phys.* **2005**, *7*, 3297–3305.
- (46) Weigend, F. Hartree-Fock Exchange Fitting Basis Sets for H to Rn. *J. Comput. Chem.* **2008**, *29*, 167–175.
- (47) Grimme, S.; Antony, J.; Ehrlich, S.; Krieg, H. A Consistent and Accurate Ab Initio Parametrization of Density Functional Dispersion Correction (DFT-D) for the 94 Elements H-Pu. *J. Chem. Phys.* **2010**, *132*, 154104.
- (48) Kassel, L. S. The Limiting High Temperature Rotational Partition Function of Nonrigid Molecules I. General Theory. II. CH<sub>4</sub>, C<sub>2</sub>H<sub>6</sub>, C<sub>3</sub>H<sub>8</sub>, CH(CH<sub>3</sub>)<sub>3</sub>, C(CH<sub>3</sub>)<sub>4</sub> and CH<sub>3</sub>(CH<sub>2</sub>)<sub>2</sub>CH<sub>3</sub>. III. Benzene and Its Eleven Methyl Derivatives. *J. Chem. Phys.* **1936**, *4*, 276–282.
- (49) Trisolini, M. G.; Cromwell, J.; Pope, G. C.; Mitchell, J. B.; Greenwald, L. M.; Trisolini, M. G.; Cromwell, J.; Pope, G. C. Conclusions: Planning for Second-Generation Pay for Performance. *Pay for Performance in Health Care: Methods and Approaches*, RTI International, 2011; pp 341–370.
- (50) Becke, A. D. A new mixing of Hartree-Fock and local density-functional theories. *J. Chem. Phys.* **1993**, *98*, 1372–1377.
- (51) Vosko, S. H.; Wilk, L.; Nusair, M. Accurate Spin-Dependent Electron Liquid Correlation Energies for Local Spin Density Calculations: A Critical Analysis. *Can. J. Phys.* **1980**, *58*, 1200–1211.
- (52) Lee, C.; Yang, W.; Parr, R. G. Development of the Colle-Salvetti Correlation-Energy Formula into a Functional of the Electron Density. *Phys. Rev. B: Condens. Matter Mater. Phys.* **1988**, *37*, 785–789.

## Supporting Information

### **The nature of the ligand-centered triplet state in Gd<sup>3+</sup> $\beta$ -diketonate complexes as revealed by Time-Resolved EPR spectroscopy and DFT calculations.**

Silvia Carlotto,<sup>1,2,\*</sup> Luca Babetto,<sup>1</sup> Marco Bortolus,<sup>1,\*</sup> Alice Carlotto,<sup>1</sup> Marzio Rancan,<sup>2</sup> Gregorio Bottaro,<sup>2</sup> Lidia Armelao,<sup>1,3</sup> Donatella Carbonera<sup>1</sup> and Maurizio Casarin<sup>1</sup>

<sup>1</sup>Department of Chemistry, University of Padova, via F. Marzolo 1, 35131 Padova, Italy

<sup>2</sup>Institute of Condensed Matter Chemistry and Technologies for Energy (ICMATE), National Research Council (CNR), c/o Department of Chemistry, University of Padova, via F. Marzolo 1, 35131 Padova, Italy

<sup>3</sup>Department of Chemical Sciences and Technology of Materials (DSCTM), National Research Council (CNR), Piazzale A. Moro 7, 00185 Roma, Italy

Corresponding authors:

Silvia Carlotto, email: [silvia.carlotto@unipd.it](mailto:silvia.carlotto@unipd.it)

Marco Bortolus, email: [marco.bortolus@unipd.it](mailto:marco.bortolus@unipd.it)

**Table of contents:**

TR-EPR Simulations (Table S1, Figure S1, S2)	Pages S3-S6
Figure S3	Page S7
Figure S4	Page S8
Figure S5	Page S8
Figure S6	Page S9
Figure S7	Page S10
Figure S8	Page S11
Figure S9	Page S12
Table S2	Page S13
Table S3	Page S14
Table S4	Page S15
Table S5	Page S16

### TR-EPR simulations

Experimental and simulated Time-Resolved-EPR (TR-EPR) spectra of the ligands and Gd<sup>3+</sup> complexes in frozen solution (80 K) are reported in Figure S1 and S2, respectively, while the parameters obtained from the simulations are collected in Table S1. The simulations were performed using the development version of EasySpin, version 6.0.0 – dev34. In greater detail, the ZFS parameters were estimated directly from the experimental spectra and simulations were performed to obtain the starting parameters (ZFS parameters, zero-field populations, relative abundance in the case of multiple species, gaussian anisotropic linewidths – as full width at half height) to be optimized. Then, the populations and relative abundance (and when needed the linewidths) were optimized using the Levenberg-Marquardt algorithm within EasySpin using the *esfit* function. Note that, before the final optimization, Monte Carlo fitting was run to explore the parameter space and to ensure that the starting parameters were not representative of a local minimum.

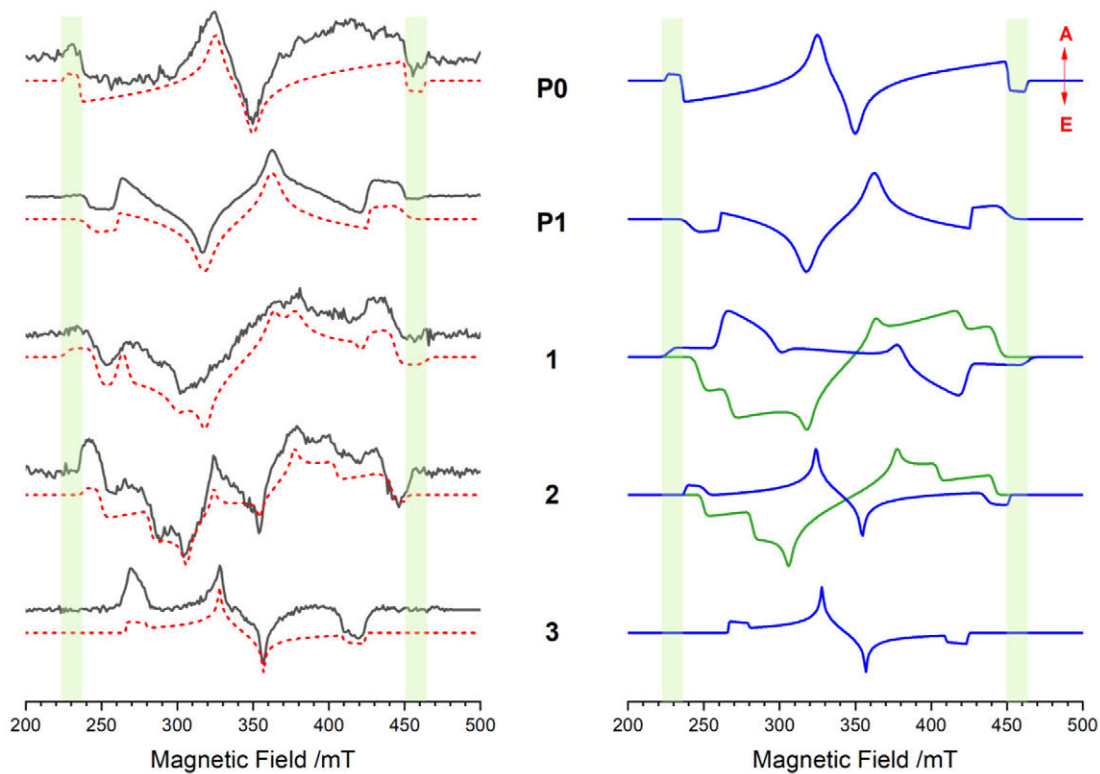
The TR-EPR spectra of the excited triplet states, unlikely conventional EPR spectra, are not displayed as first derivative lineshapes and can be either in emission or enhanced absorption (indicated by the E/A red arrows in Figures S1 and S2). The E/A intensities originate from the non-Boltzmann populations of the three triplet sublevels. The line shapes of all the TR-EPR spectra of **GdP1**, **Gd1** – **Gd3** are compatible with the formation of the triplet states via Intersystem Crossing (ISC) from the first excited singlet state. The TR-EPR spectrum of **GdP1** is dominated by one triplet species with EEE/AAA line shape. Although there are hints of a second triplet species with a larger  $|D|$  ZFS parameter, this second species is too weak to be fully identified and simulated (<5% of relative abundance) and only its width (i.e. the Z component) is visible (green bands in Figure S2). The spectra of **Gd1** and **Gd2** are characterized by two triplet species, each one characterized by different ZFS parameters and polarization patterns (Figure S2). The spectrum of **Gd3** shows only a single triplet state with a AAA/EEE line shape. The widest visible species, highlighted by the green bands in Figure S2, is present in **GdP1** and **Gd1**, while the spectra narrow in **Gd2** and significantly in **Gd3**.

Table S1. Triplet parameters obtained from the simulations of the TR-EPR spectra, when two species are present each row reports two sets of parameters. Absolute values of the ZFS parameters  $|D|$  and  $|E|$  ( $\text{cm}^{-1}$ );  $|E/D|$  ratio; triplet sublevels population ( $P_x$ ,  $P_y$  and  $P_z$ ); relative amount of each spectral component (%); anisotropic linewidths ( $Lw_x$ ,  $Lw_y$ ,  $Lw_z$  in Mhz). The g tensor, collinear with the D tensor, is  $g_{xx}=2.006$ ,  $g_{yy}=g_{zz}=2.009$  for all compounds. n.d. = not determined.

	$ D $	$ E $	$ E/D $	$P_x : P_y : P_z$	%	$Lw_x : Lw_y : Lw_z$ /Mhz
<b>P0</b>	0.111	0.030	0.270	0.80 : 0.00 : 0.20	100	50 : 180 : 50
<b>P1</b>	0.098	0.019	0.194	0.00 : 0.49 : 0.51	>95	10 : 230 : 230
	0.111	n.d.	n.d.	n.d.	n.d.	n.d.
<b>GdP1</b>	0.098	0.019	0.194	0.00 : 0.39 : 0.61	>95	45 : 250 : 50
	0.111	n.d.	n.d.	n.d.	n.d.	n.d.
<b>1 &amp; Gd1</b>	0.092	0.017	0.185	0.00 : 0.00 : 1.00	63	150 : 154 : 180
	0.111	0.013	0.117	1.00 : 0.00 : 0.00	37	155 : 186 : 180
<b>2</b>	0.090	0.008	0.089	0.07 : 0.00 : 0.93	62	100 : 100 : 100
	0.100	0.024	0.240	0.93 : 0.07 : 0.00	38	150 : 50 : 50
<b>Gd2</b>	0.090	0.008	0.089	0.00 : 0.02 : 0.98	73	200 : 50 : 200
	0.100	0.024	0.240	0.90 : 0.00 : 0.10	27	50 : 100 : 100
<b>3</b>	0.074	0.016	0.216	0.79 : 0.21 : 0.00	100	10 : 21 : 10
<b>Gd3</b>	0.070	0.016	0.229	0.49 : 0.51 : 0.00	100	50 : 50 : 50



**Figure S1.** Left. Time-resolved EPR experimental (black lines) spectra and simulations (red dotted lines) ( $\lambda_{\text{exc}} = 355 \text{ nm}$ ) of the precursors **P0** and **P1** and ligands **1** – **3** in frozen toluene solution at X-band (microwave frequency  $\nu = 9.705 \text{ GHz}$ ),  $T = 80 \text{ K}$ . Right. The normalized individual components of the simulations (broader component blue, narrower green). The green side-bands correspond to the maximum width of the spectra of **P0**, **P1**, **1** (equal to  $2|D|*h/g\mu_B$ ) and highlight the progressive narrowing of the EPR spectra along the series. The red arrows denote the signals in enhanced absorption (A) and emission (E).



**Figure S2.** Left. Time-resolved EPR experimental (green lines) spectra and simulations (red dotted lines) ( $\lambda_{\text{exc}} = 355 \text{ nm}$ ) of complexes **GdP1**, **Gd1** – **Gd3** in frozen toluene solution at X-band (microwave frequency  $\nu = 9.705 \text{ GHz}$ ),  $T = 80 \text{ K}$ . Right. The normalized individual components of the simulations (broader component blue, narrower green). The green side-bands correspond to the maximum width of the spectra of **GdP1** and **Gd1** (equal to  $2|D|*h/g_{\mu\text{B}}$ ) and highlight the progressive narrowing of the EPR spectra along the series. The red arrows denote the signals in enhanced absorption (A) and emission (E).

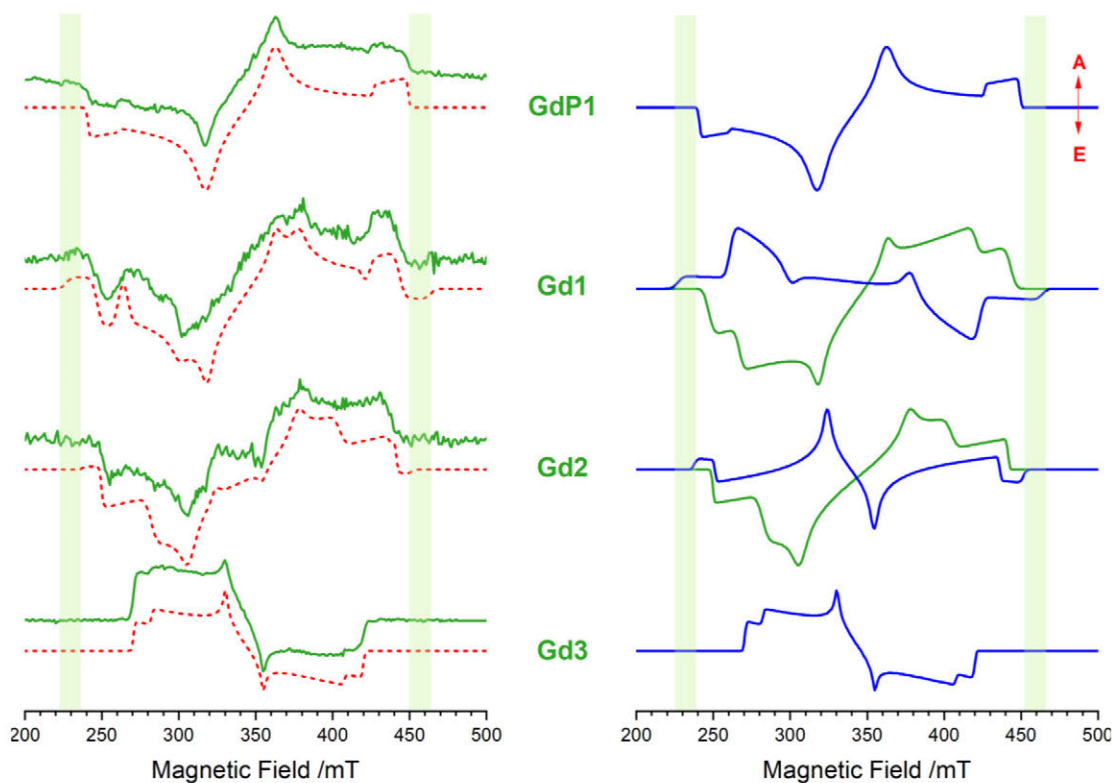


**Figure S3.** Adsorption spectra for the precursor **P1** and ligands **1 - 3**. The vertical dotted line at 355 nm is the  $\lambda_{\text{exc}}$  used in the Time-resolved EPR spectra.

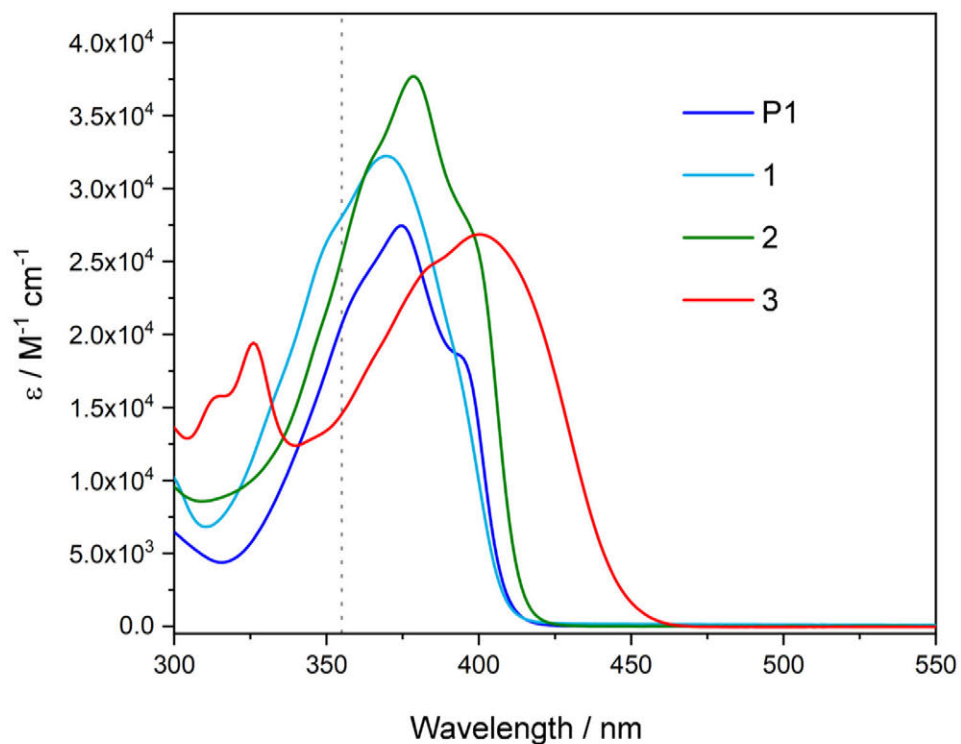
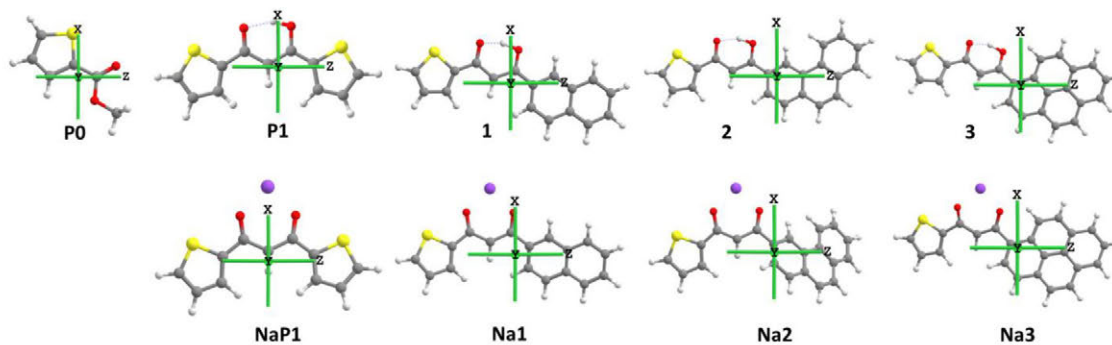


**Figure S4.** ZFS principal axes system in the molecular frame as obtained by DFT calculations. Top row shows the precursors and the neutral ligands, bottom row the deprotonated systems with a sodium atom as a counterion. Grey, white, yellow, violet, and red spheres are C, H, S, Na and O atoms, respectively.



S7

**Figure S5.** Comparison between thienyl or PAH group orientations in precursor/Gd complexes and ligands/Gd complexes (singlet ground states). Grey, yellow, red and green spheres are C, S, O and La atoms, respectively. H atoms are omitted for clarity. Dihedral angles are given in deg.

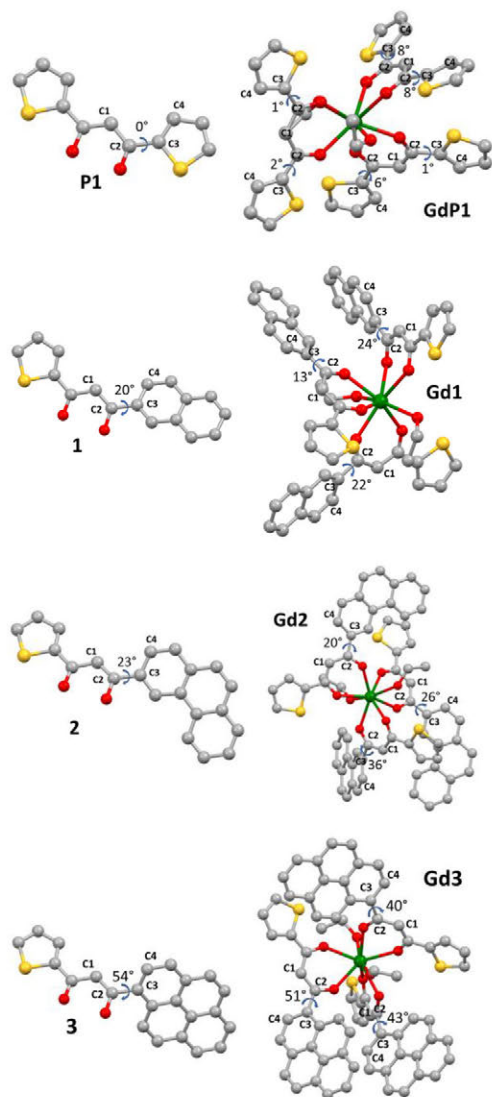


**Figure S6.** Optimized structures for the different rotamers of **P0**, **P1** and **1 - 3** calculated at the PBE0 level for the triplet states. Grey, white, yellow, and red spheres are C, H, S and O atoms, respectively. The energy differences  $\Delta$  (kcal/mol) are given with respect to the most stable form.

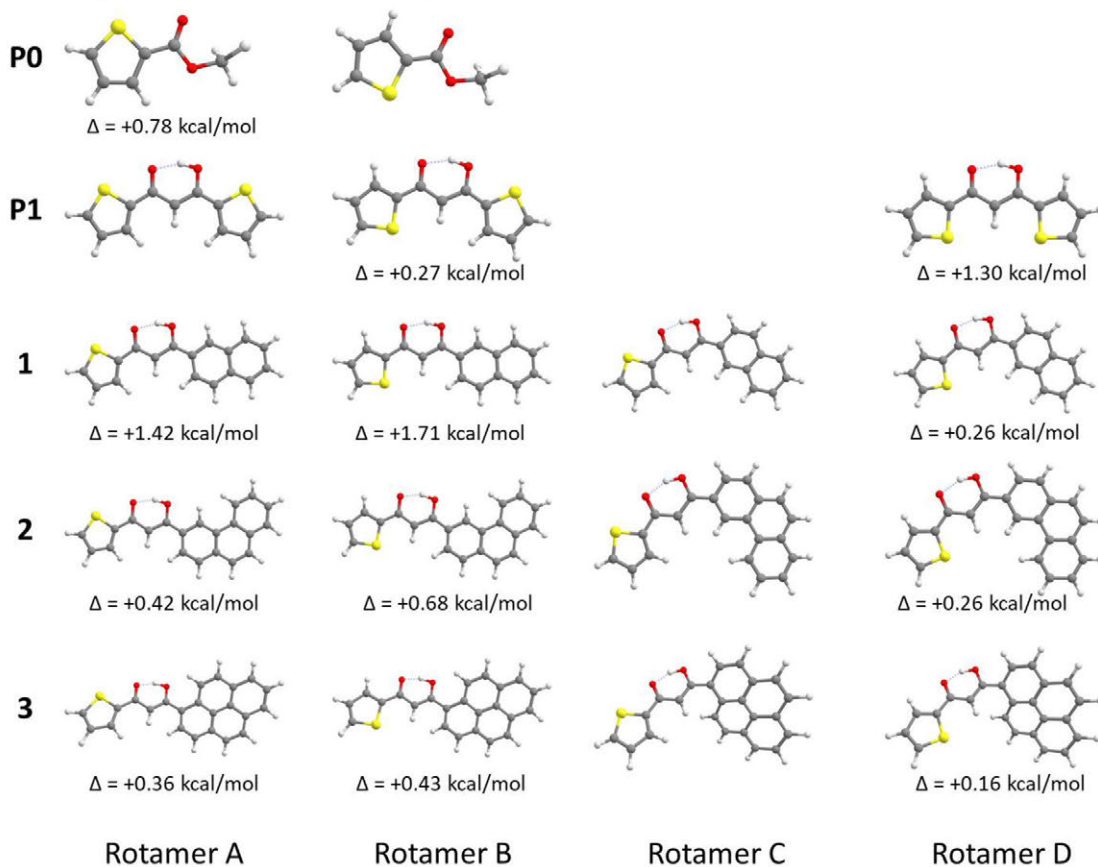


**Figure S7.** The **Na1** optimized model. Grey, white, yellow, violet, and red spheres are C, H, S, Na and O atoms, respectively. The O-Na distance is given in Å.

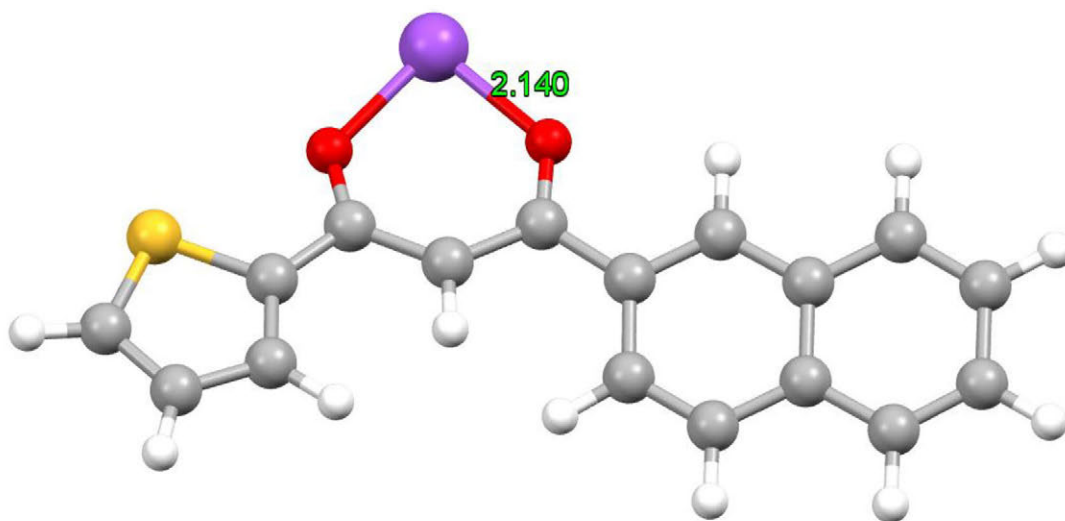


**Figure S8.** Comparison between spin density of protonated and deprotonated forms for the precursor **P1** and all ligands, considering all and rotamers, calculated at the RO-BP86 level. Displayed isosurfaces correspond to  $0.003 e^{1/2} \times \text{\AA}^{-3/2}$  values. Grey, white, yellow, violet, and red spheres are C, H, S, Na and O atoms, respectively.

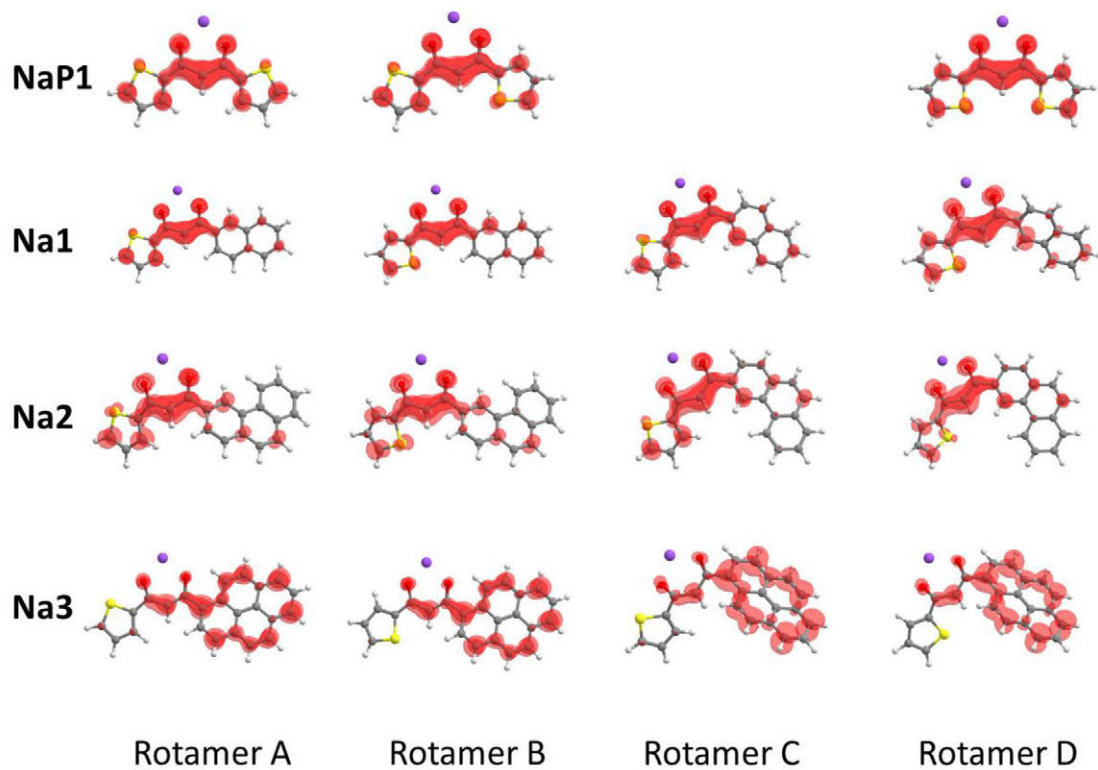


**Figure S9.** Comparison between spin density of protonated and deprotonated forms for the precursor **P1** and all ligands (rotamer A), calculated at the RO-BP86 level. Displayed isosurfaces correspond to  $0.003 e^{1/2} \times \text{\AA}^{-3/2}$  values. Grey, white, yellow, and red spheres are C, H, S and O atoms, respectively.

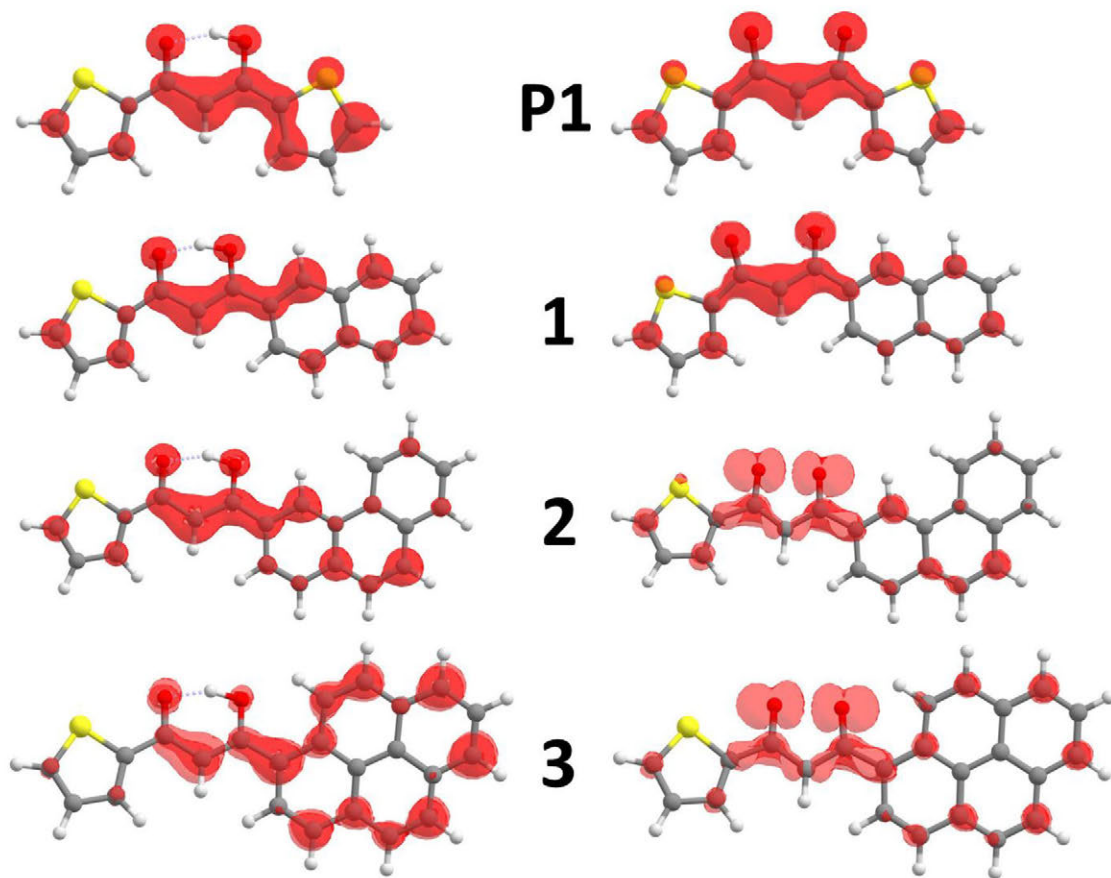
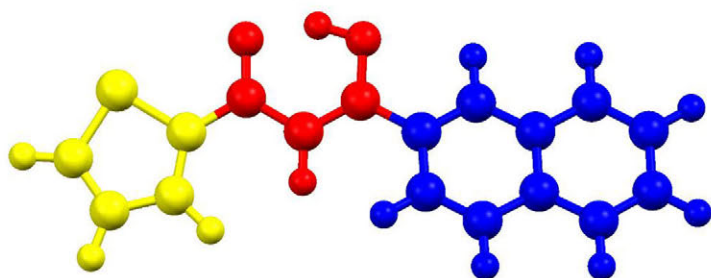




**Table S2.** Comparison between DFT ZFS parameters  $D$  and  $E/D$  for **P0**, **P1** and **1 - 3**, rotamer A.  $D$  and  $E$  parameters are given in  $\text{cm}^{-1}$ .

	RO-BP86		RO-B3LYP		Experimental	
	$D$	$E/D$	$D$	$E/D$	$ D $	$ E/D $
<b>P0</b>	-0.070	0.329	-0.068	0.324	0.111	0.270
<b>P1</b>	-0.067	0.254	-0.068	0.191	0.098	0.194
<b>1</b>	-0.071	0.085	-0.080	0.063	0.092	0.185
<b>2</b>	-0.070	0.100	-0.080	0.075	0.090	0.089
<b>3</b>	-0.039	0.103	-0.038	0.132	0.074	0.216

**Table S3.** RO-BP86 Löwdin spin populations (Mulliken in parenthesis) in % for the precursor **P1**, ligands **1 - 3** and in the NaL models (**NaP1**, **Na1 - Na3**). % have been calculated by summing the individual atomic spin population contribution for each fragment (Thiophene, Diketone, PAH fragments). The different fragments are shown in figure below.



	Thiophene (yellow)	Diketone (red)	PAH (blue)
<b>P1</b>	10.2% (9.9%)	50.5% (51.1%)	39.3% (39.0%) <sup>a</sup>
<b>1</b>	12.3% (12.0%)	43.9% (44.4%)	43.8% (43.6%)
<b>2</b>	9.6% (9.3%)	45.9% (46.6%)	44.5% (44.1%)
<b>3</b>	4.1% (4.0%)	21.7% (21.3%)	74.2% (71.7%)
<b>NaP1<sup>b</sup></b>	20.4% (20.0%)	59.2% (60.1%)	20.4% (19.9%)
<b>Na1<sup>b</sup></b>	21.0% (20.6%)	60.6% (61.5%)	18.4% (17.9%)
<b>Na2<sup>b</sup></b>	22.0% (21.5%)	58.2% (59.2%)	19.8% (19.3%)
<b>Na3<sup>b</sup></b>	3.6% (3.5%)	19.3% (19.0%)	77.1% (77.5%)

<sup>a</sup> The PAH group in **P1** is the thiophene group in the enol side.

<sup>b</sup> In the NaL models, the Na atom is included in the diketone fragment

**Table S4.** RO-BP86 ZFS parameters  $D$  and  $E/D$  for all rotamers of optimized NaL models (**NaP1**, **Na1** – **Na3**).  $D$  and  $E$  parameters are given  $\text{cm}^{-1}$ . Absolute experimental values are reported for  $\text{Gd}^{3+}$  complexes (**GdP1**, **Gd1** – **Gd3**).

	Rotamer A		Rotamer B		Rotamer C		Rotamer D		Experimental	
	$D$	$E/D$	$D$	$E/D$	$D$	$E/D$	$D$	$E/D$	$ D $	$ E/D $
<b>NaP1</b>	-0.078	0.137	-0.081	0.125	//	//	-0.086	0.119	0.098	0.194
<b>Na1</b>	-0.080	0.114	-0.085	0.092	-0.070	0.153	-0.075	0.112	0.092	0.185
<b>Na2</b>	-0.072	0.097	-0.076	0.071	-0.069	0.142	-0.073	0.095	0.090	0.089
<b>Na3</b>	-0.040	0.118	-0.039	0.118	-0.037	0.149	-0.036	0.156	0.070	0.228

**Table S5.** Comparison between DFT ZFS parameters  $D$  and  $E/D$  and the absolute experimental values for **P1**, **1** - **3** in protonate and deprotonate forms (rotamer A).  $D$  and  $E$  parameters are given in  $\text{cm}^{-1}$ .

	Protonated		Deprotonated		Experimental	
	$D$	$E/D$	$D$	$E/D$	$ D $	$ E/D $
<b>P1</b>	-0.067	0.209	-0.068	0.176	0.098	0.194
<b>1</b>	-0.071	0.085	-0.063	0.143	0.092	0.185
<b>2</b>	-0.070	0.100	-0.057	0.070	0.090	0.089
<b>3</b>	-0.039	0.128	0.169	0.071	0.074	0.216

## 8. THERMOCHEMISTRY OF SUPRAMOLECULAR ASSEMBLY IN HETERODINUCLEAR LN-AL COMPLEXES

The interest for the synthesis and the properties of heterometallic lanthanide *-d* or *-p* metal (Ln-M) complexes is continuously growing as a consequence of their potential use in many fields, such as diagnostic medicine<sup>1,2</sup> and biology;<sup>3,4</sup> molecular switches;<sup>5</sup> magnetic<sup>6-8</sup> and luminescent materials.<sup>9-11</sup> Heterometallic Ln-M compounds can be obtained through different synthetic procedures by exploiting the marked preference of lanthanide ions towards oxygen donor ligands,<sup>12-14</sup> their considerably larger ionic radius,<sup>15,16</sup> or both.<sup>17</sup> A simpler and more attractive route involves the reaction between a mononuclear *-d* or *-p* metal complex featuring Lewis basic sites and either a formally coordinatively unsaturated lanthanide fragment,<sup>18</sup> or a lanthanide complex having labile donors in the coordination sphere.<sup>19</sup> In these systems, some of the Lewis basic sites coordinate both the aluminium and the lanthanide ions, bridging the two fragments (Figure 7).

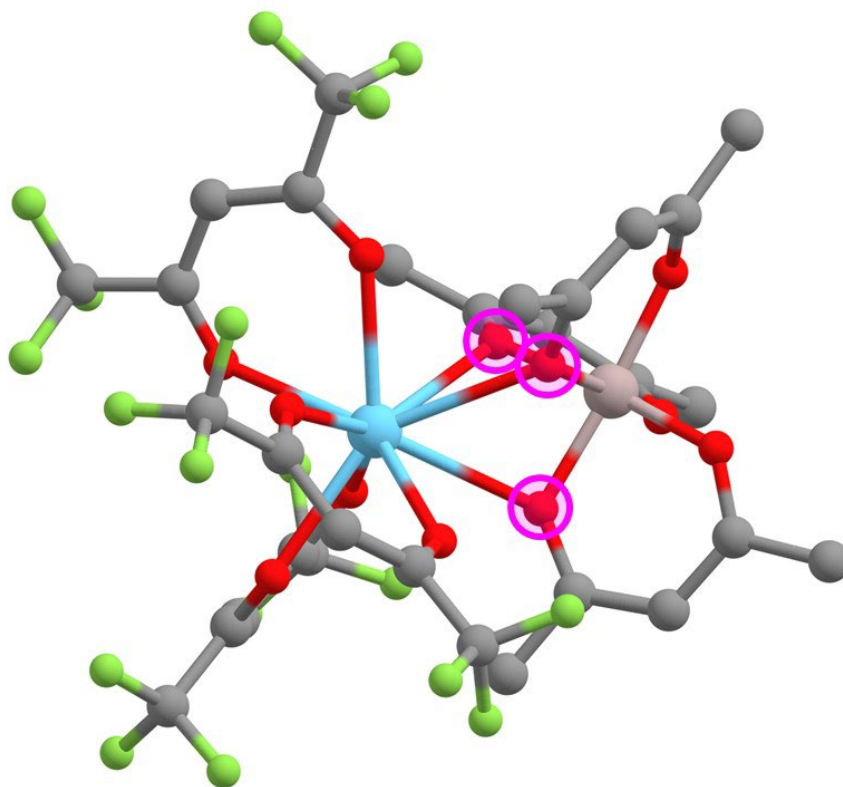


**Figure 7.** Example of a heterodinuclear Ln-Al complex  $[Eu(acac)_3][Al(acac)_3]$ , in which the bridging Lewis basic sites have been highlighted in magenta. Atom colour code is as follows: grey = C; red = O; green = F; blue = Eu; pink = Al. Hydrogen atoms have been omitted to improve clarity.

Fluorinated groups such as hexafluoroacetylacetonate (hfac) make the lanthanide centre susceptible to attack even by relatively weak bases. This route has been used for dipositive ( $M^{2+} = Cu^{2+}$ )<sup>20,21</sup> and tripisitive ( $M^{3+} = Cr^{3+}$ ,  $Fe^{3+}$  and  $Ga^{3+}$ )<sup>18,22,23</sup> metal complexes, mainly for magnetic studies. Different bridging arrangements are possible, depending on the ligand and the M ion considered. In square planar or a square pyramidal<sup>20,21</sup> copper(II) mononuclear complexes with acetylacetonato (acac) and salen ligands, two oxygen atoms on the same side of the square base coordinate the lanthanide centre (Figure 8a). Conversely, in octahedral tripisitive M mononuclear complexes,<sup>18</sup> all with acetylacetonato ligands, three donor atoms from three different acac ligands lying on the same triangular face are bridging the two metal ions (Figure 8b).

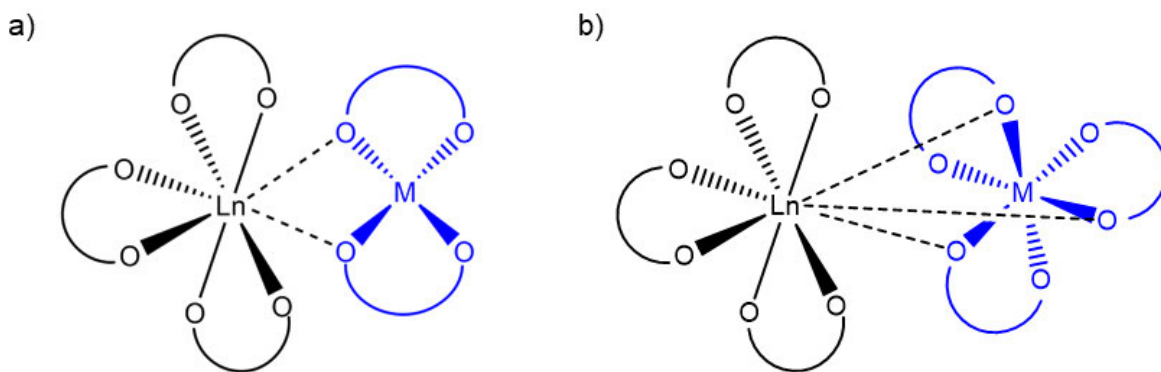


**Figure 8.** Schematic representation of the donor atoms bridging the  $[Ln(hfac)_3]$  moiety (in black) in a) a  $M$  square planar or square based pyramidal geometry and b) a  $M$  octahedral geometry (in blue).

$Al^{3+}$  forms easily accessible octahedral mononuclear complexes with chelate oxygen donors ligands<sup>24–26</sup> potentially useful for the synthesis of heterometallic complexes, and is not a very labile centre ( $k_{H_2O} \approx 1 \text{ s}^{-1}$ ),<sup>27</sup> a relevant issue when the ligand scrambling has to be minimized. Moreover, only a few europium-aluminium complexes have already been studied for their photo-luminescence properties.<sup>28–30</sup>

The (at least partial) supramolecular nature of the bond between the two moieties is inherently weaker than the “strong” types of bonds which hold the isolated fragments together; this entails that the stability of such systems is not a given and an *a priori* methodology able to predict whether a certain complex will form is of fundamental importance in this field. When studying an ionic/covalent complexation process from a theoretical standpoint, it is usual to consider only the contribution from the change in electronic energy due to the formation of the bonds between ligand and metal, which represents the main source of stabilisation for the system.<sup>31–35</sup> On the other hand, when researching supramolecular systems, entropy can often become the primary driving factor for the formation of the supramolecular entity.<sup>36–38</sup> In the case of Ln-M complexes, we are presented with a situation halfway in between, as these heterodinuclear complexes can be thought of as a supramolecular system formed by the two complexes, but in which there are also significant ionic/covalent interactions involving the bridging atoms. Both enthalpic and entropic contributions must therefore be considered, and the formation of the complex given by its formation Gibbs free energy needs to take both into account.

## 8.1 Formation thermodynamics

The Gibbs free energy is given by the standard thermodynamic definition:

$$G = H - T \cdot S \quad (122)$$

where  $H$  is the enthalpy,  $S$  is the entropy, and  $T$  is the temperature. These thermodynamic quantities can be further broken down into specific contributions. For the enthalpy:

$$H = U + k_B T = E_{el} + ZPE + E_{vib} + E_{rot} + E_{trans} + k_B T \quad (123)$$

where  $k_B$  is the Boltzmann constant and  $U$  is the inner energy. The latter can be decomposed into:  $E_{el}$ , the total electronic energy term taken from the SCF procedure;  $ZPE$ , the zero temperature vibrational energy (*i.e.*, the Zero Point Energy);  $E_{vib}$ , the finite temperature correction due to population of excited vibrational states;  $E_{rot}$  and  $E_{trans}$ , the thermal rotational and translational energies. For the entropy:

$$S = S_{el} + S_{vib} + S_{rot} + S_{trans} \quad (124)$$

where  $S_{el}$  is the electronic entropy due to the eventual degeneracy of the electronic ground state,  $S_{vib}$ ,  $S_{rot}$ , and  $S_{trans}$  are the vibrational, rotational, and translational entropies, respectively.

When considering the formation of a supramolecular complex of size and type such as those under investigation, the electronic energy  $E_{el}$  is expected to be the primary term defining the stability of the complex, with values for formation energies typically in the range of tens of kcal/mol. The vibronic contributions ( $ZPE$  and  $E_{vib}$ ) are usually in the order of 1-3 kcal/mol and favour the formation of the complex, while  $E_{rot}$  and  $E_{trans}$  are each equal to  $3/2 k_B T$  for any given molecule, therefore contributing to an overall destabilization of 1.78 kcal/mol for the formation of a heterodinuclear system starting from two mononuclear complexes. The electronic entropy  $S_{el}$  does not contribute to the free energy of formation unless a change in spin multiplicity occurs.  $S_{rot}$  and  $S_{trans}$  each contribute to a destabilization of approx. 10 kcal/mol at room temperature for systems of this size due to the loss of rotational and translational entropy after the formation of a single unit from two separate moieties.  $S_{vib}$  is also expected to account for a few kcal/mol at room temperature but its sign cannot be identified *a priori*.

The stability of various heterodinuclear  $[\text{Eu}(\mathbf{L}_{\text{Eu}})_3][\text{Al}(\mathbf{L}_{\text{Al}})_3]$  complexes, in which the system is held together via three bridging oxygen atoms provided by the  $\mathbf{L}_{\text{Al}}$  ligand, was evaluated *via* DFT numerical simulations at the PBE/TZVP level, through a geometry optimisation and a subsequent frequency analysis.  $\mathbf{L}_{\text{Eu}}$  and  $\mathbf{L}_{\text{Al}}$  indicate the ligands of the rare earth and aluminium mononuclear complexes, respectively. The thermodynamic quantities relative to the formation of the dinuclear complex – *i.e.*, enthalpies, entropies, and Gibbs free energies – were taken as the difference between those of the heterodinuclear  $[\text{Eu}(\mathbf{L}_{\text{Eu}})_3][\text{Al}(\mathbf{L}_{\text{Al}})_3]$  complex and the sum of those of the mononuclear (anhydrous)  $\text{Eu}(\mathbf{L}_{\text{Eu}})_3$  and  $\text{Al}(\mathbf{L}_{\text{Al}})_3$  complexes:

$$\begin{aligned}
\Delta H_{[Eu(L_{Eu})_3][Al(L_{Al})_3]}^f &= H_{[Eu(L_{Eu})_3][Al(L_{Al})_3]} - (H_{Eu(L_{Eu})_3} + H_{Al(L_{Al})_3}) \\
\Delta S_{[Eu(L_{Eu})_3][Al(L_{Al})_3]}^f &= S_{[Eu(L_{Eu})_3][Al(L_{Al})_3]} - (S_{Eu(L_{Eu})_3} + S_{Al(L_{Al})_3}) \\
\Delta G_{[Eu(L_{Eu})_3][Al(L_{Al})_3]}^f &= G_{[Eu(L_{Eu})_3][Al(L_{Al})_3]} - (G_{Eu(L_{Eu})_3} + G_{Al(L_{Al})_3})
\end{aligned}
\tag{125}$$

To simplify the calculations, especially the SCF procedure, La was chosen instead of Eu as the rare earth due to its closed-shell electronic structure. This introduces a constant shift in the values of the calculated thermodynamic quantities, but the observed trends hold for other lanthanides as well (*vide infra*).

**Table 2.** Calculated formation enthalpies and free energies for a series of heterodinuclear complexes with general formula  $[Eu(L_{Eu})_3][Al(L_{Al})_3]$ . The last column indicates whether the dinuclear complex is experimentally observed. Eu was replaced by La in the DFT calculations to simplify the SCF convergence.

$L_{Al}$	$L_{Eu}$	$\Delta H^f$ (kcal/mol)	$\Delta G^f$ (kcal/mol)	Exp.
acetylacetone (acac)	hexafluoroacetylacetone (hfac)	-43.36	-24.61	Y
methyl acetoacetate (meac)	hexafluoroacetylacetone (hfac)	-43.46	-23.95	Y
dibenzoylmethane (dbm)	hexafluoroacetylacetone (hfac)	-48.48	-23.45	Y
salicylaldehyde (sal)	hexafluoroacetylacetone (hfac)	-45.73	-22.95	Y
2-hydroxynaphthaldehyde (naf)	hexafluoroacetylacetone (hfac)	-48.44	-22.00	Y
1,1,1-trichloroacetylacetone (acacCl <sub>3</sub> )	hexafluoroacetylacetone (hfac)	-36.32	-20.73	
acetylacetone (acac)	4,4,4-trifluoro-1-phenyl-1,3-butane-dione (bta)	-39.32	-20.54	Y
methyl acetoacetate (meac)	4,4,4-trifluoro-1-phenyl-1,3-butane-dione (bta)	-37.03	-19.36	
2-hydroxynaphthaldehyde (naf)	4,4,4-trifluoro-1-phenyl-1,3-butane-dione (bta)	-43.55	-18.54	Y
1,1,1-trifluoroacetylacetone (tfac)	hexafluoroacetylacetone (hfac)	-36.62	-15.04	N
1,1,1-triiodoacetylacetone (acacI <sub>3</sub> )	hexafluoroacetylacetone (hfac)	-41.63	-14.43	
1,1,1-tribromoacetylacetone (acacBr <sub>3</sub> )	hexafluoroacetylacetone (hfac)	-40.68	-14.15	
acetylacetone (acac)	1,1,1-trifluoroacetylacetone (tfac)	-32.87	-13.01	
dipivaloylmethane (dpa)	hexafluoroacetylacetone (hfac)	-34.39	-11.87	N
acetylacetone (acac)	acetylacetone (acac)	-24.74	-7.24	N
hexafluoroacetylacetone (hfac)	hexafluoroacetylacetone (hfac)	-23.30	-4.93	N



**Table 3.** Calculated formation entropy correction terms at  $T = 298.15$  K for the series of heterodinuclear complexes with general formula  $[Eu(L_{Eu})_3][Al(L_{Al})_3]$ . Eu was substituted by La in the calculations to simplify SCF convergence.

$L_{Al}$	$L_{Eu}$	$-T\Delta S_{vib}^f$ (kcal/mol)	$-T\Delta S_{rot}^f$ (kcal/mol)	$-T\Delta S_{trans}^f$ (kcal/mol)
acetylacetone (acac)	hexafluoroacetylacetone (hfac)	-3.66	9.84	12.57
methyl acetoacetate (meac)	hexafluoroacetylacetone (hfac)	-3.12	9.97	12.66
dibenzoylmethane (dbm)	hexafluoroacetylacetone (hfac)	1.24	11.80	11.89
salicylaldehyde (sal)	hexafluoroacetylacetone (hfac)	-0.14	10.23	12.68
2-hydroxynaphthaldehyde (naf)	hexafluoroacetylacetone (hfac)	2.89	10.69	12.86
1,1,1-trichloroacetylacetone (acacCl <sub>3</sub> )	hexafluoroacetylacetone (hfac)	-7.73	10.37	12.94
acetylacetone (acac)	4,4,4-trifluoro-1-phenyl-1,3-bu- tanedione (bta)	7.32	9.90	12.62
methyl acetoacetate (meac)	4,4,4-trifluoro-1-phenyl-1,3-bu- tanedione (bta)	6.01	10.03	12.70
2-hydroxynaphthaldehyde (naf)	4,4,4-trifluoro-1-phenyl-1,3-bu- tanedione (bta)	12.41	10.76	12.92
1,1,1-trifluoroacetylacetone (tfac)	hexafluoroacetylacetone (hfac)	-1.47	9.84	12.57
1,1,1-triiodoacetylacetone (acacI <sub>3</sub> )	hexafluoroacetylacetone (hfac)	3.16	10.77	13.27
1,1,1-tribromoacetylacetone (acacBr <sub>3</sub> )	hexafluoroacetylacetone (hfac)	2.77	10.60	13.15
acetylacetone (acac)	1,1,1-trifluoroacetylacetone (tfac)	-2.31	9.66	12.50
dipivaloylmethane (dpa)	hexafluoroacetylacetone (hfac)	-0.87	10.49	12.90
acetylacetone (acac)	acetylacetone (acac)	-4.29	9.39	12.39
hexafluoroacetylacetone (hfac)	hexafluoroacetylacetone (hfac)	-5.16	10.58	12.95

In Table 2 the formation enthalpies and free energies for all the heterodinuclear complexes investigated are reported. The first observation is that all complexes with a formation free energy less negative than  $\Delta G_{unst} = -15.04$  kcal/mol ( $[Eu(hfac)_3][Al(tfac)_3]$ ) are not experimentally observed, whereas for all complexes with a formation free energy more negative than  $\Delta G_{st} = -18.54$  kcal/mol ( $[Eu(bta)_3][Al(naf)_3]$ ) there is experimental evidence. Given the very similar chemical nature of lanthanides, this is expected to hold true for any other rare earth.

The minimum formation free energy necessary to provide a stable complex therefore lies somewhere between -15.0 and -18.5 kcal/mol when considering Ln = La in the DFT calculation. These numerical experiments also indicate that the free energy is indeed the most reliable indicator for the overall stability of the complex. In fact, despite the bridge being a bond with mostly ionic/covalent nature, considering only the formation enthalpy (which for the most part is equal to the SCF electronic energy) would not allow to discriminate between stable and unstable complexes:  $[La(bta)_3][Al(meac)_3]$  and  $[La(hfac)_3][Al(tfac)_3]$  have a formation enthalpy of -37.03 and -36.62 kcal/mol, respectively, which is within the margin of

error of the numerical simulation, *i.e.* for all intended purposes of DFT calculations they represent the same value.<sup>39</sup>

Another interesting aspect emerges, namely that formation enthalpies and free energies are not directly proportional: for the complexes in which  $\mathbf{L}_{Eu} = \text{hfac}$  and  $\mathbf{L}_{Al} = \text{acac}$ ,  $\text{sal}$ ,  $\text{naf}$ , the formation enthalpy decreases ( $\text{acac} = -43.36$ ,  $\text{sal} = -45.73$ ,  $\text{naf} = -48.44$  kcal/mol) while the formation Gibbs free energy increases ( $\text{acac} = -24.61$ ,  $\text{sal} = -22.95$ ,  $\text{naf} = -22.00$  kcal/mol). As  $G = H - T \cdot S$ , it follows naturally that entropic contributions must play a key role in determining the stability of the dinuclear complex and are not just a constant shift for the conversion between enthalpy and Gibbs free energy, highlighting the supramolecular nature of the systems.

To better illustrate this point, complexes in which  $\mathbf{L}_{Eu} = \text{hfac}$  and  $\mathbf{L}_{Al} = 1,1,1\text{-trichloroacetylacetone}$  ( $\text{acacCl}_3$ ) or  $1,1,1\text{-tribromoacetylacetone}$  ( $\text{acacBr}_3$ ) were evaluated. Unfortunately, it was not possible to synthesise these ligands, therefore the following speculations remain entirely theoretical in nature. The formation enthalpy for the dinuclear complex favours the bromated complex:  $\Delta H^f([\text{La}(\text{hfac})_3][\text{Al}(\text{acacCl}_3)_3]) = -36.32$  kcal/mol;  $\Delta H^f([\text{La}(\text{hfac})_3][\text{Al}(\text{acacBr}_3)_3]) = -40.68$  kcal/mol, possibly due to the higher electronegativity of Cl, which withdraws electron density from the oxygen atoms in the bridge and therefore weakens the Ln-O-Al bond. However, the formation free energies follow an inverse trend:  $\Delta G^f([\text{La}(\text{hfac})_3][\text{Al}(\text{acacCl}_3)_3]) = -20.73$  kcal/mol;  $\Delta G^f([\text{La}(\text{hfac})_3][\text{Al}(\text{acacBr}_3)_3]) = -14.15$  kcal/mol; accordingly, the complex in which  $\mathbf{L}_{Al} = \text{acacCl}_3$  should be stable ( $\Delta G^f < \Delta G_{\text{st}}$ ), whereas the one in which  $\mathbf{L}_{Al} = \text{acacBr}_3$  should not form ( $\Delta G^f > \Delta G_{\text{unst}}$ ), and the reason is entirely due to entropic factors.

Since rotational and translational contributions are roughly the same for every system of this nature and size (see Table 3), the difference must lie in the vibronic contribution to the overall entropy. A thorough inspection of the vibronic structure of the mononuclear and dinuclear complexes highlights a peculiar situation. Normal modes with frequencies below  $\sim 100$   $\text{cm}^{-1}$  are treated in the rigid-rotor-harmonic-oscillator approximation<sup>40</sup> and contribute equally in the dinuclear complex and in the separate fragments, while vibrations with frequencies above  $\sim 200$   $\text{cm}^{-1}$  are not thermally accessible at RT ( $k_B T$  at 298.15 K = 207  $\text{cm}^{-1}$ ) and therefore do not contribute to the vibrational entropy in a significant manner. Thus, vibrations with energy between 100 and 200  $\text{cm}^{-1}$  seem to play a leading role in determining the entropic stabilisation or destabilisation of the dinuclear complexes. Specifically, if the dinuclear complex normal modes number in this region is larger than the sum of those of the mononuclear complexes, its vibronic entropy results higher than that corresponding to the sum of the individual fragments and this destabilises its formation. To verify such a conjecture, the entropic term  $T\Delta S$  at 298.15K has been estimated against the difference between the number of vibrational modes with energy in the 100-200  $\text{cm}^{-1}$  range in the dinuclear complex and the sum of the vibrational modes in the isolated fragments (Figure 8). Systems with  $\mathbf{L}_{Al} = \text{tfac}$  and  $\mathbf{L}_{Al} = \text{acacI}_3$  were also included for completeness.

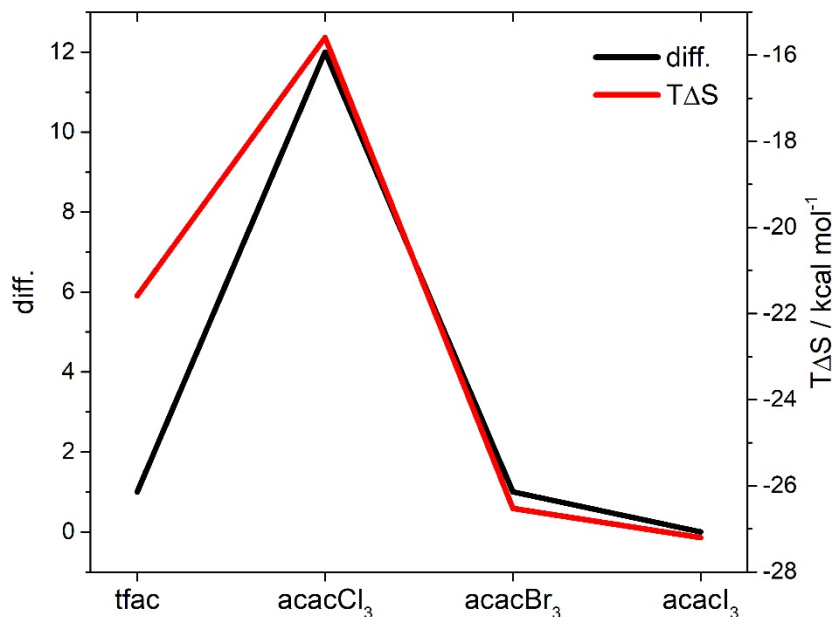


**Figure 8.** Correlation between the entropic term  $T\Delta S$  and the difference in the number of vibrational normal modes in the dinuclear complexes and the sum of the normal modes in the isolated fragments, with energy in the  $100\text{-}200\text{ cm}^{-1}$  range. A higher number of normal modes in the dinuclear complex compared to the isolated fragments entails a higher vibrational entropy and therefore a less stable complex.

The inspection of Figure 8 confirms that, even restricting the attention to the number of vibrations in the  $100\text{-}200\text{ cm}^{-1}$  range, and disregarding both the energies and the intensities of the normal modes, the correlation is well evident. We tentatively attribute such a behaviour to some particular “goldilocks” condition in the  $[\text{La}(\text{hfac})_3][\text{Al}(\text{acacCl}_3)_3]$  complex, where the  $\text{acacCl}_3$  ligand has just the correct mass and inertia to resonate with some of the vibrational modes of  $\text{hfac}$ , thus enabling a higher degree of “cross-talk” between the two moieties and increasing the number of vibrations for the dinuclear complex in this energetic region, whereas F, Br, and I are either too light or too heavy to allow this type of resonance and the normal modes remain akin to those of the isolated fragments (Figure 9).

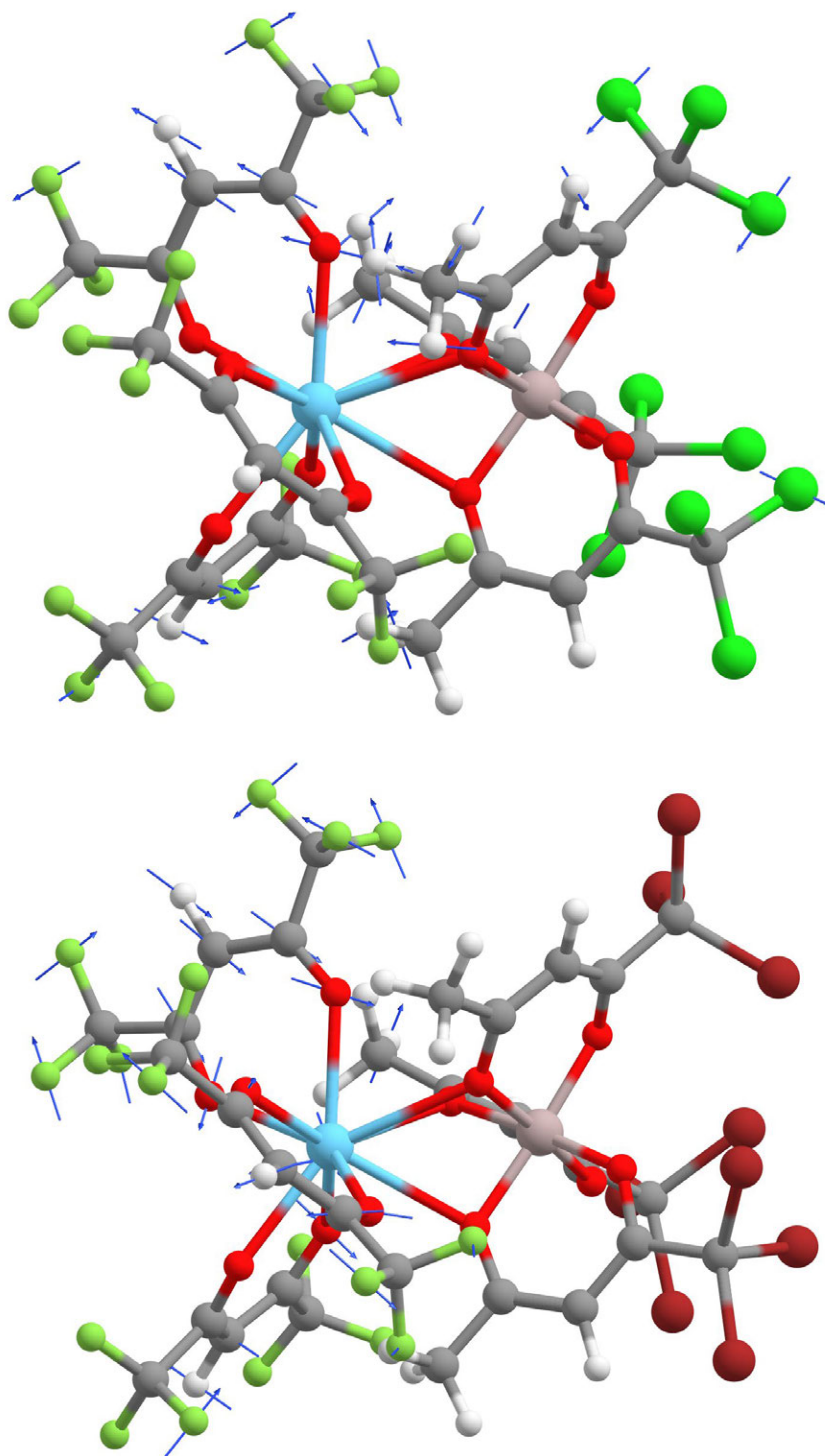


**Figure 9.** Comparison between the same type of normal mode in  $[Eu(hfac)_3][Al(acacCl_3)_3]$  (top) and  $[Eu(hfac)_3][Al(acacBr_3)_3]$  (bottom). Displacement vectors are highlighted as blue arrows. It can be seen that in the chlorinated complex the vibration involves both the  $L_{Eu}$  and  $L_{Al}$  ligands, whereas in the bromated complex the vibration is entirely localized on the  $L_{Eu}$  ligand. This resonance might be the deciding factor contributing to the higher number of vibrations in the chlorinated complex compared to the others. Atom colour code is as follows: grey = C; red = O; pale green = F; blue = Eu; pink = Al; white = H; brown = Br; bright green = Cl.

## 8.2 Effects of different lanthanides on the coordination topology

Even though the substitution of Eu with La simplifies the SCF convergence (no unpaired electrons), speeds up numerical experiments and correctly predicts the stability of heterodinuclear Eu-Al complexes, it prevents the identification of subtle differences determined by the specific lanthanide ion considered.

In particular, it was noticed from X-ray crystallographic structures that, if the 8-hydroxyquinoline-N-oxide (hqNO) ligand is taken as  $L_{Al}$ , with hfac as  $L_{Ln}$ , the Ln-Al heterodinuclear complexes with Ln = Eu, Gd, and Er all form, but the  $[Er(hfac)_3][Al(hqNO)_3]$  shows only two oxygen atoms involved in a bridge bond, instead of three (Figure 10).

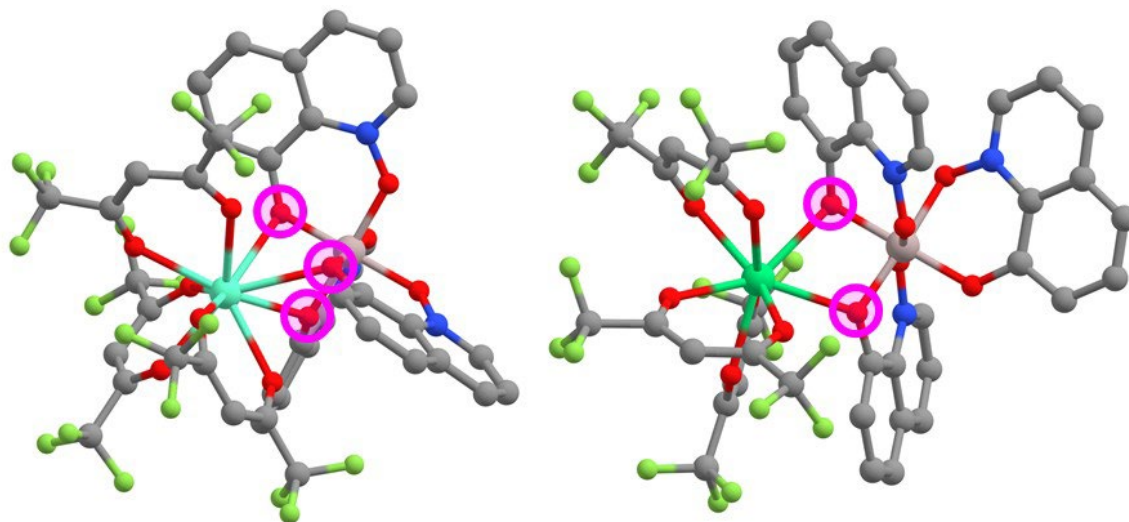


**Figure 10.** Comparison between the coordination topology of  $[Eu(hfac)_3][Al(hqNO)_3]$  (left) and  $[Er(hfac)_3][Al(hqNO)_3]$  (right). Bridging oxygen atoms in both cases have been highlighted in magenta. Atom colour code is as follows: grey = C; red = O; pale green = F; blue = N; pink = Al; turquoise = Eu; bright green = Er. Hydrogen atoms have been omitted to improve clarity.

DFT calculations were able to capture this specific behaviour. The formation free Gibbs energy of the heterodinuclear complex featuring Eu or Gd, in which three oxygen atoms bridge the metals, are indeed more negative than the corresponding systems with only two bridge atoms. The opposite is true for the system featuring Er, for which the complex with 2 bridging oxygens has a lower energy than the one with 3 bridges (Table 4).

**Table 4.** Calculated formation enthalpies, entropies ( $T = 298.15$  K), and Gibbs free energies for various  $[Ln(hfac)_3][Al(hqNO)_3]$  complexes, where  $Ln = La, Eu, Gd, Er, Y$ . The suffix  $-\mu_3(-\mu_2)$  indicates that the complex features three(two) bridging oxygen atoms. The numbers in parentheses refer to the difference between the complex with two bridging oxygens and the one with three, for the thermodynamic quantity of interest.

	$\Delta H^f$ (kcal/mol)	$-T\Delta S^f$ (kcal/mol)	$\Delta G^f$ (kcal/mol)
$[La(hfac)_3][Al(hqNO)_3]-\mu_3$	-52.67	26.18	-26.49
$[La(hfac)_3][Al(hqNO)_3]-\mu_2$	-46.30 (+6.36)	23.77 (-2.41)	-22.53 (+3.96)
$[Eu(hfac)_3][Al(hqNO)_3]-\mu_3$	-42.46	22.43	-20.03
$[Eu(hfac)_3][Al(hqNO)_3]-\mu_2$	-38.36 (+4.10)	22.18 (-0.25)	-16.18 (+3.85)
$[Gd(hfac)_3][Al(hqNO)_3]-\mu_3$	-42.94	15.10	-27.83
$[Gd(hfac)_3][Al(hqNO)_3]-\mu_2$	-39.82 (+3.12)	15.91 (+0.80)	-23.91 (+3.92)
$[Er(hfac)_3][Al(hqNO)_3]-\mu_3$	-50.04	21.01	-29.02
$[Er(hfac)_3][Al(hqNO)_3]-\mu_2$	-53.02 (-2.98)	22.08 (+1.07)	-30.94 (-1.92)
$[Y(hfac)_3][Al(hqNO)_3]-\mu_3$	-45.01	27.22	-17.79
$[Y(hfac)_3][Al(hqNO)_3]-\mu_2$	-42.78 (+2.22)	25.98 (-1.24)	-16.81 (+0.98)

The enthalpic contribution is the primary factor in deciding the stability of the complex with three or two bridging oxygens. In particular, the complexes featuring Er are the only ones for which the system with two bridges has a more negative formation enthalpy than that with three bridges. It was not possible to identify the specific reason for the different behaviour on the basis of charge distributions or geometries, as no marked difference was found in the systems with Er compared with the ones with Eu and Gd. We suspected the smaller ionic radius of  $Er^{3+}$  (1.00 Å)<sup>41</sup> could be a reason, when compared to the slightly larger  $Eu^{3+}$  (1.07 Å)<sup>41</sup> and  $Gd^{3+}$  (1.06 Å)<sup>41</sup> ions. However, when substituting another trivalent ion with a very similar ionic radius such as  $Y^{3+}$  (1.015 Å),<sup>41</sup> the system with three bridging atoms was again the most stable one, therefore indicating there must be other aspects at play. Another interesting aspect is the confirmation that La is indeed a good substitute for Eu/Gd despite its significantly larger ionic radius (1.18 Å).<sup>41</sup> The enthalpic and entropic contributions are slightly overestimated, but the overall Gibbs free energy is very similar to the systems with Eu/Gd thanks to a cancellation of errors.

### 8.3 Fukui function and bridging atom selectivity

Deeper insights into the nature of the bridge between the two fragments and the role played by the ligands in the formation of the dinuclear complex, have been obtained by carrying out a further series of calculations devoted to the estimation of the condensed Fukui function for the  $\text{Eu}^{3+}$  centre in the case of the  $\text{Eu}(\mathbf{L}_{\text{RE}})_3$  fragment, and for the bridge oxygen atoms in the case of the  $\text{Al}(\mathbf{L}_{\text{Al}})_3$  moiety.

The Fukui function reflects the reactivity of a site and was defined by Parr and Yang<sup>42</sup> as the functional derivative of the chemical potential  $\mu$  with respect to a change in the external potential  $v(r)$ , taken at a constant number of electrons  $N$ :

$$f(r) = \left[ \frac{\delta\mu}{\delta v(r)} \right]_N \quad (126)$$

Due to a discontinuity for integer number of electrons, it is not possible to exactly evaluate this quantity.<sup>43</sup> However, it is possible to evaluate the chemical potential from either side of this discontinuity. This is equivalent to a situation in which the molecule either loses ( $\mu^-$ ) or gains ( $\mu^+$ ) one electron; at  $T = 0$  K, these are exactly the ionization potential  $I$  and the electron affinity  $A$ , respectively. By considering  $I = E(N) - E(N - 1)$  and  $A = E(N + 1) - E(N)$ , where  $E(M)$  is the total energy of the system with  $M$  electrons, we can define the Fukui function for the molecule when either losing or accepting an electron, as the difference in electron density  $\rho(r)$  in the two states (at the same molecular geometry):

$$\begin{aligned} f^-(r) &= \rho_N(r) - \rho_{N-1}(r) \\ f^+(r) &= \rho_{N+1}(r) - \rho_N(r) \end{aligned} \quad (127)$$

This now assumes a distinct chemical meaning, with  $f^-(r)$  ( $f^+(r)$ ) corresponding to the capability of losing (gaining) an electron, and then identifiable with the nucleophilic (electrophilic) character of a molecule. One last step involves the discretization<sup>44</sup> of the Fukui function in atomic contributions based on a Mulliken population analysis. The condensed Fukui function on the atom  $k$  is defined as:

$$\begin{aligned} f_k^- &= q_k(N - 1) - q_k(N) \\ f_k^+ &= q_k(N) - q_k(N + 1) \end{aligned} \quad (128)$$

where  $q_k$  is the Mulliken atom charge of atom  $k$ , calculated either in the neutral state with  $N$  electrons, or in the positively/negatively charged molecule ( $N - 1$  /  $N + 1$  electrons). Note that the sign is inverted with respect to the corresponding continuous Fukui functions, as we are considering electrons bearing a negative charge.

We started by studying two complexes, in which  $\mathbf{L}_{\text{Eu}} = \text{hfac}$  and  $\mathbf{L}_{\text{Al}} = \text{meac, sal}$  (Figure 11).

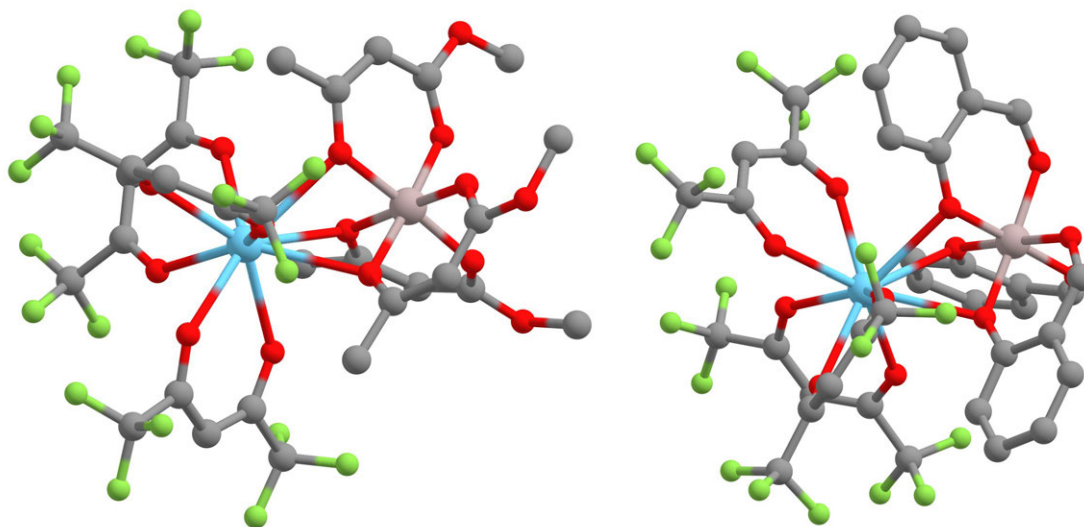


**Figure 11.** X-ray crystallographic structures of  $[\text{Eu}(\text{hfac})_3][\text{Al}(\text{meac})_3]$  (left) and  $[\text{Eu}(\text{hfac})_3][\text{Al}(\text{sal})_3]$  (right). Atom colour code is as follows: grey = C; red = O; green = F; blue = Eu; pink = Al. Hydrogen atoms have been omitted to improve clarity.

The X-ray crystallographic structure of  $[\text{Eu}(\text{hfac})_3][\text{Al}(\text{meac})_3]$  shows that the methoxy fragment of all three  $\text{L}_{\text{Al}}$  ligands points away from the centre of the complex, suggesting that the system tends to reduce steric interactions. However, the structure of  $[\text{Eu}(\text{hfac})_3][\text{Al}(\text{sal})_3]$  seems to contradict this, as the bulky aromatic portion of the salicylaldehyde ligand is pointed towards the rest of the complex.

The 3D plot of the nucleophilic Fukui function  $f^-(r)$  clears this issue and allows the identification of the more nucleophilic oxygen atoms in both  $\text{Al}(\text{meac})_3$  and  $\text{Al}(\text{sal})_3$  as the ones with the larger value of  $f^-(r)$  (Figure 12). These stronger Lewis bases are the preferred ones in the formation of the Ln-O-Al bridge.



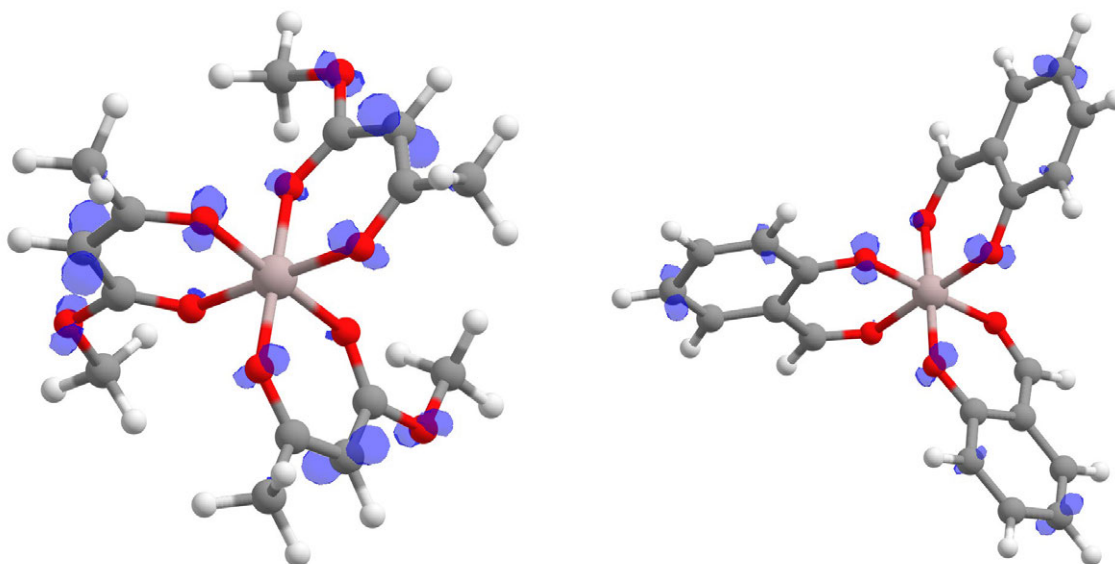


**Figure 12.** Fukui function plot for  $\text{Al}(\text{meac})_3$  (left), and  $\text{Al}(\text{sal})_3$  (right). Atom colour code is as follows: grey = C; red = O; white = H; pink = Al.

A more quantitative evaluation of the nucleophilic character of each oxygen atom is given by the nucleophilic condensed Fukui function  $f_k^-$ . In  $\text{Al}(\text{meac})_3$   $f_k^- = 0.036$  for the bridging oxygen, while  $f_k^- = 0.017$  for the other. Similarly, in  $\text{Al}(\text{sal})_3$   $f_k^- = 0.029$  for the bridging oxygen, while  $f_k^- = 0.015$  for the other. This is perfectly consistent with the X-ray crystallographic structures and highlights that steric factors for these relatively small ligands are much less important than the Lewis base character of the bridging atom. It is worth stressing that these calculations can be carried out on the small mononuclear Al complex, without needing to optimise the geometry for the much larger Ln-Al dinuclear system, massively reducing the computational requirements for these types of numerical simulations.

An edge case is presented by the  $[\text{Eu}(\text{hfac})_3][\text{Al}(\text{naf})_3]$  complex. The evaluation of the condensed Fukui function for  $\text{Al}(\text{naf})_3$  reveals a minimal difference between the two oxygen atoms ( $f_k^- = 0.018$  for the bridging oxygen as given by the X-ray crystallographic structure vs.  $f_k^- = 0.016$  for the other). To confirm whether such a small variance is sufficient to correctly identify the bridging atom, both geometries were fully optimised at the DFT/PBE level of theory and their energies evaluated (Figure 13). The form in which the hydroxyl oxygen bridges the two ions (*i.e.*, the X-ray crystallographic structure) is 5.45 kcal/mol more stable than the alternative form, which at room temperature would result in a 99.99% fraction of the most stable isomer when considering a Boltzmann distribution.

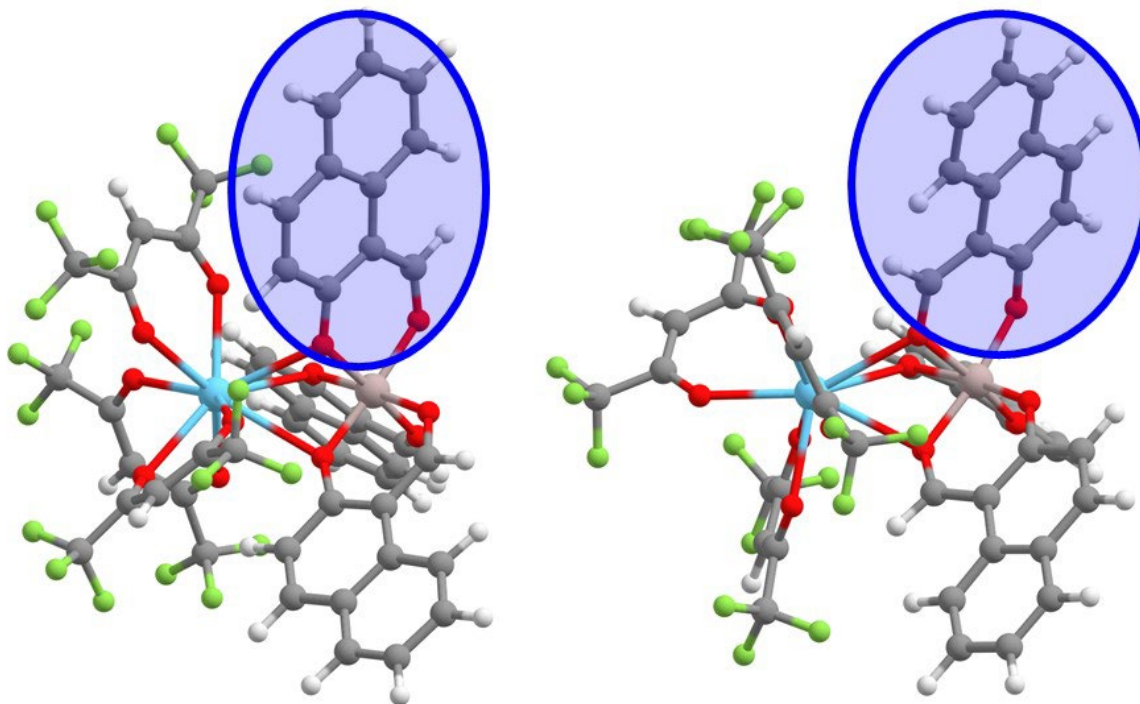


**Figure 13.** X-ray crystallographic structure of  $[Eu(hfac)_3][Al(naf)_3]$  (left) and alternative isomer featuring the other  $L_{Al}$  oxygen atom in the bridge (right). Atom colour code is as follows: grey = C; red = O; green = F; blue = Eu; pink = Al. The two different orientations of the naf ligand have been highlighted.

The relative Brønsted base character of the two oxygens in each ligand was also evaluated, to see whether it correlates with the relative strength as Lewis bases. A thorough and quantitative evaluation of the Brønsted base strength would involve calculating the relative energy of the neutral and deprotonated forms in water, by taking into account the contribution of the free proton as well, which is not straightforward. However, it is possible to evaluate the relative acid/base character of these two oxygens by simply optimizing the geometry of the two forms in which either oxygen binds the hydrogen atom. In these two limit cases one oxygen behaves as the base, while the other as the acid, rendering possible a direct comparison. For all three ligands, when starting from the geometry in which the less nucleophilic oxygen atom bears the proton, the optimization inevitably converges to the geometry in which the proton is transferred to the more nucleophilic one, clearly indicating that the latter is also a much stronger Brønsted base (Figure 14).

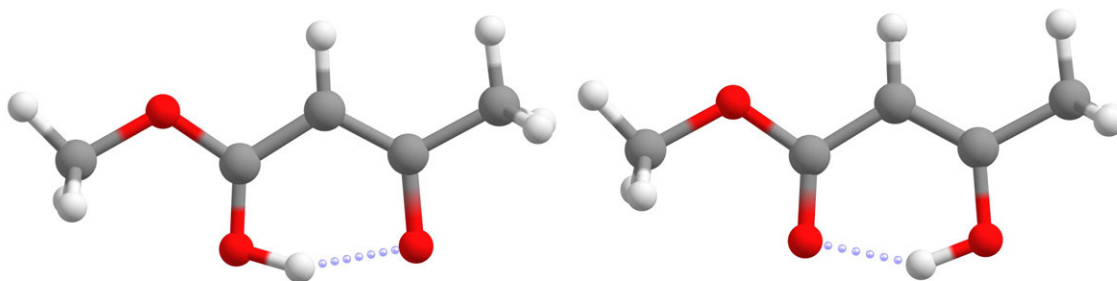


**Figure 14:** Evaluation of the Brønsted base character of the two oxygen atoms in the meac ligand. When starting from the geometry in which the more nucleophilic O=C-CH<sub>3</sub> oxygen atom is deprotonated (left), the final geometry has this atom protonated (right), indicating that it is a significantly stronger Brønsted base than the O=C-OCH<sub>3</sub> one.

To quantify the relative energies of these two forms, a constrained geometry optimization in which the proton is fixed at the O-H distance seen in the other form has been carried out. For meac, sal, and naf, the less stable form was found to be 8.67, 11.98, and 6.80 kcal/mol higher in energy than the more stable one, respectively. The Brønsted and Lewis character of different species cannot be correlated rigorously in principle; nevertheless, it might be worth evaluating if interested in a rapid pre-screening of a ligands set and aimed to identify which side the ligand is more likely to place itself as a bridge. Corresponding calculations on the isolated ligands are in fact very simple and quick.

An interesting pattern emerges when comparing the condensed Fukui function with the dinuclear complex formation energy, taken as the purely electronic term  $E_{el}$ , which ensures that only electronic effects are considered disregarding the vibronic or entropic ones, and then isolating the ligand contributions from the strength of the bridging bond (Figure 15).

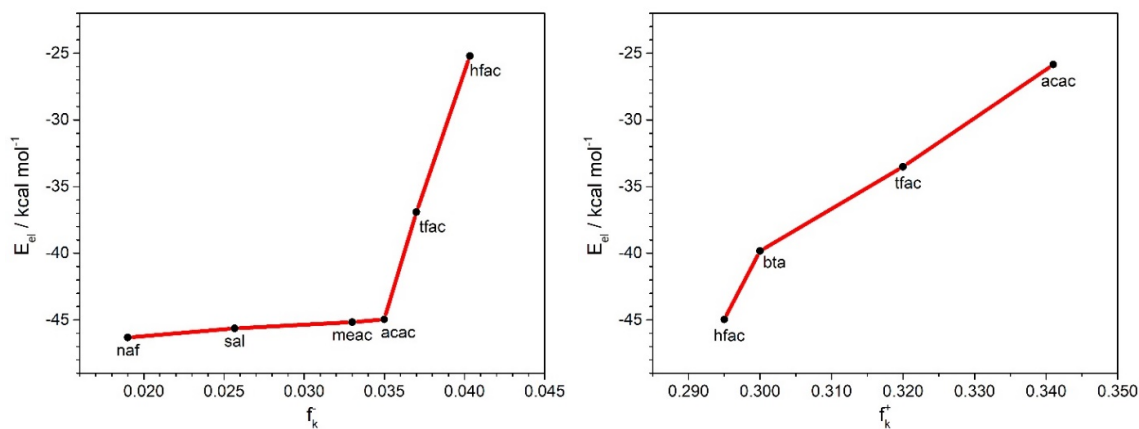


**Figure 15.** Correlation between the formation electronic energy  $E_{el}$  for the dinuclear complex and the condensed Fukui function  $f_k^\pm$  for the bridging oxygen atoms in the Al(LAl)<sub>3</sub> fragment (left) or for the Eu<sup>3+</sup> ion in the Eu(LEu)<sub>3</sub> one (right). For the left and right plots, the Eu(hfac)<sub>3</sub> and Al(acac)<sub>3</sub> fragments are maintained throughout, while the other moiety is changed.

Despite the fact that the more nucleophilic oxygen atom is the favourite bridging unit due to its higher nucleophilicity, there is an inverse proportionality between the condensed Fukui function for this oxygen atom and the stability of the dinuclear complex (note that a less

negative formation energy means a less stable complex). This is consistent with the electrostatic nature of the bond between the  $\text{Eu}^{3+}$  centre and the surrounding ligands, for which the hard and soft acid/base (HSAB) concept predicts a stronger bond for harder pairs (*i.e.*, smaller condensed Fukui functions).

Indeed, the progressive fluorination of the acac ligand ( $\text{acac} \rightarrow \text{tfac} \rightarrow \text{hfac}$ ) increases both the condensed Fukui function for the oxygen bridge atom and the electronic formation energy of the complex in an almost perfectly linear way (Figure 15, left). This linearity is somewhat maintained even for ligands with a very different chemical nature (naf, sal vs. meac, acac) but the slope is significantly lower. It appears there is a threshold around 0.035 electric charge units (acac), below which the bridge is sufficiently stabilized, and above which the ligand is too soft (in HSAB terms) to provide a strong bond.

This is confirmed by an analogous evaluation, in which  $L_{\text{Eu}}$  is changed (Figure 15, right). This indirectly affects the  $\text{Eu}^{3+}$  ion and its Lewis acid character, which is represented by the nucleophilic condensed Fukui function  $f_k^+$ . In this case, a higher degree of fluorination ( $\text{acac} \rightarrow \text{tfac} \rightarrow \text{hfac}$ ) progressively reduces the lanthanide ion of electron density, rendering it a harder unit (in HSAB terms); this translates to a stronger bond between the ion and the bridge acac oxygen atom, as expected.

## 8.4 Materials and instrumentation (experimental characterisation)

The studies presented in this chapter were rendered possible by the collaboration with the research group of Prof. Luca Labella at the University of Pisa, who has recently started investigating heterometallic Ln-Al complexes in which  $\text{Ln} = \text{Eu}, \text{Tb}, \text{Gd}$ . All experimental syntheses and characterisations have been collected by the aforementioned group. Optical (absorption and luminescence studies) have been carried out by the research group of Prof. Lidia Armelao at the University of Padova. Please note these are preliminary results, as this is still an ongoing research project.

All manipulations were performed under a dinitrogen atmosphere using anhydrous solvents.  $[\text{Al}(\text{L}_{\text{Al}})_3]$  complexes were synthesized according to the literature.<sup>25,45</sup> Anhydrous  $[\text{Ln}(\text{L}_{\text{Ln}})_3]$  species ( $\text{Ln}^{3+} = \text{Eu}^{3+}, \text{Gd}^{3+}$  and  $\text{Er}^{3+}$ ) were obtained by dehydration of the corresponding dihydrate complex  $[\text{Ln}(\text{L}_{\text{Ln}})_3(\text{H}_2\text{O})_2]$  according to the procedure reported in the literature.<sup>46</sup> FTIR spectra on solid samples were recorded with a Perkin–Elmer “Spectrum One” spectrometer, equipped with an ATR accessory.  $^1\text{H}$  and  $^{19}\text{F}$  NMR spectra were recorded with a Bruker “Avance DRX400” spectrometer. Chemical shifts were measured in ppm ( $\delta$ ) from TMS by residual solvent peaks for  $^1\text{H}$ , from  $\text{CFCl}_3$  for  $^{19}\text{F}$ . Elemental analysis (C, H, N) were performed with an Elementar “vario MICRO cube” instrument at Dipartimento di Chimica e Chimica Industriale, Università di Pisa. Absorption spectra were recorded using a Cary 5000 UV-Vis Spectrometer equipped with a diffuse reflectance accessory consisting of an integrating sphere. The spectra were acquired and plotted as the Kubelka–Munk function  $F(R)$ .<sup>47</sup> Luminescence spectra of sample powders were recorded with a Horiba Jobin-Yvon *Fluorolog-3* spectrofluorimeter in a front-face acquisition geometry. The instrument was equipped with a double-grating monochromator in both the excitation and emission sides coupled to a *R928P* Hamamatsu photomultiplier and a 450 W Xe arc lamp as the

excitation source. Emission spectra were corrected for detection and optical spectral response of the spectrofluorimeter supplied by the manufacturer. The excitation spectra were corrected for the spectral distribution of the lamp intensity using a photodiode reference detector. The luminescence lifetimes ( $\tau_{\text{exp}}$ ) were measured with an experimental uncertainty of  $\pm 10\%$ , using a pulsed Xe lamp with variable repetition rate and elaborated with standard software fitting procedures. Absolute photoluminescence quantum yields on samples powders were calculated from corrected emission spectra obtained by means of an integrating sphere.

## 8.5 Computational details

DFT calculations were carried out by using the Orca suite of programs (version 4.2.0).<sup>48</sup> The hybrid B3LYP functional<sup>49–52</sup> coupled to an all-electron triple- $\zeta$  quality Ahlrichs basis set with one polarization function (def2-TZVP)<sup>53</sup> for all atoms were employed to optimize the ground state molecular structures of the isolated ligands, while the complexes were optimized using the GGA PBE functional;<sup>54–57</sup> Coulomb and exchange integrals in hybrid calculations were approximated by using the Resolution of Identity approximation with the def2/JK auxiliary basis set.<sup>58</sup> Dispersion corrections were included by adopting Grimme's DFT-D3 method.<sup>59</sup> As the lanthanide primarily interacts with the ligands via electrostatic forces and the eventual  $4f$  electrons do not actively take part in the complexation, Eu was substituted with La to obtain a closed-shell system and simplify the SCF convergence in the geometry optimization, unless otherwise specified. The Fukui functions were evaluated by carrying out a single-point calculation on the ground state geometry, first considering the neutral system and then considering it as singly charged, in a doublet state (one unpaired electron). The condensed Fukui function was then calculated as the difference between the Mulliken atom charge in the two conditions, for the atoms of interest.

## References

- (1) Pierre, V. C.; Botta, M.; Aime, S.; Raymond, K. N. *J. Am. Chem. Soc.* **2006**, *128* (29), 9272–9273.
- (2) Crowston, B. J.; Shipp, J. D.; Chekulaev, D.; McKenzie, L. K.; Jones, C.; Weinstein, J. A.; Meijer, A. J. H.; Bryant, H. E.; Natrajan, L.; Woodward, A.; et al. *Dalt. Trans.* **2019**, *48* (18), 6132–6152.
- (3) Li, H.; Lan, R.; Chan, C. F.; Jiang, L.; Dai, L.; Kwong, D. W. J.; Lam, M. H. W.; Wong, K. L. *Chem. Commun.* **2015**, *51* (74), 14022–14025.
- (4) Al-Busaidi, I. J.; Ilmi, R.; Dutra, J. D. L.; Oliveira, W. F.; Haque, A.; Al Rasbi, N. K.; Marken, F.; Raithby, P. R.; Khan, M. S. *Dalt. Trans.* **2021**, *50* (4), 1465–1477.
- (5) Tropiano, M.; Kilah, N. L.; Morten, M.; Rahman, H.; Davis, J. J.; Beer, P. D.; Faulkner, S. *J. Am. Chem. Soc.* **2011**, *133* (31), 11847–11849.
- (6) Shiga, T.; Ohba, M.; Ōkawa, H. *Inorg. Chem.* **2004**, *43* (14), 4435–4446.
- (7) Yamaguchi, T.; Sunatsuki, Y.; Ishida, H.; Kojima, M.; Akashi, H.; Re, N.; Matsumoto, N.; Pochaba, A.; Mrozin, J.; Farmacia, F. **2008**, *47* (13), 5736–5745.
- (8) Shen, F. X.; Li, H. Q.; Miao, H.; Shao, D.; Wei, X. Q.; Shi, L.; Zhang, Y. Q.; Wang, X. Y. *Inorg. Chem.* **2018**, *57* (24), 15526–15536.
- (9) Yang, Q. Y.; Li, K.; Luo, J.; Pan, M.; Su, C. Y. *Chem. Commun.* **2011**, *47* (14), 4234–4236.
- (10) Beer, P. D.; Szemes, F.; Passaniti, P.; Maestri, M.; Ox, U. K.; Ciamician, C. G.; Uni, V.; Selmi, V.; Bologna, I.-. **2004**, *43* (13), 3965–3975.
- (11) Zhu, Q. Y.; Zhou, L. P.; Sun, Q. F. *Dalt. Trans.* **2019**, *48* (14), 4479–4483.
- (12) Ziessel, R.; Diring, S.; Kadjane, P.; Charbonnière, L.; Retailleau, P.; Philouze, C. *Chem. - An Asian J.* **2007**, *2* (8), 975–982.
- (13) Mori, F.; Nyui, T.; Ishida, T.; Nogami, T.; Choi, K. Y.; Nojiri, H. *J. Am. Chem. Soc.* **2006**, *128* (5), 1440–1441.
- (14) Armelao, L.; Belli Dell'Amico, D.; Bottaro, G.; Bellucci, L.; Labella, L.; Marchetti, F.; Mattei, C. A.; Mian, F.; Pineider, F.; Poneti, G.; et al. *Dalt. Trans.* **2018**, *47* (25), 8337–8345.
- (15) Costes, J. P.; Dahan, F.; Dupuis, A.; Laurent, J. P. *Inorg. Chem.* **1997**, *36* (16), 3429–3433.
- (16) Gao, T.; Yan, P. F.; Li, G. M.; Hou, G. F.; Gao, J. S. *Inorganica Chim. Acta* **2008**, *361* (7), 2051–2058.
- (17) Visinescu, D.; Alexandru, M. G.; Madalan, A. M.; Pichon, C.; Duhayon, C.; Sutter, J. P.; Andruh, M. *Dalt. Trans.* **2015**, *44* (38), 16713–16727.
- (18) Øwre, A.; Vinum, M.; Kern, M.; van Slageren, J.; Bendix, J.; Perfetti, M. *Inorganics* **2018**, *6* (3), 72–81.
- (19) Lindoy, L. F.; Lip, H. C.; Louie, H. W.; Drew, M. G. B.; Hudson, M. J. *J. Chem. Soc. Chem. Commun.* **1977**, No. 21, 778.
- (20) Ramade, I.; Kahn, O.; Jeannin, Y.; Robert, F. *Inorg. Chem.* **1997**, *36* (5), 930–936.
- (21) Rogachev, A. Y.; Mironov, A. V.; Nemukhin, A. V. *J. Mol. Struct.* **2007**, *831* (1–3), 46–54.
- (22) Kameta, N.; Imura, H.; Ohashi, K.; Aoyama, T. *Inorg. Chem. Commun.* **1999**, *2* (4), 124–127.
- (23) Kameta, N.; Imura, H.; Ohashi, K.; Aoyama, T. *Polyhedron* **2002**, *21* (8), 805–810.
- (24) Sanwaria, A. R.; Nagar, M.; Bohra, R.; Chaudhary, A.; Mobin, S. M.; Mathur, P.; Choudhary, B. L. *RSC Adv.* **2014**, *4* (57), 30081–30089.
- (25) Lichtenberger, R.; Puchberger, M.; Baumann, S. O.; Schubert, U. *J. Sol-Gel Sci. Technol.* **2009**, *50* (2), 130–140.
- (26) Li, H.; Zhang, F.; Wang, Y.; Zheng, D. *Mater. Sci. Eng. B Solid-State Mater. Adv.*

- Technol.* **2003**, *100* (1), 40–46.
- (27) Lincoln, S. F. *Helv. Chim. Acta* **2005**, *88* (3), 523–545.
- (28) Yamamoto, M.; Nakanishi, T.; Kitagawa, Y.; Seki, T.; Ito, H.; Fushimi, K.; Hasegawa, Y. *Bull. Chem. Soc. Jpn.* **2018**, *91* (1), 6–11.
- (29) Xu, H.-B.; Chen, X.-M.; Zhang, Q.-S.; Zhang, L.-Y.; Chen, Z.-N. *Chem. Commun.* **2009**, *2* (47), 7318.
- (30) Wang, S. T.; Zhang, S. H.; Fang, W. H.; Zhang, J. *Inorg. Chem.* **2020**, *59* (18), 13760–13766.
- (31) Basiuk, V. A. *J. Comput. Theor. Nanosci.* **2005**, *2* (3), 370–377.
- (32) Spinello, A.; Terenzi, A.; Barone, G. *J. Inorg. Biochem.* **2013**, *124*, 63–69.
- (33) Tripathi, S.; Islam, S.; Seth, S. K.; Bauzá, A.; Frontera, A.; Mukhopadhyay, S. *CrystEngComm* **2020**, *22* (47), 8171–8181.
- (34) Manna, P.; Seth, S. K.; Das, A.; Hemming, J.; Prendergast, R.; Helliwell, M.; Choudhury, S. R.; Frontera, A.; Mukhopadhyay, S. *Inorg. Chem.* **2012**, *51* (6), 3557–3571.
- (35) Bhattacharyya, A.; Bauzá, A.; Sproules, S.; Natrajan, L. S.; Frontera, A.; Chattopadhyay, S. *Polyhedron* **2017**, *137*, 332–346.
- (36) Pfltscher, M.; Wysoglad, J.; Gutmann, J. S.; Giese, M. *RSC Adv.* **2019**, *9* (15), 8444–8453.
- (37) Wu, L.; Nieto-Ortega, B.; Naranjo, T.; Pérez, E. M.; Cabanillas-Gonzalez, J. *J. Phys. Chem. C* **2019**, *123* (27), 16596–16601.
- (38) Matsuhira, T.; Sakai, H. *Biomacromolecules* **2021**, *22* (5), 1944–1954.
- (39) Zhao, Y.; Truhlar, D. G. *Theor. Chem. Acc.* **2008**, *120* (1–3), 215–241.
- (40) Grimme, S. *Chem. - A Eur. J.* **2012**, *18* (32), 9955–9964.
- (41) Shannon, R. D.; Prewitt, C. T. *Acta Crystallogr. Sect. B Struct. Crystallogr. Cryst. Chem.* **1969**, *25* (5), 925–946.
- (42) Parr, R. G.; Yang, W. *J. Am. Chem. Soc.* **1984**, *106* (14), 4049–4050.
- (43) Perdew, J. P.; Parr, R. G.; Levy, M.; Balduz, J. L. *Phys. Rev. Lett.* **1982**, *49* (23), 1691–1694.
- (44) Yang, W.; Mortier, W. J. *J. Am. Chem. Soc.* **1986**, *108* (19), 5708–5711.
- (45) Sanwaria, A. R.; Nagar, M.; Bohra, R.; Chaudhary, A.; Mobin, S. M.; Mathur, P.; Choudhary, B. L. *RSC Adv.* **2014**, *4* (57), 30081–30089.
- (46) Armelao, L.; Belli Dell’Amico, D.; Bellucci, L.; Bottaro, G.; Labella, L.; Marchetti, F.; Samaritani, S. *Polyhedron* **2016**, *119*, 371–376.
- (47) De Bellis, J.; Bellucci, L.; Bottaro, G.; Labella, L.; Marchetti, F.; Samaritani, S.; Belli Dell’Amico, D.; Armelao, L. *Dalt. Trans.* **2020**, *49* (18), 6030–6042.
- (48) Neese, F. *Wiley Interdiscip. Rev. Comput. Mol. Sci.* **2018**, *8* (1), 4–9.
- (49) Lee, C.; Yang, W.; Parr, R. G. *Phys. Rev. B* **1988**, *37* (2), 785–789.
- (50) Vosko, S. H.; Wilk, L.; Nusair, M. *Can. J. Phys.* **1980**, *58* (8), 1200–1211.
- (51) Stephens, P. J.; Devlin, F. J.; Chabalowski, C. F.; Frisch, M. J. *J. Phys. Chem.* **1994**, *98* (45), 11623–11627.
- (52) Becke, A. D. *J. Chem. Phys.* **1993**, *98* (2), 1372–1377.
- (53) Weigend, F.; Ahlrichs, R. *Phys. Chem. Chem. Phys.* **2005**, *7* (18), 3297.
- (54) Perdew, J. P.; Wang, Y. *Phys. Rev. B* **1992**, *45* (23), 13244–13249.
- (55) Perdew, J. P.; Burke, K.; Ernzerhof, M. *Phys. Rev. Lett.* **1996**, *77* (18), 3865–3868.
- (56) Dirac, P. A. M. *Proc. R. Soc. Lond. A* **1929**, *123* (792), 714–733.
- (57) Slater, J. C. *Phys. Rev.* **1951**, *81* (3), 385–390.
- (58) Weigend, F. *J. Comput. Chem.* **2007**, *29*, 167–175.
- (59) Grimme, S.; Antony, J.; Ehrlich, S.; Krieg, H. *J. Chem. Phys.* **2010**, *132* (15).